Defect Chemistry in Halide Perovskites
Material Characterisation and Device Integration

Thi Thuy Nga Phung

Univ.-Diss.

zur Erlangung des akademischen Grades
"doctor rerum naturalium"
(Dr. rer. nat.)
in der Wissenschaftsdisziplin " Materialwissenschaft"

eingereicht an der
Mathematisch-Naturwissenschaftlichen Fakultät
Institut für Chemie
der Universität Potsdam
und
Helmholtz-Zentrum Berlin für Materialien und Energie

Ort und Tag der Disputation: Potsdam, 2020/09/02

Betreuer:

Prof. Dieter Neher

Prof. Antonio Abate

Prof. Iván Mora-Seró

https://doi.org/10.25932/publishup-47652
https://nbn-resolving.org/urn:nbn:de:kobv:517-opus4-476529

Summary

Metal halide perovskites have merged as an attractive class of materials for photovoltaic applications due to their excellent optoelectronic properties. However, the long term stability is a roadblock for this class of material's industrial pathway. Increasing evidence shows that intrinsic defects in perovskite promote material degradation. Consequently, understanding defect behaviours in perovskite materials is essential to further improve device stability and performance. This dissertation, hence, focuses on the topic of defect chemistry in halide perovskites.

The first part of the dissertation gives a brief overview of the defect properties in halide perovskite. Subsequently, the second part shows that doping methylammonium lead iodide with a small amount of alkaline earth metals (Sr and Mg) creates a higher quality, less defective material resulted in high open circuit voltages in both n-i-p and p-i-n architecture. It has been found that the mechanism of doping has two distinct regimes in which a low doping concentration enables the inclusion of the dopants into the lattice whereas higher doping concentrations lead to phase segregation. The material can be more n-doped in the low doping regime while being less n-doped in the high doping regime. The threshold of these two regimes is based on the atomic size of the dopants.

The next part of the dissertation examines the photo-induced degradation in methylammonium lead iodide. This degradation mechanism links closely to the formation and migration of ionic defects. After they are formed, these ionic defects can migrate, however, not freely depending on the defect concentration and their distribution. In fact, a highly concentrated defect region such as the grain boundaries can inhibit the migration of ionic defects. This has implications for material design as perovskite solar cells normally employ a polycrystalline thin-film which has a high density of grain boundary.

The final study presented in this PhD dissertation focuses on the stability of the state-of-the-art triple cation perovskite-based solar devices under external bias. Prolonged bias (more than three hours) is found to promote amorphization in halide perovskite. The amorphous phase is suspected to accumulate at the interfaces especially between the hole selective layer and perovskite. This amorphous phase inhibits the charge collection and severely affects the device performance. Nonetheless, the devices can recover after resting without bias in the dark. This amorphization is attributed to ionic defect migration most likely halides. This provides a new understanding of the potential degradation mechanisms in perovskite solar cells under operational conditions.

Zusammenfassung

Metallhalogenid-Perowskite haben sich aufgrund ihrer hervorragenden optoelektronischen Eigenschaften zu einer attraktiven Materialklasse für die Photovoltaikindustrie entwickelt. Die Langzeitstabilität ist jedoch noch immer ein Hindernis für die industrielle Realisierung dieser Materialklasse. Zunehmend zeigen sich Hinweise dafür, dass intrinsische Defekte im Perowskit die Material-Degradation fördern. Das Verständnis der Defekte im Perowskit ist wichtig, um seine Stabilität und optoelektronische Qualität weiter zu verbessern. Diese Dissertation konzentriert sich daher auf das Thema Defektchemie im Perowskit.

Der erste Teil der Dissertation gibt einen kurzen Überblick über die Defekteigenschaften von Halogenid-Perowskiten. Anschließend zeigt der zweite Teil, dass das Dotieren von Methylammoniumbleiiodid mit einer kleinen Menge von Erdalkalimetallen (Sr und Mg) ein höherwertiges, weniger fehlerhaftes Material erzeugt, was zu hohen Leerlaufspannungen sowohl in der n-i-p als auch in der p-i-n Architektur von Solarzellen führt. Es wurde beobachtet, dass die Dotierung in zwei Domänen stattfindet: eine niedrige Dotierungskonzentration führt zum Einschluss der entsprechenden Elemente in das Kristallgitter ermöglicht, während eine hohe Dotierungskonzentration zu einer Phasentrennung führt. Das Material kann im Niedrigdotierungsbereich mehr n-dotiert sein, während es im Hochdotierungsbereich weniger n-dotiert ist. Die Schwelle dieser beiden Regime hängt von der Atomgröße der Dotierelemente ab.

Der nächste Teil der Dissertation untersucht die photoinduzierte Degradation von Methylammonium-Bleiiodid. Dieser Abbaumechanismus hängt eng mit der Bildung und Migration von defekten zusammen. Nach der Bildung können sich diese in Abhängigkeit von der Defektdichte und ihrer Verteilung bewegen. Demnach kann eine hohe Defektdichte wie an den Korngrenzen eines Perowskitfilms die Beweglichkeit von ionischen Punktdefekten hemmen. Diese Erkenntnis ließe sich auf das zukünftige Materialdesign in der Photovoltaikindustrie anwenden, da die Perowskit-Solarzellen normalerweise einen polykristallinen Dünnfilm mit hoher Korngrenzendichte verwenden.

Die abschließende Studie, die in dieser Dissertation vorgestellt wird, konzentriert sich auf die Stabilität der neuesten „dreifach-kationen“ Perowskit-basierten Solarzellen unter dem Einfluss einer permanent angelegten elektrischen Spannung. Eine längere Betriebsdauer (mehr als drei Stunden permanente Spannung) fördert die Amorphisierung im Halogenid-Perowskiten. Es wird hierbei vermutet, dass sich eine amorphe Phase an den Grenzflächen bildet, insbesondere zwischen der lochselektiven Schicht und dem Perowskit. Diese amorphe Phase hemmt den Ladungstransport und beeinträchtigt die Leistung der Perowskit-Solarzelle erheblich. Sobald jedoch keine Spannung mehr anliegt können sich die Perowskitschichten im Dunkeln bereits nach einer kurzen Pause regenerieren. Die Amorphisierung wird auf die Migration von ionischen Fehlordnungen zurückgeführt, höchstwahrscheinlich auf die Migration von Halogeniden. Dieser Ansatz zeigt ein neues Verständnis des Abbau-Mechanismus in Perowskit-Solarzellen unter Betriebsbedingungen.

Declaration

I here declare that this dissertation is from the author's original works, except the parts which give rightful references to other people's works, and that this dissertation has not been submitted to any other university.

Nga Phung

Berlin, 2020

Table of Contents

List of abbreviation

PCE	Power conversion efficiency
J_{SC}	Short circuit current density
V_{OC}	Open circuit voltage
FF	Fill factor
XPS	X-ray photoemission spectroscopy
HAXPES	Hard X-ray photoelectron spectroscopy
XRD	X-ray diffraction
XRF	X-ray fluorescence
PL	Photoluminesence
EL	Electroluminesence
MA	Methylammonium
FA	Formamidinium
SEM	Scanning electron microscopy
TEM	Transmission electron microscopy
EDX	Energy dispersion X-ray
PSC	Perovskite solar cell
GB	Grain boundary
PV	Photovoltaic
DFE	Defect formation energy
ESL	Electron selective layer
HSL	Hole selective layer
VBM	Valence band maximum
CBM	Conduction band minimum
SRH	Shockley-Read-Hall
DFT	Density Functional Theory
MD	Molecular dynamic
MPPT	Maximum power point tracking
JV	Current density-voltage
NMF	Non-negative matrix factorisation
TPV	Transient photovoltage
CE	Charge extraction
EQE	External quantum efficiency

Chapter 1 Introduction

1.1 Climate change and the important role of solar energy

There is undeniable evidence that anthropogenic greenhouse gases are the main cause of climate change. Climate change has increased the frequency of extreme weather events which cause an enormous loss in human lives, extinction of species and economic damage.[1] Since commencing burning of carbon reserves in the form of underground fossil fuels during the industrial revolution, humans have greatly increased the amount of atmospheric CO_2 (and equivalent gases), as shown in **Figure 1.1** causing the global temperature to soar. As the greenhouse gasses accumulate, the world is observing temperature records one year after another. Without an adequate societal response to this, climate scientists fear that ~4-5°C of global temperature increase will be a significant tipping point for so-called "runaway climate change".[2] Here, positive feedback mechanisms within the planet's climate system would amplify the greenhouse effect, accelerate climate destabilisation, and likely be cataclysmic for life on Earth. Hence, it is vital to shift energy production to renewable technologies to reduce emissions and to have a chance of keeping below a 2°C increase in the global mean temperature.

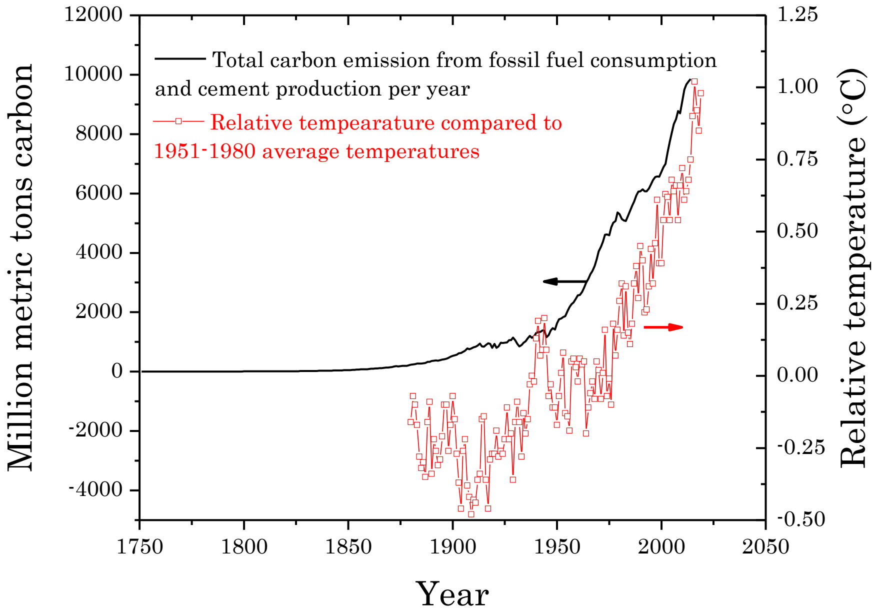

Figure 1.1 The amount of CO_2 equivalent emissions from fossil fuel combustion and cement production (black line). The global surface temperature difference relative to the 1951-1980 average temperature. Data plotted from the US Department of Energy for carbon emission[3] and NASA record for global temperature.[4]

Among all of the renewable energy technologies, solar energy has the highest potential to supply the world energy usage requirement, due to its natural abundance and global availability.[5] As the cost of solar energy has declined sharply in recent decades, the technology has become an even more attractive source for a large share of electricity production. In 2018, total global solar energy capacity was 97 GW, generating 585 TWh.[6] There has been a quick rise of installed capacity of photovoltaics (PV) in China, where new installed capacity is more than half global value in 2017 as the government emphasised on the use of renewable energies to combat negative effects of pollutions. Nonetheless, PV and wind energy only generate less than 7% of total global energy used in 2018 despite having the potential to meet all global energy need[7] whereas usages of fossil fuels (coal and oil) still account for 64% of global energy.[8] Therefore, a massive increase of renewables' share of the global energy mix is required to cut CO_2-equivalent emissions. In the laboratory research, the trajectory for development is towards the exploration of cheaper materials with lower intrinsic energy cost; as well as for more efficient PV devices, which can reduce the cost of electricity production which offers an appealing strategy to enable more rapid uptake of photovoltaic technologies.

1.2 Motivation of the work

1.2.1 Overview of solar energy

The conversion of solar energy to electricity is based on the photovoltaic effect in a light-absorbing semiconductor. A semiconductor can absorb photons with energy above its bandgap, with the energy transferred into the promotion of electrons to the conduction band of the material. These charge carriers can be selectively extracted to the external circuit, with a useful current produced by the completed cell. Various materials can be used as a solar absorber, however, the dominant PV technology is based on silicon, which accounts for 95% of total global PV production.[9] The first generation of solar cells made from silicon was realised in Bell Labs in the 1950s,[10] and today, lab-based monocrystalline silicon cells have reached certified efficiency values of 26.7%.[9] Whereas, the most efficient PV module on the market is 24.4% efficient, with further resistive and optical losses preventing efficiencies for small cells being completely transferrable to modules.[9]

The second type of PV technology is thin-film PV technology such as cadmium telluride (CdTe) or copper indium gallium selenide (CIGS). As per the name suggests, this type of technology has cells with a thickness of a few micrometres as opposed to typical hundreds of micrometres thick Si wafers.[10] Hence, some can be used to produce flexible PV panels, which are lightweight and can be incorporated into the building's architecture. Aside from the two mentioned technologies, III-V solar cells, which consist of elements from group III and V such as gallium and arsenic, are holding the world efficiency record.[9] However, this technology has so far been expensive to produce, generally limiting their use to space applications, which requires a high ratio between power output and mass, or solar concentrators, where only small cells are required.

The fourth category is the new emerging material for PV application. This includes novel material such as organic PV, up/down conversion, quantum dots, and especially metal halide perovskite. Metal halide perovskites have generated a lot of interest as a novel class of material for highly efficient, cheap and easy to produce solar cells. After the first demonstration in 2009,[11] the efficiency of halide perovskite solar cells has progressed quickly owning to its excellent optoelectronic properties. However, as a young technology, more research is required to understand the material behaviours for further optimisation.

1.2.2 Halide perovskites: opportunities and challenges[1]

Perovskite solar cells (PSCs) progressed extremely fast, reaching more than 25% power conversion efficiency (PCE)[12] in a decade from the first demonstration in 2009.[11] The current record PCE of this halide perovskite-based devices surpasses those of established photovoltaic (PV) technologies such as multi-crystalline silicon and cadmium telluride.[12] However, one of the most pressing challenges of the field is the long-term stability under the working condition, *i.e.* light and voltage bias and the intrinsic instability of the material against environmental factors, *i.e.* oxygen and water.

Commercially available PVs, such as silicon modules, can retain most of the initial PCE for years whereas PSCs lose their initial PCE much faster because of a complex combination of external as well as intrinsic degradation factors. For example, the prototypical methylammonium lead iodide ($MAPbI_3$) based PSCs loses its efficiency quickly at 65°C,[13] which is within the range of standard working temperature for solar cells (-40 to +85°C). The PV active black phase of $MAPbI_3$ at high temperature tends to decompose into the thermodynamic favoured precursors - methylammonium iodide and lead iodide.[14] In addition to the thermal instabilities, halide perovskites suffer from atmospheric-induced degradation (mostly caused by oxygen and water[15-16]) and light-induced degradation.[17] Nevertheless, the mixed ions compositional approach enabled PSCs to retain 90% of their initial efficiency after a few hundreds of hours under continuous operating conditions.[18] While encouraging, this result is still poor compared to 25 years stability standard required for the commercial PV panels.

Although extraordinary high efficiency has been achieved for solution-processed PSCs,[18] the solution-processed films are typically polycrystalline with high grain boundaries (GBs) concentration. The grain boundary and the material's surface are the defect concentrated areas of the material. These defects can trigger the degradation caused by the presence of oxygen, moisture, and light.[19-21] In the ambient environment, moisture and oxygen are the culprits in most cases for severe damage to the PSCs performances. The endurance against oxygen and moisture is also a concern for other PV technologies because water and O_2 can oxidise some components in PV panels.[22] Hence, even widely commercialised PV technologies need proper encapsulation which can be used in PSCs. Efforts have been made to find good encapsulation for PSCs which can preserve the initial efficiency in the damp heat test.[23] Nevertheless, the intrinsic stability improvement of

---

[1] This section is adapted from my own first-author published reviews (https://doi.org/10.1002/smll.201802573 and https://doi.org/10.1016/B978-0-12-814727-6.00009-8) with permission from Elsevier and John Wiley and Sons.

PSCs can partially reduce the strict requirements of encapsulation. Furthermore, PSCs have a huge potential for flexible PV modules and the more stable the devices are, the less difficult (and most likely less expensive) to produce flexible PSCs.[24]

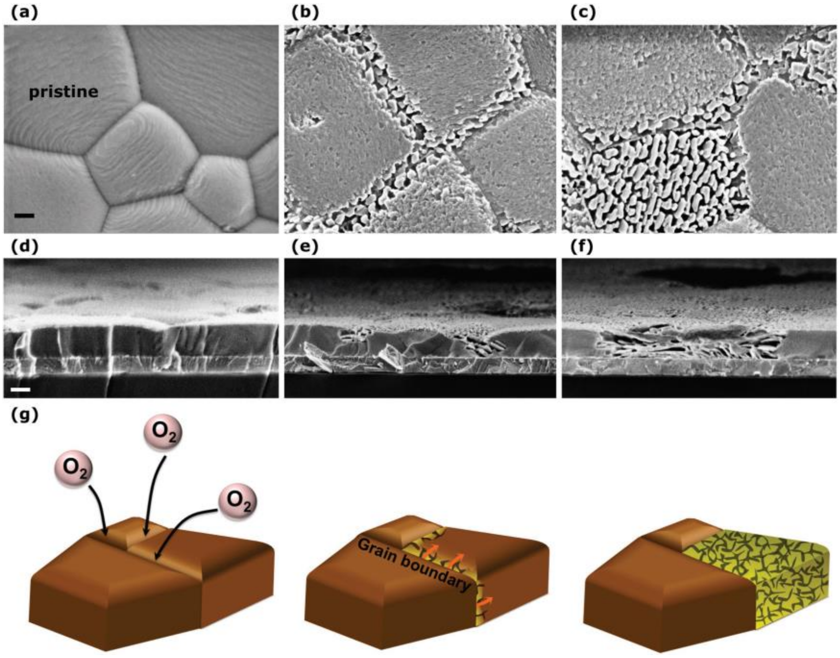

Figure 1.2 Scanning electron microscope images of the top view and the cross-section of pristine, and degraded films by oxygen (scale bar of 200 nm), with the schematic diagram of the proposed degradation route by oxygen penetration from grain boundary.[18] Reproduced with permission. Copyright 2017, John Wiley and Sons.

In the presence of a combination of light and oxygen, halide perovskites, *e.g.* $MAPbI_3$, degrades rapidly. The black perovskite film turns yellow (formation of lead iodide) after 48 hours exposing to ambient condition.[25] The photo-generated electrons within the perovskite are accepted by molecular oxygen from the atmosphere forming superoxide O_2^- species. Negatively charged superoxide deprotonates $CH_3NH_3^+$ and eventually decomposes the material into lead iodide and methylamine gas. The speed of this degradation pathway strongly correlates with the crystal size.[15, 25] The smaller the crystals are, the faster the degradation is due to a higher GBs concentration. This is because the superoxide species are likely to occupy iodide defects, which concentrate on the GBs.[15] The oxygen decomposition starts from GBs and progresses towards the bulk consuming the whole grain (shown in **Figure 1.2**).[19] Moreover, in films comprising smaller grains, the oxygen has to diffuse less, thus accelerating the degradation.[15]

Similarly, moisture is known to degrade the perovskite layer[26] even with encapsulation.[27] A theoretical calculation shows that $MAPbI_3$ is unstable in the presence of water because of highly reactive and water-soluble $CH_3NH_3^+$ cations within the perovskite film product. One of the proposed routes of moisture-induced irreversible degradation in halide perovskite is via trap state-assisted decomposition mechanism.[28] Defects within the perovskite layer, especially at the grain boundaries, trap the photo-generated charges, which leads to local electric fields. This electric field promotes the deprotonation of the organic cations forming amine products, which evaporate at room temperature. Also, the electric fields distort the PbI_6^{4-} octahedral structure and allow more water to penetrate inside the perovskite lattice.[28]

In addition, the presence of defects in $MAPbI_3$ contributes to light-induced degradation. Light induces changes in the dipole moment of $MAPbI_3$ which consequently leads to material degradation.[29-31] The hydrogen bonds of MA^+ are weakened under illumination, and hence, MA^+ can rotate more freely.[31] The dipole cation can respond to an electric field (if present) or align by interaction among dipoles. This dipole motion may cause a structural change of $MAPbI_3$ lattice under illumination.[29] Moreover, ionic defect diffusion is also accelerated under illumination in combination with heat. These two effects expand the lattice and activate the diffusion of $CH_3NH_3^+$ causing the material to decompose into PbI_2.[32] Also, the ionic defect migration increases the defect concentration in the material[33] which promotes further the material degradation.[34] Due to the MA vacancies, the bond angle of Pb-I-Pb changes in prolonged illumination until the structure disintegrates permanently to lead iodide.[34] Hence, ionic defect migration introduces a degradation pathway for halide perovskite under working conditions.

The interfacial defect concentration at the perovskite and the contact materials also impact the device stability due to the formation and migration of perovskite ionic defects, which then accumulate at the interface.[35] A study from Gagliardi and Abate illustrates that the structure of the interface (whether mesoporous or planar) strongly influences the behaviour of PSCs.[35] The mesoporous interface results in a lower density of defects due to the larger interfacial area. Under the working condition, because of ionic defect migration, they accumulate at the interface and reduce the efficiency of PSCs. Thus, owing to lower interfacial defect concentration, the mesoporous device remains more efficient over time.[35] Moreover, impedance spectroscopy supports that the mesoporous layer reduces ionic migration.[36] Indeed, compared to the planar device, the mesoporous device shows a smaller low-frequency capacitance,[36] which might relate to lower ionic defects concentration.[37-38]

Therefore, ionic defects presence in halide perovskite strongly relate to its long-term stability. As long-term stability is the main roadblock for perovskite to be commercially available, a deep understanding of defect chemistry in perovskite is required for further material optimisation.

1.3 Scope and outline

The previous section shows clearly that to improve the stability of perovskite, and thus, to harvest its potential as an attractive material for optoelectronic devices, a deep fundamental understanding of the defect chemistry in perovskite is vital. The focus of the project, thus, is *the ionic defect formation, and their migration dynamics as well as the effect of ionic defect migration on the stability of perovskite solar cells*.

The outline of the dissertation is as followed. **Chapter 2** presents a background for the studies in the dissertation. After the introduction of the properties of halide perovskite, a brief literature review is provided covering the defect chemistry of halide perovskites. **Chapter 3** gives a short introduction to the main experimental techniques and perovskite fabrication processes used throughout the studies. Thereafter, the dissertation is comprised of three publications as three chapters in a cumulative format.

Chapter 4 presents the doping mechanism using divalent alkaline earth metal cations in the prototypical material methylammonium lead iodide. This study shows that depending on the dopant radii, the dopants can be included in the perovskite lattice up to a certain concentration. At low doping concentration, this would affect the intrinsic defect formation of the perovskite, and thus, leads to n-type doping. In addition, the material quality improves due to defect reduction evidenced by the increase of V_{OC} in both p-i-n and n-i-p device structures. At high doping concentration, the material becomes less n-type and the dopants tend to segregate into a secondary phase. This is rather unexpected as one dopant can shift Fermi level in both directions depending on the doping concentrations. Combining theoretical calculation and experimental evidence, the study elucidates the effects of impurity on material's crystal structure, ionic defect formation, coupling with device performance upon doping.

The formed ionic defects in halide perovskite can subsequently migrate in stimuli especially in light and bias. Hence, the kinetic of ionic defect migration becomes important to understand its effect on device performance. It is an ongoing debate in the literature whether the defect concentrated grain boundary facilitates the ionic defect migration. However, most of the studies focus on the indirect effect of ionic defect migration, *i.e.* hysteresis. Herein, **Chapter 5** examines the ionic defect migration in the presence of grain boundaries commonly found in polycrystalline thin-films used in perovskite solar cells. As the ionic defects form and migrate, they can affect the luminescence yield of the material which could be captured by photoluminescence microscopic measurement. Observing light-induced ionic defect migration in different microstructure samples shows that the grain boundary blocks the ionic defect migration. Thus, the study illustrates how the defect concentration distribution in the material affects the ionic defect migration.

This ionic defect migration has a significant impact on the long-term stability of the solar cells. Therefore, **Chapter 6** focuses on the migration of ions concerning the long-term stability of the perovskite solar cells. PSCs are subjected to biases during the operation condition, which inherently causes ionic defect migration. However, little has been known in the literature about the structural evolution due to this migration. Using forward bias stress in 6-12 hours (typical daily working time of solar cells), the study investigates the optoelectronic and material property modification because of bias induced ionic defect migration. It is shown that halide segregation and perovskite amorphization occurs in the mix cation mix halide perovskite. Even though the bias stress leads to an open circuit voltage enhancement, the formation of amorphous bromide rich phase inhibits interfacial charge collection. Thus, PSCs' efficiency significantly decreases. The study highlights the detrimental effect of ionic defect migration on the device's long-term stability.

Finally, **Chapter 7** provides the conclusions, which highlights the findings from the research linking the published work to the dissertation's topic. This chapter also discusses the outlook for future work.

1.4 List of publications to be included in the cumulative dissertation

Chapter 4: The Doping Mechanism of Halide Perovskite Unveiled by Alkaline Earth Metals

Nga Phung,[$] Roberto Félix,[$] Daniele Meggiolaro, Amran Al-Ashouri, Gabrielle Sousa e Silva, Claudia Hartmann, Juanita Hidalgo, Hans Köbler, Edoardo Mosconi, Barry Lai, Rene Gunder, Meng Li, Kai-Li Wang, Zhao-Kui Wang, Kaiqi Nie, Evelyn Handick, Regan G. Wilks, Jose A. Marquez, Bernd Rech, Thomas Unold, Juan-Pablo Correa-Baena, Steve Albrecht, Filippo De Angelis, Marcus Bär, Antonio Abate*

[$]These authors contribute equally

Status: Published (DOI: 10.1021/jacs.9b11637)

My contribution: I conceived the project under the supervision of Prof. Dr. Antonio Abate. I fabricated most of the samples investigated in the study. I characterised the solar cells. I measured XRD and performed microstrain analysis. I wrote the first draft of the manuscript.

Chapter 5: The Role of Grain Boundaries on Ionic Defect Migration in Metal Halide Perovskites

Nga Phung, Amran Al-Ashouri, Simone Meloni, Alessandro Mattoni, Steve Albrecht, Eva L. Unger, Aboma Merdasa,* Antonio Abate*

Status: Accepted (DOI: 10.1002/aenm.201903735)

My contribution: I conceived the project under the supervision of Dr. Aboma Merdasa and Prof. Dr. Antonio Abate. I fabricated the samples investigated in the study (including thin-films, crystals, and devices). I characterised the solar cells. I involved in EDX, and PL measurements. I wrote the first draft of the manuscript.

Chapter 6: Ion Migration-Induced Amorphization and Phase Segregation as a Degradation Mechanism in Planar Perovskite Solar Cells

Diego Di Girolamo,[§] Nga Phung,[§] Felix Utama Kosasih, Francesco Di Giacomo, Fabio Matteocci, Joel A. Smith, Marion A. Flatken, Silver H. Turren Cruz, Lucio Cinà, Alessandro Latini, Giorgio Divitini, Caterina Ducati, Aldo Di Carlo,* Danilo Dini,* and Antonio Abate*

§These authors contribute equally

Status: Under review

My contribution: Together with Dr. Diego Di Girolamo, I conceived the project under the supervision of Prof. Aldo Di Carlo, Prof. Danilo Dini and Prof. Dr. Antonio Abate. I fabricated the devices investigated in the study. I characterised the solar cells and participated in stressing measurement. I conducted a part of XRD measurements and involved in GIWAXS measurements. I largely involved in manuscript writing and revising.

Reference

1. Rogelj, J.; McCollum, D. L.; Reisinger, A.; Meinshausen, M.; Riahi, K., Probabilistic cost estimates for climate change mitigation. *Nature* **2013,** *493* (7430), 79.
2. Pachauri, R. K.; Allen, M. R.; Barros, V. R.; Broome, J.; Cramer, W.; Christ, R.; Church, J. A.; Clarke, L.; Dahe, Q.; Dasgupta, P.; Dubash, N. K., *Climate change 2014: synthesis report. Contribution of Working Groups I, II and III to the fifth assessment report of the Intergovernmental Panel on Climate Change*. Ipcc: 2014.
3. Boden, T.; Marland, G.; Andres, R. *Global, Regional, National Fossil-Fuel CO2 Emissions*; Carbon Dioxide Information Analysis Center, Oak Ridge National Laboratory, U.S. Department of Energy: 2013.
4. NASA/GISS Global Temperature. https://climate.nasa.gov/vital-signs/global-temperature/ (accessed 28/01).
5. Turner, J. A., A realizable renewable energy future. *Science* **1999,** *285* (5428), 687-689.
6. Bahar, H.; D'Ambrosio, D.; Malischek, R.; Paillere, H. Tracking power 2019. https://www.iea.org/reports/tracking-power-2019/ (accessed 24/01/2020).
7. Perez, R.; Perez, M. *A Fundamental Look At Supply Side Energy Reserves For The Planet*; International Energy Agency: 2015.
8. World Energy Outlook 2019. https://www.iea.org/reports/world-energy-outlook-2019/ (accessed 24/01/2020).
9. Photovoltaic Report. https://www.ise.fraunhofer.de/content/dam/ise/de/documents/publications/studies/Photovoltaics-Report.pdf (accessed 28/01/2020).
10. Smets, A.; Jäger, K.; Isabella, O.; Van Swaaij, R.; Zeman, M., The physics and engineering of photovoltaic conversion, technologies and systems. **2016**.
11. Kojima, A.; Teshima, K.; Shirai, Y.; Miyasaka, T., Organometal halide perovskites as visible-light sensitizers for photovoltaic cells. *Journal of the American Chemical Society* **2009,** *131* (17), 6050-6051.
12. NREL NREL Best Research-Cell Efficiencies. https://www.nrel.gov/pv/assets/images/efficiency-chart.png.
13. Domanski, K.; Alharbi, E. A.; Hagfeldt, A.; Grätzel, M.; Tress, W., Systematic investigation of the impact of operation conditions on the degradation behaviour of perovskite solar cells. *Nature Energy* **2018,** *3*, 61–67.
14. Tenuta, E.; Zheng, C.; Rubel, O., Thermodynamic origin of instability in hybrid halide perovskites. *Scientific reports* **2016,** *6*, 37654.
15. Aristidou, N.; Eames, C.; Sanchez-Molina, I.; Bu, X.; Kosco, J.; Islam, M. S.; Haque, S. A., Fast oxygen diffusion and iodide defects mediate oxygen-induced degradation of perovskite solar cells. *Nature Communications* **2017,** *8*, 15218.
16. Yun, J. S.; Kim, J.; Young, T.; Patterson, R. J.; Kim, D.; Seidel, J.; Lim, S.; Green, M. A.; Huang, S.; Ho-Baillie, A., Humidity-Induced Degradation via Grain Boundaries of HC (NH2) 2PbI3 Planar Perovskite Solar Cells. *Advanced Functional Materials* **2018,** *28* (11), 1705363.
17 Xu, R.-P.; Li, Y.; Jin, T.-Y.; Liu, Y.-Q.; Bao, Q.-Y.; O'Carroll, C.; Tang, J.-X., In-Situ Observation of Light Illumination-Induced Degradation in Organometal Mixed-Halide Perovskite Films. *ACS applied materials & interfaces* **2018,** *10* (7), 6737-6746.
18. Saliba, M.; Matsui, T.; Seo, J.-Y.; Domanski, K.; Correa-Baena, J.-P.; Nazeeruddin, M. K.; Zakeeruddin, S. M.; Tress, W.; Abate, A.; Hagfeldt, A.; Grätzel, M., Cesium-containing triple cation perovskite solar cells: improved stability, reproducibility and high efficiency. *Energy & environmental science* **2016,** *9* (6), 1989-1997.
19. Sun, Q.; Fassl, P.; Becker-Koch, D.; Bausch, A.; Rivkin, B.; Bai, S.; Hopkinson, P. E.; Snaith, H. J.; Vaynzof, Y., Role of Microstructure in Oxygen Induced Photodegradation of Methylammonium Lead Triiodide Perovskite Films. *Advanced Energy Materials* **2017,** *7* (20), 1700977.
20. Wang, Q.; Chen, B.; Liu, Y.; Deng, Y.; Bai, Y.; Dong, Q.; Huang, J., Scaling behavior of moisture-induced grain degradation in polycrystalline hybrid perovskite thin films. *Energy & Environmental Science* **2017,** *10* (2), 516-522.
21. Gomez, A.; Sanchez, S.; Campoy-Quiles, M.; Abate, A., Topological distribution of reversible and non-reversible degradation in perovskite solar cells. *Nano Energy* **2017,** *45*, 94-100.

22. Sharma, V.; Sastry, O.; Kumar, A.; Bora, B.; Chandel, S., Degradation analysis of a-Si,(HIT) hetro-junction intrinsic thin layer silicon and mC-Si solar photovoltaic technologies under outdoor conditions. *Energy* **2014,** *72*, 536-546.

23. Shi, L.; Young, T. L.; Kim, J.; Sheng, Y.; Wang, L.; Chen, Y.; Feng, Z.; Keevers, M. J.; Hao, X.; Verlinden, P. J.; Green, M. A.; Ho-Baillie, A. W. Y., Accelerated Lifetime Testing of Organic–Inorganic Perovskite Solar Cells Encapsulated by Polyisobutylene. *ACS Applied Materials & Interfaces* **2017,** *9* (30), 25073-25081.

24. Leijtens, T.; Bush, K.; Cheacharoen, R.; Beal, R.; Bowring, A.; McGehee, M. D., Towards enabling stable lead halide perovskite solar cells; interplay between structural, environmental, and thermal stability. *Journal of Materials Chemistry A* **2017,** *5*, 11483-11500.

25. Bryant, D.; Aristidou, N.; Pont, S.; Sanchez-Molina, I.; Chotchunangatchaval, T.; Wheeler, S.; Durrant, J. R.; Haque, S. A., Light and oxygen induced degradation limits the operational stability of methylammonium lead triiodide perovskite solar cells. *Energy & Environmental Science* **2016,** *9* (5), 1655-1660.

26. Noh, J. H.; Im, S. H.; Heo, J. H.; Mandal, T. N.; Seok, S. I., Chemical management for colorful, efficient, and stable inorganic–organic hybrid nanostructured solar cells. *Nano letters* **2013,** *13* (4), 1764-1769.

27. Han, Y.; Meyer, S.; Dkhissi, Y.; Weber, K.; Pringle, J. M.; Bach, U.; Spiccia, L.; Cheng, Y.-B., Degradation observations of encapsulated planar CH 3 NH 3 PbI 3 perovskite solar cells at high temperatures and humidity. *Journal of Materials Chemistry A* **2015,** *3* (15), 8139-8147.

28. Ahn, N.; Kwak, K.; Jang, M. S.; Yoon, H.; Lee, B. Y.; Lee, J.-K.; Pikhitsa, P. V.; Byun, J.; Choi, M., Trapped charge-driven degradation of perovskite solar cells. *Nature communications* **2016,** *7*, 13422.

29. Gottesman, R.; Gouda, L.; Kalanoor, B. S.; Haltzi, E.; Tirosh, S.; Rosh-Hodesh, E.; Tischler, Y.; Zaban, A.; Quarti, C.; Mosconi, E.; De Angelis, F., Photoinduced reversible structural transformations in free-standing CH3NH3PbI3 perovskite films. *The journal of physical chemistry letters* **2015,** *6* (12), 2332-2338.

30. Gottesman, R.; Haltzi, E.; Gouda, L.; Tirosh, S.; Bouhadana, Y.; Zaban, A.; Mosconi, E.; De Angelis, F., Extremely slow photoconductivity response of CH3NH3PbI3 perovskites suggesting structural changes under working conditions. *The journal of physical chemistry letters* **2014,** *5* (15), 2662-2669.

31. Pazoki, M.; Jacobsson, T. J.; Kullgren, J.; Johansson, E. M.; Hagfeldt, A.; Boschloo, G.; Edvinsson, T., Photoinduced stark effects and mechanism of ion displacement in perovskite solar cell materials. *ACS nano* **2017,** *11* (3), 2823-2834.

32. Bag, M.; Renna, L. A.; Adhikari, R. Y.; Karak, S.; Liu, F.; Lahti, P. M.; Russell, T. P.; Tuominen, M. T.; Venkataraman, D., Kinetics of ion transport in perovskite active layers and its implications for active layer stability. *J. Am. Chem. Soc* **2015,** *137* (40), 13130-13137.

33. Azpiroz, J. M.; Mosconi, E.; Bisquert, J.; De Angelis, F., Defect migration in methylammonium lead iodide and its role in perovskite solar cell operation. *Energy & Environmental Science* **2015,** *8* (7), 2118-2127.

34. Merdasa, A.; Bag, M.; Tian, Y.; Källman, E.; Dobrovolsky, A.; Scheblykin, I. G., Super-resolution luminescence microspectroscopy reveals the mechanism of photoinduced degradation in CH3NH3PbI3 perovskite nanocrystals. *The Journal of Physical Chemistry C* **2016,** *120* (19), 10711-10719.

35. Gagliardi, A.; Abate, A., Mesoporous Electron Selective Contacts Enhance the Tolerance to Interfacial Ions Accumulation in Perovskite Solar Cells. *ACS Energy Letters* **2017,** *3* (1), 163-169.

36. Anaya, M.; Zhang, W.; Hames, B. C.; Li, Y.; Fabregat-Santiago, F.; Calvo, M. E.; Snaith, H. J.; Míguez, H.; Mora-Seró, I., Electron injection and scaffold effects in perovskite solar cells. *Journal of Materials Chemistry C* **2017,** *5* (3), 634-644.

37. Almora, O.; Zarazua, I.; Mas-Marza, E.; Mora-Sero, I.; Bisquert, J.; Garcia-Belmonte, G., Capacitive dark currents, hysteresis, and electrode polarization in lead halide perovskite solar cells. *The journal of physical chemistry letters* **2015,** *6* (9), 1645-1652.

38. Zarazua, I.; Bisquert, J.; Garcia-Belmonte, G., Light-induced space-charge accumulation zone as photovoltaic mechanism in perovskite solar cells. *The journal of physical chemistry letters* **2016,** *7* (3), 525-528.

Chapter 2 Fundamentals

2.1 Photovoltaic effect

2.1.1 Solar spectrum

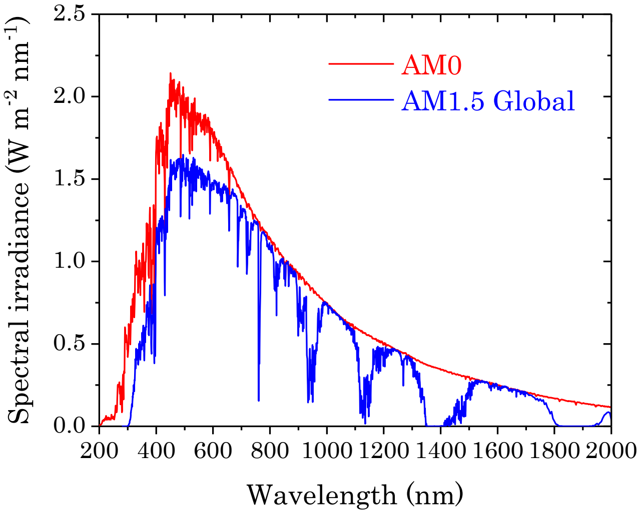

Figure 2.1 Red line: Solar spectrum outside the atmosphere (AM0). Blue line: Solar spectrum as seen on the Earth's surface with a tilt angle of 48°, *i.e.* optical air mass of 1.5. Plot from data reported by NREL.[1]

The temperature of the sun is around 5800 K which emits photons as a black body. A black body can completely absorb all the photon energies. The black body radiation can be described by Planck's law.[2] This photon emission or solar radiation reaches the Earth at a certain solid angle, which gives the solar radiation as shown in **Figure 2.1**. The energy flux is around 1367 W/m^2 at the outer atmosphere of the Earth.[2] As the sunlight passing through the atmosphere, due to the light absorption by air molecules (*e.g.* H_2O and O_2) and scattering by dust particles, the solar spectrum has a different shape (comparison between red and blue lines in **Figure 2.1**). Hence, the energy flux reaching the Earth's surface depends on the distance, which the sunlight needs to travel through the Earth's atmosphere. At the zenith position, the distance is the shortest. The ratio between sunlight's actual distance and this shortest distance is called optical air mass (AM). The sun with a certain angle θ with respect to the zenith direction, the air mass is calculated by **equation 2.1**. The standard solar spectrum used in PV performance tests is with an air mass of 1.5 (*i.e.* θ = 48°), this gives an energy flux of around 1000 W/m^2.[2]

$$\mathrm{AM} = \frac{1}{\cos\theta} \tag{2.1}$$

2.1.2 Photovoltaic effect in a semiconductor material

For electrons to occupy energy levels, their distribution of electron states needs to satisfy three rules:[3]

i. Pauli's principle where no more than one particle can have the same quantum state

ii. The occupation of electrons in the states only depend on energy (no contribution of electron momentum)

iii. The occupation needs to lead to a minimum of free energy

Then, the distribution can be described with Fermi function as can be seen in **equation 2.2**.[3]

$$f(\varepsilon_e) = \frac{1}{\exp\left(\frac{\varepsilon_e - \varepsilon_F}{kT}\right) + 1} \tag{2.2}$$

This contains the probability of electrons to occupy states. For the electrons with energy ε_e which is much smaller than Fermi energy ε_F then $f(\varepsilon_e) \approx 1$, the states are occupied and vice versa. In an atom, the electrons have discrete energy state. As the atoms are surrounded by each other and their orbitals overlap, the discrete energy states of material become energy ranges. These energy values are very close to each other such that they form a continuum that can permit electrons to reside. This is called energy bands. Unlike metal which has continuous states, a semiconductor has a bandgap in which the energy range in the valence band (VB) (below the gap) is almost filled with electron whereas above the gap, the conduction band (CB) is nearly depleted of electrons. The bandgap is essentially the difference between the valence band maximum (VBM) and the conduction band minimum (CBM).

Therefore, when a photon is absorbed, if the energy is greater than or equal to the bandgap of the semiconductor, it can excite an electron from the valence band to the conduction band leaving a positive charge in valence band or hole. Photons below the bandgap cannot be absorbed and so the semiconductor is transparent to them. Photons with higher energy than bandgap can excite electrons into higher energy state compared to CBM, and charge carrier thermalisation can occur as the electrons relax back to CBM. This process generates phonons (lattice vibration). This is described in **Figure 2.2A**. After the charge carriers are generated, it can recombine or be extracted to the external circuit.

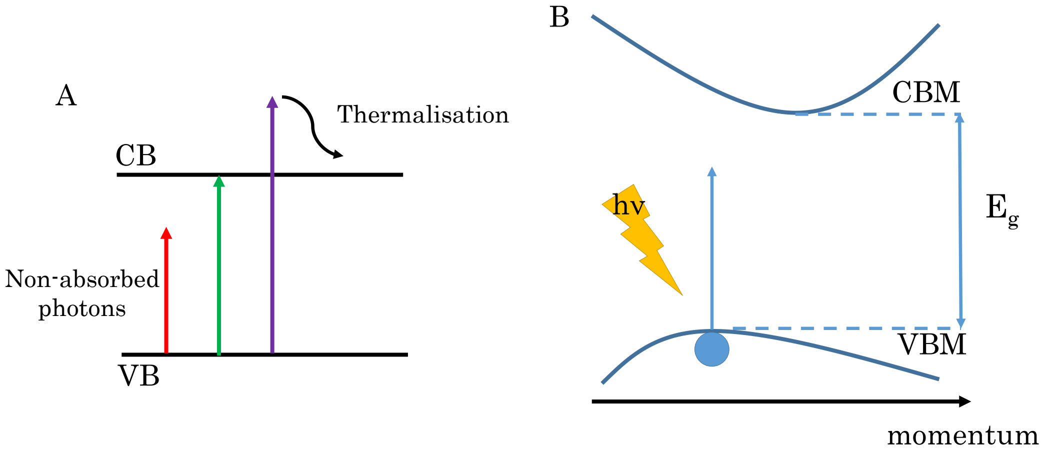

Figure 2.2 A. Schematic of photon absorption in a semiconductor. The photon which has energy lower than bandgap cannot be absorbed whereas the absorption of photons which has energy higher than bandgap leads to thermalisation losses. CB and VB stand for conduction band and valence band respectively. B. Simplified schematic of an indirect semiconductor. CBM and VBM are the conduction band minimum and valence band maximum, the difference between CBM and VBM is the bandgap of the material (E_g).

Semiconductors can be a direct bandgap material, this means that VBM and CBM are well-aligned having same momentum in contrast with the indirect bandgap. Hence, electrons which are excited from valence band of an indirect bandgap semiconductor (as shown schematically in **Figure 2.2B**) require a phonon (lattice vibration) to be transferred to CBM. The phonon absorption is to conserve the momentum, hence, this process involves 3 particles (electron, photon, and phonon). This means that the photon absorption probability in an indirect bandgap semiconductor is lower compared to the direct bandgap semiconductor. As Si has an indirect bandgap, Si-based solar cells need a thick absorber layer to absorb more photons whereas direct bandgap materials such as GaAs and halide perovskite can have high photon absorption, thus, the cells can be thinner. This strong absorption allows direct bandgap materials to be used in thin-film PV technology.

2.2 Halide perovskite as an attracting material for PV application

Metal halide perovskites are a class of materials having a general composition of ABX_3 in which A is a monovalent cation, B is a divalent ion and X is a halide. The choice of A is broad from inorganic (Cs^+, Rb^+) to organic molecules ($CH_3NH_3^+$, $(NH_2)_2CH^+$ *etc.*) whereas the divalent ions are generally Pb^{2+} and Sn^{2+}. The so-called 3D halide perovskite consists of a monovalent cation A residing inside a cavity made of an inorganic framework of PbI_6. Although halide perovskite can also adopt a layer molecules formation or so-called low dimensional perovskites, this dissertation will only refer to the 3D type which resembles the crystal structure of $CaTiO_3$ having an ideal cubic structure. Based on the choice of A, B and X, perovskite can have a slight distortion from a cubic structure, for example, the most investigated methylammonium lead iodide ($MAPbI_3$) adopts a tetragonal structure at room temperature whereas the material exhibits a cubic structure at high temperature ($\geq$327 K), and has an orthorhombic structure at low temperature ($\leq$162 K) as shown in **Figure 2.3A**.[4]

Due to the composition versatility, the bandgap of halide perovskite can be easily tuned (**Figure 2.3B**) which enables high efficiency in both single junction and tandem solar cells. By substituting I^- in $MAPbI_3$ with Br^-, the bandgap of $MAPbX_3$ can be tuned from roughly 1.6 eV to 1.8 eV depending on the halide ratio.[5] The high bandgap perovskites can be used effectively to be the top cell in a tandem cell with Si, which has a higher theoretical efficiency limit than a single junction cell.[6] The covalent bonds between metal (B) and halide (X) construct the material band structure. Specifically, the valence band is dominated by Pb-s and I-p orbitals whereas the conduction band is mostly contributed by the empty Pb-p orbital.[5] Although cation A has a negligible contribution to the density of states, its size and rotation can affect the metal-halide bond by changing the volume of the lattice or introducing distortion.[7] Therefore, changing the composition can modify the bandgap of the material.

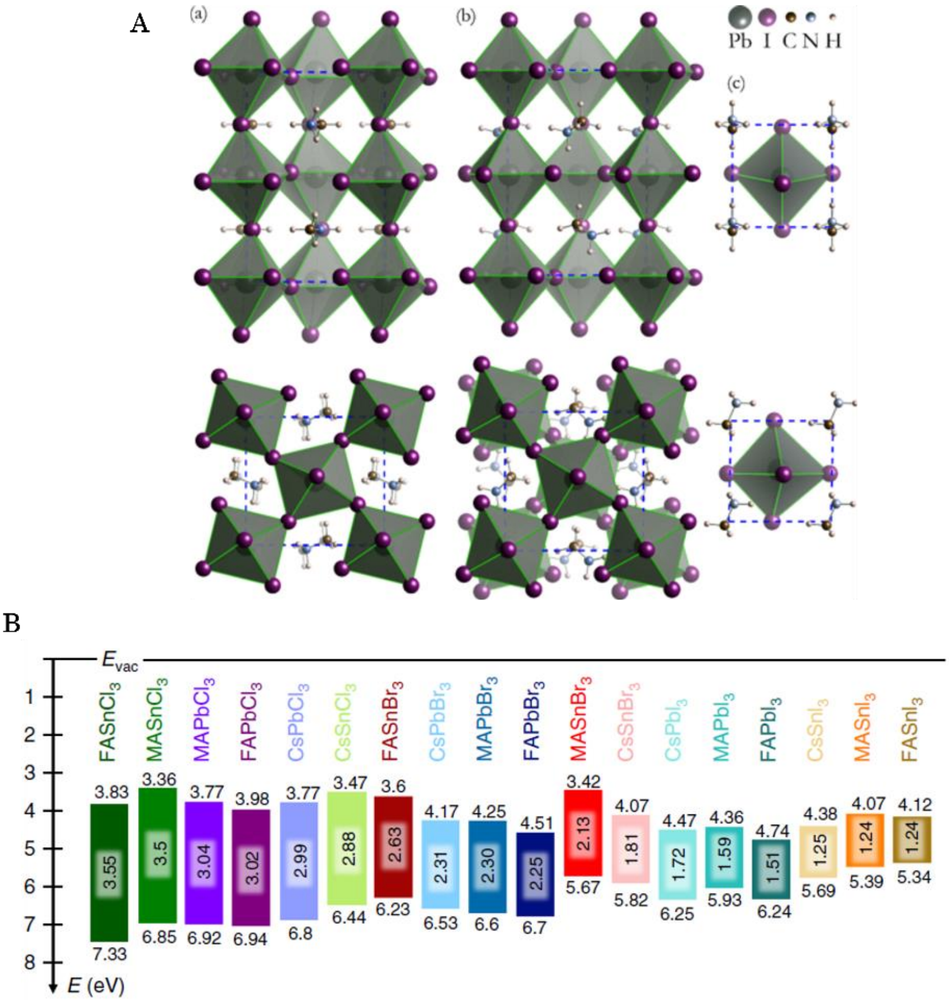

Figure 2.3 A. The crystal structure of $MAPbI_3$ at (a) orthorhombic, (b) tetragonal, (c) cubic structure.[4] Published by the American Physical Society. Reprint under the terms of the Creative Commons Attribution 3.0 License. B. The band structure of different metal halide perovskite where MA^+ and FA^+ stand for methylammonium and formamidinium respectively.[7] Published by Springer Nature. Reprint under a Creative Commons Attribution 4.0 International License.

Perovskite has achieved great progress in terms of efficiency in the last decade, now reaching more than 25% single junction cell and 29% for a tandem cell with Si as of January, 2020.[8] This is thanks to its excellent optoelectronic properties such as sharp absorption onset, long charge carrier diffusion length,[9] and long charge carrier lifetime.[10-11] The steep slope of absorbance profile of $MAPbI_3$ with a low Urbach energy (around 15 meV) is comparable with highly efficient GaAs.[12-13] This means that the material has a low degree of disorder and a high-quality structure. The direct bandgap nature of halide perovskite (*i.e.*, the lowest point of CB and highest point of VB are aligned) results in a strong photon absorption in the material.

The charge carrier lifetime and diffusion length of perovskite are long despite having high defect density (this point will be discussed in detail in **section 2.5**). In solar cells, not only the material needs to absorb as many photons as possible (hence, high absorption is important); but also the charge carriers need to be extracted. Thus, the material is required:

(i) to have low defect concentration (which reduces the number of charge carriers being recombined without arriving to the contacts);
(ii) and/or to have benign defects (the defects have low trapping efficiency).

Hence, having a long lifetime despite a large defect concentration in halide perovskite leads to an opportunity to have material fabricated from various methods including solution processing which will be described in **section 3.1**. To put it into perspective, the main material optoelectronic parameters of MAPbI$_3$ compared to established technologies are summarised in **Table 2.1**. Except for mobility, MAPbI$_3$ has comparable parameters with c-Si and GaAs which enable this material to achieve high efficiency.

Table 2.1 Optoelectronic properties of MAPbI$_3$ compared with established technologies, *i.e.* c-Si and GaAs. The values are taken from the reference number embedded in the table.

Parameters	MAPbI$_3$ polycrystalline film	c-Si (p-type)	GaAs
Charge carrier lifetime (ns)	628[*]	1000[3] (doping density 10^{14}cm^{-3})	19[14] (hole's in n-type with doping density <10^{18}cm^{-3})
Diffusion length (μm)	1-2[15]	≈300[16-17]	6.6[18] (p-type)
Mobility (cm^{2}V^{-1}s^{-1})	35[15][**]	≈1300[19] (doping density 10^{15}cm^{-3})	≈7000 (doping density 10^{15}cm^{-3})
Urbach energy (meV)	15[13]	11[13, 20]	7.5[21]
Absorption coeffient at 550 nm (cm^{-1})	1e5[13]	6.39e03[22]	5e4[13]

[*] Measured value in this work (fitting from time resolved photoluminescence assuming intrinsic material)

[**] Summation of both holes and electrons

2.3 Crystal structure of halide perovskites

As briefly mentioned in the previous section, halide perovskites consist of an octahedral structure of BX_6 forming a cage with A fitting inside the cavity of the unit cell.[23] Depending on the rotation of BX_6, orthorhombic, tetragonal, cubic, trigonal and monoclinic polymorphs phases exist.[24] To estimate whether the 3D perovskite can be obtained, the Goldschmidt tolerance factor is often used for perovskite oxides,[25] and also adapted to halide perovskite.[26] Lower dimensional frameworks can also be obtained. The so-called 2D perovskite can have a layered structure that can accommodate larger cation than 3D structure[27] or perovskite can exist as 1D chain.[28] The tolerance factor t can be calculated as shown in **equation 2.3** where R_A, R_B and R_X are ionic radii of A, B, and X respectively.

$$t = \frac{R_A + R_X}{\sqrt{2}(R_B + R_X)} \tag{2.3}$$

In most cases, the halide perovskites are photoactive at its black phase (or also called α phase) satisfying the tolerance factor in a range from 0.8 to 1.[29] For example, $MAPbI_3$ has the tolerance factor of 0.91 (calculated from ionic radii presented in **Table 2.2**) predicting its possibility to form 3D perovskite, which is the case in practice. ($MAPbI_3$'s black phases are tetragonal phase at room temperature and cubic phase at high temperature.) Depending on the composition, the desirable black phase exists at different temperatures, *e.g.* $CsPbI_3$ only forms a black phase at 300°C which can be meta-stable as can be seen in **Table 2.3**. In order to have stable perovskite solar cells (PSCs) through the lifetime of the devices, composition engineering can be used to keep the black phase within the operational conditions.

Table 2.2 Ionic radii of A, B, X which can be used to calculate the possibility to form 3D halide perovskite.

	Ionic radii (pm)	Ref
$CH_3NH_3^+$	217	26
$HC(NH_2)_2^+$	253	
Cs^+	177	
Pb^{2+}	119	30
I^-	220	
Br	196	
Cl	181	

*Note: B and X ionic radii are in the octahedral coordination

Table 2.3 Representative halide perovskite compounds and their crystal structure, space group, and lattice parameters.

Perovskite	Crystal structure	Space group	Lattice parameters	Ref
$CH_3NH_3PbI_3$ ($MAPbI_3$)	Orthorhombic (<165 K)	$Pnma$	a = 8.87 b = 12.63 c = 8.58	31
	Tetragonal (165-327 K)	$I4/mcm$	a = 8.81 b = 8.81 c = 12.71	
	Cubic (>327 K)	$Pm\bar{3}m$	a = 6.32 b = 6.32 c = 6.32	
$CH_3NH_3PbBr_3$ ($MAPbBr_3$)	Orthorhombic (<144.5 K)	$Pna2_1$	a = 7.97 b = 8.58 c = 11.85	32
	Tetragonal (149.5-155.1 K)	$P4/mmm$	a = 5.89 b = 5.89 c = 5.86	
	Tetragonal (155.1-236.9 K)	$I4/mcm$	a = 8.32 b = 8.32 c = 11.83	
	Cubic (>155 K)	$Pm\bar{3}m$	a = 5.90 b = 5. 90 c = 5. 90	
$CH_3NH_3PbCl_3$ ($MAPbCl_3$)	Orthorhombic (<172.9 K)	$P222_1$	a = 5.67 b = 5.63 c = 11.18	32
	Tetragonal (172.9-178.8 K)	$P4/mmm$	a = 5.66 b = 5.66 c = 5.63	
	Cubic (>178.8 K)	$Pm\bar{3}m$	a = 5.67 b = 5.67 c = 5.67	
$HC(NH_2)_2PbI_3$ ($FAPbI_3$)	Trigonal (<150 K)	$P3$	a = 17.79 b = 17.79 c = 10.90	33-34
	Hexagonal (293 K)	$P6_3mc$	a = 8.66 b = 8.66 c = 7.90	
	Trigonal (>393 K)	$P\bar{3}m1$	a = 8.98 b = 8.98 c = 11.00	
	Cubic (>393 K)	$Pm\bar{3}m$	a = 6.36 b = 6.36 c = 6.36	
$HC(NH_2)_2PbBr_3$ ($FAPbBr_3$)	Orthorhombic (<150 K)	$Pnma$	a = 8.37 b = 11.86 c = 8.38	35
	Tetragonal (150-275 K)	$P4/mbm$	a = 8.42 b = 8.42 c = 5.95	
	Cubic (>275 K)	$Pm\bar{3}m$	a = 5.99 b = 5.99 c = 5.99	
$HC(NH_2)_2PbCl_3$ ($FAPbCl_3$)	Cubic	$Pm\bar{3}m$	a = 5.67 b = 5.67 c = 5.67	36
$CsPbI_3$	Orthorhombic (<587 K)	$Pbma$	a = 6.10 b = 6.26 c = 6.25	37

	Orthorhombic (<450 K)	$Pnma$	a = 6.34 b = 5.61 c = 6.11	
	Tetragonal (450-550 K)	$P4/mbm$	a = 6.24 b = 6.24 c = 6.30	
	Cubic (>550 K)	$Pm\bar{3}m$	a = 6.30 b = 6.30 c = 6.30	
$CsPbBr_3$	Orthorhombic (<361 K)	$Pnma$	a = 8.24 b = 11.74 c = 8.20	38-40
	Tetragonal (361-403 K)	$P4/mbm$	a = 8.45 b = 8.45 c = 8.46	
	Cubic (>403 K)	$Pm\bar{3}m$	a = 6.02 b = 6.02 c = 6.02	
$CsPbCl_3$	Orthorhombic (<315 K)	$Pnma$	a = 5.75 b = 11.44 c = 8.09	41-43
	Tetragonal (315-320 K)	$P4/mbm$	-	
	Cubic (>320 K)	$Pm\bar{3}m$	a = 5.74 b = 5.74 c = 5.74	

2.4 Working principle of perovskite solar cells

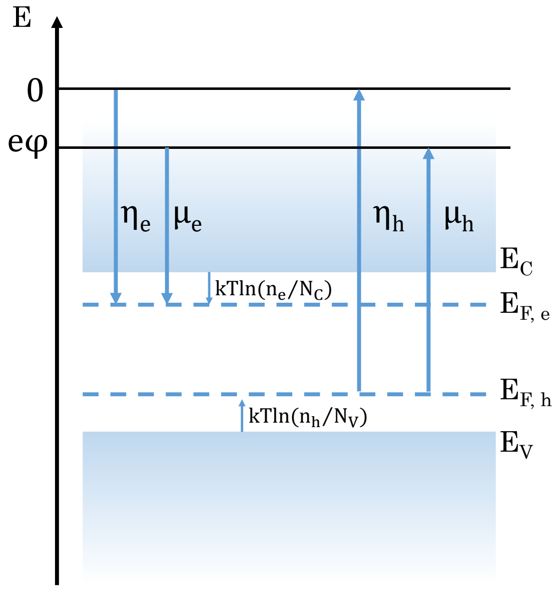

Figure 2.4 The illustration of electrochemical potentials of electrons (η_e) and holes (η_h) in the semiconductor. The vacuum level is eφ.

Mathematically, the density of electrons in the conduction band can be described as in **equation 2.4a** where Nc is the effective density of states of the conduction band and Ec is the conduction band energy. Similarly, **equation 2.4b** is used to describe the distribution of holes in the conduction band.[3]

$$n_e = N_C \exp\left(\frac{E_C - E_{F,e}}{k_B T}\right) \qquad 2.4a$$

$$n_h = N_V \exp\left(-\frac{E_{F,h} - E_V}{k_B T}\right) \qquad 2.4b$$

where k_B is the Boltzmann constant and T is the temperature of the solar cell.

In the dark, the thermal generated charge carriers inside the semiconductor is n_i as in **equation 2.5**.

$$n_i^2 = N_C N_V \exp\left(-\frac{E_C - E_V}{k_B T}\right) = N_C N_V \exp\left(-\frac{E_g}{k_B T}\right) \qquad 2.5$$

When the semiconductor absorbs photons and generates charge carriers, the photogenerated charges distributions are described as the quasi-Fermi levels of electrons ($E_{F,e}$) and holes ($E_{F,h}$). The quasi-Fermi levels are the electrochemical potentials of electrons (η_e) and holes (η_h) which are dependent on the chemical potential of electrons (μ_e) and holes (μ_h) as shown in **Figure 2.4**. This difference is the potential energy, which can be used as useful work. This potential difference correlates with the voltage which can be measured from the solar cells. At the maximum voltage that the solar cells can deliver, the open circuit voltage (V_{OC}) relates to the number of charge carriers inside the semiconductor as in **equation 2.6** where e is the elementary charge.

$$V_{OC} = \frac{E_g}{e} + \frac{k_B T}{e} \ln\left(\frac{n_e n_h}{N_C N_V}\right) = \frac{k_B T}{e} \ln\left(\frac{n_e n_h}{n_i^2}\right) \qquad 2.6$$

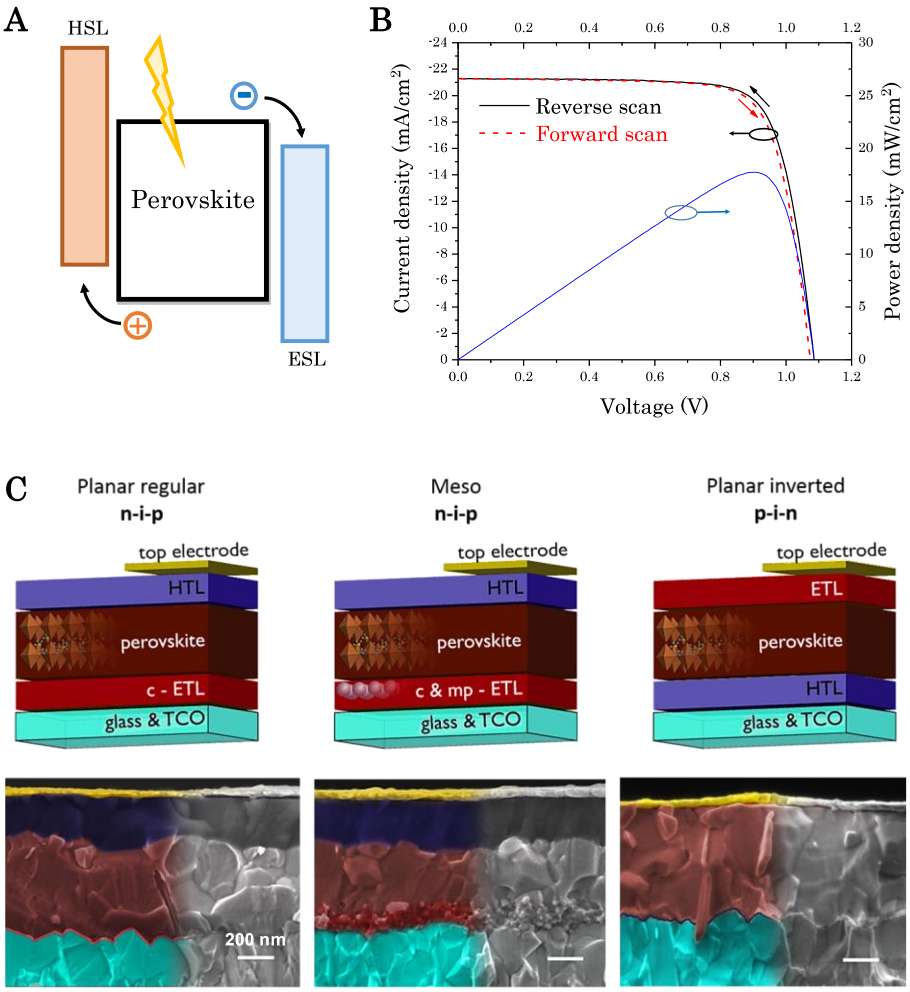

Figure 2.5 A. The schematic of halide perovskite sandwiched between electron selective layer (ESL) and hole selective layer (HSL). B. One example of current density-voltage (J-V) and power density (P-V) curves of a perovskite solar cell. C. The most common architectures of perovskite solar cells.[44] Reprint from American Chemical Society with permission.

PSCs generally consist of a perovskite absorber layer sandwiched between two contact layers to extract the photo-generated charge carriers in the absorber to the electrodes. The contact layers can collect the photogenerated charge carriers inside perovskite to the electrodes, namely hole selective layer (HSL) and electron selective layer (ESL). These layers ideally have a favourable band alignment, which helps to select the desirable charge carrier (holes or electrons respectively) and block the other type of charge carriers. **Figure 2.5A** depicts a schematic of the alignment between the contact layers and the perovskite absorber layer. ESL can have an offset with the perovskite layer so that it is favourable for electrons to move and reach the metal electrode. The layer can also have an energetic barrier for holes, which block holes coming to the wrong contact, *i.e.* the negative contact. A similar concept is applied for HSL. This increases charge extraction efficiency and reduces charge recombination at the interface.[45] To avoid interfacial recombination, it is also desirable to have low defect concentration at the interfaces.[46] In addition, the contact layer is normally doped or very thin to improve the conductivity for fast charge extraction. Another requirement for HSLs and ESLs is their transparency in usable wavelengths. This is an important consideration because if the contact layer has strong parasitic absorption, the perovskite current generation reduces and so does the efficiency.[47] Therefore, HSLs and ESLs are wide bandgap materials.

To evaluate the performance of a solar cell, current density-voltage (J-V) measurements are employed. During a J-V measurement, a voltage sweep is applied to the cells which can be in light (sunlight or sun simulator which has a similar spectrum and light intensity) or in dark. The current density is measured for each voltage formulating a J-V curve which is shown in **Figure 2.5B**. A J-V measurement gives PV parameters, namely short circuit current density (J_{SC}), open circuit voltage (V_{OC}), and maximum power point (MPP) at which the solar cells deliver the highest power output. The fill factor (FF) is defined as the ratio between J_{MPP}*V_{MPP} and J_{SC}*V_{OC}. As shown earlier, V_{OC} can be written as a function of photogenerated charge carriers. Subsequently, the current density relates to the voltage as a diode equation (**equation 2.7**) which explains the exponential shape of the J-V curve:

$$\mathrm{J} = \mathrm{J_0}\left[\exp\left(\frac{qV}{\mathrm{nk_BT}}\right) - 1\right] - \mathrm{J_{ph}} \qquad 2.7$$

where J_{ph} is the photogenerated current, J_0 is the dark current or the leakage current density, V is the applied voltage at the diode terminals, n is the ideality factor (for an ideal solar cell, the ideality factor is 1).

Figure 2.5C shows the typical device architecture used for PSCs. The layers are normally deposited on glass and transparent conductive oxide layers such as In-SnO_2 (ITO) or F-SnO_2 (FTO). In an n-i-p structure, the ESL is the first layer in the deposition steps whereas p-i-n structure has the p-layer or HSL as the first layer. The selective layer can be a thin-film in the planar structure or a layer consisting of nanoparticles forming a mesoporous structure. Finally, metal electrodes are deposited on top of selective layers normally by thermal evaporation.[44] For PSCs, general metal electrode choices are Au, Ag, Al, and Cu.

2.5 Defects in halide perovskites

2.5.1 Overview of defects in semiconductor

One of the most important reasons for perovskite to achieve high efficiency is the defect chemistry of the material. To understand defects, first, it is essential to recall that semiconductor has numerous states of energy for electrons to occupy. Defects are the energy states within the band structure introduced by impurities or lattice imperfection. Shallow defects have energy states placing near the VBM and CBM, typically within the range of tens of meV meanwhile deep defects reside in the middle third of the bandgap.[48] Defects can trap photogenerated charge carriers preventing them from contributing to useful energy in a form of electricity from solar cells. The shallow defects, due to its location near the VBM or CBM, are less harmful because the electrons or holes can escape after trapping. However, introducing impurities can be an effective way to dope semiconductor materials, most notably silicon. The most commonly used n-type dopants is phosphorus, which has one valance electron more than Si. Thus, when phosphorus replaces silicon in the lattice, it has one extra electron more than necessary to form covalent bonds with neighbour Si atoms. Including P in Si lattice results in a loosely bound electron to the P atom which becomes an extra electron of the system. This electron has a state which is close to CBM, thus, incorporating P in Si lattice provides shallow donor states. The picture is the same for acceptor which can donate holes.[3]

In a photon-excited semiconductor, the charge carriers are generated and without extraction, they will recombine. Typically, the recombination of charge carriers is described by a simplified equation (**equation 2.8**) where n stands for charge carrier density assuming equal numbers of electrons and holes.

$$-\frac{\mathrm{dn}}{\mathrm{dt}} = \mathrm{k_1 n + k_2 n^2 + k_3 n^3} \qquad 2.8$$

The recombination of charge carriers can occur via three processes. The first process with k_1 is related to monomolecular recombination, which can relate to exciton recombination (bound state of electrons and holes) or the trap assisted recombination. The trap assisted recombination happens when an electron (or hole) is captured in a trap, hence, it is only proportional to n. The bimolecular recombination (with a rate constant of k_2) depends both on the density of electrons and holes, thus, it relates to n^2. This recombination can be radiative, meaning that the recombination events emit photons (luminescence). The higher the luminescence yield, the better the material quality. The last process is Auger recombination involving three particles: recombination of electrons and holes coupling with energy and momentum transfer to another charge carrier, either electron or holes. This means that Auger recombination strongly depends on charge carrier density which has a rate k_3. For $MAPbI_3$ based solar cells in one sun AM1.5 illumination (light intensity equals to 100 mW/cm^2), the typical charge carrier density is $10^{15\text{-}16}$ cm^{-3} at which the dominant charge recombination is trap-assisted monomolecular recombination process.[49] At room temperature and with one sun illumination, $MAPbI_3$ exhibits an absence of excitonic effects,[50] thus, the k_1 is strongly related to non-radiative recombination which is undesirable in solar cell design. This non-radiative recombination can severely reduce the voltage generated from a PSC.[51]

The non-radiative recombination via defect states is described by Shockley-Read-Hall (SRH) theory (**equation 2.9**).[52]

$$R = \frac{n_e n_h - n_i^2}{\tau_p \left(n_e + N_C \exp\left(-\frac{E_C - E_T}{k_B T} \right) \right) + \tau_e \left(n_h + N_V \exp\left(-\frac{E_T - E_V}{k_B T} \right) \right)} \qquad 2.9$$

Where τ_e and τ_p are lifetimes of electrons and holes and E_T is the energy level of the defect.

The recombination rate will depend on the number of trap states, the capture cross-section of the traps as the probability of trapping event, and the release rate of trapped charges. If E_T is at mid-gap then the distances between conduction band and valence band to the trap state are equal. This means that after electrons (holes) are trapped, it is difficult for the carriers to be released back to the bandegde. Assuming the densities of electrons and holes are approximately the same and much greater than n_i then the recombination rate is $R = n/2\tau$. The SRH lifetime is inverse proportional to the product of the number of traps (N_T) and capture cross-section (σ_T). As $MAPbI_3$ has high dielectric constant (*i.e.* the ability of the material to screen charge), it enables low capture cross-section. In addition to low defect concentration, this allows halide perovskite to have long charge carrier lifetime,[53] comparable with high efficient solar absorber as can be seen in **Table 2.1**.

2.5.2 Type of defects in halide perovskite

It is a general notion that halide perovskite is a defect tolerant material. Even though the material can be made by solution processing which results in a material with a high defect concentration, the material exhibits a high luminescence yield. That is why thin-film perovskite as a polycrystalline material with numerous grain boundaries (defect concentrated areas) can still achieve high efficiency. At the beginning of perovskite optoelectronic development, it has been shown that most of the defects with low defect formation energy are shallow defects whereas the harmful deep defects are difficult to form.[54-56] This is due to the anti-bonding nature of VBM and CBM of halide perovskite, *i.e.* valance band is constructed by hybridisation of Pb 6s and I 5p orbitals whereas the conduction band is mainly from empty Pb 6p orbitals.[7, 57] Therefore, the dangling bonds of either Pb or I vacancies have states near the band edge or inside the bandgap which results in shallow defect levels. Nonetheless, various methods have been used to reduce defect density and improve the efficiencies of PSCs.[58-60] Moreover, there is increasing evidence that defects are the main source of perovskite intrinsic instability.[61-62] Hence, it is vital to understand more about the defects which are present in the material.

In a semiconductor crystalline material, defects can be categorised as impurities and crystallographic defects. Impurities are foreign atoms introduced in the material. They can create traps which are detrimental to the device performance. One of the most harmful impurities in halide perovskites is metal, especially metal atoms can diffuse from the electrode forming harmful recombination centers.[63] On the other hand, the crystallographic defects are defects arisen from the lattice imperfection. They can be point defects namely vacancy, interstitial, and anti-site as shown in **Figure 2.6A**. The vacancies are formed when one atom is missing from its proper lattice site, whereas an anti-site defect is an atom occupying a wrong site. The interstitial site is in between the atom sites in the lattice. Point defects can also couple to form pair defects such as Frenkel pair defects and Schottky pair defects. The former constitutes of two opposite charged vacancies and the latter is formed by one atom moving to an interstitial site leaving one vacancy behind. The higher dimensions of crystallographic defects include dislocation, stacking faults, *etc.* which construct grain boundary, domain boundary, and precipitation (commonly involves an impurity).

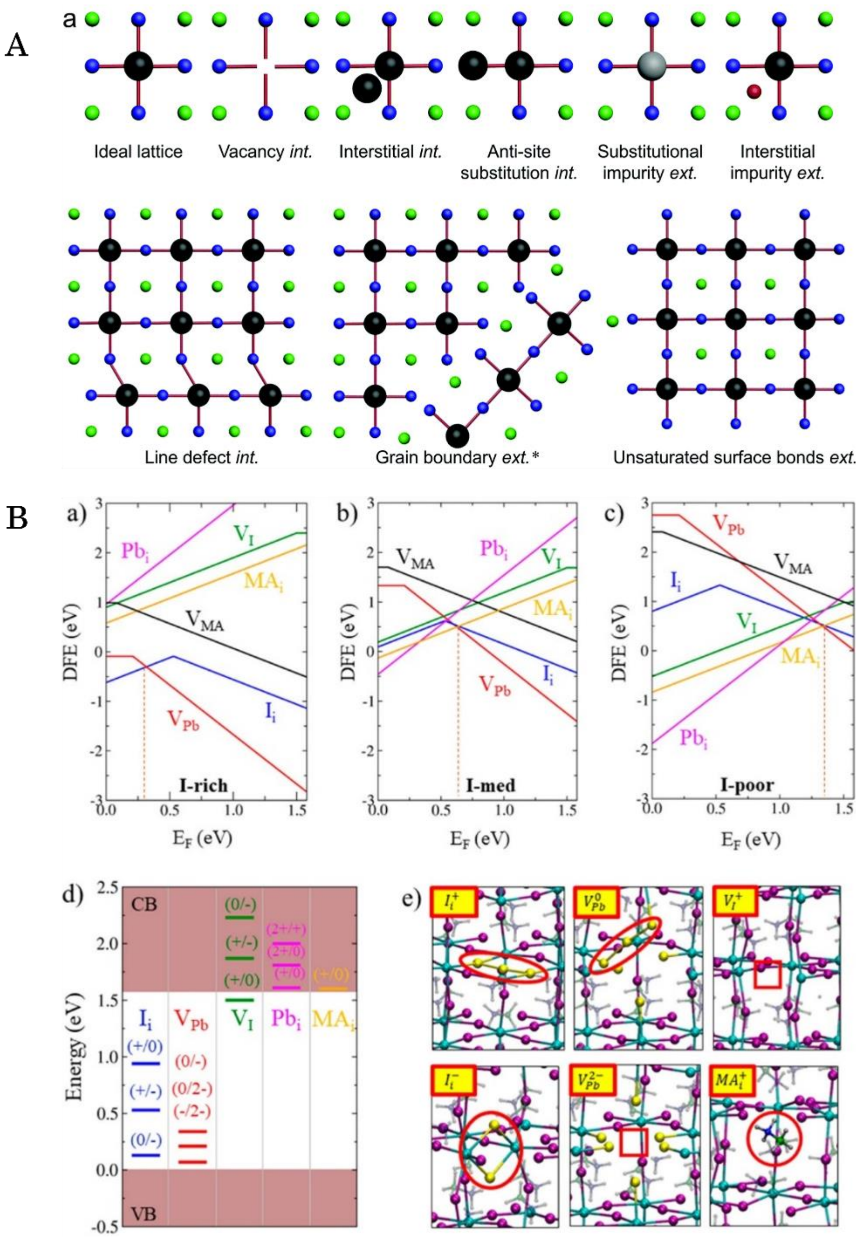

Figure 2.6 A. Type of point defects namely vacancy, anti-site (substitution) which are intrinsic (int.), whereas extrinsic (ext.) point defects include impurity at substitution site or interstitial site. The lower line shows the high dimension defects namely line defect, grain boundary and surface defects. The stars indicate experimental confirmation of existence in halide perovskite. Published by The Royal Society of Chemistry.[64] Reproduced under a Creative Commons Attribution-NonCommercial 3.0 Unported Licence. B. Calculated defect formation energy (DFE) of different point defects in $MAPbI_3$ in different growth conditions with 2x2x2 supercell a) I-rich, b) I-medium, c) I-poor. Dash red lines represent the Fermi levels. d) The ionisation level of the most stable point defects calculated in I-rich growth condition. e) Visualisation of defects in the lattice. Reproduced from American Chemical Society with permission.[65]

2.5.3 Defect concentration and their energetic levels

Since the complex of halide perovskite compositions introduces variation in defect properties, the following part will focus on the defect chemistry in the $MAPbI_3$ perovskite which is the most investigated halide perovskite. Using electronic techniques, the estimated defect densities in $MAPbI_3$ polycrystalline thin-film is 10^{15-16},[66] and as low as 10^{10} in the single crystal.[67] Numerous experimental methods have been used to understand what is the dominant defects and the most harmful ones in $MAPbI_3$. Combining elemental quantification information from hard X-ray photoelectron spectroscopy and radiative recombination of charge carriers by photoluminescence, Sadoughi *et al.* showed that metallic Pb could be one of the defects formed in the material and severely reduced the luminescence yield.[68] It also demonstrated that when $MAPbI_3$ is exposed to I_2 vapour under light, the material degrades quickly due to iodide related photochemical reaction.[69] These experiments emphasise the relevance of Pb and I defects to material stability.

Table 2.4 presents the halide perovskite defect concentrations and their depth inside the bandgap from thermal admittance spectroscopy, thermally stimulated current and deep level transient spectroscopy. All of these methods rely on the trapping of charge carriers in the defects which can be released thermally. However, it is worth noting that due to limit temperature in which perovskite is thermally stable and the ionic defect migration, these methods might not access all defect levels and/or give an inaccurate defect concentration.[70]

Table 2.4 Defect concentration and their depth inside the bandgap determined by experimental methods. Trap depth is with respect to conduction band minimum. Adpated with more data points from ref [70] under a a Creative Commons Attribution (CC BY) license.

Method	Defect concentration (cm^{-3})	Trap depth (eV)	Ref
Thermally stimulated current	$> 10^{15}$	0.5*	71
	9.14×10^{16}	0.18* 0.49*	72
	1.60×10^{16}	0.186*	73
Deep level transient spectroscopy	1.30×10^{15} 3.90×10^{14} 9.50×10^{14}	0.62 0.75 0.76	66
	8.81×10^{13} 5.24×10^{14}	0.78* 0.78*	74

	5.60×10^{12}	0.23	75
	6.90×10^{12}	0.5	
	1.20×10^{13}	0.59	
	1.30×10^{13}	0.6	
	1.80×10^{16}	0.49	76
	1.20×10^{14}	0.64	77
	3.70×10^{14}	0.75	
	2.80×10^{14}	0.81	
Thermal admittance spectroscopy	$\approx 10^{16}$	1.44	78
	$\approx 7.2 \times 10^{15}$	≈0.41	79

*The trap depth with respect to the band edge, however, not specified whether if it's CBM or VBM

Despite their inarguable importance, the experimental evidence generally requires an accompanying theoretical calculation. Theoretical calculations have been performed to calculate the defect formation energies and their positions in the bandgap. Although different calculation methods can yield different results, in general, they show that the nature of deep defects in $MAPbI_3$ can be V''_{Pb} (vacancy of Pb), MA_i (interstitial MA), or $Pb_I^{\bullet\bullet}$ (Pb substitutes I site) depending on the used functions.[55, 80] A letter by Meggiolaro *et al.* highlighted these differences and provided its own corrected values for most stable point defects in $MAPbI_3$.[65]

This dissertation provides a representative result that has been reported for intrinsic point defects, as well as a schematic result of the calculated ionisation levels for the most stable defects as shown in **Figure 2.6B**.[65] At first glance, also similar to other reports, it can be seen that different growth conditions give rise to different defect formation energies. Under a condition with iodide rich precursor (excess iodide), the most stable defects with lowest formation energy are I_i (iodide interstitial) and V''_{Pb} (lead vacancy). This can pin the Fermi level at 0.27 eV above the VBM which makes the material more p-type. At this Fermi level, the ionisation levels of the defects can be seen in panel d of **Figure 2.6B**, where the positive charge I_i is almost at the midgap, 0.86 eV above the VBM, which can be disastrous for device performance. However, later studies from the same group show that the defect tolerance of halide perovskite comes from its unique iodide chemistry. This interstitial iodide defect has low formation energy, hence, it is expected to have a high concentration of I_i in the material. The negative interstitials can trap holes, however, they can be quickly converted to electron trap species to tri-iodide by oxidising agents commonly used in perovskite precursor or water in the atmosphere. Due to a long lattice reorganisation, this electron trapping results into a long kinetically inactive trap, thus, non-radiative recombination does not occur.[81-82] This partially explains why halide perovskites can have high defect density but high luminescence.

Nonetheless, aside iodide defects, lead defects can still be non-radiative recombination centres.[83] Although MA related defects are predicted to have high formation energy at all growth conditions,[65] it plays an important role in material[84] (and device[85]) stability. It has been proposed that superoxide species (oxygen which accepts photogenerated electron) can deprotonate the MA molecule inside the perovskite lattice to form volatile products, *i.e.* CH_3NH_2 and I_2 which eventually degrades the material.[61] Therefore, it is important to reduce defect concentration in perovskite which can improve device stability.

Table 2.5 provides an overview of stable point defects and pair defects formation energies in $MAPbI_3$. In halide perovskites, vacancies and interstitials defects are more stable in halide perovskite whereas the anti-site defects can quickly transform into respective vacancy and interstitial,[86] hence, anti-site defects are excluded in the overview table. In addition to native defects, chemical doping by metal can also introduce impurity defects or interact with the material defects, which are also included in **Table 2.5**.

Table 2.5 Representative calculated values for the most stable intrinsic defects of $MAPbI_3$;[54, 56, 87] and extrinsic impurities (additives) in $MAPbI_3$ unless stated otherwiseBi,[88-89]Ni,[90]Al,[91] Ce,[92] Sb,[93] Mn,[94] Sr, Mg,[95] Ca, Co,[96] Cd,[97] Zn,[98] Fe,[99] Li,[100-102] Na,[103] Cu, Ag,[104] Au,[105] K,[106] Rb,[58] Cs.[107]

	Defect	Concentration (cm3)	Defect formation energy (eV)	Energetic level	Proposed impacts on the material native defects
Point defects	$V_I^\bullet$	5×10^{20}	0.08	(0/+) Shallow near CBM	-
	V_{Pb}''		0.08	(-/2-) Shallow near VBM (0/2-); (0/-) Deep trap states	-
	V_{MA}'		0.16	(0/-); (0/2-) Shallow near VBM	-
	I_i'		0.32	(0/-) (-/+); (0/+) Deep trap states	-
	$Pb_i^{\bullet\bullet}$		1.03	(All oxidation states) Inside conduction band	-
	$MA_i^\bullet$		0.75		-
Pair defects	nil $\rightarrow V_{MA}' + V_{Pb}'' + 3V_I^\bullet + MAPbI_3$	2×10^{19}	0.14	-	-
	nil $\rightarrow V_{MA}' + V_I^\bullet + MAI$	2×10^{20}	0.08	-	-
	nil $\rightarrow V_{Pb}'' + 2V_I^\bullet + PbI_2$	8×10^{17}	0.22	-	-

Trivalent metals	$Bi_{Pb}^{\bullet}$ (in $MAPbBr_3$)	Up to 10%		(+/0) Shallow near CBM delocalised causing bandgap narrowing	
	$Bi_{Pb}^{\bullet}$ (in $CsFAPbI_3$)	Less than 1%		(+/0) Shallow near CBM delocalised (+/0) Deep trap states localised	
	Al^{3+}	0.15%			Assisting the growth resulted in more oriented film
	$Ce_{Pb}^{\bullet}$ (in $CsPbBr_3$)		<2 for all growth conditions	Shallow near CBM	
	$Sb_{Pb}^{\bullet}$	Up to 25% investigated		Deep trap states n-type doping	
Divalent metals	Ni^{2+}	Less than 10%			Absorbed into PbI_3' at grain boundary reducing deep trap
	Mg_{Pb}	Less than 5% to be included in the lattice	-0.11		No contribution to band edge n-doping at low doping regime due to reduction in V_{Pb}'' and V_{MA}' concentration

Divalent metals	Ca_{Pb}				Increase grain size, reducing the defect concentrations increasing V_{OC}
	Sr_{Pb}	Less than 1% to be included in the lattice	-0.24		No contribution to band edge n-doping at low doping regime due to reduction in V''_{Pb} and V'_{MA} concentration
	Mn_{Pb}	Up to 3% can be included to the lattice			Slightly lower non-radiative recombination
	Co_{Pb}	Up to 3% to have positive impact		Modifying band edges. Introducing lattice defects at high concentrations	
	Cd_{Pb} (in $CsFAMAPb(I_xBr_{1-x})_3$	Around 2%			Increasing the harmful intrinsic defects formation energy (vacancies) by reducing lattice strain
	Zn_{Pb}	2.5%			Acting as reducing agents to prevent iodide defects formation
	$Fe_i^{\bullet\bullet}$	Up to 0.03% in perovskite without effects on device performance		Deep trap states	

Monovalent metal	$\mathrm{Li_i^{\bullet}}$	Up to 10%	0.02-0.1		Occupying interstitial site: - Increasing background charge carrier (n-type doping), subsequently filling traps - Increasing the activation energy for ionic defect migration - Increasing the I Frenkel pair defect formation energy
	$\mathrm{Na_{Pb}^{'}}$			p-type doping (hole concentration increases significantly)	
	$\mathrm{Cu_{Pb}^{'}}$ $\mathrm{Ag_{Pb}^{'}}$	0.1%		No state within the bandgap, however lattice distortion causes VBM and CBM positions change leading to Fermi level change (more intrinsic material)	Halide vacancies charge compensation

Monovalent metal	$Au_{Pb}^{'}$		-0.31	Deep trap states	
	K^+	Up to 10% to have positive impact			Passivating halide vacancy Depleting bromide from the bulk
	Rb^+	5% as optimal			Promoting crystallisation Defect passivation
	Cs^+ (in $(MAPbBr_3)_{0.15}(FAPbI_3)_{0.85}$)	5% as optimal			Stabilising perovskite phase Promoting crystallisation

2.5.4 Mitigation of defects by chemical doping

Chemical doping of perovskite has been a widely used method to achieve high efficiency and stability in PSCs. Here, we define chemical doping as the incorporation of a small amount of metal ions ($\leq 5\%$) into the perovskite fabrication process. Although doping in the classical semiconductor is reserved for metals that can be included in the host lattice, in the halide perovskite field, it has been used for any small amount of foreign ions regardless of the lattice inclusion ability. Note that tolerance factor can be first guidance to estimate the metal ions inclusion, however, as will be shown in **Chapter 4**, the tolerance factor is an important consideration, yet, not the only factor that affects the doping process. Using foreign atoms in (most commonly) perovskite precursor solution have mainly four effects: (1) influences during crystallisation process which affects the final film's morphology; (2) electronic doping (n/p-type doping); and (3) introduction of trap states; and (4) interaction with existing perovskite defects. These effects can occur separately or simultaneously depending on the used ions as is shown in **Table 2.4**.

Saliba *et al.* used Cs in a mixed cation mixed halide perovskite, *i.e.* $(MAPbBr_3)_{0.15}(FAPbI_3)_{0.85}$.[107] $FAPbI_3$ has a bandgap of 1.48 eV[108] which enables high efficient single-junction PSCs. However, it has a non-photoactive yellow phase at room temperature due to an energetically unfavourable strain of the black phase. This lattice strain can be relaxed by incorporating smaller cations such as Cs and MA,[109] which can promote the formation of α phase even at room temperatures improving the reproducibility of the perovskite film with monolithic grains.[107] Moreover, during the formation of perovskite, because of the substantial difference in the yellow phases atomic arrangement between $FAPbI_3$ and $CsPbI_3$, they cannot form simultaneously. In contrast, $FAPbI_3$ and $CsPbI_3$ black phase phases can accommodate each other.[110] Thus, the mixed cation perovskite exhibits black phase despite individual compounds being non-photoactive at room temperature. Thus, a clever composition engineering results in a desirable perovskite phase material with good morphology. Nonetheless, lattice inclusion is not obligatory for metal ions to affect the crystallisation process. Using as little as 0.15% Al^{3+} can promote the preferred growth orientation forming a smooth and low bulk strain $MAPbI_3$ material. After assisting the grain growth, Al^{3+} ions stay at the grain boundary and surface of the perovskite film.[91] This high quality doped film has lower defect concentrations and thus has a positive impact on PSCs performance.

Moreover, using chemical doping can modify the bandgap of the material especially in the substitutional case with Pb. Since the anti-bonding of Pb and I orbitals forms the halide perovskite bandgap,[7, 57] Pb substitution can affect to some extent the band edge by theoretical prediction,[111] and experimental validation.[96] This, in turn, can modify the Fermi level position within the bandgap. Thus, Cu and Ag doping induces more intrinsic $MAPbI_3$ material from n-type undoped material.[104] Dopants can also actively contribute to the charge carrier concentrations. For example, Na'_{Pb} doping increases the hole concentration (p-type doping) by an order of magnitude which is predicted by theoretical calculation[112] and evidenced in experiments[103] (though another study shows no doping effect from Na[104]). Another interesting dopant is Sb^{3+}, which is suggested to broaden the bandgap due to hybridisation with I orbital. This is accompanied by n-type doping since Sb^{3+} has one more valence electron than Pb^{2+}.[93]

Not all doping is beneficial, the impurity in the halide perovskite system can introduce deep traps in the material. The diffusion of gold inside the perovskite has a detrimental effect on device performance,[63] as its substitution of Pb creates a deep trap state within the bandgap with low formation energy.[105] Similarly, Fe^{2+} at interstitial position form a deep trap state which reduces PSCs efficiency.[99] Nonetheless, the metal ions can also be included in the lattice without introducing states within the bandgap. A notable example is lithium. Due to its small radius, it is more favourable for Li^+ to occupy the interstitial site instead of cation site substitution.[101] This has been proposed to have a good impact on the device performance by increases the iodide Frenkel pair defects formation energy[102] as well as the ionic defect migration activation energy.[101]

The convolution effects of dopants on the film formation and their contribution to energy bands of halide perovskite are often complicated and depend on the doping concentrations. This is further highlighted by different doping regimes found with Sr and Mg doping investigated in **Chapter 4**, in which lattice inclusion can occur at low concentration causing more n-type doping whereas segregation at high concentration can to some degree introduce less n-type doping.

2.6 Ionic defect migration in halide perovskites

2.6.1 Ionic defect migration pathway

It has been known for perovskite oxide that the ionic bond nature of the material allows it to have high ionic conductivity.[113] This means that the constituent ions in the material can migrate inside the material. Over the years, many studies have calculated the activation energy of the ions, whose results distribute in a broad range. However, all calculations have agreed that iodide ionic defects are the most mobile ions with the lowest activation energy whereas lead ionic defects are immobile due to high activation energy. Representative values from literature can be found in **Table 2.6**. Note that the experimental values cannot distinguish the nature of migrating defects, however, a general consensus assigns slow migration with high activation energy to MA related defects whereas fast ions with low activation energy are I related defects.

Table 2.6 Activation energy of ionic defects in $MAPbI_3$ which are determined by theoretical calculations and temperature dependence experiments

MA defects (eV)	Pb defects (eV)	I defects (eV)	Method	Ref
0.84	2.31	0.58	DFT calculations	113
0.57		0.32	DFT calculations	114
0.46	0.8	0.08	DFT calculations	115
0.68		0.55	Temperature dependence impedance, Intensity modulated photovoltage spectroscopy	116
0.41		0.1	Temperature dependence capacitive discharge currents	117
		0.14	Temperature dependence photoluminescence	118
0.9		0.29	Temperature capacitance transient measurements	119

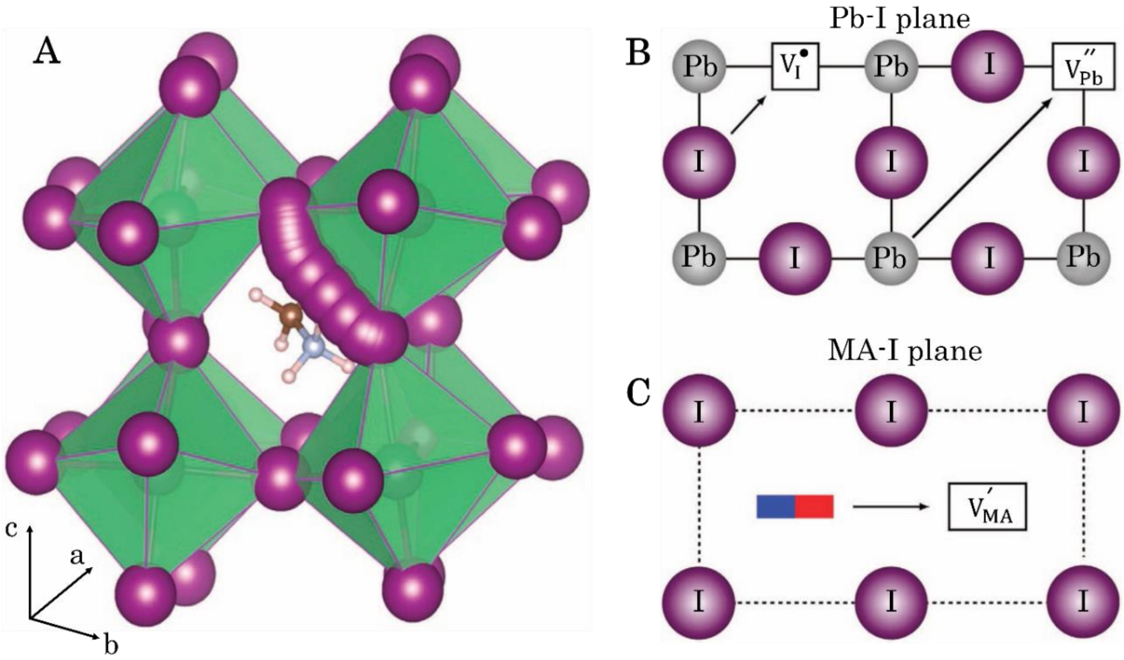

Figure 2.7 A. The migration of iodide ions along the octahedron. B. The ab plane or Pb-I plane of octahedron shows the path of an iodide vacancy ($V_I^{\bullet}$) and a lead vacancy (V_{Pb}''). C. The plane along c-axis (MA-I plane) shows the migration path of a methylammonium vacancy (V_{MA}'). Adapted from reference [113]. Published by Springer Nature. Reprint under a Creative Commons Attribution 4.0 International License.

The migration of iodide vacancies ($V_I^{\bullet}$), which is essentially coupling with the migration of iodide anion, is along the PbI_6 octahedron. The iodide ions, hence, migrate via vacancy hopping mechanism.[113] The $V_I^{\bullet}$ prefers to migrate from equatorial site to axial site shown in **Figure 2.7A** since the migration between two equatorial sites costs energy to overcome the charged Pb ion.[114] The lead vacancy (V_{Pb}'') is predicted to migrate within the same unit cell on the ab plane or Pb-I plane as can be seen in **Figure 2.7B**, however, it has much higher activation energy compared to $V_I^{\bullet}$ (**Table 2.6**),[113, 115] thus Pb is considered stationary in practice. **Figure 2.7**C exhibits the migration pathway of the cation vacancy (V_{MA}') to the adjacent unit cell along the ab plane.

Here, it is worth noting that by definition, the ionic defect migration is bias-driven whereas diffusion occurs due to concentration gradients. However, it is nontrivial to distinguish the two phenomena in practice, since in the device's operation conditions, both light and bias are present. Moreover, it has been proposed that inhomogeneous distribution of photogenerated charge carriers leads to electric fields causing ionic defect migration.[120-121] On the contrary, the study in **Chapter 5** emphasises the role of defect concentration gradients on the movement pathway of ionic defects. Owing to this complexity, in this dissertation, ionic defect migration refers to both migration and diffusion events.

Aside from bias-induced ionic defect migration, illumination also stimulates the ion movement inside the material without contact layers. The ionic defect migration activation energy is several times lower in light than in dark,[122] this is a strong indication for the material defect activity. Due to the acceleration of mobile iodide interstitial, the Frenkel pair defect is destabilised and eventually annihilated in light to restore the perfect crystal.[118] The combination of both light and oxygen results in defect healing,[123-124] which is attributed to the transformation to a shallow trap (interstitial iodate) from an intrinsic deep trap (interstitial iodide).[125] However, prolonged oxygen exposure degrades the material.[126]

Although MA related defects have high activation energy, it has been evidenced that the defects can migrate to some extent in light[127] and electric field.[128-129] As mentioned in the previous section, MA defects do not introduce deep traps, hence they have a negligible effect on PV performance of the solar cells. Nonetheless, by removing MA from the unit cell, it can cause a severe structural modification which results in a bandgap widening and eventually a decomposition into PbI_2.[130-131] In addition, the migration of cation vacancies in hours timescale results in a loss of device performance.[85] Hence, not only ionic defect migration can affect the material intrinsic stability, but it can also affect how the devices perform under operational conditions.

2.6.2 Effects on device performance

In the early development of the field, hysteresis (the discrepancy of cell's performance between different scan directions: reverse and forward) has been observed in PSCs. The reverse scan is defined as from V_{OC} to 0 V and the forward scan is from 0 V to V_{OC}. This is mostly attributed to ionic defect migration in the electric field, which can modify the potential distribution in the devices and affects the charge collection properties. The extent of hysteresis in PSCs depends on the scan rates due to the redistribution of slow migrating ions. The selective layers in PSCs can provide a field which is used to extract the photogenerated charge carrier. When the solar cell is under illumination, the photogenerated voltage together with built-in voltage induces ionic defect migration to the selective layers. Subsequently, an ion accumulation can form very thin charged layers at the interfaces. For example, in forwards bias, I^- can move to form a negatively charged layer at the interface with hole selective layers. This can reduce the charge extraction power and hence yield the difference between different scan directions.

The scan rate (*i.e.* how fast the J-V sweep is) also affects the degree of hysteresis because ions cannot respond to a too fast scan rate, and so the device has a different built-in potential compared to the case without ions. Hence, it poses a problem of how to compare different solar cells fabricated in different laboratories. It is much more reliable to track the device efficiency for longer timescale to account for any transient arising from the ionic movement. For this, a maximum power point (MPP) tracking is used. By the time of writing, a consensus has been reached to include MPP in the testing protocol of PSCs in which fixed voltage tracking and active tracking are both included depending on the testing level.[132]

In the PV industry, there are two main algorithm categories namely indirect or direct MPP tracking. Indirect MPP tracking estimates operational points according to known voltage/current in different weather conditions (fixed voltage/current methods, fraction open circuit voltage/short circuit current methods). Direct MPPT includes perturb and observe method (P&O), and incremental conduction method. These two methods decide the MPP based on real-time J-V scans.[133] Compared to indirect MPPT, direct ones are more accurate to estimate MPP, however, more complicated to implement.[133] One of the most commonly used algorithms in the laboratory is "perturb and observe" method.[134] This method works as follow: (1) the device is applied a certain voltage based on prior J-V scan, (2) after a certain time (usually in hundreds ms), the applied voltage is increased or decreased in a small step, which can yield a different power output; (3) if the power output increases, then the voltage will continue to increase/decrease; if the power output decreases, then the voltage will change in the opposite direction. By tracking MPP for 2-5 minutes, a stabilised output can be achieved which is reported in the field as stabilised or quasi steady-state efficiency.[132]

In addition to hysteresis during operation, the ion diffusion and migration can contribute to the net self-doping of the perovskite layer,[55, 135] induced by the applied biases to the perovskite layer.[128, 136] This may change the band alignment between perovskite and contact layers. The p-type doping is due to the presence of negatively charged vacancies (V_{Pb}'' and V_{MA}') whereas n-type doping can be induced by iodide vacancies[136] or the traps state introduced by metallic lead (Pb^0).[83] This means that with different ionic defect concentrations, the material can be more n or p-type doping. This self-doping in perovskite can occur due to variations during the fabrication process. For $MAPbI_3$, due to the volatile nature of MA-based products under heat,[137] annealing for solvent removal step can remove partially MA^+ in the film which changes the composition of the perovskite.[138] A more controllable method can be achieved by changing the $MAI:PbI_2$ ratio in the precursor which can affect the final perovskite's Fermi level position.[139-141] In particular, MAI-rich precursors yield more p-type film and PbI_2-rich precursors result in a more n-type $MAPbI_3$.[140-142] The substrate choice can also influence the growth of $MAPbI_3$ resulting in more n or p-type material.[143] It is worth noting that most studies employ photoelectron spectroscopy techniques to probe the distance between CB/VB to Fermi level which can only provide information from the very surface of the films. Nonetheless, this self-doping has been proposed to enable p-n junction PSCs.[142]

Finally, it has been shown that ionic defect migration during operational condition can impact the recombination at the surface and in the bulk of a solar device.[144-145] A high ionic defect concentration at the interface can screen the built-in voltage which can cause carrier trapping and nonradiative recombination at the interface. Moreover, the ionic defect migration in the electric field can create defects that can form recombination centres further reducing the device performance.[146] However, the possibility for the material to recover in the dark is vital to assess whether ionic defect migration has a negative impact on the long-term performance of the devices. Hence, in **Chapter 6**, electrical bias is used to investigate the ionic defect migration driven degradation and recovery that gives further insight into the role of ionic defect migration in a timescale of hours.

2.6.3 Phase segregation due to ionic defect migration

In the mixed halide perovskite, illumination induces reversible phase segregation in addition to the light-induced irreversible change which is discussed in previous sections. This is first introduced by Hoke *et al.* [147] and being observed and investigated by many others.[148-151] Halide segregation is thought to be closely related to halide migration/diffusion via vacancies in the material leading to I-rich and I-poor domains in the material due to light exposure. After resting in dark, the material can recover its initial composition, nonetheless, the recovery can be incomplete.[152] This phenomenon leads to wide bandgap phase which acts as recombination centres reducing the V_{OC} of mixed halide perovskite based devices during operation.[147]

A study by Bischak *et al.* found that photogenerated charge carriers could cause localised lattice strain.[149] Hence, halide segregation depends on the generated charge carriers concentration[148] regardless of the presence of light.[153] Owing to lattice distortion, demixing of halides becomes energetically favourable in the system.[149] After the material rests in the dark, the lattice strains are reduced confirming by X-ray diffraction (XRD) measurement.[154] Despite the recovery in the dark, the XRD peaks of perovskite shift after halide segregation, which can be attributed to defect formation.[154] Because this phenomenon depends on transportation of halide through halide vacancies,[154-155] halide phase segregation can be subdued in the halide rich (concerning lead) material.[155] Halide deficiency increases the concentration of halide vacancies and in turn, increases the rate of halide segregation. In contrast, the halide rich material takes a longer time to reach the stabilised halide segregation phases. Nonetheless, halide-poor perovskites have a faster rate of recovery in the dark after phase segregation compared to halide-rich analogue.[155]

Interestingly, depending on the A site, the threshold in which this phenomenon happens is different. For example, less than 20% Br in the mix for MA based perovskite provide photostability under one sun illumination[147] and the stable composition can stretch further with the inclusion of nonpolar A site such as Cs.[156] Moreover, since lattice strain is a characteristic of halide segregation, films with smaller grains, *i.e.* more grain boundaries, have faster halide segregation. The reason is that the distorted lattice can accommodate easier at grain boundaries or low-quality crystal because of less energy cost.[157] Another explanation is that the defect concentrated grain boundary which has a positive charge can attract the iodide anions, thus, promote the halide segregation near the grain boundary region.[158] Therefore, halide segregation can be suppressed by defect reduction especially at the grain boundary.

2.6.4 Impact of ionic defect migration on long-term stability

The ion diffusion and migration have a substantial effect on the long-term stability of PSCs. In operational conditions, the devices have a photovoltage across the perovskite layer. The potential difference at the contact layers can induce ionic defect migration. The accumulation of ions at the interfaces can become detrimental for the device performance due to possible reactions with the contact layers or the electrode. The iodide ions can react with Spiro-OMETAD (2,2',7,7'-Tetrakis[N,N-di(4-methoxyphenyl)amino]-9,9'-spirobifluorene), which is a commonly used hole selective layer in n-i-p structure. This reaction reduces the conductivity of Spiro-OMETAD and finally causes device degradation.[159] After penetration through the contact layers, ions can react with the metal electrode to form iodide compounds.[160-162] This further degrades the device performance due to the loss of perovskite material. In addition, metal ions can diffuse inside the perovskite which can create deep traps as mentioned in **section 2.5.**[22] To mitigate this metal diffusion and chemical reaction between the metal electrode and constituent ions from perovskites, various barrier layers have been used notably Cr and In-SnO_2.[163-164] In addition to metal diffusion, other ionic species from selective contacts can also diffuse inside the perovskite layer contributing to hysteresis seen in devices.[165]

Although much of the literature has focused on halide migration,[123] it is reported that MA^+ can migrate under electric field,[128-129] and diffuse limitedly in light.[127] This migration is much slower than I defects and can affect the long-term stability of the devices employing halide perovskite as a solar absorber.[85, 166] Domanski *et al.* reported that reversible degradation of PSCs is attributed to MA^+ diffusion. This migration of cation vacancies over the timescale of 6-10 hours can introduce a negative layer at the interface between perovskite and ESL which can repel electrons, reducing the performance of the cells.[85] The cation vacancies can migrate back and restore the device’s efficiency during the night when the device is resting in dark. This day-night cycling reversible degradation needs to be taken in consideration for lifetime estimation of PSCs.[85, 166-167]

Reference

1. NREL Reference Solar Spectral Irradiance. https://rredc.nrel.gov/solar//spectra/ (accessed 15/02/2020).
2. Smets, A.; Jäger, K.; Isabella, O.; Van Swaaij, R.; Zeman, M., The physics and engineering of photovoltaic conversion, technologies and systems. **2016**.
3. Würfel, P.; Würfel, U., *Physics of solar cells: from basic principles to advanced concepts*. John Wiley & Sons: 2016.
4. Brivio, F.; Frost, J. M.; Skelton, J. M.; Jackson, A. J.; Weber, O. J.; Weller, M. T.; Goni, A. R.; Leguy, A. M.; Barnes, P. R.; Walsh, A., Lattice dynamics and vibrational spectra of the orthorhombic, tetragonal, and cubic phases of methylammonium lead iodide. *Physical Review B* **2015,** *92* (14), 144308.
5. Unger, E.; Kegelmann, L.; Suchan, K.; Sörell, D.; Korte, L.; Albrecht, S., Roadmap and roadblocks for the band gap tunability of metal halide perovskites. *Journal of Materials Chemistry A* **2017,** *5* (23), 11401-11409.
6. Albrecht, S.; Rech, B., Perovskite solar cells: On top of commercial photovoltaics. *Nature Energy* **2017,** *2* (1), 16196.
7. Tao, S.; Schmidt, I.; Brocks, G.; Jiang, J.; Tranca, I.; Meerholz, K.; Olthof, S., Absolute energy level positions in tin-and lead-based halide perovskites. *Nature communications* **2019,** *10* (1), 2560.
8. NREL PV Efficiency Chart. https://www.nrel.gov/pv/assets/pdfs/pv-efficiency-chart.20181221.pdf (accessed 28/01/2020).
9. Dong, Q.; Fang, Y.; Shao, Y.; Mulligan, P.; Qiu, J.; Cao, L.; Huang, J., Electron-hole diffusion lengths> 175 μm in solution-grown CH3NH3PbI3 single crystals. *Science* **2015,** *347* (6225), 967-970.
10. Stranks, S. D.; Eperon, G. E.; Grancini, G.; Menelaou, C.; Alcocer, M. J.; Leijtens, T.; Herz, L. M.; Petrozza, A.; Snaith, H. J., Electron-hole diffusion lengths exceeding 1 micrometer in an organometal trihalide perovskite absorber. *Science* **2013,** *342* (6156), 341-344.
11. de Quilettes, D. W.; Vorpahl, S. M.; Stranks, S. D.; Nagaoka, H.; Eperon, G. E.; Ziffer, M. E.; Snaith, H. J.; Ginger, D. S., Impact of microstructure on local carrier lifetime in perovskite solar cells. *Science* **2015,** *348* (6235), 683-686.
12. Stranks, S. D.; Hoye, R. L.; Di, D.; Friend, R. H.; Deschler, F., The physics of light emission in halide perovskite devices. *Advanced Materials* **2018**, 1803336.
13. De Wolf, S.; Holovsky, J.; Moon, S.-J.; Löper, P.; Niesen, B.; Ledinsky, M.; Haug, F.-J.; Yum, J.-H.; Ballif, C., Organometallic halide perovskites: sharp optical absorption edge and its relation to photovoltaic performance. *The journal of physical chemistry letters* **2014,** *5* (6), 1035-1039.
14. Hwang, C., Doping dependence of hole lifetime in n-type GaAs. *Journal of Applied Physics* **1971,** *42* (11), 4408-4413.
15. Milot, R. L.; Eperon, G. E.; Snaith, H. J.; Johnston, M. B.; Herz, L. M., Temperature-dependent charge-carrier dynamics in CH3NH3PbI3 perovskite thin films. *Advanced Functional Materials* **2015,** *25* (39), 6218-6227.
16. Hinken, D.; Bothe, K.; Ramspeck, K.; Herlufsen, S.; Brendel, R., Determination of the effective diffusion length of silicon solar cells from photoluminescence. *Journal of Applied Physics* **2009,** *105* (10), 104516.
17. Würfel, P.; Trupke, T.; Puzzer, T.; Schäffer, E.; Warta, W.; Glunz, S., Diffusion lengths of silicon solar cells from luminescence images. *Journal of Applied Physics* **2007,** *101* (12), 123110.
18. Yamaguchi, M.; Amano, C., 60Co γ-ray and electron irradiation damage of GaAs single crystals and solar cells. *Journal of applied physics* **1983,** *54* (9), 5021-5029.
19. Thurber, W.; Mattis, R.; Liu, Y.; Filliben, J., Resistivity-dopant density relationship for boron-doped silicon. *Journal of the Electrochemical society* **1980,** *127* (10), 2291.
20. Green, M. A., Self-consistent optical parameters of intrinsic silicon at 300 K including temperature coefficients. *Solar Energy Materials and Solar Cells* **2008,** *92* (11), 1305-1310.
21. Johnson, S.; Tiedje, T., Temperature dependence of the Urbach edge in GaAs. *Journal of applied physics* **1995,** *78* (9), 5609-5613.
22. Green, M. A.; Keevers, M. J., Optical properties of intrinsic silicon at 300 K. *Progress in Photovoltaics: Research and applications* **1995,** *3* (3), 189-192.
23. Roth, R. S., Classification of perovskite and other ABO3-type compounds. *J. Res. Nat. Bur. Stand* **1957,** *58* (2), 75-88.
24. Glazer, A., The classification of tilted octahedra in perovskites. *Acta Crystallographica Section B: Structural Crystallography and Crystal Chemistry* **1972,** *28* (11), 3384-3392.

25. Goldschmidt, V. M., Die gesetze der krystallochemie. *Naturwissenschaften* **1926,** *14* (21), 477-485.

26. Gholipour, S.; Ali, A. M.; Correa-Baena, J. P.; Turren-Cruz, S. H.; Tajabadi, F.; Tress, W.; Taghavinia, N.; Grätzel, M.; Abate, A.; De Angelis, F.; Gaggioli, C. A.; Mosconi, E.; Hagfeldt, A.; Saliba, M., Globularity-Selected Large Molecules for a New Generation of Multication Perovskites. *Advanced materials* **2017,** *29* (38), 1702005.

27. Mitzi, D. B., Templating and structural engineering in organic–inorganic perovskites. *Journal of the Chemical Society, Dalton Transactions* **2001,** (1), 1-12.

28. Wang, S.; Mitzi, D. B.; Feild, C. A.; Guloy, A., Synthesis and Characterization of [NH2C (I): NH2] 3MI5 (M= Sn, Pb): Stereochemical Activity in Divalent Tin and Lead Halides Containing Single. ltbbrac. 110. rtbbrac. Perovskite Sheets. *Journal of the American Chemical Society* **1995,** *117* (19), 5297-5302.

29. Gholipour, S.; Ali, A. M.; Correa-Baena, J. P.; Turren-Cruz, S. H.; Tajabadi, F.; Tress, W.; Taghavinia, N.; Grätzel, M.; Abate, A.; De Angelis, F., Globularity-Selected Large Molecules for a New Generation of Multication Perovskites. *Advanced Materials* **2017,** *29* (38).

30. Shannon, R. D., Revised effective ionic radii and systematic studies of interatomic distances in halides and chalcogenides. *Acta crystallographica section A: crystal physics, diffraction, theoretical and general crystallography* **1976,** *32* (5), 751-767.

31. Weller, M. T.; Weber, O. J.; Henry, P. F.; Di Pumpo, A. M.; Hansen, T. C., Complete structure and cation orientation in the perovskite photovoltaic methylammonium lead iodide between 100 and 352 K. *Chemical Communications* **2015,** *51* (20), 4180-4183.

32. Poglitsch, A.; Weber, D., Dynamic disorder in methylammoniumtrihalogenoplumbates (II) observed by millimeter-wave spectroscopy. *The Journal of chemical physics* **1987,** *87* (11), 6373-6378.

33. Stoumpos, C. C.; Malliakas, C. D.; Kanatzidis, M. G., Semiconducting tin and lead iodide perovskites with organic cations: phase transitions, high mobilities, and near-infrared photoluminescent properties. *Inorganic chemistry* **2013,** *52* (15), 9019-9038.

34. Weller, M. T.; Weber, O. J.; Frost, J. M.; Walsh, A., Cubic perovskite structure of black formamidinium lead iodide, α-[HC (NH2) 2] PbI3, at 298 K. *The journal of physical chemistry letters* **2015,** *6* (16), 3209-3212.

35. Schueller, E. C.; Laurita, G.; Fabini, D. H.; Stoumpos, C. C.; Kanatzidis, M. G.; Seshadri, R., Crystal structure evolution and notable thermal expansion in hybrid perovskites formamidinium tin iodide and formamidinium lead bromide. *Inorganic chemistry* **2018,** *57* (2), 695-701.

36. Imran, M.; Caligiuri, V.; Wang, M.; Goldoni, L.; Prato, M.; Krahne, R.; De Trizio, L.; Manna, L., Benzoyl halides as alternative precursors for the colloidal synthesis of lead-based halide perovskite nanocrystals. *Journal of the American Chemical Society* **2018,** *140* (7), 2656-2664.

37. Marronnier, A.; Roma, G.; Boyer-Richard, S.; Pedesseau, L.; Jancu, J.-M.; Bonnassieux, Y.; Katan, C.; Stoumpos, C. C.; Kanatzidis, M. G.; Even, J., Anharmonicity and disorder in the black phases of cesium lead iodide used for stable inorganic perovskite solar cells. *ACS nano* **2018,** *12* (4), 3477-3486.

38. Stoumpos, C. C.; Malliakas, C. D.; Peters, J. A.; Liu, Z.; Sebastian, M.; Im, J.; Chasapis, T. C.; Wibowo, A. C.; Chung, D. Y.; Freeman, A. J.; Wessels, B. W.; Kanatzidis, M. G., Crystal growth of the perovskite semiconductor $CsPbBr_3$: a new material for high-energy radiation detection. *Crystal growth & design* **2013,** *13* (7), 2722-2727.

39. Persson, K. *Materials Data on CsPbBr3 (SG:140) by Materials Project*; LBNL Materials Project; Lawrence Berkeley National Lab: United States, 2016.

40. Persson, K. *Materials Data on CsPbBr3 (SG:221) by Materials Project*; LBNL Materials Project; Lawrence Berkeley National Lab: United States, 2016.

41. Persson, K. *Materials Data on $CsPbCl_3$ (SG:38) by Materials Project*; LBNL Materials Project; Lawrence Berkeley National Lab: United States, 2016.

42. Persson, K. *Materials Data on $CsPbCl_3$ (SG:221) by Materials Project*; LBNL Materials Project; Lawrence Berkeley National Lab: United States, 2016.

43. Yang, R. X.; Skelton, J. M.; Da Silva, E. L.; Frost, J. M.; Walsh, A., Spontaneous octahedral tilting in the cubic inorganic cesium halide perovskites CsSnX3 and $CsPbX_3$ (X= F, Cl, Br, I). *The journal of physical chemistry letters* **2017,** *8* (19), 4720-4726.

44. Saliba, M.; Correa-Baena, J.-P.; Wolff, C. M.; Stolterfoht, M.; Phung, N.; Albrecht, S.; Neher, D.; Abate, A., How to make over 20% efficient perovskite solar cells in regular (n–i–p) and inverted (p–i–n) architectures. *Chemistry of Materials* **2018,** *30* (13), 4193-4201.

45. Stolterfoht, M.; Caprioglio, P.; Wolff, C. M.; Márquez, J. A.; Nordmann, J.; Zhang, S.; Rothhardt, D.; Hörmann, U.; Amir, Y.; Redinger, A.; Kegelmann, L.; Zu, F.; Albrecht, S.; Koch, N.; Kirchartz, T.; Saliba, M.; Unold, T.; Neher, D., The impact of energy alignment and interfacial recombination on the internal and external open-circuit voltage of perovskite solar cells. *Energy & Environmental Science* **2019,** *12* (9), 2778-2788.

46. Zheng, X.; Chen, B.; Dai, J.; Fang, Y.; Bai, Y.; Lin, Y.; Wei, H.; Zeng, X. C.; Huang, J., Defect passivation in hybrid perovskite solar cells using quaternary ammonium halide anions and cations. *Nature Energy* **2017,** *2* (7), 1-9.

47. Magomedov, A.; Al-Ashouri, A.; Kasparavičius, E.; Strazdaite, S.; Niaura, G.; Jošt, M.; Malinauskas, T.; Albrecht, S.; Getautis, V., Self-Assembled Hole Transporting Monolayer for Highly Efficient Perovskite Solar Cells. *Advanced Energy Materials* **2018,** *8* (32), 1801892.

48. Queisser, H. J.; Haller, E. E., Defects in semiconductors: some fatal, some vital. *Science* **1998,** *281* (5379), 945-950.

49. Johnston, M. B.; Herz, L. M., Hybrid perovskites for photovoltaics: charge-carrier recombination, diffusion, and radiative efficiencies. *Accounts of chemical research* **2015,** *49* (1), 146-154.

50. Saba, M.; Cadelano, M.; Marongiu, D.; Chen, F.; Sarritzu, V.; Sestu, N.; Figus, C.; Aresti, M.; Piras, R.; Lehmann, A. G.; Cannas, C.; Musinu, A.; Quochi, F.; Mura, A.; Bongiovanni, G., Correlated electron–hole plasma in organometal perovskites. *Nature communications* **2014,** *5*, 5049.

51. Stolterfoht, M.; Wolff, C. M.; Márquez, J. A.; Zhang, S.; Hages, C. J.; Rothhardt, D.; Albrecht, S.; Burn, P. L.; Meredith, P.; Unold, T.; Neher, D., Visualization and suppression of interfacial recombination for high-efficiency large-area pin perovskite solar cells. *Nature Energy* **2018,** *3* (10), 847.

52. Shockley, W.; Read Jr, W., Statistics of the recombinations of holes and electrons. *Physical review* **1952,** *87* (5), 835.

53. Tress, W., Maximum Efficiency and Open-Circuit Voltage of Perovskite Solar Cells. In *Organic-inorganic halide perovskite photovoltaics*, Park, N.-G.; Miyasaka, T.; Grätzel, M., Eds. Springer: Switzerland, 2016.

54. Walsh, A.; Scanlon, D. O.; Chen, S.; Gong, X.; Wei, S. H., Self-regulation mechanism for charged point defects in hybrid halide perovskites. *Angewandte Chemie International Edition* **2015,** *54* (6), 1791-1794.

55. Yin, W.-J.; Shi, T.; Yan, Y., Unusual defect physics in CH3NH3PbI3 perovskite solar cell absorber. *Applied Physics Letters* **2014,** *104* (6), 063903.

56. Ming, W.; Chen, S.; Du, M.-H., Chemical instability leads to unusual chemical-potential-independent defect formation and diffusion in perovskite solar cell material CH 3 NH 3 PbI 3. *Journal of Materials Chemistry A* **2016,** *4* (43), 16975-16981.

57. Meloni, S.; Palermo, G.; Ashari-Astani, N.; Grätzel, M.; Rothlisberger, U., Valence and conduction band tuning in halide perovskites for solar cell applications. *Journal of Materials Chemistry A* **2016,** *4* (41), 15997-16002.

58. Saliba, M.; Matsui, T.; Domanski, K.; Seo, J.-Y.; Ummadisingu, A.; Zakeeruddin, S. M.; Correa-Baena, J.-P.; Tress, W. R.; Abate, A.; Hagfeldt, A.; Grätzel, M., Incorporation of rubidium cations into perovskite solar cells improves photovoltaic performance. *Science* **2016,** *354* (6309), 206-209.

59. Noel, N. K.; Abate, A.; Stranks, S. D.; Parrott, E. S.; Burlakov, V. M.; Goriely, A.; Snaith, H. J., Enhanced photoluminescence and solar cell performance via Lewis base passivation of organic–inorganic lead halide perovskites. *ACS nano* **2014,** *8* (10), 9815-9821.

60. Wang, R.; Xue, J.; Wang, K.-L.; Wang, Z.-K.; Luo, Y.; Fenning, D.; Xu, G.; Nuryyeva, S.; Huang, T.; Zhao, Y.; Yang, J. L.; Zhu, J.; Wang, M.; Tan, S.; Yavuz, I.; Houk, K. N.; Yang, Y., Constructive molecular configurations for surface-defect passivation of perovskite photovoltaics. *Science* **2019,** *366* (6472), 1509-1513.

61. Aristidou, N.; Eames, C.; Sanchez-Molina, I.; Bu, X.; Kosco, J.; Islam, M. S.; Haque, S. A., Fast oxygen diffusion and iodide defects mediate oxygen-induced degradation of perovskite solar cells. *Nature communications* **2017,** *8*, 15218.

62. Sun, Q.; Fassl, P.; Becker-Koch, D.; Bausch, A.; Rivkin, B.; Bai, S.; Hopkinson, P. E.; Snaith, H. J.; Vaynzof, Y., Role of microstructure in oxygen induced photodegradation of methylammonium lead triiodide perovskite films. *Advanced Energy Materials* **2017,** *7* (20), 1700977.

63. Domanski, K.; Correa-Baena, J.-P.; Mine, N.; Nazeeruddin, M. K.; Abate, A.; Saliba, M.; Tress, W.; Hagfeldt, A.; Grätzel, M., Not all that glitters is gold: metal-migration-induced degradation in perovskite solar cells. *ACS nano* **2016,** *10* (6), 6306-6314.

64. Jin, H.; Debroye, E.; Keshavarz, M.; Scheblykin, I. G.; Roeffaers, M. B.; Hofkens, J.; Steele, J. A., It's a trap! On the nature of localised states and charge trapping in lead halide perovskites. *Materials Horizons* **2020**.

65. Meggiolaro, D.; De Angelis, F., First-Principles Modeling of Defects in Lead Halide Perovskites: Best Practices and Open Issues. *ACS Energy Letters* **2018,** *3* (9), 2206-2222.

66. Heo, S.; Seo, G.; Lee, Y.; Lee, D.; Seol, M.; Lee, J.; Park, J.-B.; Kim, K.; Yun, D.-J.; Kim, Y. S.; Shin, J. K.; Ahn, T. K.; Nazeeruddin, M. K., Deep level trapped defect analysis in CH 3 NH 3 PbI 3 perovskite solar cells by deep level transient spectroscopy. *Energy & Environmental Science* **2017,** *10* (5), 1128-1133.

67. Shi, D.; Adinolfi, V.; Comin, R.; Yuan, M.; Alarousu, E.; Buin, A.; Chen, Y.; Hoogland, S.; Rothenberger, A.; Katsiev, K.; Losovyj, Y.; Zhang, X.; Dowben, P. A.; Mohammed, O. F.; Sargent, E. H.; Bakr, O. M., Low trap-state density and long carrier diffusion in organolead trihalide perovskite single crystals. *Science* **2015,** *347* (6221), 519-522.

68. Sadoughi, G.; Starr, D. E.; Handick, E.; Stranks, S. D.; Gorgoi, M.; Wilks, R. G.; Bär, M.; Snaith, H. J., Observation and mediation of the presence of metallic lead in organic–inorganic perovskite films. *ACS applied materials & interfaces* **2015,** *7* (24), 13440-13444.

69. Wang, S.; Jiang, Y.; Juarez-Perez, E. J.; Ono, L. K.; Qi, Y., Accelerated degradation of methylammonium lead iodide perovskites induced by exposure to iodine vapour. *Nature Energy* **2016,** *2* (1), 1-8.

70. Kirchartz, T.; Krückemeier, L.; Unger, E. L., Research Update: Recombination and open-circuit voltage in lead-halide perovskites. *Apl Materials* **2018,** *6* (10), 100702.

71. Baumann, A.; Väth, S.; Rieder, P.; Heiber, M. C.; Tvingstedt, K.; Dyakonov, V., Identification of trap states in perovskite solar cells. *The journal of physical chemistry letters* **2015,** *6* (12), 2350-2354.

72. Gordillo, G.; Otálora, C.; Reinoso, M., Trap center study in hybrid organic-inorganic perovskite using thermally stimulated current (TSC) analysis. *Journal of Applied Physics* **2017,** *122* (7), 075304.

73. Moghadamzadeh, S.; Hossain, I. M.; Jakoby, M.; Nejand, B. A.; Rueda-Delgado, D.; Schwenzer, J. A.; Gharibzadeh, S.; Abzieher, T.; Khan, M. R.; Haghighirad, A. A.; Howard, I. A.; Richards, B. S.; Lemmerabd, U.; Paetzold, U. W., Spontaneous enhancement of the stable power conversion efficiency in perovskite solar cells. *Journal of Materials Chemistry A* **2020**.

74. Yang, W. S.; Park, B.-W.; Jung, E. H.; Jeon, N. J.; Kim, Y. C.; Lee, D. U.; Shin, S. S.; Seo, J.; Kim, E. K.; Noh, J. H.; Seok, S. I., Iodide management in formamidinium-lead-halide–based perovskite layers for efficient solar cells. *Science* **2017,** *356* (6345), 1376-1379.

75. Cao, H.; Li, J.; Dong, Z.; Su, J.; Chang, J.; Zhao, Q.; Li, Z.; Yang, L.; Yin, S., Reducing Defects in Perovskite Solar Cells with White Light Illumination-Assisted Synthesis. *ACS Energy Letters* **2019,** *4* (12), 2821-2829.

76. Dong, Q.; Ho, C. H. Y.; Yu, H.; Salehi, A.; So, F., Defect passivation by fullerene derivative in perovskite solar cells with aluminum-doped zinc oxide as electron transporting layer. *Chemistry of Materials* **2019,** *31* (17), 6833-6840.

77. Heo, S.; Seo, G.; Lee, Y.; Seol, M.; Kim, S. H.; Yun, D. J.; Kim, Y.; Kim, K.; Lee, J.; Lee, J.; Jeon, W. S.; Shin, J. K.; Park, J.; Lee, D.; Nazeeruddin, M. K., Origins of high performance and degradation in the mixed perovskite solar cells. *Advanced Materials* **2019,** *31* (8), 1805438.

78. Duan, H.-S.; Zhou, H.; Chen, Q.; Sun, P.; Luo, S.; Song, T.-B.; Bob, B.; Yang, Y., The identification and characterization of defect states in hybrid organic–inorganic perovskite photovoltaics. *Physical chemistry chemical physics* **2015,** *17* (1), 112-116.

79. Xu, W.; Hu, Q.; Bai, S.; Bao, C.; Miao, Y.; Yuan, Z.; Borzda, T.; Barker, A. J.; Tyukalova, E.; Hu, Z.; Kawecki, M.; Wang, H.; Yan, Z.; Liu, X.; Shi, X.; Uvdal, K.; Fahlman, M.; Zhang, W.; Duchamp, M.; Liu, J.-M.; Petrozza, A.; Wang, J.; Liu, L.-M.; Huang, W.; Gao, F., Rational molecular passivation for high-performance perovskite light-emitting diodes. *Nature Photonics* **2019,** *13* (6), 418-424.

80. Buin, A.; Comin, R.; Xu, J.; Ip, A. H.; Sargent, E. H., Halide-dependent electronic structure of organolead perovskite materials. *Chemistry of Materials* **2015,** *27* (12), 4405-4412.

81. Meggiolaro, D.; Motti, S. G.; Mosconi, E.; Barker, A. J.; Ball, J.; Perini, C. A. R.; Deschler, F.; Petrozza, A.; De Angelis, F., Iodine chemistry determines the defect tolerance of lead-halide perovskites. *Energy & Environmental Science* **2018,** *11* (3), 702-713.

82. Motti, S. G.; Meggiolaro, D.; Martani, S.; Sorrentino, R.; Barker, A. J.; De Angelis, F.; Petrozza, A., Defect Activity in Lead Halide Perovskites. *Advanced Materials* **2019,** *31* (47), 1901183.

83. Zu, F. S.; Amsalem, P.; Salzmann, I.; Wang, R. B.; Ralaiarisoa, M.; Kowarik, S.; Duhm, S.; Koch, N., Impact of white light illumination on the electronic and chemical structures of mixed halide and single crystal perovskites. *Advanced Optical Materials* **2017,** *5* (9), 1700139.

84. Juarez-Perez, E. J.; Ono, L. K.; Maeda, M.; Jiang, Y.; Hawash, Z.; Qi, Y., Photodecomposition and thermal decomposition in methylammonium halide lead perovskites and inferred design principles to increase photovoltaic device stability. *Journal of Materials Chemistry A* **2018,** *6* (20), 9604-9612.

85. Domanski, K.; Roose, B.; Matsui, T.; Saliba, M.; Turren-Cruz, S.-H.; Correa-Baena, J.-P.; Carmona, C. R.; Richardson, G.; Foster, J. M.; De Angelis, F.; Ball, J. M.; Petrozza, A.; Mine, N.; Nazeeruddin, M. K.; Tress, W.; Grätzel, M.; Steiner, U.; Hagfeldt, A.; Abate, A., Migration of cations induces reversible performance losses over day/night cycling in perovskite solar cells. *Energy & Environmental Science* **2017,** *10* (2), 604-613.

86. Du, M. H., Efficient carrier transport in halide perovskites: theoretical perspectives. *Journal of Materials Chemistry A* **2014,** *2* (24), 9091-9098.

87. Du, M.-H., Density functional calculations of native defects in CH3NH3PbI3: effects of spin–orbit coupling and self-interaction error. *The journal of physical chemistry letters* **2015,** *6* (8), 1461-1466.

88. Abdelhady, A. L.; Saidaminov, M. I.; Murali, B.; Adinolfi, V.; Voznyy, O.; Katsiev, K.; Alarousu, E.; Comin, R.; Dursun, I.; Sinatra, L.; Sargent, E. H.; Mohammed, O. F.; Bakr, O. M., Heterovalent dopant incorporation for bandgap and type engineering of perovskite crystals. *The journal of physical chemistry letters* **2016,** *7* (2), 295-301.

89. Yavari, M.; Ebadi, F.; Meloni, S.; Wang, Z. S.; Yang, T. C.-J.; Sun, S.; Schwartz, H.; Wang, Z.; Niesen, B.; Durantini, J.; Rieder, P.; Tvingstedt, K.; Buonassisi, T.; Choy, W. C. H.; Filippetti, A.; Dittrich, T.; Olthof, S.; Correa-Baena, J.-P.; Tress, W., How far does the defect tolerance of lead-halide perovskites range? The example of Bi impurities introducing efficient recombination centers. *Journal of Materials Chemistry A* **2019,** *7* (41), 23838-23853.

90. Gong, X.; Guan, L.; Pan, H.; Sun, Q.; Zhao, X.; Li, H.; Pan, H.; Shen, Y.; Shao, Y.; Sun, L.; Cui, Z.; Ding, L.; Wang, M., Highly efficient perovskite solar cells via nickel passivation. *Advanced Functional Materials* **2018,** *28* (50), 1804286.

91. Wang, J. T.-W.; Wang, Z.; Pathak, S.; Zhang, W.; deQuilettes, D. W.; Wisnivesky-Rocca-Rivarola, F.; Huang, J.; Nayak, P. K.; Patel, J. B.; Yusof, H. A. M.; Vaynzof, Y.; Zhu, R.; Ramirez, I.; Zhang, J.; Ducati, C.; Grovenor, C.; Johnston, M. B.; Ginger, D. S.; Nicholas, R. J.; Snaith, H. J., Efficient perovskite solar cells by metal ion doping. *Energy & Environmental Science* **2016,** *9* (9), 2892-2901.

92. Yin, J.; Ahmed, G. H.; Bakr, O. M.; Brédas, J.-L.; Mohammed, O. F., Unlocking the Effect of Trivalent Metal Doping in All-Inorganic CsPbBr3 Perovskite. *ACS Energy Letters* **2019,** *4* (3), 789-795.

93. Zhang, J.; Shang, M.-h.; Wang, P.; Huang, X.; Xu, J.; Hu, Z.; Zhu, Y.; Han, L., n-type doping and energy states tuning in $CH_3NH_3Pb_{1-x}Sb_{2x/3}I_3$ perovskite solar cells. *ACS Energy Letters* **2016,** *1* (3), 535-541.

94. Bartesaghi, D.; Ray, A.; Jiang, J.; Bouwer, R. K.; Tao, S.; Savenije, T. J., Partially replacing Pb2+ by Mn2+ in hybrid metal halide perovskites: Structural and electronic properties. *APL Materials* **2018,** *6* (12), 121106.

95. Phung, N.; Félix, R.; Meggiolaro, D.; Al-Ashouri, A.; Sousa e Silva, G.; Hartmann, C.; Hidalgo, J.; Köbler, H.; Mosconi, E.; Lai, B.; Gunder, R.; Li, M.; Wang, K.-L.; Wang, Z.-K.; Nie, K.; Handick, E.; Wilks, R. G.; Marquez, J. A.; Rech, B.; Unold, T.; Correa-Baena, J.-P.; Albrecht, S.; De Angelis, F.; Bär, M.; Abate, A., The doping mechanism of halide perovskite unveiled by alkaline earth metals. *Journal of the American Chemical Society* **2020,** *142* (5), 2364-2374.

96. Klug, M. T.; Osherov, A.; Haghighirad, A. A.; Stranks, S. D.; Brown, P. R.; Bai, S.; Wang, J. T.-W.; Dang, X.; Bulović, V.; Snaith, H. J.; Belcher, A. M., Tailoring metal halide perovskites through metal substitution: influence on photovoltaic and material properties. *Energy & Environmental Science* **2017,** *10* (1), 236-246.

97. Saidaminov, M. I.; Kim, J.; Jain, A.; Quintero-Bermudez, R.; Tan, H.; Long, G.; Tan, F.; Johnston, A.; Zhao, Y.; Voznyy, O.; Sargent, E. H., Suppression of atomic vacancies via incorporation of isovalent small ions to increase the stability of halide perovskite solar cells in ambient air. *Nature Energy* **2018,** *3* (8), 648-654.

98. Muscarella, L. A.; Petrova, D.; Jorge Cervasio, R.; Farawar, A.; Lugier, O.; McLure, C.; Slaman, M. J.; Wang, J.; Ehrler, B.; Von Hauff, E.; Williams, R. M., Air-stable and oriented mixed lead halide perovskite (FA/MA) by the one-step deposition method using Zinc Iodide and an Alkylammonium additive. *ACS applied materials & interfaces* **2019,** *11* (19), 17555-17562.

99. Poindexter, J. R.; Hoye, R. L.; Nienhaus, L.; Kurchin, R. C.; Morishige, A. E.; Looney, E. E.; Osherov, A.; Correa-Baena, J.-P.; Lai, B.; Bulović, V.; Stevanović, V.; Bawendi, M. G.; Buonassisi, T., High tolerance to iron contamination in lead halide perovskite solar cells. *ACS nano* **2017,** *11* (7), 7101-7109.

100. Fang, Z.; He, H.; Gan, L.; Li, J.; Ye, Z., Understanding the Role of Lithium Doping in Reducing Nonradiative Loss in Lead Halide Perovskites. *Advanced Science* **2018,** *5* (12), 1800736.

101. Cao, J.; Tao, S. X.; Bobbert, P. A.; Wong, C. P.; Zhao, N., Interstitial occupancy by extrinsic alkali cations in perovskites and its impact on ion migration. *Advanced Materials* **2018,** *30* (26), 1707350.

102. Son, D.-Y.; Kim, S.-G.; Seo, J.-Y.; Lee, S.-H.; Shin, H.; Lee, D.; Park, N.-G., Universal approach toward hysteresis-free perovskite solar cell via defect engineering. *Journal of the American Chemical Society* **2018,** *140* (4), 1358-1364.

103. Yang, Y.; Zou, X.; Pei, Y.; Bai, X.; Jin, W.; Chen, D., Effect of doping of NaI monovalent cation halide on the structural, morphological, optical and optoelectronic properties of $MAPbI_3$ perovskite. *Journal of Materials Science: Materials in Electronics* **2018,** *29* (1), 205-210.

104. Abdi-Jalebi, M.; Pazoki, M.; Philippe, B.; Dar, M. I.; Alsari, M.; Sadhanala, A.; Divitini, G.; Imani, R.; Lilliu, S.; Kullgren, J.; Rensmo, H.; Grätzel, M.; Friend, R. H., Dedoping of lead halide perovskites incorporating monovalent cations. *ACS nano* **2018,** *12* (7), 7301-7311.

105. Ming, W.; Yang, D.; Li, T.; Zhang, L.; Du, M. H., Formation and diffusion of metal impurities in perovskite solar cell material $CH_3NH_3PbI_3$: implications on solar cell degradation and choice of electrode. *Advanced Science* **2018,** *5* (2), 1700662.

106. Abdi-Jalebi, M.; Andaji-Garmaroudi, Z.; Cacovich, S.; Stavrakas, C.; Philippe, B.; Richter, J. M.; Alsari, M.; Booker, E. P.; Hutter, E. M.; Pearson, A. J.; Lilliu, S.; Savenije, T. J.; Rensmo, H.; Divitini, G.; Ducati, C.; Friend, R. H.; Stranks, S. D., Maximizing and stabilizing luminescence from halide perovskites with potassium passivation. *Nature* **2018,** *555* (7697), 497-501.

107. Saliba, M.; Matsui, T.; Seo, J.-Y.; Domanski, K.; Correa-Baena, J.-P.; Nazeeruddin, M. K.; Zakeeruddin, S. M.; Tress, W.; Abate, A.; Hagfeldt, A., Cesium-containing triple cation perovskite solar cells: improved stability, reproducibility and high efficiency. *Energy & environmental science* **2016,** *9* (6), 1989-1997.

108. Eperon, G. E.; Stranks, S. D.; Menelaou, C.; Johnston, M. B.; Herz, L. M.; Snaith, H. J., Formamidinium lead trihalide: a broadly tunable perovskite for efficient planar heterojunction solar cells. *Energy & Environmental Science* **2014,** *7* (3), 982-988.

109. Zheng, X.; Wu, C.; Jha, S. K.; Li, Z.; Zhu, K.; Priya, S., Improved phase stability of formamidinium lead triiodide perovskite by strain relaxation. *ACS Energy Letters* **2016,** *1* (5), 1014-1020.

110. Yi, C.; Luo, J.; Meloni, S.; Boziki, A.; Ashari-Astani, N.; Grätzel, C.; Zakeeruddin, S. M.; Röthlisberger, U.; Grätzel, M., Entropic stabilization of mixed A-cation ABX 3 metal halide perovskites for high performance perovskite solar cells. *Energy & Environmental Science* **2016,** *9* (2), 656-662.

111. Navas, J.; Sánchez-Coronilla, A.; Gallardo, J. J.; Hernández, N. C.; Piñero, J. C.; Alcántara, R.; Fernández-Lorenzo, C.; Desireé, M.; Aguilar, T.; Martín-Calleja, J., New insights into organic–inorganic hybrid perovskite CH 3 NH 3 PbI 3 nanoparticles. An experimental and theoretical study of doping in Pb 2+ sites with Sn 2+, Sr 2+, Cd 2+ and Ca 2+. *Nanoscale* **2015,** *7* (14), 6216-6229.

112. Shi, T.; Yin, W.-J.; Yan, Y., Predictions for p-type $CH_3NH_3PbI_3$ perovskites. *The Journal of Physical Chemistry C* **2014,** *118* (44), 25350-25354.

113. Eames, C.; Frost, J. M.; Barnes, P. R.; O'regan, B. C.; Walsh, A.; Islam, M. S., Ionic transport in hybrid lead iodide perovskite solar cells. *Nature communications* **2015,** *6* (1), 1-8.

114. Haruyama, J.; Sodeyama, K.; Han, L.; Tateyama, Y., First-principles study of ion diffusion in perovskite solar cell sensitizers. *Journal of the American Chemical Society* **2015,** *137* (32), 10048-10051.

115. Azpiroz, J. M.; Mosconi, E.; Bisquert, J.; De Angelis, F., Defect migration in methylammonium lead iodide and its role in perovskite solar cell operation. *Energy & Environmental Science* **2015,** *8* (7), 2118-2127.

116. Pockett, A.; Eperon, G. E.; Sakai, N.; Snaith, H. J.; Peter, L. M.; Cameron, P. J., Microseconds, milliseconds and seconds: deconvoluting the dynamic behaviour of planar perovskite solar cells. *Physical Chemistry Chemical Physics* **2017,** *19* (8), 5959-5970.

117. Game, O. S.; Buchsbaum, G. J.; Zhou, Y.; Padture, N. P.; Kingon, A. I., Ions matter: description of the anomalous electronic behavior in methylammonium lead halide perovskite devices. *Advanced Functional Materials* **2017,** *27* (16), 1606584.

118. Mosconi, E.; Meggiolaro, D.; Snaith, H. J.; Stranks, S. D.; De Angelis, F., Light-induced annihilation of Frenkel defects in organo-lead halide perovskites. *Energy & Environmental Science* **2016,** *9* (10), 3180-3187.

119. Futscher, M. H.; Lee, J. M.; McGovern, L.; Muscarella, L. A.; Wang, T.; Haider, M. I.; Fakharuddin, A.; Schmidt-Mende, L.; Ehrler, B., Quantification of ion migration in CH3NH3PbI3 perovskite solar cells by transient capacitance measurements. *Materials Horizons* **2019,** *6* (7), 1497-1503.

120. DeQuilettes, D. W.; Zhang, W.; Burlakov, V. M.; Graham, D. J.; Leijtens, T.; Osherov, A.; Bulović, V.; Snaith, H. J.; Ginger, D. S.; Stranks, S. D., Photo-induced halide redistribution in organic–inorganic perovskite films. *Nature communications* **2016,** *7* (1), 1-9.

121. Zhang, H.; Fu, X.; Tang, Y.; Wang, H.; Zhang, C.; William, W. Y.; Wang, X.; Zhang, Y.; Xiao, M., Phase segregation due to ion migration in all-inorganic mixed-halide perovskite nanocrystals. *Nature communications* **2019,** *10* (1), 1-8.

122. Xing, J.; Wang, Q.; Dong, Q.; Yuan, Y.; Fang, Y.; Huang, J., Ultrafast ion migration in hybrid perovskite polycrystalline thin films under light and suppression in single crystals. *Physical Chemistry Chemical Physics* **2016,** *18* (44), 30484-30490.

123. Tian, Y.; Peter, M.; Unger, E.; Abdellah, M.; Zheng, K.; Pullerits, T.; Yartsev, A.; Sundström, V.; Scheblykin, I. G., Mechanistic insights into perovskite photoluminescence enhancement: light curing with oxygen can boost yield thousandfold. *Physical Chemistry Chemical Physics* **2015,** *17* (38), 24978-24987.

124. Motti, S. G.; Gandini, M.; Barker, A. J.; Ball, J. M.; Srimath Kandada, A. R.; Petrozza, A., Photoinduced emissive trap states in lead halide perovskite semiconductors. *ACS Energy Letters* **2016,** *1* (4), 726-730.

125. Meggiolaro, D.; Mosconi, E.; De Angelis, F., Mechanism of reversible trap passivation by molecular oxygen in lead-halide perovskites. *ACS Energy Letters* **2017,** *2* (12), 2794-2798.

126. Galisteo-López, J. F.; Anaya, M.; Calvo, M.; Míguez, H., Environmental effects on the photophysics of organic–inorganic halide perovskites. *The journal of physical chemistry letters* **2015,** *6* (12), 2200-2205.

127. Senocrate, A.; Moudrakovski, I.; Acartürk, T.; Merkle, R.; Kim, G. Y.; Starke, U.; Grätzel, M.; Maier, J., Slow CH3NH3+ diffusion in CH3NH3PbI3 under light measured by solid-state NMR and tracer diffusion. *The Journal of Physical Chemistry C* **2018,** *122* (38), 21803-21806.

128. Yuan, Y.; Chae, J.; Shao, Y.; Wang, Q.; Xiao, Z.; Centrone, A.; Huang, J., Photovoltaic switching mechanism in lateral structure hybrid perovskite solar cells. *Advanced Energy Materials* **2015,** *5* (15), 1500615.

129. Yuan, Y.; Wang, Q.; Shao, Y.; Lu, H.; Li, T.; Gruverman, A.; Huang, J., Electric-field-driven reversible conversion between Methylammonium lead triiodide perovskites and lead iodide at elevated temperatures. *Advanced Energy Materials* **2016,** *6* (2), 1501803.

130. Filip, M. R.; Eperon, G. E.; Snaith, H. J.; Giustino, F., Steric engineering of metal-halide perovskites with tunable optical band gaps. *Nature communications* **2014,** *5*, 5757.

131. Merdasa, A.; Bag, M.; Tian, Y.; Källman, E.; Dobrovolsky, A.; Scheblykin, I. G., Super-resolution luminescence microspectroscopy reveals the mechanism of photoinduced degradation in CH3NH3PbI3 perovskite nanocrystals. *The Journal of Physical Chemistry C* **2016,** *120* (19), 10711-10719.

132. Khenkin, M. V.; Katz, E. A.; Abate, A.; Bardizza, G.; Berry, J. J.; Brabec, C.; Brunetti, F.; Bulović, V.; Burlingame, Q.; Di Carlo, A.; Cheacharoen, R.; Cheng, Y.-B.; Colsmann, A.; Cros, S.; Domanski, K.; Dusza, M.; Fell, C. J.; Forrest, S. R.; Galagan, Y.; Di Girolamo, D.; Grätzel, M.; Hagfeldt, A.; von Hauff, E.; Hoppe, H.; Kettle, J.; Köbler, H.; Leite, M. S.; Liu, S. F.; Loo, Y.-L.; Luther, J. M.; Ma, C.-Q.; Madsen, M.; Manceau, M.; Matheron, M.; McGehee, M.; Meitzner, R.; Nazeeruddin, M. K.; Nogueira, A. F.; Odabaşı, Ç.; Osherov, A.; Park, N.-G.; Reese, M. O.; De Rossi, F.; Saliba, M.; Schubert, U. S.; Snaith, H. J.; Stranks, S. D.; Tress, W.; Troshin, P. A.; Turkovic, V.; Veenstra, S.; Visoly-Fisher, I.; Walsh, A.; Watson, T.; Xie, H.; Yıldırım, R.; Zakeeruddin, S. M.; Zhu, K.; Lira-Cantu, M., Consensus statement for stability assessment and reporting for perovskite photovoltaics based on ISOS procedures. *Nature Energy* **2020,** *5* (1), 35-49.

133. Smets, A. H.; Jäger, K.; Isabella, O.; van Swaaij, R. A.; Zeman, M., *Solar Energy: The physics and engineering of photovoltaic conversion, technologies and systems*. UIT Cambridge Limited: 2016.

134. Cimaroli, A. J.; Yu, Y.; Wang, C.; Liao, W.; Guan, L.; Grice, C. R.; Zhao, D.; Yan, Y., Tracking the maximum power point of hysteretic perovskite solar cells using a predictive algorithm. *Journal of Materials Chemistry C* **2017,** *5* (39), 10152-10157.

135. Wang, Q.; Shao, Y.; Xie, H.; Lyu, L.; Liu, X.; Gao, Y.; Huang, J., Qualifying composition dependent p and n self-doping in CH3NH3PbI3. *Applied Physics Letters* **2014,** *105* (16), 163508.

136. Xiao, Z.; Yuan, Y.; Shao, Y.; Wang, Q.; Dong, Q.; Bi, C.; Sharma, P.; Gruverman, A.; Huang, J., Giant switchable photovoltaic effect in organometal trihalide perovskite devices. *Nature materials* **2015,** *14* (2), 193-198.

137. Dualeh, A.; Gao, P.; Seok, S. I.; Nazeeruddin, M. K.; Grätzel, M., Thermal behavior of methylammonium lead-trihalide perovskite photovoltaic light harvesters. *Chemistry of Materials* **2014,** *26* (21), 6160-6164.

138. Song, D.; Cui, P.; Wang, T.; Wei, D.; Li, M.; Cao, F.; Yue, X.; Fu, P.; Li, Y.; He, Y.; Jiang, B.; Trevor, M., Managing carrier lifetime and doping property of lead halide perovskite by postannealing processes for highly efficient perovskite solar cells. *The Journal of Physical Chemistry C* **2015,** *119* (40), 22812-22819.

139. Chang, J.; Zhu, H.; Xiao, J.; Isikgor, F. H.; Lin, Z.; Hao, Y.; Zeng, K.; Xu, Q.-H.; Ouyang, J., Enhancing the planar heterojunction perovskite solar cell performance through tuning the precursor ratio. *Journal of Materials Chemistry A* **2016,** *4* (20), 7943-7949.

140. Shin, D.; Kang, D.; Jeong, J.; Park, S.; Kim, M.; Lee, H.; Yi, Y., Unraveling the charge extraction mechanism of perovskite solar cells fabricated with two-step spin coating: interfacial energetics between methylammonium lead iodide and C60. *The journal of physical chemistry letters* **2017,** *8* (21), 5423-5429.

141. Fassl, P.; Lami, V.; Bausch, A.; Wang, Z.; Klug, M. T.; Snaith, H. J.; Vaynzof, Y., Fractional deviations in precursor stoichiometry dictate the properties, performance and stability of perovskite photovoltaic devices. *Energy & environmental science* **2018,** *11* (12), 3380-3391.

142. Dänekamp, B.; Müller, C.; Sendner, M.; Boix, P. P.; Sessolo, M.; Lovrincic, R.; Bolink, H. J., Perovskite–perovskite homojunctions via compositional doping. *The journal of physical chemistry letters* **2018,** *9* (11), 2770-2775.

143. Olthof, S.; Meerholz, K., Substrate-dependent electronic structure and film formation of MAPbI 3 perovskites. *Scientific reports* **2017,** *7* (1), 1-10.

144. Pockett, A.; Carnie, M. J., Ionic influences on recombination in perovskite solar cells. *ACS Energy Letters* **2017,** *2* (7), 1683-1689.

145. Walter, D.; Fell, A.; Wu, Y.; Duong, T.; Barugkin, C.; Wu, N.; White, T.; Weber, K., Transient photovoltage in perovskite solar cells: interaction of trap-mediated recombination and migration of multiple ionic species. *The Journal of Physical Chemistry C* **2018,** *122* (21), 11270-11281.

146. Tong, C.-J.; Li, L.; Liu, L.-M.; Prezhdo, O. V., Synergy between Ion Migration and Charge Carrier Recombination in Metal-Halide Perovskites. *Journal of the American Chemical Society* **2020.**

147. Hoke, E. T.; Slotcavage, D. J.; Dohner, E. R.; Bowring, A. R.; Karunadasa, H. I.; McGehee, M. D., Reversible photo-induced trap formation in mixed-halide hybrid perovskites for photovoltaics. *Chemical Science* **2015,** *6* (1), 613-617.

148. Slotcavage, D. J.; Karunadasa, H. I.; McGehee, M. D., Light-induced phase segregation in halide-perovskite absorbers. *ACS Energy Letters* **2016,** *1* (6), 1199-1205.

149. Bischak, C. G.; Hetherington, C. L.; Wu, H.; Aloni, S.; Ogletree, D. F.; Limmer, D. T.; Ginsberg, N. S., Origin of reversible photoinduced phase separation in hybrid perovskites. *Nano Letters* **2017,** *17* (2), 1028-1033.

150. Gratia, P.; Grancini, G.; Audinot, J.-N.; Jeanbourquin, X.; Mosconi, E.; Zimmermann, I.; Dowsett, D.; Lee, Y.; Grätzel, M.; De Angelis, F., Intrinsic halide segregation at nanometer scale determines the high efficiency of mixed cation/mixed halide perovskite solar cells. *Journal of the American Chemical Society* **2016,** *138* (49), 15821-15824.

151. Yoon, S. J.; Draguta, S.; Manser, J. S.; Sharia, O.; Schneider, W. F.; Kuno, M.; Kamat, P. V., Tracking iodide and bromide ion segregation in mixed halide lead perovskites during photoirradiation. *ACS Energy Letters* **2016,** *1* (1), 290-296.

152. Samu, G. F.; Janáky, C.; Kamat, P. V., A Victim of Halide Ion Segregation. How Light Soaking Affects Solar Cell Performance of Mixed Halide Lead Perovskites. *ACS Energy Letters* **2017,** *2* (8), 1860-1861.

153. Braly, I. L.; Stoddard, R. J.; Rajagopal, A.; Uhl, A. R.; Katahara, J. K.; Jen, A. K.-Y.; Hillhouse, H. W., Current-Induced Phase Segregation in Mixed Halide Hybrid Perovskites and its Impact on Two-Terminal Tandem Solar Cell Design. *ACS Energy Letters* **2017,** *2* (8), 1841-1847.

154. Barker, A. J.; Sadhanala, A.; Deschler, F.; Gandini, M.; Senanayak, S. P.; Pearce, P. M.; Mosconi, E.; Pearson, A.; Wu, Y.; Srimath Kandada, A. R., Defect-Assisted Photoinduced Halide Segregation in Mixed-Halide Perovskite Thin Films. *ACS Energy Letters* **2017.**

155. Yoon, S. J.; Kuno, K.; Kamat, P. V., Shift Happens. How Halide Ion Defects Influence Photoinduced Segregation in Mixed Halide Perovskites. *ACS Energy Letters* **2017**.

156. Bischak, C. G.; Wong, A. B.; Lin, E.; Limmer, D. T.; Yang, P.; Ginsberg, N. S., Tunable polaron distortions control the extent of halide demixing in lead halide perovskites. *The journal of physical chemistry letters* **2018,** *9* (14), 3998-4005.

157. Rehman, W.; McMeekin, D. P.; Patel, J. B.; Milot, R. L.; Johnston, M. B.; Snaith, H. J.; Herz, L. M., Photovoltaic mixed-cation lead mixed-halide perovskites: links between crystallinity, photo-stability and electronic properties. *Energy & Environmental Science* **2017,** *10* (1), 361-369.

158. Tang, X.; van den Berg, M.; Gu, E.; Horneber, A.; Matt, G. J.; Osvet, A.; Meixner, A. J.; Zhang, D.; Brabec, C. J., Local observation of phase segregation in mixed-halide perovskite. *Nano letters* **2018,** *18* (3), 2172-2178.

159. Carrillo, J.; Guerrero, A.; Rahimnejad, S.; Almora, O.; Zarazua, I.; Mas-Marza, E.; Bisquert, J.; Garcia-Belmonte, G., Ionic reactivity at contacts and aging of methylammonium lead triiodide perovskite solar cells. *Advanced Energy Materials* **2016,** *6* (9), 1502246.

160. Kato, Y.; Ono, L. K.; Lee, M. V.; Wang, S.; Raga, S. R.; Qi, Y., Silver iodide formation in methyl ammonium lead iodide perovskite solar cells with silver top electrodes. *Advanced Materials Interfaces* **2015,** *2* (13), 1500195.

161. Han, Y.; Meyer, S.; Dkhissi, Y.; Weber, K.; Pringle, J. M.; Bach, U.; Spiccia, L.; Cheng, Y.-B., Degradation observations of encapsulated planar CH 3 NH 3 PbI 3 perovskite solar cells at high temperatures and humidity. *Journal of Materials Chemistry A* **2015,** *3* (15), 8139-8147.

162. Shlenskaya, N. N.; Belich, N. A.; Grätzel, M.; Goodilin, E. A.; Tarasov, A. B., Light-induced reactivity of gold and hybrid perovskite as a new possible degradation mechanism in perovskite solar cells. *Journal of Materials Chemistry A* **2018,** *6* (4), 1780-1786.

163. Guerrero, A.; You, J.; Aranda, C.; Kang, Y. S.; Garcia-Belmonte, G.; Zhou, H.; Bisquert, J.; Yang, Y., Interfacial degradation of planar lead halide perovskite solar cells. *ACS nano* **2016,** *10* (1), 218-224.

164. Boyd, C. C.; Cheacharoen, R.; Bush, K. A.; Prasanna, R.; Leijtens, T.; McGehee, M. D., Barrier design to prevent metal-induced degradation and improve thermal stability in perovskite solar cells. *ACS Energy Letters* **2018,** *3* (7), 1772-1778.

165. Li, Z.; Xiao, C.; Yang, Y.; Harvey, S. P.; Kim, D. H.; Christians, J. A.; Yang, M.; Schulz, P.; Nanayakkara, S. U.; Jiang, C.-S.; Luther, J. M.; Berry, J. J.; Beard, M. C.; Al-Jassima, M. M.; Zhu, K., Extrinsic ion migration in perovskite solar cells. *Energy & Environmental Science* **2017,** *10* (5), 1234-1242.

166. Khenkin, M. V.; Anoop, K.; Visoly-Fisher, I.; Galagan, Y.; Di Giacomo, F.; Patil, B. R.; Sherafatipour, G.; Turkovic, V.; Rubahn, H.-G.; Madsen, M.; Merckx, T.; Uytterhoeven, G.; Bastos, J. P. A.; Aernouts, T.; Brunetti, F.; Lira-Cantu, M.; Katz, E. A., Reconsidering figures of merit for performance and stability of perovskite photovoltaics. *Energy & Environmental Science* **2018,** *11* (4), 739-743.

167. Saliba, M.; Stolterfoht, M.; Wolff, C. M.; Neher, D.; Abate, A., Measuring aging stability of perovskite solar cells. *Joule* **2018,** *2* (6), 1019-1024.

Chapter 3 Methods

3.1 Halide perovskites fabrication

The employed perovskite layers in these studies compiling this dissertation are fabricated from spin coating one-step method with anti-solvent treatment adopted from Jeon *et al.*[1] The perovskite precursors consist of stoichiometry or near stoichiometry of lead salts (PbI_2) and organic salts (MAI) in mixed solvents between dimethylformamide (DMF) and dimethyl sulfoxide (DMSO). This deposition method is a solution process where the perovskite precursor solutions are drop on the substrate, then a spinning program starts (commonly more than 4000 rpm). When substrates spin, excess solution is removed to form a very thin layer of solution. Then, the solvent evaporates during spinning which increases the concentration of the precursor promoting crystallisation. To form a compact and smooth film, an anti-solvent is used during spinning which can accelerate the nucleation process with high nucleation density. The anti-solvent is miscible with the solvents used in precursor and cannot dissolve perovskite. Hence, it can remove the solvent quicker than only evaporation; and by reducing the solubility of perovskite in the mixed solvent/anti-solvent, it favours the fast and homogeneous nucleation.[2] This method has first introduced by Jeon *et al.*,[1] and has been used to obtain high efficient devices.[3-4]

In this project, the choices of solvent and anti-solvent were based on the empirical method presented in **Appendix A**. In short, it was found that using DMF:DMSO 6:1 (volume ratio) as the solvent for $MAPbI_3$ perovskite and ethyl acetate as anti-solvent. Aside $MAPbI_3$, this dissertation also adapts the triple cation perovskite (CsFAMA) recipe from Saliba *et al.* using mixed solvent DMF:DMSO 4:1 (volume ratio).[5] All perovskite film fabrication steps were done in an N_2-filled glovebox to avoid air exposure.

Aside from thin-film prepared by spin coating, this study also used an inverse crystallisation method to grow $MAPbI_3$ single crystal. The method is relied on the different solubility limits of $MAPbI_3$ in γ-Butyrolactone (GBL) (Sigma Aldrich) at different temperatures.[6] As the temperature increases, the solubility of $MAPbI_3$ reduces, thus, allows nuclei formation and crystal growth. This method can be used to grow mm size crystals or recently has been used to grow single crystal for thin-film PSCs achieving impressive more than 21% efficiency.[7]

In this project, all chemicals are used as received. The $MAPbI_3$ perovskite solution is mixed from 1.2 M of PbI_2 (Tokyo Chemical Industry, 99.99%), and CH_3NH_3I (Dyenamo) in mixed solvent DMF:DMSO (6:1 volume ratio). The dopant SrI_2 (Alfa Aesar) is dissolved in DMSO (1 M) and MgI_2 (Santa Cruz) is dissolved in DMF:DMSO 6:1 (0.7 M). The amount of dopants in the perovskite solution is calculated according to the molar ratio with PbI_2. The final perovskite solution is shaken at 60 °C for 5 minutes to dissolve all components. 100 µL of perovskite solution is dropped on room temperature substrate before starting the spin coating program (4000 rpm for 30 s, ramping for 5 s). After 20 s of spin coating, 500 µL of ethyl acetate is dropped on the substrate to form a smooth and compact film. The perovskite film is immediately annealed at 100 °C for 60 minutes. Finally, C60 (20 nm) (Sigma Aldrich), BCP (bathocuproine or 2,9-Dimethyl-4,7-diphenyl-1) (10 nm) (Sigma Aldrich) and Cu (100 nm) (Alfa Aesar, 99.95% purity) are evaporated on the perovskite layer to complete the device. All of these fabrication steps are done in an inert atmosphere with minimised air exposure.

For $Cs_{0.05}((FAPbI_3)_{0.83}(MAPbBr_3)_{0.17})_{0.95}$ perovskite, $PbBr_2$ (1.5 M) (Tokyo Chemical Industry, 99.99%) and PbI_2 (1.5 M) (Tokyo Chemical Industry, 99.99%) are dissolved in a mixture of anhydrous DMF:DMSO (4:1 volume ratio) (Sigma Aldrich) and added to FAI (1.09:1 molar ratio) and MABr (1.09:1 molar ratio) powders respectively, to obtain $MAPbBr_3$ and $FAPbI_3$ solutions with a final concentration of 1.24 M. These two solutions are then mixed in a 17:83 volume ratio. Finally, the Caesium cation is added from a 1.5 M CsI (abcr GmbH, 99.999%) solution in DMSO in a 5:95 volume ratio. The perovskite solution is spin-coated using the following program: 4000 rpm (5 s acceleration) for 35 s (total time – 40 s). After 25 s, 500 µl of Ethyl Acetate (Sigma Aldrich) is dropped on the spinning substrate. After the spin-coating program, the perovskite-coated sample is annealed at 100°C for 60 min on a hotplate.

3.2 Device characterisation

As mentioned in **Chapter 2**, current density-voltage (J-V) measurement can give an initial assessment of PV performance of PSCs. The current density of the solar cells is measured during a voltage sweep. In this study, we used an Oriel LCS-100 class ABB solar simulator in an inert atmosphere for the J-V measurement. The sun simulator is calibrated with a Fraunhofer ISE silicon diode to assure a light intensity of 100 mW/cm^2. The scan rate is 100 mW/s starting from forward scan (V_{OC} to J_{SC}) using Keithley Model 2400 as a voltage source. All of the devices in **Chapter 4** and **Chapter 5** are measured without cooling. The devices in **Chapter 6** are measured with a home built sample holder with cooling water flow to cool the sample during the measurement. In one sun illumination exposure, the cells' temperature can increase rapidly which can decrease the V_{OC}. It has been reported that the V_{OC} of PSCs has a temperature dependence of approximately -2.27 mV/K.[8] Hence, the devices' voltage can be underestimated while measure without cooling compared to standard testing conditions (STC: cell's temperature is at 25°C, 100 mW/cm^2 global AM1.5).

The J-V measurements use the cell's area from a metal mask, *i.e.* the area of metal electrode to identify the current density. Thus, a mismatch of a defined cell's area and real active area can occur, which can be corrected by measure external quantum efficiency measurement (EQE). The EQE is the ratio between the number of photogenerated charge carriers and the incident photons coming on the solar cells surface. This is under the assumption that one photon generates one pair of charge carriers (electron and hole). Hence, the EQE is a wavelength-dependent parameter calculated as in **equation 3.1**.

$$\mathrm{EQE}(\lambda) = \frac{I_{ph}}{e\phi_{ph}(\lambda)} \qquad 3.1$$

where I_{ph} is the current generated from the solar cell, e is the elementary charge, $\Phi_{ph}(\lambda)$ is the number of photons per wavelength in the AM1.5G spectrum.

Hence, integrated EQE(λ) over wavelengths with a known laser spot will give the J_{SC}. EQE measurements used in this dissertation are recorded by an Oriel Instruments QEPVSI-b system with a Xenon lamp (Newport 300 W). The white light is chopped at a frequency of 78 Hz by a Newport Cornerstone 260 monochromator. Before each measurement, the reference Si diode with a known spectrum is used. The response from the solar cells is measured with a Stanford Research SR830 Lock-In amplifier and evaluated by a commercial software named TracQ.

3.3 X-ray diffraction

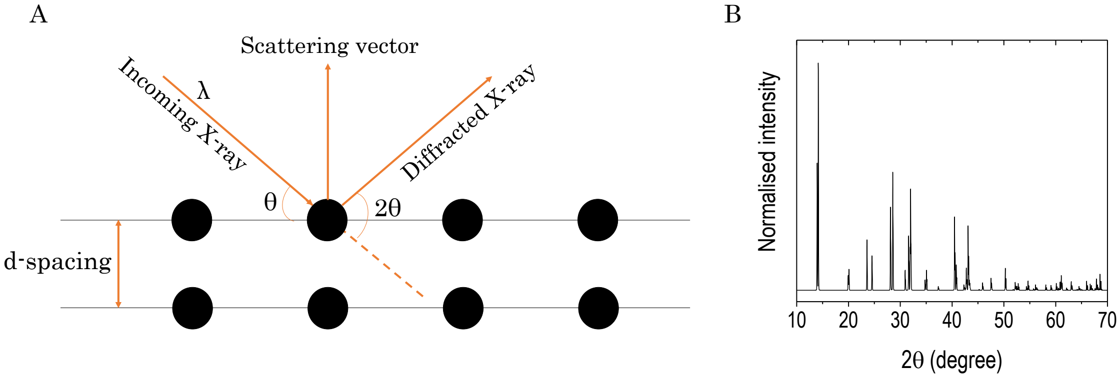

Figure 3.1 X-ray diffraction principle: the X-ray source hits the atoms which have a unique arrangement of the material. As the atoms are repeated in space forming an ordered structure, the diffracted X-ray from a certain angle (2θ) will have constructive interference forming peaks in the XRD pattern. B. An example of a theoretical calculated pattern of $MAPbI_3$ is shown.[9]

X-ray diffraction (XRD) measurement is based on the refection of X-ray by atoms in the material, which is call diffracted light. This is based on the interaction between X-ray and the crystalline material resulted in a coherent elastic scattering event. When the X-ray hits the atom, the oscillation of electrons has the same frequency of the incoming X-ray and emits electromagnetic radiation.[10] The scattering power of an atom is the summation of these radiations. In a crystalline material, the atoms are arranged in an order structure, repeated through the material. Hence, the angle in which the diffracted waves are constructive gives a high intensity as can be seen in **Figure 3.1A**. At all remaining directions, destructive interference occurs.[10] Thus, the diffracted X-ray can form a pattern as shown in **Figure 3.1B**. The distance between the crystal plane (d-spacing) can be calculated using Bragg's law (**equation 3.2**).

$$nd = 2\lambda\sin\theta \qquad 3.2$$

The XRD pattern is unique and can be used to identify the material. Every peak in the XRD pattern represents a family of lattice planes hkl which are parallel planes inside a crystal which has a distance of d. In this dissertation, the XRD pattern is mainly collected using grazing incidence XRD (GIXRD) except in **Chapter 6** some of the in situ XRD measurements are measured with Bragg-Brentano geometry. The GIXRD uses a very small incidence angle (0.5-1 degree in this project) which is fixed during the measurement so that the probing volume is mainly within the thin film. Moreover, due to a long pathway of X-ray in the sample at a small incidence angle, the total diffraction volume is large, thus, improves the statistic of the measurement.

Since changing X-ray incidence angles has different probing depths, one can distinguish the surface and bulk phase in a specimen. The Bragg angle (2θ) is changed by varying the detector positions. Due to a fixed incoming X-ray, the scattering vector changes its direction during the measurement, hence, it is only suitable for randomly oriented thin film to collect all the diffraction peaks.[10] In Bragg-Brentano geometry, the X-ray tube and the detector both vary with θ and 2θ respectively. Hence, the scattering vector (**Figure 3.1A**) is always perpendicular to the sample surface, which means only the out-of-plane orientation is probed (the lattice planes parallel to the substrate). Thus, Bragg-Brentano geometry generated XRD patterns provide the preferred orientation in the out-of-plane direction of the sample (the highest intensity peaks). The lab-based X-ray source is commonly from Cu K alpha with a wavelength of around 1.54 Å.

Aside from identifying the material crystal structure, the XRD pattern analysis can generate the material lattice parameters and its domain size. In a polycrystalline material, the domain (or in some cases crystallite) is defined as a coherent diffracted structure where all unit cells are arranged in an exact same manner. A grain, by definition, is the smallest unit, which resembles a single crystal.[2] This means that surrounding a grain is grain boundaries, interface, and surface, whereas, only one crystallographic orientation and its derivatives (for example, twin boundary) are inside the grain. Refinement of XRD patterns can give the domain size (coherent diffraction unit) (if not outside the detection limit), yet, not grain size. The grain size is generally determined from scanning electron microscopy (SEM) defining by the groove or different contrast between grain interior and grain boundary. However, the most accurate way to measure grain size is using electron backscatter diffraction, which is not employed in this dissertation.

Le Bail method uses a calculated XRD pattern of a perfect crystal without defects to analyse the microstructure of the material. This does not require the exact atomic positions and their scattering power which can reduce the computation effort. This method fits the measure XRD patterns with lattice parameters, and broadening factors caused by small domain size (Scherrer broadening of nanometre size domain[11]) and by microstrain, as well as taking into account the instrumental induced broadening. The peak broadening by microstrain is due to an inhomogeneous change in the domain whereas the peak shift is caused by a homogeneous modification of the crystal structure. Different from a single crystal, in the polycrystalline film, the XRD peaks can be described by pseudo Voigt functions. The function considers both Gaussian and Lorentzian contribution to the shape of the peaks in the pattern. Hence, we can assume that the angular dependence microstrain will affect to Gaussian peak broadening contribution (the case of Lorentzian contribution to microstrain is rare), whereas the broadening due to crystallite size is from Lorentzian contribution.[12] The refinement is done by calculating the peak position and their corresponded hkl values obtained from known material lattice parameters and its space group.

In this dissertation, the measurement is conducted in the air with the PANalytical X'Pert Pro MPD (multi-purpose diffractometer) using grazing incidence geometry. Grazing incident X-ray diffraction (GIXRD) patterns are collected with a step size of 0.02 degree, for 1-10 seconds each step.

3.4 X-ray techniques for elemental investigation

3.4.1 X-ray photoemission spectroscopy

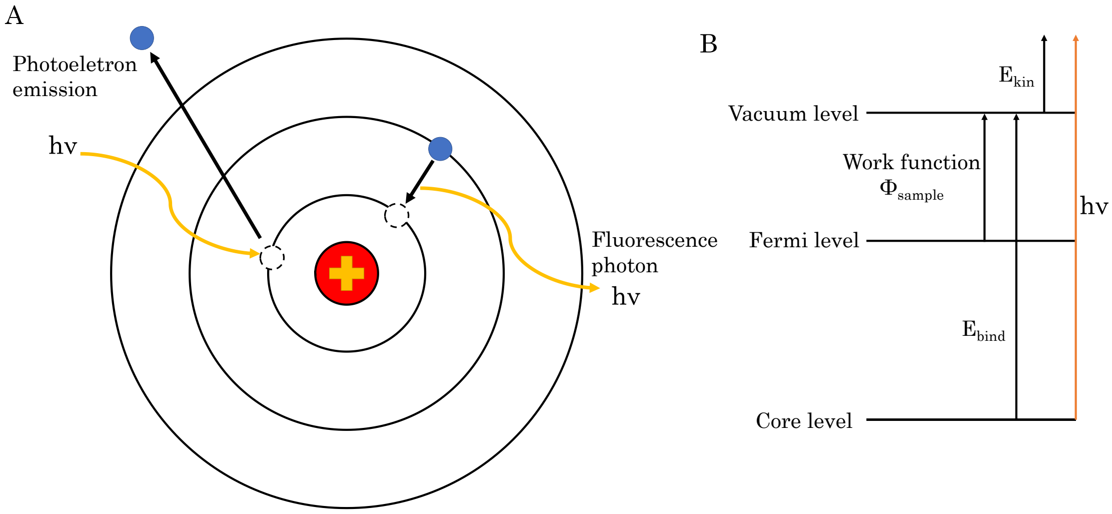

Figure 3.2 A. Principle of photoemission and fluorescence emission. The electron is denoted as blue circle and hole is an unfiled circle. B. The schematic energy diagram to calculate the binding energy of core-level electrons.

X-ray photoemission spectroscopy (XPS) depends on photoelectric phenomena in which an X-ray can remove an electron from the material. If the X-ray has sufficient energy, it can excite the inner shells electrons or core-level electrons (**Figure 3.2A**).[13] After the X-ray removes the electrons from their orbitals, the electrons have kinetic energy which can be used to calculate the binding energy of the electron to its nuclei knowing the sample's work function.[13] This unique binding energy is element dependent and can be used to distinguish certain chemical bonds of the compound.[14] The binding energy of core-level electrons can be calculated in **equation 3.3** (schematic in **Figure 3.2B**).

$$E_{bind} = h\nu - E_{kin} - \phi_{sample} \qquad 3.3$$

where E_{bind} is the binding energy of the electron, $h\nu$ is the photon energy, and ϕ_{sample} is the work function of the sample.

Due to a short inelastic mean free path of an electron as it is escaping from the sample, only electrons near the surface of the sample can be removed, hence, XPS is inherently a surface-sensitive technique where most of the information comes from few nm of the sample. Because core level electron has orbital without overlapping with orbitals of neighbour atoms, the detected binding energy of core electrons gives information of its specific orbital, and thus, is characteristic to one element. A small shift in binding energy is called a chemical shift and it relates to the chemical environment of the atom and its oxidation state. Compared to the electron of ground state metal atom, the electron of oxidised metal is subjected to a stronger Columbic force to the core, hence, it requires higher energy to be removed. Therefore, one can obtain the oxidation state of an element.[15] Aside from the elemental analysis of the semiconductor, XPS spectra provide the information of the valence band maximum to the Fermi level. This is because XPS spectra contain the energy of the occupied states in the material (an electron). The measurement of the density of states can give the VBM position.[14]

Moreover, peak intensity analyses from XPS spectra give an approximation of the relative amount between two elements in the sample. Although it is possible to quantify the amount of element in the sample based on this method, there are many factors inherent to the experimental technique for the different core levels quantification that needs to be considered (*e.g.*, differences in photoionization cross sections, inelastic mean free path, the transmission function of the analyser, *etc.*)[15] Furthermore, the obtained spectra and their analysis may act as sources of experimental uncertainty (*e.g.*, signal-to-noise ratio, curve fit analysis parameters of the spectra, *etc.*). The consideration of all these factors (and their margins of uncertainty) in the analysis can lead to the propagation of large absolute margins of error in the results. An approach to minimise these uncertainty factors inherent for quantification analysis of photoelectron spectroscopy data (*i.e.*, in the ideal case they "cancel out" each other) is evaluating photoemission lines in close energetic proximity, effectively making differences in inelastic mean free path and transmission function values negligible for quantification. Thus, instead of the absolute concentration of an element of the sample, one can derive the ratio between two elements in the sample simply by taking the ratio of the areas under the peaks. Thus, XPS is a powerful tool to determine the composition and the chemical environment of a material.[16]

In **Chapter 4**, hard X-ray photoelectron spectroscopy (HAXPES) measurements were carried out at the HiKE endstation located at the BESSY II KMC-1 beamline at Helmholtz-Zentrum Berlin (HZB).[17-18] The HiKE endstation is equipped with a Scienta R4000 electron analyser and excitation energies of 2003 eV and 6009 eV are employed. The binding energy (BE) scale of the HAXPES measurements was calibrated by measuring the Au 4f energy region of a clean Au foil in electrical contact with the (grounded) sample and setting the BE of the Au $4f_{7/2}$ line to 84.0 eV. The pressure in the endstation's analysis chamber during the HAXPES measurements remained <1 x 10^{-8} mbar. Curve fit analysis of measured detail HAXPES spectra were simultaneously conducted using the Fityk software.[19]

3.4.2 X-ray fluorescence

X-ray fluorescence (XRF) can give information about the elemental distribution in the sample. The principle of XRF lies behind the fluorescence emission from the excited sample by X-ray source. The electrons at the core levels can be displaced to the outer shell of the atom by X-ray which leaves behind vacancies in the inner shell as can be seen in **Figure 3.2A**). As, the outer shell electrons relax back to the inner shell, they emit photons that can be detected and unique for the element. Using a synchrotron source, the penetration depth can be up to a few micrometers, which means that the probed volume is throughout the sample. The method is used to map the elemental distribution and quantify the elements inside the probe volume.[20]

The synchrotron-based nano X-ray fluorescence (nXRF) measurements used in **Chapter 4** for the elemental mapping of the perovskite films are done in the 2-ID-D beamline at an excitation energy of 16 keV, X-ray step size of 0.15 μm, and a dwell time of 50 ms at the Advanced Photon Source, Argonne National Laboratory.

3.5 Energy dispersion X-ray

Instead of using an X-ray source, the electron beam can be used to promote an electron from inner shell to outer shell leaving holes. When an outer shell electron fills the hole, an X-ray can be emitted which is unique for the element (**Figure 3.3**). This is the principle of energy dispersion X-ray (EDX). Similar to XRF, EDX can be used to detect the elements in the material as well as provides elemental distribution map of a sample. This method has penetration depth in micrometre scale.

3.6 Scanning electron microscopy

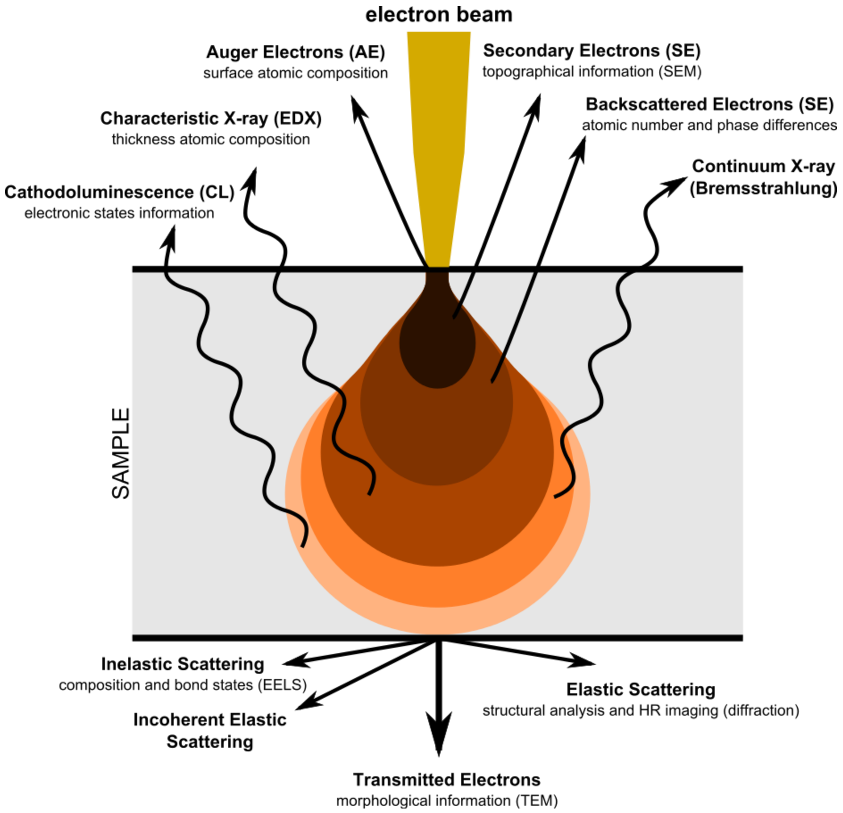

Figure 3.3 The interaction between electron and matter used for different techniques for imaging and material characterisation. Reproduced from ref. 21 under the Creative Commons Attribution-Share Alike 4.0 International.

The interaction between the electrons of the sample and the electron beam with high acceleration voltage can generate a secondary electron detectable in the scanning electron microscopy (SEM). This provides valuable information on the sample morphology and can give an indication of the grain size in the polycrystalline film.

The high voltage electrons interact with the atoms in the material, which produce secondary electrons and backscattered electron as can be seen in **Figure 3.3**.[22] The secondary electrons are ejected from the material's atoms due to the high energy primary electron beam hitting the sample, which are recorded as an image. The contrast of the image is due to the different topology of the sample. This is because the irregularity of the sample leads to different electrons trajectories. The backscattered electrons are the primary electron that “reflect” out from the sample due to elastic scattering events. Due to the difference between the atomic numbers, heavy atoms can deflect electrons strongly which then appears to be bright in the image. Moreover, the backscattered electrons can also provide the crystal orientation of the sample. The electrons can be scattered at the crystal plane obeying Bragg’s law giving Kikuchi patterns. A detailed description of this method can be found elsewhere.[23]

To detect the electrons from the specimen, SEM detectors use a scintillation material or a semiconductor. As for the former, the electrons convert to photons, which then are converted to an electric signal. As for the later, the electron-hole pair generation results in a current which is proportional to the number of detected electrons. Semiconductor detector is mainly used for backscattered electrons while scintillation detector is used for detection of both secondary and backscattered electron.[22]

The SEM/EDX images in this dissertation are acquired with Hitachi S4100 at 30k magnification. The voltages used for SEM and EDX are 5 keV and 12.5 keV respectively.

3.7 Transmission electron microscopy

The transmission electron microscopy (TEM) is a powerful technique for imaging and material analysis. To detect the (in)elastic scattered electrons behind the sample (**Figure 3.3**), the specimen needs to be thin (in order of 5 nm-0.5 µm for 100 keV primary electrons).[24] The image depends on the density of the sample and its elemental characteristic. In a conventional TEM, the electrons are emitted from an electron gun by thermionic emission from cathodes (tungsten or LaB_6). The electrons from the sample are imaged through various lens on a fluorescent screen.

There are two modes in which TEM image can be recorded. The bright-field mode only records the transmitted electrons passing through the aperture. The contrast of the image is based on how many electrons passing through the sample. Thus, the dark area of the image corresponds to the thick area and/or heavy atoms. In contrast, in the dark-field mode, the imaging comes from electrons which are highly scattered, which can give a high resolution image.[25]

TEM imaging of perovskite is challenging due to the sample degradation subjected to high energetic electrons. To minimise the damage, the sample can be actively cooled and a low dose primary beam should be used. However, a low dose beam leads to low signal to noise and low image contrast.[26] This requires a more advanced analysis for data processing to obtain a meaningful analysis. Examples of these data analysing tools are the use of principal component analysis (PCA) and non-negative matrix factorisation (NMF). PCA can be used to reconstruct data to only have information from the material while discarding the noise signal. NMF is a machine learning algorithm to decompose the obtained signal into factors. These factors are related to the chemical composition of the material.[27]

In **Chapter 6**, high-angle annular dark-field imaging and STEM-EDX spectroscopy are carried out in an FEI Tecnai Osiris operated at 200 kV and equipped with a Bruker Super-X EDX silicon drift detector with a total collection solid angle of ~0.9 sr. To minimize beam damage, STEM-EDX spectrum images are acquired with a defocused beam with a probe current of ~250 pA, spatial sampling of 10 nm/pixel, and dwell time of 50 ms/pixel. Data were acquired with Tecnai Imaging and Analysis (TIA) and analysed with HyperSpy.

3.8 Luminescence

Luminescence measurements are based on the photon emission from the radiative recombination of charge carriers. While electroluminescence (EL) uses injected current into complete devices, photoluminescence (PL) employs light to generate photogenerated charge carriers in the semiconductor layer. In PV industry, EL mapping is widely used to assess the uniformity of the solar cells or modules. A good cell will be bright (high yield) in the mapping whereas any imperfections and cracks can introduce non-radiative recombination which reduces the EL yield. On the other hand, PL has been widely used with a halide perovskite layer to examine the quality of the material and its optoelectronic.

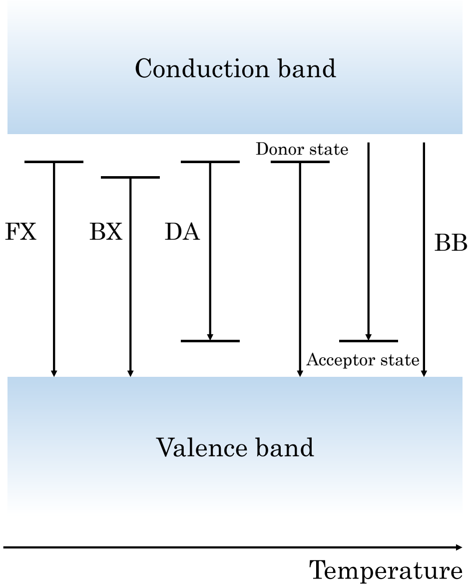

Figure 3.4 Different optical transitions can be seen in a photoluminescence measurement. The probability of the transition depends on the temperature in which more likely processes at higher temperature are on the right side. FX is free exciton transition, BX is bound exciton transition, DA is a transition occurs with a donor and an acceptor state, BB is a band-to-band transition. Redraw from ref. 10.

The spontaneous radiative emission from a semiconductor has a rate as in **equation 3.4**.[10]

$$R = B(np - n_0p_0) = Bn_i^2\left(\exp\frac{\Delta\mu}{k_BT} - 1\right) \qquad 3.4$$

where n and p are the total electron and hole density, n_0 and p_0 are the intrinsic carrier density, Δμ is the quasi Fermi level splitting (QFLS) in the sample due to generated charge carrier, B is the coefficient for direct radiative free carrier recombination.

The **equation 3.4** shows that the rate of radiative recombination depends on the charge carrier densities. At high photon flux, the photogenerated charge carrier densities are much larger than intrinsic charge carrier densities ($n \gg n_0$ and $p \gg p_0$) then the luminescence yield is proportional to Bnp, then the radiative lifetime is inverse proportional to Bn and depends on the injected charge concentration. When $p \approx p_0$ for p-type material ($n \approx n_0$ for n-type material), the PL flux depends on the majority charge carrier and the lifetime $\tau_{rad} = 1/(Bp_0)$ and thus independent of injection level. Assuming a flat and homogeneous sample and the emitted light is within a narrow cone $1/(4n_r^2)$, the photon emission flux is expressed in **equation 3.5a**.[10] Hence, from PL, one can calculate the QFLS $\Delta\mu$ relating to the maximum open-circuit voltage V_{OC} obtainable in a solar device. However, due to the difficulty to measure exact the absorption coefficient, high energy tail fitting can be used to calculate QFLS assuming $a(E) = 1$ for photons with energy larger than the bandgap.[10] Then, the **equation 3.5b** can be used and the linear fit gives the QFLS of the perovskite layer.

$$Y_{PL}(E) = \frac{1}{4\pi\hbar^3c^2}\frac{a(E)E^2}{\exp\frac{E-\Delta\mu}{k_BT}-1} \qquad 3.5a$$

Where $Y_{PL}(E)$ is PL emission yield as a function of photon energy, $\hbar$ is reduced Planck constant, c is the speed of light, a(E) is the absorptivity, k_BT is the thermal voltage approximately 26 mV at 300 K.

$$\ln\left(\frac{Y_{PL}(E)}{10^{23}E^2}\right) = -\frac{E-\Delta\mu}{k_BT} \qquad 3.5b$$

Figure 3.4 presents the basic transition events that can be radiative and emit a photon.[10] At low temperature (around 10 K), the recombination event of bound electron-hole (exciton) is considerable and its transition energy (FX) depends on the exciton binding energy. The exciton optical transition is only detectable at low temperatures due to thermal dissociation at the higher temperatures. The free exciton can bound to a localised impurity, hence, the transition energy also depends on the binding energy of exciton to the impurity (BX). At sufficiently low temperature, the charge carriers captured by donor and acceptor states within the bandgap can recombine radiatively. At higher temperature, this recombination event is less likely because the charge carriers are thermally re-emitted to the bands before recombination happens.[10]

Considering only one donor (or acceptor state), the captured electron (hole) can recombine with the hole (electron) in the valence band (conduction band) as can be seen in **Figure 3.4**. This is called a free-to-bound transition. In this case, the shallow transition of donor and acceptor to CB and VB are less likely to emit a photon. If the concentration of donor/acceptor states is large, it can form an impurity band making the free-to-bound and band-to-band transition difficult to distinguish.[10] As room temperature (and higher), the band-to-band transition occurring between the electron in the CBM and the hole in the

VBM are more probable. Hence, the transition energy equals to the bandgap of the semiconductor. That is why PL peak can be used to determine the bandgap of the material.

In addition, PL can be used to detect ionic defect formation and migration in halide perovskite material. Light-induced ion movement has been observed by several studies such as the work by deQuilettes *et al.*[28] where they observed the link between PL yield with the iodide distribution of the film. This indicates that when ions move out of its lattice site, it generates defects (vacancies and interstitials) which can introduce non-radiative recombination (reducing the yield) or has defect healing effect (increasing the yield). With a good agreement, a theoretical calculation has shown that light can introduce excess energy to break Pb-I bond which eventually forms Frenkel pair defects affecting the PL signal.[29]

Moreover, it has been shown that not only ionic defects formation and migration modify the PL yield from the sample, the spectral variation can also relate to defects formation and degradation of halide perovskite.[30-31] Thus, PL spectra can also give an indication of the material property. It is used to determine the bandgap of the material and has been the first tool to detect the photo-induced halide segregation where the segregated low bandgap emission dominates the PL spectra. In addition, the PL spectral shift to higher bandgap or blue-shift has been attributed to the loss of MA which alters the bond angle of I-Pb-I.[30, 32]

In this dissertation, **Chapter 4** uses two 450 nm LEDs for excitation whose fluence is calibrated to 1 sun equivalent. A calibrated CCD camera is used to collect PL emission, coupled to a tunable liquid crystal filter. The setup is calibrated to absolute photon numbers with light sources of known fluences,[33] thus enabling to estimate the quasi Fermi-level splitting (QFLS) from the generalised Planck law using the high-energy tail fit method of the PL spectra.[34] Time-resolved photoluminescence (trPL) measurements use an excitation wavelength of 660 nm from a pulsed supercontinuum laser light source (SuperK Extreme) operating at 304 kHz repetition rate. The spot size is 25-35 μm in diameter and the pulse fluence of 10-30 nJ/cm^2 is chosen in order to generate an equivalent number of charge carriers as would be expected under 1 sun conditions (1.5E+21 photons $\cdot$m^{-2} $\cdot$s^{-1}). PL is collected panchromatically and the decay was recorded using time-correlated single photon counting with a PicoHarp TCSPC Module by PicoQuant.

Chapter 5 measurement is performed in a homebuilt inverted microscope based on the Olympus IX-71 body. For excitation, a 458 nm line of a CW Argon and a 450 nm diode laser (Thorlabs CPS450) are employed. The excitation is either focused or collimated at the back aperture of the objective (Olympus LUCPlanFL 40, NA 0.6) with the use of a collimating lens where the former yields a wide-field excitation spot ("defocused mode") and the latter yields a focused spot ("focused mode").

Electroluminescence (EL) in **Chapter 6** is performed with a commercial modular instrument for advanced photo-electrical characterization (Arkeo from Cicci Research s.r.l.). The EL spectra were acquired at a driving voltage of 2.25V and with a fast acquisition time (the measurement takes less than 5 seconds).

3.9 Transient photovoltage

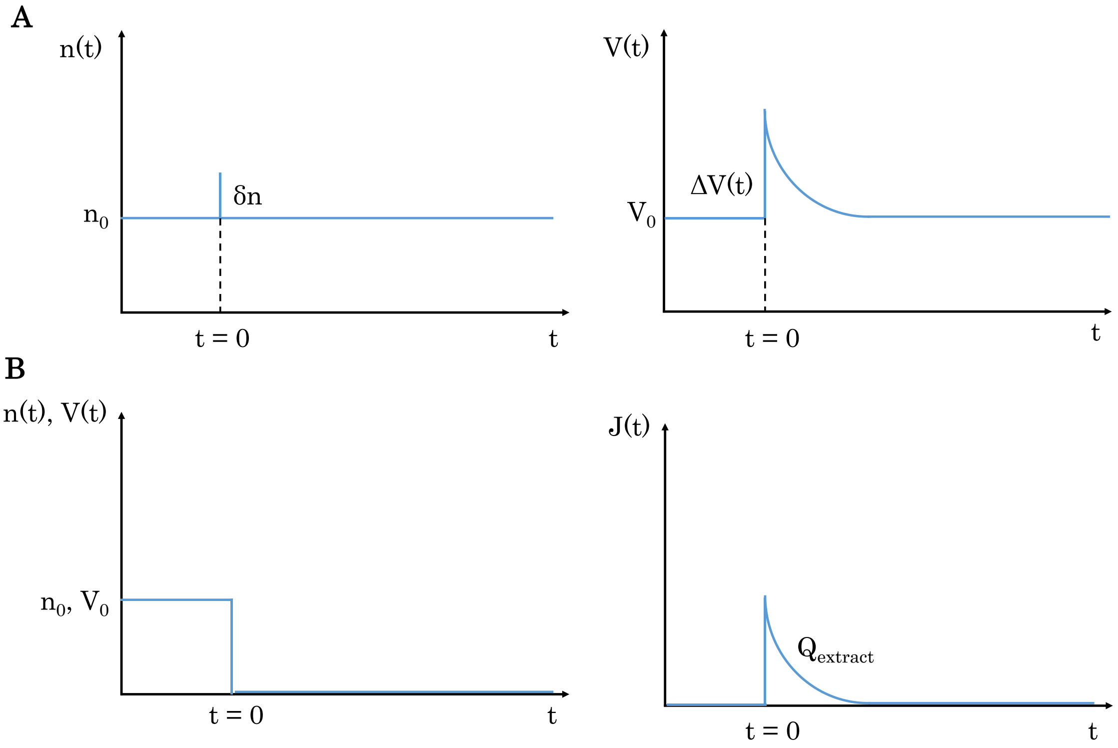

Figure 3.5 A. Transient photovoltage measurement. A steady-state illumination is applied, at t = 0, a small light pulse is applied which generates an extra charge carrier concentration (δn) which gives a raise to a voltage. The decay of this extra charge carrier gives a recombination lifetime. B. Charge extraction measurement: A steady-state illumination is applied corresponding to n_0 and V_0, at t = 0 the light is switched off and the voltage is 0 V, thus, the extracted charge carrier concentration can be measured as the current extracted from the sample. Adapted from ref. [230].

This method is used to investigate the charge carrier recombination dynamic in a complete device. The device is subjected to a steady-state illumination at a fixed voltage condition (normally at open circuit voltage when there is no charge). This steady state illumination generates a steady charge carrier population n_0 inside the device (**Figure 3.5A**). At t = 0, a weak laser pulse is used on top of steady-state illumination to generate an excess charge carrier concentration (δn). The decay of photovoltage after the pulse is subsequently recorded. This decay of photovoltage is due to the excess charge being recombined, hence, it can be used to estimate the lifetime τ of the charge carriers.[35] In the case of second-order recombination $R = \beta n^2$ (considering equal concentrations of electron and hole), the charge carrier concentration changes over time is expressed in **equation 3.6**.[36]

$$\frac{dn}{dt} = G_0 - \beta(n_0 + \delta n)^2 \approx -\frac{\delta n}{\tau} \tag{3.6}$$

Where G_0 is steady-state generation, β is a second-order recombination coefficient.

For a weak light pulse, the excess charge carriers concentration is much smaller than steady state concentration ($\delta n \ll n_0$), the lifetime is $\tau^{-1} = \sqrt{\beta G_0}$. Since V_{OC} is proportional to $\ln(G_0)$, fitting the decay of voltage with exponential function gives an indication of recombination kinetic.[37] However, the carrier lifetime can be longer due to re-emission of captured charge at the trap states. Thus the lifetime analysis is not straightforward. Hence, transient photovoltage measurement is often coupled with charge extraction measurement (**Figure 3.5B**). In this measurement, the steady-state illumination is applied at open circuit voltage to generate a constant charge carrier concentration. At t = 0, the illumination is switched off and the device is switched to be at short circuit condition. This creates a current flow which is the charge carrier being extracted from the device.[35] The recombination rate and the extracted current at V_{OC} relate by a power law function, thus, the dominant recombination process can be analysed. If the recombination is via free charge carrier recombining with deep trap captured charge carrier, the recombination is a first-order process.[38] The recombination between two free charge carriers would be a second-order process. Nonetheless, the analysis is complex due to the energetic disorder which gives rise to a broad electronic state distribution. This discussion of this topic can be found elsewhere.[38]

In **Chapter 6**, transient photovoltage (TPV) and charge extraction (CE) are performed with a commercial modular instrument for advanced photo-electrical characterization (Arkeo from Cicci Research s.r.l.). In the case of TPV and CE the setup is based on a high speed Waveform Generator that drives a high speed LED (5000 Kelvin). The device is connected to a trans-impedance amplifier and a differential voltage amplifier to monitor short circuit current or open circuit voltage. The light intensity can be varied between 0.1 and 2 equivalent suns.

Reference

1. Jeon, N. J.; Noh, J. H.; Kim, Y. C.; Yang, W. S.; Ryu, S.; Seok, S. I., Solvent engineering for high-performance inorganic–organic hybrid perovskite solar cells. *Nature materials* **2014,** *13* (9), 897-903.
2. Dunlap-Shohl, W. A.; Zhou, Y.; Padture, N. P.; Mitzi, D. B., Synthetic approaches for halide perovskite thin films. *Chemical reviews* **2018,** *119* (5), 3193-3295.
3. Turren-Cruz, S.-H.; Hagfeldt, A.; Saliba, M., Methylammonium-free, high-performance, and stable perovskite solar cells on a planar architecture. *Science* **2018,** *362* (6413), 449-453.
4. Yoo, J. J.; Wieghold, S.; Sponseller, M. C.; Chua, M. R.; Bertram, S. N.; Hartono, N. T. P.; Tresback, J. S.; Hansen, E. C.; Correa-Baena, J.-P.; Bulović, V.; Buonassisi, T.; Shin, S. S.; Bawendia, M. G., An interface stabilized perovskite solar cell with high stabilized efficiency and low voltage loss. *Energy & Environmental Science* **2019,** *12* (7), 2192-2199.
5. Saliba, M.; Matsui, T.; Seo, J.-Y.; Domanski, K.; Correa-Baena, J.-P.; Nazeeruddin, M. K.; Zakeeruddin, S. M.; Tress, W.; Abate, A.; Hagfeldt, A., Cesium-containing triple cation perovskite solar cells: improved stability, reproducibility and high efficiency. *Energy & environmental science* **2016,** *9* (6), 1989-1997.
6. Saidaminov, M. I.; Abdelhady, A. L.; Murali, B.; Alarousu, E.; Burlakov, V. M.; Peng, W.; Dursun, I.; Wang, L.; He, Y.; Maculan, G.; Goriely, A.; Wu, T.; Mohammed, O. F.; Bakr, O. M., High-quality bulk hybrid perovskite single crystals within minutes by inverse temperature crystallization. *Nature communications* **2015,** *6* (1), 1-6.
7. Chen, Z.; Turedi, B.; Alsalloum, A. Y.; Yang, C.; Zheng, X.; Gereige, I.; AlSaggaf, A.; Mohammed, O. F.; Bakr, O. M., Single-crystal MAPbI3 perovskite solar cells exceeding 21% power conversion efficiency. *ACS Energy Letters* **2019,** *4* (6), 1258-1259.
8. Leong, W. L.; Ooi, Z. E.; Sabba, D.; Yi, C.; Zakeeruddin, S. M.; Graetzel, M.; Gordon, J. M.; Katz, E. A.; Mathews, N., Identifying fundamental limitations in halide perovskite solar cells. *Advanced Materials* **2016,** *28* (12), 2439-2445.
9. Yamada, Y.; Yamada, T.; Phuong, L. Q.; Maruyama, N.; Nishimura, H.; Wakamiya, A.; Murata, Y.; Kanemitsu, Y., Dynamic optical properties of CH3NH3PbI3 single crystals as revealed by one-and two-photon excited photoluminescence measurements. *Journal of the American Chemical Society* **2015,** *137* (33), 10456-10459.
10. Abou-Ras, D.; Kirchartz, T.; Rau, U., *Advanced characterization techniques for thin film solar cells*. John Wiley & Sons: 2016.
11. Langford, J. I.; Wilson, A., Scherrer after sixty years: a survey and some new results in the determination of crystallite size. *Journal of applied crystallography* **1978,** *11* (2), 102-113.
12. Thompson, P.; Cox, D.; Hastings, J., Rietveld refinement of Debye–Scherrer synchrotron X-ray data from Al2O3. *Journal of Applied Crystallography* **1987,** *20* (2), 79-83.
13. Zambonin, P.; Desimoni, E., X-ray photoelectron spectroscopy: principles, instrumentation, data processing and molten salt applications. In *Molten Salt Chemistry*, Springer: 1987; pp 425-445.
14. Moulder, J. F.; Stickle, W. F.; Sobol, P. E.; Bomben, K. D., *Handbook of X-ray Photoelectron Spectroscopy*. 2nd ed.; Physical Electronics Division, Perkin-Elmer Corporation: 1992.
15. Cappel, U. B.; Lanzilotto, V.; Johansson, E. M.; Edvinsson, T.; Rensmo, H., X-ray photoelectron spectroscopy for understanding molecular and hybrid solar cells. In *Molecular Devices for Solar Energy Conversion and Storage*, Springer: 2018; pp 433-476.
16. Philippe, B.; Saliba, M.; Correa-Baena, J.-P.; Cappel, U. B.; Turren-Cruz, S.-H.; Grätzel, M.; Hagfeldt, A.; Rensmo, H. k., Chemical distribution of multiple cation (Rb+, Cs+, MA+, and FA+) perovskite materials by photoelectron spectroscopy. *Chemistry of Materials* **2017,** *29* (8), 3589-3596.
17. Gorgoi, M.; Svensson, S.; Schäfers, F.; Öhrwall, G.; Mertin, M.; Bressler, P.; Karis, O.; Siegbahn, H.; Sandell, A.; Rensmo, H., The high kinetic energy photoelectron spectroscopy facility at BESSY progress and first results. *Nuclear Instruments and Methods in Physics Research Section A: Accelerators, Spectrometers, Detectors and Associated Equipment* **2009,** *601* (1-2), 48-53.
18. Schaefers, F.; Mertin, M.; Gorgoi, M., KMC-1: A high resolution and high flux soft x-ray beamline at BESSY. *Review of Scientific Instruments* **2007,** *78* (12), 123102.
19. Wojdyr, M., Fityk: a general-purpose peak fitting program. *Journal of Applied Crystallography* **2010,** *43* (5-1), 1126-1128.
20. Hidalgo, J.; Castro-Méndez, A. F.; Correa-Baena, J. P., Imaging and mapping characterization tools for perovskite solar cells. *Advanced Energy Materials* **2019,** *9* (30), 1900444.

21. Electron Interaction with Matter. https://commons.wikimedia.org/wiki/File:Electron_Interaction_with_Matter.svg (accessed 08/03/2020).
22. Hawkes, P. W.; Spence, J. C., *Springer Handbook of Microscopy*. Springer Nature: 2019.
23. Carter, C. B.; Williams, D. B., *Transmission electron microscopy: A Textbook for Materials Science*. Second edition ed.; Springer: 2009.
24. Reimer, L., *Transmission electron microscopy: physics of image formation and microanalysis*. Springer: 2013; Vol. 36.
25. Klein, N. D.; Hurley, K. R.; Feng, Z. V.; Haynes, C. L., Dark field transmission electron microscopy as a tool for identifying inorganic nanoparticles in biological matrices. *Analytical chemistry* **2015,** *87* (8), 4356-4362.
26. Kosasih, F. U.; Ducati, C., Characterising degradation of perovskite solar cells through in-situ and operando electron microscopy. *Nano Energy* **2018,** *47*, 243-256.
27. Cacovich, S.; Divitini, G.; Ireland, C.; Matteocci, F.; Di Carlo, A.; Ducati, C., Elemental mapping of perovskite solar cells by using multivariate analysis: An insight into degradation processes. *ChemSusChem* **2016,** *9* (18), 2673-2678.
28. deQuilettes, D. W.; Zhang, W.; Burlakov, V. M.; Graham, D. J.; Leijtens, T.; Osherov, A.; Bulović, V.; Snaith, H. J.; Ginger, D. S.; Stranks, S. D., Photo-induced halide redistribution in organic–inorganic perovskite films. *Nature communications* **2016,** *7*, 11683.
29. Motti, S. G.; Meggiolaro, D.; Barker, A. J.; Mosconi, E.; Perini, C. A. R.; Ball, J. M.; Gandini, M.; Kim, M.; De Angelis, F.; Petrozza, A., Controlling competing photochemical reactions stabilizes perovskite solar cells. *Nature Photonics* **2019,** *13*, 532–539.
30. Merdasa, A.; Bag, M.; Tian, Y.; Källman, E.; Dobrovolsky, A.; Scheblykin, I. G., Super-resolution luminescence microspectroscopy reveals the mechanism of photoinduced degradation in CH3NH3PbI3 perovskite nanocrystals. *The Journal of Physical Chemistry C* **2016,** *120* (19), 10711-10719.
31. Yuan, H.; Debroye, E.; Janssen, K.; Naiki, H.; Steuwe, C.; Lu, G.; Moris, M. l.; Orgiu, E.; Uji-i, H.; De Schryver, F.; Samorì, P.; Hofkens, J.; Roeffaers, M., Degradation of methylammonium lead iodide perovskite structures through light and electron beam driven ion migration. *The journal of physical chemistry letters* **2016,** *7* (3), 561-566.
32. Filip, M. R.; Eperon, G. E.; Snaith, H. J.; Giustino, F., Steric engineering of metal-halide perovskites with tunable optical band gaps. *Nature communications* **2014,** *5*, 5757.
33. Delamarre, A.; Lombez, L.; Guillemoles, J.-F., Contactless mapping of saturation currents of solar cells by photoluminescence. *Applied Physics Letters* **2012,** *100* (13), 131108.
34. Unold, T.; Gütay, L., Photoluminescence analysis of thin-film solar cells. In *Advanced Characterization Techniques for Thin Film Solar Cells*, Abou-Ras, D.; Kirchartz, T.; Rau, U., Eds. Wiley-VCH Verlag GmbH & Co. KGaA.: 2016; Vol. 1, pp 275-297.
35. Sandberg, O. J.; Tvingstedt, K.; Meredith, P.; Armin, A., Theoretical perspective on transient photovoltage and charge extraction techniques. *The Journal of Physical Chemistry C* **2019,** *123* (23), 14261-14271.
36. Shuttle, C.; O'regan, B.; Ballantyne, A.; Nelson, J.; Bradley, D.; De Mello, J.; Durrant, J., Experimental determination of the rate law for charge carrier decay in a polythiophene: Fullerene solar cell. *Applied Physics Letters* **2008,** *92* (9), 80.
37. Rahimi Chatri, A.; Torabi, S.; Le Corre, V. M.; Koster, L. J. A., Impact of electrodes on recombination in bulk heterojunction organic solar cells. *ACS applied materials & interfaces* **2018,** *10* (14), 12013-12020.
38. Kirchartz, T.; Nelson, J., Meaning of reaction orders in polymer: fullerene solar cells. *Physical Review B* **2012,** *86* (16), 165201.

Chapter 4 The Doping Mechanism of Halide Perovskite

This chapter is based on the peer-reviewed article "**The Doping Mechanism of Halide Perovskite Unveiled by Alkaline Earth Metals**" DOI: 10.1021/jacs.9b11637. Reproduced with permission.

Abstract

Halide perovskites are a strong candidate for the next generation of photovoltaics. Chemical doping of halide perovskites is an established strategy to prepare the highest efficient and the most stable perovskite-based solar cells. In this study, we unveil the doping mechanism of halide perovskites using the series of alkaline earth metals. We find that low doping levels enable the incorporation of the dopant within the perovskite lattice, whereas high doping levels induce surface segregation. The threshold from low to high doping regime correlates to the size of the doping element. We show that the low doping regime induces a more n-type while the high doping regime induces a less n-type doping character. Our work provides a comprehensive picture of the unique doping mechanism of halide perovskite, which differs from the classical semiconductors. We proved the effectiveness of the low doping regime for the first time demonstrating highly efficient methylammonium lead iodide based solar cells in both n-i-p and p-i-n architectures.

4.1 Introduction

Halide perovskite absorbers have enabled solar cells with more than 25% power conversion efficiency on a lab-scale, which makes them potentially competitive with established thin-film technologies such as those based on CdTe and Cu(In, Ga)Se_2 (CIGS) absorbers.[1] This class of material has a general composition of ABX_3 where A is a monovalent cation, B is a divalent cation, and X is a halide. The so-called 3D halide perovskites consist of cation A residing in a cage made of sharing corners eight octahedra BX_6. The addition of a small number of foreign ions into the perovskite precursor solution is a well-known strategy to improve the efficiency of perovskite-based solar cells (PSCs).[2-5] In the majority of the cases, the addition of foreign ions results in the segregation at the surface of the perovskite crystals as a secondary phase, which may still have a positive impact on the device performance[6] while leaving the perovskite crystal structure unchanged.[7]

Ionic radii control whether or not foreign cations can be incorporated into the perovskite lattice. For instance, the monovalent ions Rb, K and Na are too small to be included stably into the lattice. However, they improve PSCs performance by influencing the crystallisation and the surface defect chemistry.[6, 8] Divalent ions such as alkaline earth metals Sr, Ca and Mg, or transition metals such as Cd and Co have also been explored.[2, 9-13] In particular, theoretical calculation have predicted Sr^{2+} to replace Pb^{2+} in the perovskite lattice, as Sr^{2+} and Pb^{2+} have similar ionic radii, while Mg^{2+} can not.[9, 11, 14-15] Sr^{2+} has enabled significant efficiency enhancement in PSCs, however, it remains unclear how much Sr^{2+} can actually be incorporated in the perovskite lattice. Considering that the ionic radii of Sr^{2+} and Mg^{2+} in bonding with six halides are 118 pm and 72 pm, respectively,[16] these ionic radii, thus, can be translated directly to bond length of in the octahedron of the 3D perovskite structure. In particular, Sr-I bond length is the summation of Sr^{2+} radius and I^- radius. The tolerance factor is defined as $t = (r_A+r_X)/(\sqrt{2}(r_B+r_X))$,[17] where the MA^+ radius is taken as 217 pm and I^- is 220 pm. Hence, the tolerance factor for Sr^{2+} and Mg^{2+} replacing Pb^{2+} (119 pm) in 3D MA-based perovskite structure is 0.91 and 1.06 respectively. To form a 3D perovskite structure, the tolerance factor of the compound should be in the range of 0.8 to 1.0.[18-19] Therefore, Sr^{2+} is expected to form $MASrI_3$ 3D halide perovskite, whereas Mg^{2+} is not a suitable candidate. However, a purely synthesised 3D $MASrI_3$ halide perovskite has not yet been reported by the time of this study.[10-11] In fact, several studies have observed that Sr-doped perovskite films exhibit Sr-rich phases at the surface, which may modify the interfacial energy alignment between perovskite and the charge selective contact layers in PSCs.[20-22]

Here, we use Sr^{2+} and Mg^{2+} as representative cations to investigate the size dependence doping mechanism of halide perovskites. Combining theoretical and experimental investigation, which included synchrotron-based characterisations of the materials and device integration, we identify two doping regimes. At relatively high doping levels (3-10 mol%), such as those most commonly used in literature, the dopant is likely to segregate in a secondary phase at the surface of the perovskite. Conversely, at concentrations significantly lower (0.1-1 mol%) the dopants are incorporated into the perovskite lattice. The threshold between the low- and high-doping regimes depends on the size of the dopant. We show that the low doping regime induces a more n-type while the high doping regime induces a less n-type doping character of the perovskite semiconductor. Such behaviour is peculiar of halide perovskite and somewhat different from doping of classical semiconductors. We prove the low-doping regime as a new strategy to enhance the efficiency of perovskite solar cells demonstrating (methylammonium lead iodide) $MAPbI_3$ – based devices with an open circuit voltage exciding 1.16 V and a stabilised power conversion efficiency exceeding 19% in a p-i-n and 20% in an n-i-p solar cell.

4.2 Results and discussion

4.2.1 Doping mechanism

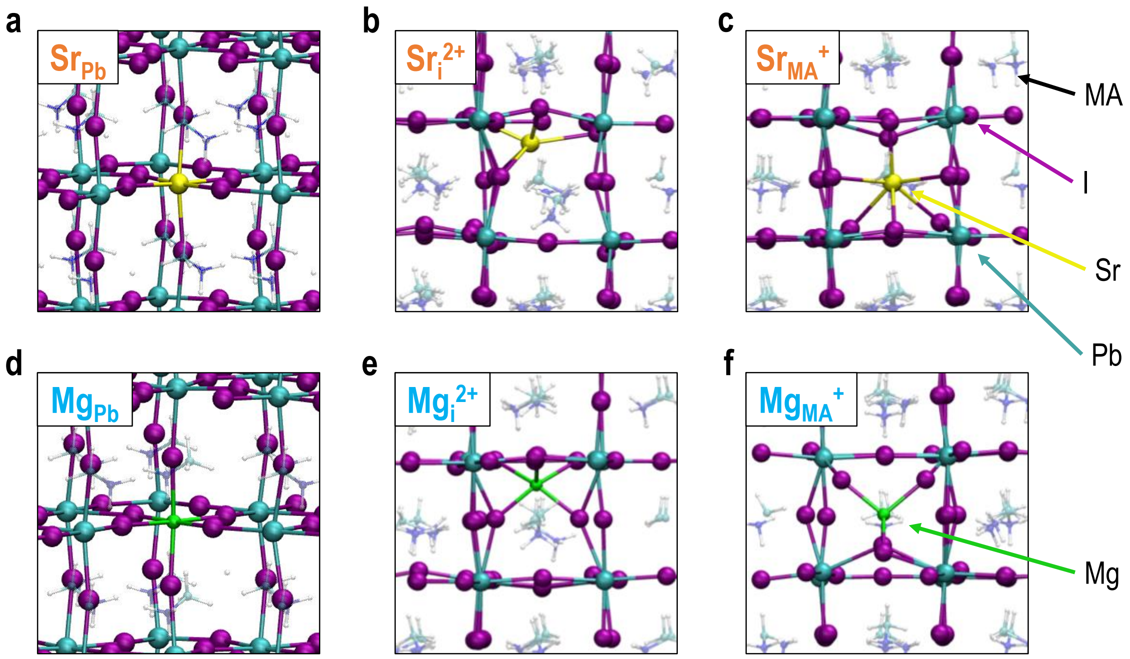

Figure 4.1 Potential doping mechanism calculated by DFT. Visualisation of Sr doping (depicted in yellow) a) Pb^{2+} substitution by Sr^{2+} (Sr_{Pb}), b) interstitial Sr^{2+} (Sr_i^{2+}), and c) methylammonium (MA) substitution by Sr^{2+} (Sr_{MA}^{+}). Similarly, Mg doping (depicted in green) as a) Pb^{2+} substitution by Mg^{2+} (Mg_{Pb}), b) interstitial Mg^{2+} (Mg_i^{2+}), and c) MA substitution by Mg^{2+} (Mg_{MA}^{+}).

The formation of halide perovskites is associated with the existence of lattice defects as for any crystalline material. Density functional theory (DFT) calculations have shown that Schottky defects, which form when oppositely charged ions leave their lattice sites creating vacancies, contribute to the defects density in halide perovskites most significantly.[23-25] The concentration of the Schottky defects in the perovskite lattice is calculated spanning from 10^{10} up to 10^{20} cm^{-3}.[23-25] Given that the Pb^{2+} concentration in a perfect perovskite crystal is in the range of 10^{21} cm^{-3}, we rationalise that the defect concentrations in halide perovskite should not be higher than 1% of the Pb^{2+}. Therefore, if chemical doping is exploded for the healing of harmful defects, the doping should be in sub-percent molar. However, most of the works in literature reports significantly higher doping levels to demonstrate improved PSCs performances.[13, 20-21, 26-28]

We hypothesise that a limited amount of dopant, which depends on the atomic size of the doping element, can be incorporated into the perovskite lattice and thus interact with the defect chemistry of the material. To demonstrate our hypothesis, we focus on Sr^{2+} and Mg^{2+} since they have similar chemical properties (elements in the same chemical group), but have different ionic radii (118 and 72 pm, respectively).[16] DFT shows that the incorporation of Sr^{2+} and Mg^{2+} in $MAPbI_3$ may occur through various processes: i) Pb^{2+} substitution (Sr_{Pb} or Mg_{Pb}); ii) interstitial (Sr_i^{2+} or Mg_i^{2+}); iii) MA^+ substitution (Sr_{MA}^+ or Mg_{MA}^+) as all illustrated in **Figure 4.1**.

Doping in the Silicon system involves the dopants providing extra electrons or holes to the Si network.[29] Changes in intrinsic point defect concentrations which shift the Fermi level occurs in CIGS absorbers,[30] and somewhat in halide perovskites.[31] However, this kind of doping is tunned by the growth method[32] without any extrinsic dopants like in doping of Si. Herein, to the best of our knowledge, this is the first report on doping a halide perovskite by intentional manipulation of the defect chemistry of the material by extrinsic dopants. The dopants (Sr and Mg) incorporation or segregation can change the defect concentrations in $MAPbI_3$. Depending on the doping regime, the (net) n-type doping of the perovskite is either increased or decreased. It is rather surprising that ***one*** dopant can introduce more or less n-type doping depending on the concentration, which is different from classical doping. The threshold between the low- and high-doping regimes depends on the size of the dopant which will be discussed in more details in the next sections.

4.2.2 Effect of different doping regimes on material property

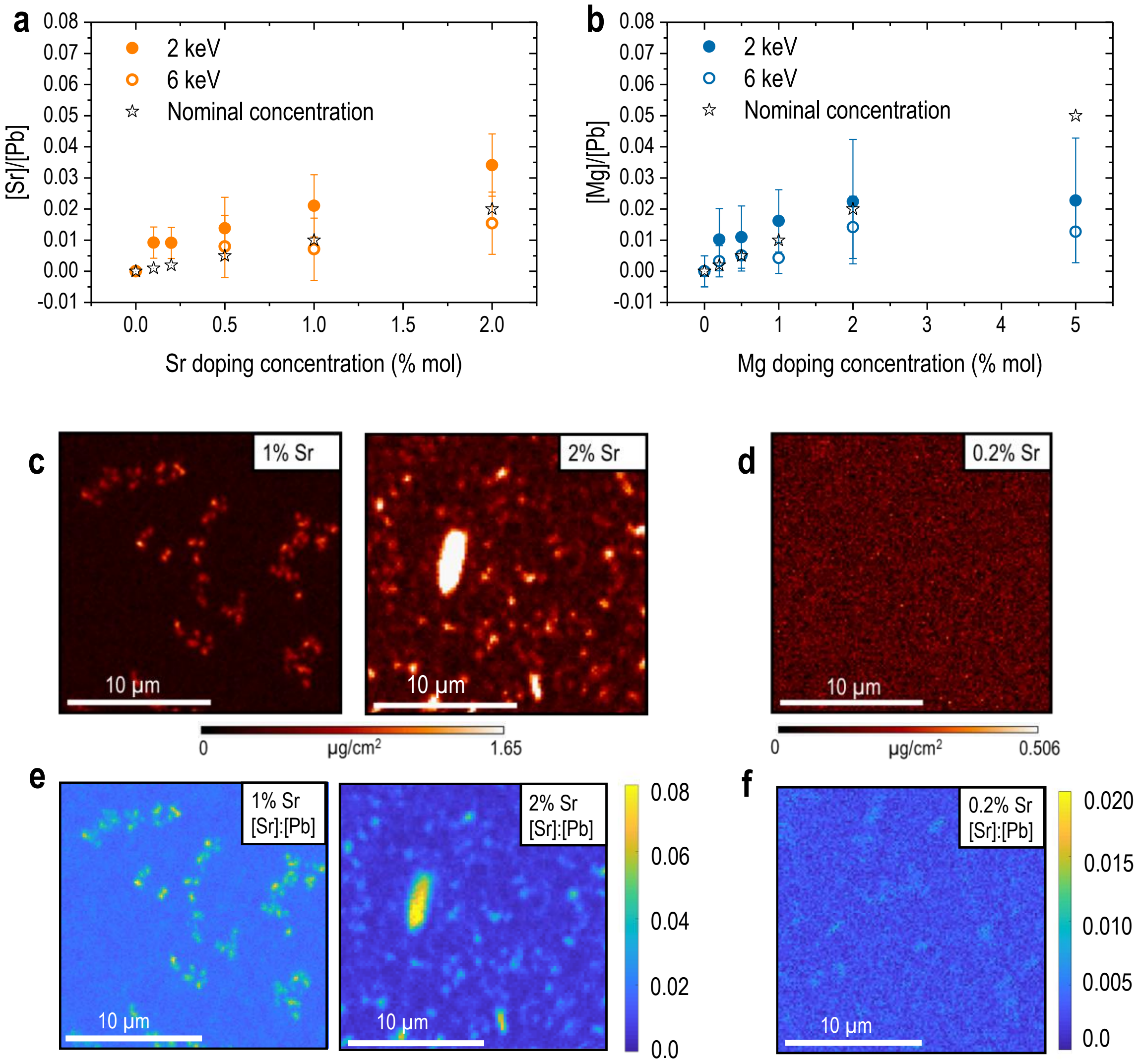

Figure 4.2 X-ray-based chemical characterisations. a) Sr and b) Mg doping levels as determined from the [Sr]:[Pb] and [Mg]:[Pb] ratio derived from the Sr 3p$_{3/2}$/Pb 4f$_{7/2}$ and Mg 1s/Pb 4f$_{7/2}$ hard x-ray photoelectron spectroscopy (HAXPES) data of the investigated sample series measured with 2 and 6 keV. No values are provided for samples for which the dopant signal could not be separated from the spectral background (due to insufficient signal-to-noise ratio and being below the detection limit). Top view of nano x-ray fluorescence (nXRF) elemental concentration maps of c) 1% and 2% Sr-doped MAPbI$_3$ thin film and d) 0.2% Sr-doped MAPbI$_3$ thin film. The colour scale indicates the amount of Sr present in the investigated area in µg/cm^2. Their corresponding ratio maps between Sr and Pb of e) 1% and 2% Sr-doped MAPbI$_3$ thin film and f) 0.2% Sr-doped MAPbI$_3$ thin film in which the ratio is presented by the colour scale on the right side of the figure.

We employed hard x-ray photoelectron spectroscopy (HAXPES) to examine the chemical composition of doped perovskite layers. The same substrate and deposition procedure used for the preparation of PSCs were used to rule out any possible side effect (see Method section).[33] **Figure 4.2a, b** presents the quantified [Sr]:[Pb] and [Mg]:[Pb] ratios derived from the HAXPES core levels (*i.e.*, Sr 3p$_{3/2}$, Mg 1s, and Pb 4f$_{7/2}$) measured with excitation energies of 2 and 6 keV (the corresponding 2 and 6 keV excited HAXPES spectra are shown in Figure S4.2 and Figure S4.3, see S.I.). By using different excitation energies, it is possible to vary the probing depths of the HAXPES measurements. For the Sr 3p and Pb 4f lines, the analyses using 2 and 6 keV result in photoelectron inelastic mean free paths (IMFP) of ≈4 nm and ≈10 nm, respectively (see Methods section for more details on how IMFP relates to probing depth).[34-35] **Figure 4.2a** shows that the [Sr]:[Pb] ratio computed from the 6 keV (*i.e.*, more bulk-sensitive) HAXPES measurements is in quite good agreement with the nominal concentration. However, the [Sr]:[Pb] ratios derived from the 2 keV (*i.e.*, more surface-sensitive) measurements are generally higher and increasingly deviate from the nominal for Sr concentrations ≥ 0.5%. This trend indicates a Sr rich $MAPbI_3$ surface with significant Sr surface segregation for 1% and 2% Sr doping.

For the Mg 1s line, the measurements using 2 keV and 6 keV have IMFP of ≈2 nm and ≈8 nm, respectively.[34-35] The calculated [Mg]:[Pb] ratios computed from the 2 keV and 6 keV measurements mainly agree with the nominal doping concentration within the experimental uncertainty as can be seen in **Figure 4.2b**. However, unlike Sr doping series, the comparison between the two measurements of different probing depth may indicate (if at all present) a less pronounced Mg surface enrichment. The 5% Mg-doped sample is a notable exception. For this sample, the HAXPES derived composition is the same as determined for the 2% Mg-doped $MAPbI_3$ and thus below the nominal doping concentration, which can be an indication for grain boundary accumulation requiring further investigation in our next study.

To further test for the non-uniform distribution profile of dopants at different doping concentration in the perovskite layer, we made use of spatially resolved synchrotron-based nano x-ray fluorescence (nXRF) mapping. nXRF is more bulk sensitive than HAXPES and offers an opportunity to obtain the lateral elemental distribution within the film. **Figure 4.2c, d** shows the surface elemental distribution imaging of the perovskite film at Sr doping levels of 1% together with 2% and 0.2% corresponding to the two different doping regimes that we proposed earlier. The relatively low fluorescence yield of Mg[36] means that its presence at this low concentrations cannot be detected by the measurement; hence, only Sr doping series are presented here. With a doping concentration of 1% and even more pronounced in the 2% map (**Figure 4.2c**), evidence of segregation as bright feature of Sr-rich phases is observed, similar to reports by Lau *et al.*[21] and Caprioglio *et al.*[22] To compare with HAXPES data, we plot ratio maps of [Sr]:[Pb]. Although the average values of [Sr]:[Pb] agree well with the nominal concentration in **Figure 4.2e**, the [Sr]:[Pb] is significantly higher in the localised regions (up to 8% in the 2% Sr-doped sample map). These regions of increased Sr content may explain the Sr enrichment suggested by the HAXPES analysis. We cannot detect clear Sr agglomeration for doping level in the low doping regime. The 0.2% sample in **Figure 4.2d** shows a reasonably uniform distribution of Sr over the investigated area with approximately 0.2% [Sr]:[Pb] (**Figure 4.2f**). The small intensity variation of this particular map is likely due to a slightly inhomogeneous sample, which is corroborated by the Pb map (Figure S4.5). Thus, we conclude that Sr can be incorporated in the perovskite lattice, but the ability to host Sr saturates at a concentration lower than 1%.

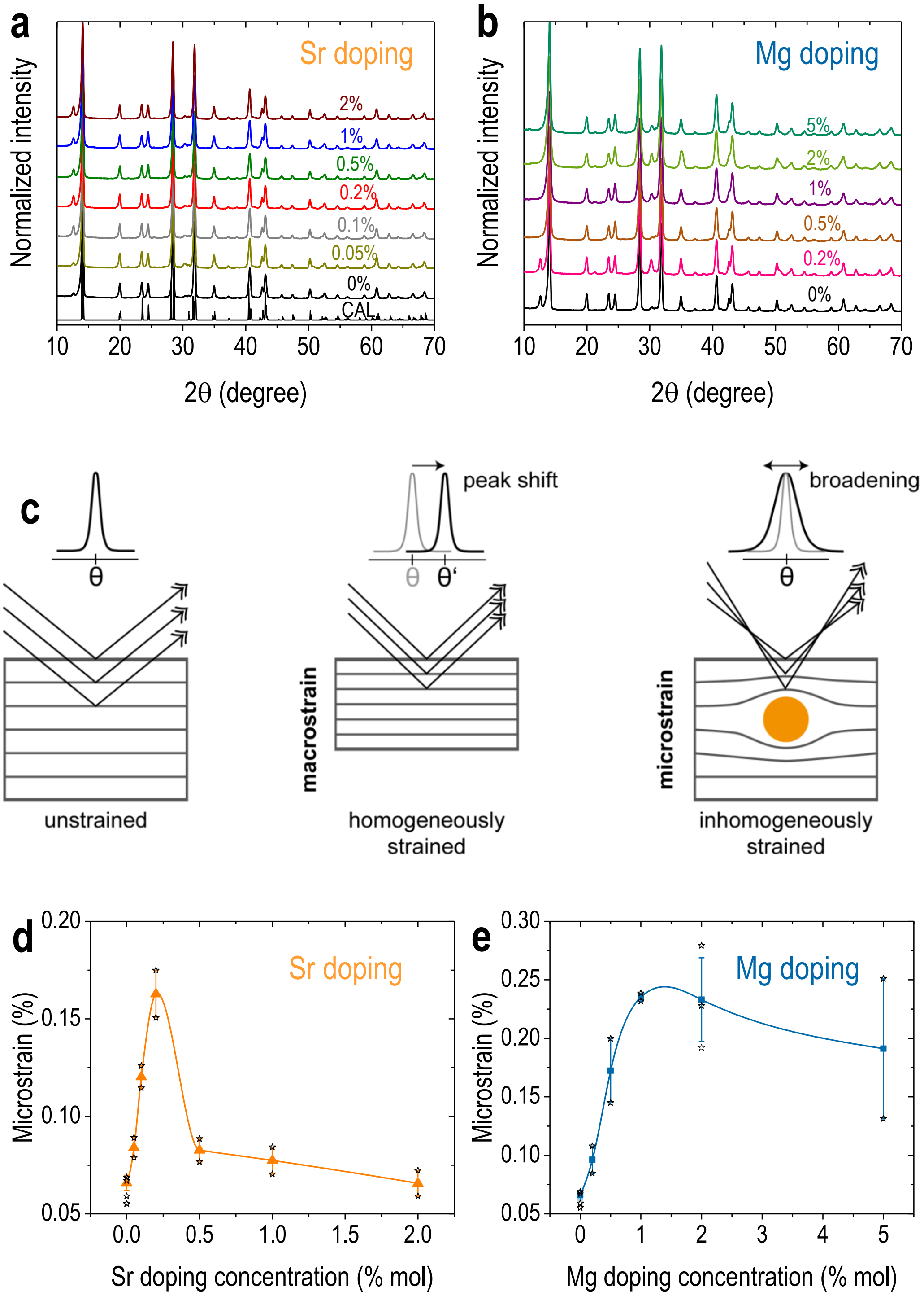

Figure 4.3 Structural characterisation. Grazing incidence x-ray diffraction (XRD) patterns of a) Sr doping series (including the theoretical calculation of $MAPbI_3$) and b) Mg doping series. c) Schematic of macrostrain which causes a peak shift in XRD pattern, and microstrain, which causes peak broadening (illustration adapted from Ref [260]). Microstrain values obtained by Le Bail refinement of d) the Sr doped $MAPbI_3$ and e) the Mg-doped $MAPbI_3$ sample series as a function of nominal dopant concentration. The depicted microstrain values are the mean of at least two different samples (individual values are shown in star points next to the mean values), and the stated error bar represents the standard deviation. Spline fits of the values are shown as a guide for visual clarification.

Figure 4.3a and **Figure 4.3b** show the grazing incidence X-ray diffraction (GIXRD) patterns, which confirm the tetragonal phase of $MAPbI_3$ in all the Sr and Mg-doped samples agreeing with theoretically calculated pattern (**Figure 4.3a**).[38] Upon the addition of Sr^{2+} and Mg^{2+}, no new peaks are detected, which indicates that no new crystalline phases are formed (although signals from the ITO substrate and PbI_2 are present in some cases; see S.I. for discussion). Thus, GIXRD does not detect any secondary phase segregated to the sample surface (as suggested by nXRF and HAXPES data of the highly Sr-doped $MAPbI_3$ samples, see **Figure 4.2**), suggesting the surface phase is amorphous or too thin/too dispersed to be detected by GIXRD. (The GIXRD detection limit for the used setup is estimated to be 0.5% of the probed volume). Nonetheless, foreign cations may still be incorporated into the perovskite lattice. To detect if any inclusion occurred, we conducted a Le Bail refinement of the GIXRD patterns, (fits are reported in Figure S4.6a and Figure S4.23, S.I.),[39] to characterise the microstrain due to doping. The effect of crystallite size broadening is also included in the refinement (see Methods section for more details). The contributions on the peak broadening from microstrain and crystallite size are further graphically shown in Williamson-Hall plots (Figure S4.6b, S.I.).

As schematically shown in **Figure 4.3c**, the microstrain represents a local distortion of the lattice, which can be detected as a broadening of the peaks. There are no systematic shifts of the XRD peaks (focused and overlapped patterns are shown in Figure S4.6c, d) indicating the absence of lattice macrostrain or homogenous changes in the crystal structure. Due to the low concentration of dopants, which can be included in the perovskite lattice, the small number of doped unit cells compared to the coherent domain can only be shown by the microstrain or inhomogeneous strain. The microstrain evolution of the Sr (**Figure 4.3d**) and Mg (**Figure 4.3e**) doping series shows that the perovskite lattice accumulates distortion up to a specific doping level, and then the lattice relaxes back when the segregation of the second phase starts. In particular, the microstrain of Sr-doped samples reaches a maximum value at 0.2% and quickly drops at higher concentrations, where segregation dominates the doping process (see HAXPES and nXRF data related discussion in conjunction with **Figure 4.2** above). The microstrain at this high doping regime, specifically 2%, declines to a value of 0.07%, similar to the undoped sample's level. As is clearly evident from Figure S4.6e, the lattice parameters of $MAPbI_3$ change upon Sr doping in both directions of the tetragonal unit cell implying to the lattice inclusion. Therefore, we have strong evidence that at 0.2% Sr doping concentration, the dopant can be incorporated into the perovskite lattice. As can be seen in **Figure 4.2**, HAXPES and nXRF have different probed volumes but derived ratios are similar within the uncertainty (1±0.5% and 0.2% respectively). Thus, this [Sr]:[Pb] ratio can give an indication of the amount of Sr in the perovskite crystal which is less than 1%. However, we acknowledge that a precise amount of Sr requires a further investigation in a following up study.

In the Mg doping series, the microstrain shows a more gradual decrease after the maximum is reached at 1% doping concentration. This might indicate that lattice incorporation and lattice relaxation due to segregation can happen simultaneously at concentrations higher than 1%. This is in agreement with the HAXPES derived conclusion of a less pronounced Mg surface segregation. Hence, Mg doping can have a higher threshold until the surface segregation occurs. Noticeably, the most significant microstrain occurs at a higher doping concentration in the case of Mg (1%) than in the case of Sr (0.2%), with higher absolute values in the Mg case. Besides, as can be seen in Figure S4.6f, the lattice indicates a contraction in the c-direction with the most significant change at 1% Mg, which is different from uniformly changes in the Sr-doped perovskite lattice in both directions, shown in Figure S4.6e. The difference can originate from the smaller ionic radius of Mg^{2+} (72 pm) compared to that of Sr^{2+} (118 pm) and Pb^{2+} (119 pm),[16] which influences the ability to incorporate the doping atom into the perovskite lattice. Notably, our DFT calculations predict very similar Pb-I and Sr-I average bond lengths of 320 and 323 pm in pristine and Sr-doped (substitutional Sr_{Pb}) perovskites, while shorter Mg-I bond of 298 pm is reported in Mg-doped (substitutional Mg_{Pb}) systems, in agreement with the tabulated ionic radii from Shannon *et al.*[16] The comparison of the microstrain trend in the case of Sr doping with the corresponding HAXPES data in **Figure 4.2** corroborates our hypothesis above that the dopant is incorporated into the perovskite lattice until a critical distortion is reached. Then, the dopant starts to segregate at the surface, resulting in a relaxation of the perovskite lattice.

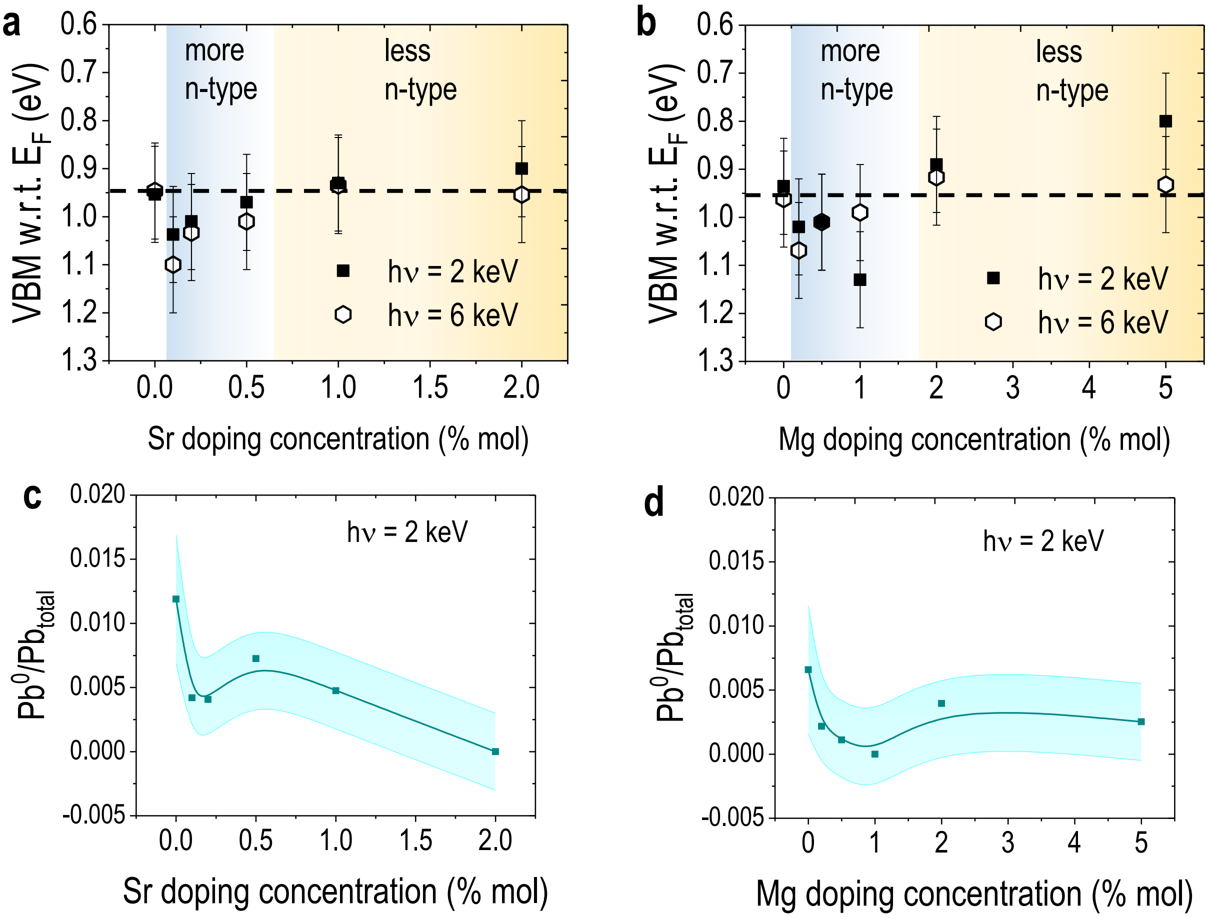

Figure 4.4 Influence of dopants on electronic properties. Position of the valence band maximum (VBM) of the studied $MAPbI_3$ samples concerning the Fermi level (E_F) for various nominal doping concentrations of a) Sr and b) Mg derived from 2 and 6 keV HAXPES data. The region in which the doped perovskite is more n-type compared to the undoped material is indicated in blue, whereas less n-type region is shown in yellow. The dashed line denotes the value obtained for the undoped samples. The fraction of metallic lead (Pb^0) compared to the total amount of lead at the surface of the samples, as determined by 2 keV HAXPES measurements is shown in c) for the Sr and in d) for the Mg-doped $MAPbI_3$ sample series. The experimental uncertainty is presented as the area along with the corresponding spline fits of the values as a guide for visual clarification.

We investigated how different doping regime influences the position of the valence band maximum (VBM) concerning the Fermi level (E_F) using HAXPES. **Figure 4.4a** and **Figure 4.4b** show the VBM position of the investigated Sr-doped and Mg-doped $MAPbI_3$ sample series, respectively (full spectra and details on VBM determination are shown in Figure S4.3, S.I.). Assuming that the bandgap (E_g) at the surface of the sample is the same as its optical E_g (*i.e.,* ≈ 1.6 eV obtained from Tauc plots of corresponding UV-vis spectra shown in Figure S4.7, S.I.), the undoped $MAPbI_3$ would exhibit a (slight) n-type character on the sample surface. With adding dopants, similar trends can be detected in the VBM position as a function of dopant concentration for 2 and 6 keV measurements. At low doping levels (*i.e.*, lower than 0.5% Sr- and 2% Mg-doped, indicated by the blue area in **Figure 4.4a**, **b**), the films become more n-type compared to the undoped $MAPbI_3$; whereas with higher doping concentration, the VBM shifts closer to E_F, which would be in agreement with a less n-type character. Note that in this doping concentration regime segregated surface phases and – independent of doping concentration – the presence of metallic lead could also impact the position of the VBM compared to E_F. However, we do not expect either to have a significant impact (see S.I. for detailed discussion).

Notably, even the small changes in absolute Sr concentration from 0.1% Sr to 0.5% Sr-doped causes a VBM shift from 1.04 ± 0.1 eV to 0.97 ± 0.1 eV concerning E_F, tending toward the VBM of the undoped sample. This tendency is similar for 1% and 2% Mg-doped samples. It indicates that different concentration regimes of *one* dopant can vary the n-type doping level. We can correlate the reasons behind this change to the change in defect concentrations of the films as the number of dominant vacancies can induce n or p-doping of perovskite.[31] Together with theoretical calculation (discussed in details in S.I.), we postulate that the dopants included in the lattice can passivate Pb (V_{Pb}^{2-}) and MA (V_{MA}^{-}) vacancies. This can result in a more n-type material whereas less n-type doping might be realised by the increase in iodine interstitials (I_i^-) due to the iodine excess in the precursors in this case. The DFT calculation shows that the V_{Pb}^{2-} passivation is favoured by 0.24 and 0.11 eV for Sr^{2+} and Mg^{2+}, respectively. This scenario would be in agreement with the significant reduction of the Pb^0 content in the sample upon doping shown in **Figure 4.4c** and **Figure 4.4d**. After Pb^{2+} site is saturated with Sr^{2+} and Mg^{2+}, the n-type doping can further be a result of V_{MA}^- passivation with the formation energy of -0.44 eV and 0.01 eV respectively. Furthermore, since Mg^{2+} has higher inclusion concentration than Sr^{2+} despite unfavourable tolerance factor to form 3D MA-based perovskite, it indicates a plausible scenario of Mg_i^{2+} included stably in interstitial position.

4.2.3 Device performance

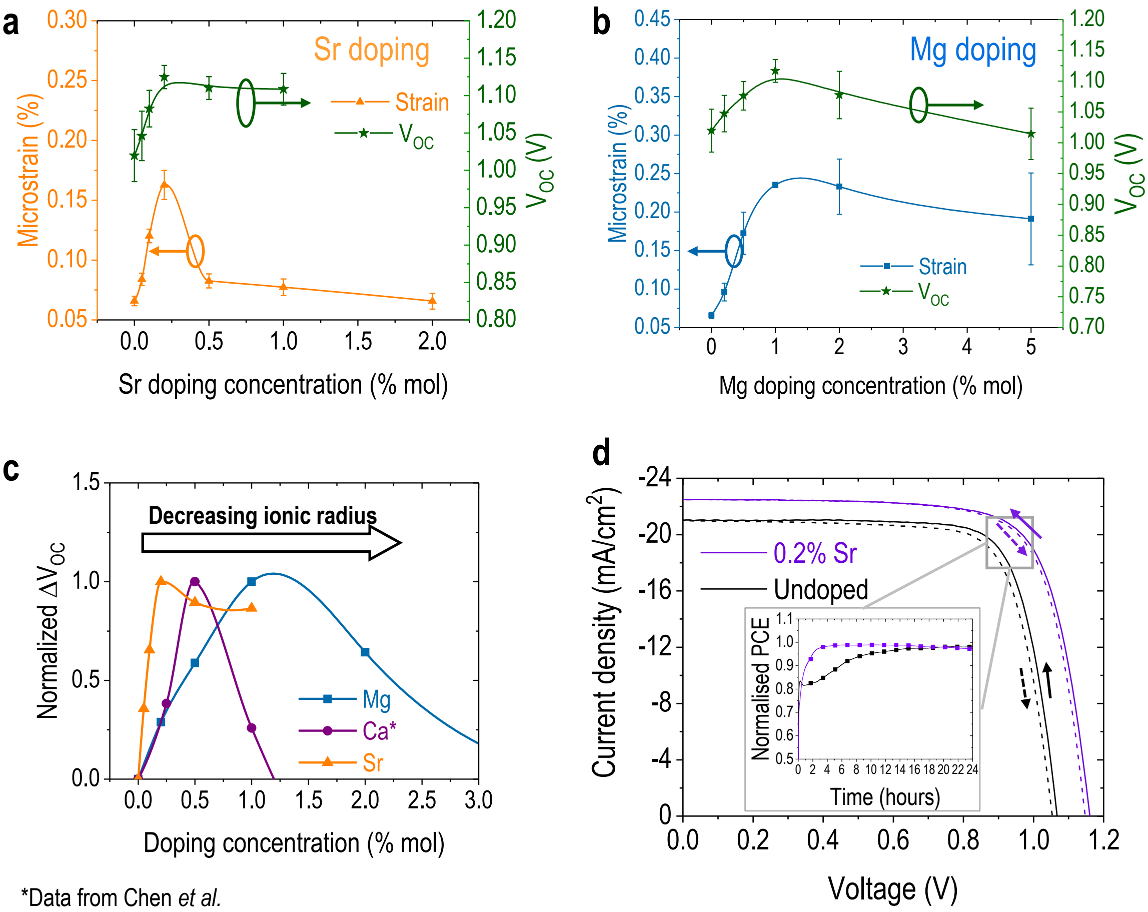

*Data from Chen *et al.*

Figure 4.5 Device performance upon doping. Correlation between open circuit voltage (V_{OC}) of solar cell devices with microstrain from GIXRD refinement of a) the Sr-doped $MAPbI_3$ series and b) the Mg-doped $MAPbI_3$ series. c) Open circuit voltage trend with respect to nominal doping concentration of 3 alkaline earth metal ions namely Mg^{2+}, Ca^{2+}, and Sr^{2+} (data for Ca^{2+} doping is collected from Chen *et al.*)[40] d) Current density-voltage (J-V) curve of the best 0.2% Sr-doped with antireflection coating and undoped $MAPbI_3$ device measured at standard AM1.5 1 sun equivalent condition with a 100 mV/s scan rate. Arrows indicate scan direction. The inset is continuous maximum power point tracking in N_2 at 25°C, in simulated global AM1.5 solar spectrum with UV cut-off at 380 nm for 24 hours.

To study the impact of the dopants on the performance of complete solar cells, we prepared p-i-n devices made of ITO/PTAA/$MAPbI_3$/C60/BCP/Cu, as previously reported (see Methods section).[41] **Figure 4.5a, b** display the device's open circuit voltage (V_{OC}) as a function of the doping level for Sr and Mg (full set of parameters are presented in Figure S4.13, S.I.). Remarkably, the microstrain of the perovskite lattice reported in **Figure 4.3**, which we re-plotted here, follows the V_{OC} trend. In particular, we observe a maximum in both microstrain and V_{OC} at 0.2% Sr- and 1% Mg-doped devices, and a (slight) decrease after the maximum has been reached. It is worth noticing that at high Sr doping levels (more than 0.5% Sr), the microstrain decreases to the undoped level, yet V_{OC} is still improved compared to undoped devices. This can be attributed to possible surface passivation by the Sr surface phase segregation also seen in literature.[20, 22]

This similar trend between V_{OC} and microstrain indicates the positive impact of lattice incorporation of the dopants to reduce defect concentration in $MAPbI_3$. As mentioned in the previous section, the DFT calculations predict defect passivation by incorporating Sr^{2+} and Mg^{2+} (see S.I. for details), which can explain the high V_{OC} with lattice incorporation of the dopants. We further calculated quasi-Fermi level splitting of perovskite layer and reinforced that the voltage improvement stems from bulk defect passivation rather than interfacial passivation at low doping concentration (see Figure S4.14 and related discussion in S.I.) Furthermore, we extend the analysis of the V_{OC} trend to literature data to include Ca into the series of dopants. The data of CaI_2 doping are plotted from Chen *et al.* with similar doping concentration range.[40] **Figure 4.5c** shows the relative change in V_{OC} of Mg^{2+}, Ca^{2+}, and Sr^{2+} doped devices concerning doping concentrations. Although the trend of V_{OC} is similar for all three dopants, the highest V_{OC} occurs at 1% for Mg, 0.5% for Ca[40] and 0.2% for Sr doping. Interestingly, this trend corresponds to the pattern of effective radii of the dopants as well (Mg^{2+} (72 pm) < Ca^{2+} (100 pm) < Sr^{2+} (118 pm)).[16] Thus, the highest V_{OC} happens at a higher doping concentration for dopants with smaller ionic radii, which implies that the ability to host dopants in $MAPbI_3$ depends on the radii of the dopants.

The low doping regime where the dopants can be included in the perovskite lattice and passivate defects results in better device performance. In particular, upon Sr and Mg doping, the average V_{OC} improves about 100 mV (from 1023 mV on average of undoped devices to averages of more than 1117 mV and 1125 mV of Sr-doped and Mg-doped devices, respectively). Full PV parameters are shown in Figure S4.13. **Figure 4.5d** displays the champion p-i-n $MAPbI_3$ device with 0.2% Sr doping, which showed J_{SC} of 22.5 mA/cm^2 (in agreement with integrated current density from external quantum efficiency plot in Figure S4.17b), FF of 74.3% and a V_{OC} of 1161 mV, resulting in an efficiency of 19.4% (stabilised at 19%) compared to 17.2% of undoped $MAPbI_3$ e device. To further prove the effectiveness of low doping regime, n-i-p 0.2% Sr-doped $MAPbI_3$ devices were fabricated, resulting in more than 20% champion device compared to 18.7% of undoped $MAPbI_3$ device shown in Figure S4.19. The long-term stability of the doped $MAPbI_3$ compared to undoped $MAPbI_3$ is shown in the inset **Figure 4.5d**. The transient of the first few hours is suppressed by doping. The Sr-doped device shows a quick transient reaching its maximum power output in 2 hours whereas it takes more than 20 hours for undoped device to reach the stabilised PCE. This trend might be attributed to faster ion migration[42] or reduction of number of mobile ionic defects upon doping.

4.3 Conclusion

In this study, we investigated the doping mechanism of halide perovskites using Sr^{2+} and Mg^{2+} to compare doping elements with similar chemical properties but different ionic radii. We found two distinct doping regimes. The low doping concentration regime, which results in incorporation of the dopant into the perovskite lattice, and the high doping concentration regime, which results in surface phase segregation. We observed that the threshold between the low and the high doping regimes depends on the size of the doping element. In particular, methylammonium lead iodide perovskite can incorporate a larger quantity of Mg^{2+} than Sr^{2+}, which has a smaller ionic radius. We discussed the impact of the dopant incorporation and the surface segregation on the n-type character of the materials as the result of the interaction of the doping element with the defect chemistry of the material. Thus, we prove the effectiveness of the low doping regime for the first time demonstrating methylammonium lead iodide based solar cells with an open circuit voltage exciding 1.16 V and stabilised PCE of more than 19% for p-i-n structure and more than 20% PCE for n-i-p solar cells. Our work provides a comprehensive picture of the doping mechanism of halide perovskite semiconductors, which is somewhat different from the classical doping of semiconductors.

Methods

Solar cells fabrication

All chemicals are used as received. The perovskite solution is mixed from 1.2 M of PbI_2 (Tokyo Chemical Industry), and CH_3NH_3I (Dyenamo) in mixed solvent DMF:DMSO 6:1 (v:v). The dopant SrI_2 (Alfa Aesar) is dissolved in DMSO (1M) and MgI_2 (Santa Cruz) is dissolved in DMF:DMSO 6:1 (0.7M). The amount of dopants in the perovskite solution is calculated according to the molar ratio with PbI_2. The final perovskite solution is shaken at 60 ^{o}C for 5 minutes to dissolve all components.

In-doped SnO_2 (ITO) substrates (Automatic Research, 15 $\Omega \cdot cm^{-2}$) are sonicated for 15 minutes with Mucasol (2% in deionised water), Acetone and isopropyl for cleaning and eventually UV-ozone treatment for 15 minutes. Prior to perovskite deposition, PTAA (poly[bis(4-phenyl)(2,4,6-trimethylphenyl)amine]) (Sigma Aldrich) with a concentration of 2 mg/mL in toluene is spin-coated on clean substrates (4000 rpm for 30 s). The substrate is then annealed at 100 ^{o}C for 10 minutes. 100 µL of perovskite solution is dropped on room temperature substrate before starting the spin coating program (4000 rpm for 30 s, ramping for 5 s). After 20 s of spin coating, 500 µL of ethyl acetate is dropped on the substrate to form a smooth and compact film. The perovskite film is immediately annealed at 100 ^{o}C for 60 minutes. Finally, C60 (20 nm) (Sigma Aldrich), BCP (bathocuproine or 2,9-Dimethyl-4,7-diphenyl-1) (10 nm) (Sigma Aldrich) and Cu (100 nm) (Alfa Aesar, 99.95% purity) are evaporated on the perovskite layer to complete the device. All of these fabrication steps are done in an inert atmosphere with minimised air exposure.

For n-i-p $MAPbI_3$, the compact TiO_2 were deposited on cleaned F-doped SnO_2 (FTO, 15 $\Omega \cdot cm^{-2}$) using method reported elsewhere.[43] In short, the cleaned FTO substrates are submerged in 200 mL $TiCl_4$ solution at 70°C for 1 hour, then the substrates are cleaned thoroughly with deionised water and dried at 100°C for 1 hour. The TiO_2 layer is treated with UV-ozone for 30 minutes before perovskite deposition. The hole selective layer is prepared as followed. 36.15 mg of Spiro-OMETAD is dissolved in 1 mL of chlorobenzene, then 14.40 µL 4-*tert*-Butylpyridine (Sigma Aldrich, 98%), 8.75 µL of Li-TFSI (bis(trifluoromethane)sulfonimide lithium salt, 99.95% trace metals basis, Sigma Aldrich) (300 mg per mL of acetonitrile), and 14.50 µL FK209 (Co(II) salt, Sigma Aldrich) (500 mg per mL of acetonitrile) are added to the Spiro-OMETAD solution. Finally, 80 nm of Au (Alfa Aesar, 99.99% purity) is evaporated on top to finish the device.

Hard x-ray photoelectron spectroscopy

Hard x-ray photoelectron spectroscopy (HAXPES) measurements were carried out at the HiKE endstation located at the BESSY II KMC-1 beamline at Helmholtz-Zentrum Berlin (HZB).[44-45] The HiKE endstation is equipped with a Scienta R4000 electron analyser and an excitation energy of 2003 eV (referred to as "2 keV") and 6009 eV (referred to as "6 keV") were employed. The binding energy (BE) scale of the HAXPES measurements was calibrated by measuring the Au 4f energy region of a clean Au foil in electrical contact with the (grounded) sample and setting the BE of the Au $4f_{7/2}$ line to 84.0 eV. The pressure in the endstation's analysis chamber during the HAXPES measurements remained $<1 \times 10^{-8}$ mbar. Curve fit analysis of measured detail HAXPES spectra were simultaneously conducted using the Fityk software.[46] Voigt profile functions, along with linear backgrounds, were employed for these fits. Spin-orbit doublets were fitted using two Voigt functions with intensity ratios set to obey the $2j + 1$ multiplicity rule. The peak intensities of the HAXPES core levels were corrected to account for differences in photoionisation cross section (σ),[47-49] and when required also for changes in the inelastic mean free path (σ),[34-35] and the transmission function of the electron analyser (T).[50] To quantify the Pb 4f spectra, two doublet peak pairs were used to account for the core level contributions and five additional (broader) pairs to account for the satellites' contribution background (derived from electron energy losses related to valence and conduction band transitions in PbX_2 systems).[51-52] The Sr 3p signal can be detected in all the Sr doped samples, whereas the Sr 3d signal is only absent for the lowest (0.1%) Sr-doped sample. This apparent difference can be explained by two factors: First, at 2 keV excitation, the σ for the Sr 3p core levels are c. 3 times higher than that of Sr 3d core levels in our experimental setup.[47] Moreover, in contrast to the Sr 3p core levels, which have a linear background, the Sr 3d core levels directly overlap with the Pb $4f_{7/2}$ line, the most prominent Pb-related photoelectron line at the used excitation energy, which explains why the Sr 3d signal is below the detection limit at low Sr concentrations (*i.e.*, 0.1% doping). For these reasons, although the close energetic proximity of the Pb 4f/Sr 3d core levels would present a straightforward opportunity to quantify the [Sr]:[Pb] ratios just by normalising the signal of each core level by its corresponding σ,[47] we chose to calculate the [Sr]:[Pb] ratios from the more prominent core lines (*i.e.*, Sr $3p_{3/2}$ and Pb $4f_{7/2}$). The HAXPES probing depth is governed by the inelastic mean free path (IMFP) of the probed photoelectrons. The main contribution stems from the surface of the sample, which decays exponentially to 1/e within IMFP. For the Sr 3p and Pb 4f lines, the measurements using 2 and 6 keV have an IMFP of ≈4 nm and ≈10 nm, respectively.[34-35] For the Mg 1s line, the measurements using 2 keV and 6 keV have IMFP values of ≈2 nm and ≈8 nm, respectively.[34-35] The position of the valence band maximum (VBM) with respect to the Fermi level (E_F) was determined by linear approximation of the leading edge of the valence band spectra.

Nano x-ray fluorescence

The synchrotron-based nano x-ray fluorescence (nXRF) measurements for the elemental mapping of the perovskite films were done in the 2-ID-D beamline at an excitation energy of 16 keV, x-ray step size of 0.15 μm, and a dwell time of 50 ms at the Advanced Photon Source, Argonne National Laboratory. The MAPS software, written in IDL programming language, was used to display the acquired XRF data. Because Sr is commonly found in glass substrates (*e.g.*, the used ITO-coated glass substrate), the perovskite films employed in the nXRF analysis were prepared on quartz substrates, following the same procedure detailed in the *Solar cells fabrication* subsection above. The purpose of the measurement is to check the possibility of two doping regimes. We chose 0.2%, 1% and 2% to have at least one order of magnitude difference in doping concentration for the two regimes.

Density functional theory calculations

Density functional theory (DFT) calculations have been carried out by modelling defects in the 2x2x2 supercell of $MAPbI_3$, by fixing cell parameters to the experimental values.[53] Energies of formation and reaction of Sr and Mg related defects have been calculated by using the Perdew-Burke-Ernzherof (PBE)[54] exchange-correlation functional and ultrasoft pseudopotentials with a cutoff on the wavefunctions of 40 Ryd (320 Ryd on the charge density) sampling the Brillouin zone (BZ) at the Gamma point. Defects formation energies diagrams of Sr and Mg defects in $MAPbI_3$ (Figure S4.9) have been calculated at the PBE level by following a widely used approach and by simulating I-medium conditions of growth of the perovskite.[55-56] The chemical potentials of Sr and Mg have been calculated by imposing the equilibrium with the relative precursors, i.e. $\mu(Mg/Sr) = \mu(MgI_2/SrI_2) - 2\mu(I)$, where $\mu(I)$ is calculated in I-medium conditions and is set according to thermodynamic equilibrium between $MAPbI_3$ and PbI_2.

Thermodynamic ionisation levels in Figure S4.8 and the plots of Kohn-Sham orbitals have been calculated by performing single point calculations at the HSE06-SOC[57] level of theory (exchange fraction $\alpha=0.43$, dispersion included a-posteriori through the DFT-D3 scheme[58]) on the equilibrium geometries found at the PBE level.[56] Hybrid calculations have been performed by using norm conserving pseudopotentials with an energy cutoff of 40 Ryd on the wavefunctions and by sampling the BZ at the Gamma point.[56]

Grazing incident x-ray diffraction

The measurement is conducted in the air with the PANalytical X'Pert Pro MPD (multi-purpose diffractometer) using grazing incidence geometry. Grazing incident x-ray diffraction (GIXRD) patterns are collected with a step size of 0.02 degree, for 10 seconds each step. Based on the signal-to-noise ratio of the collected GIXRD data, we estimate a detection limit of 0.5% crystalline phase in the probed volume.

The Le Bail method was chosen instead of the Rietveld refinement method due to the ease in the calculation without a requirement of the exact atomic positions and the scattering power of the atoms, hence reducing the computation effort.[39] The refinement is done with the FULLPROF program. Here, we could use the full line profile analysis because our XRD patterns show all theoretically predicted peaks from the lattice structure of the material. Different from the standard material, in the polycrystalline film, the XRD peaks can be described by pseudo-Voigt functions. The function is used to consider both Gaussian and Lorentzian contribution to the shape of the peaks in the pattern. Hence, we assume that the angular dependence microstrain will affect to Gaussian peak broadening contribution (the case of Lorentzian contribution to microstrain is rare, so it was excluded from the analysis) whereas the broadening due to crystallite size is from Lorentzian contribution.[59] From this contribution, the microstrain is calculated. More details on the refinement can be found in S.I.

Photoluminescence characterisation

Absolute photoluminescence (PL) spectra were recorded from hyperspectral images with a custom setup described elsewhere.[60] We used two 450 nm LEDs for excitation whose fluence are calibrated to 1 sun equivalent and a calibrated CCD camera was used to collect PL emission, coupled to a tunable liquid crystal filter. The setup was calibrated to absolute photon numbers with light sources of known fluences,[61] thus enabling to estimate the quasi Fermi-level splitting (QFLS) from the generalised Planck law using the high-energy tail fit method of the PL spectra.[62]

Current density-voltage measurement

The J-V measurement is done with 1 equivalent sun illumination from an Oriel LCS-100 class ABB solar simulator in an inert atmosphere without cooling. The device's active area is 0.16 cm^2. The lamp is calibrated with a Silicon 1 cm^2 diode certified by Fraunhofer ISE.

External quantum efficiency (EQE) measurement

The EQE is measured with a Newport 300 W xenon arc lamp using TracQ software in an Oriel Instruments QEPVSI-b system. A Newport Cornerstone 260 monochromator is used to create monochromatic light chopped at a frequency of 78 Hz. Before the measurement, the system is calibrated with a silicon reference cell with a known spectral response. The electrical response of the device is recorded with a Stanford Research SR830 Lock-In amplifier and evaluated using TracQ.

Ultraviolet-visible spectrophotometry

Transmittance and reflectance of the samples are measured with a Perkin Elmer Lambda 1050 spectrophotometer equipped with a tungsten-halogen lamp. The measurement is done with a wavelength range of 300 nm to 850 nm. The derived optical bandgap from the Tauc plot of a direct bandgap material (relation between $(\alpha h\nu)^2$ and $h\nu$) is the intercept between the linear approximation of the absorption edge with the background.

Scanning electron microscopy

The data are collected with Hitachi S-4100 at 5 kV acceleration voltage and 30k magnification to obtain top view and cross sectional images.

4.4 Supporting Information

Hard X-ray photoelectron spectroscopy (HAXPES)

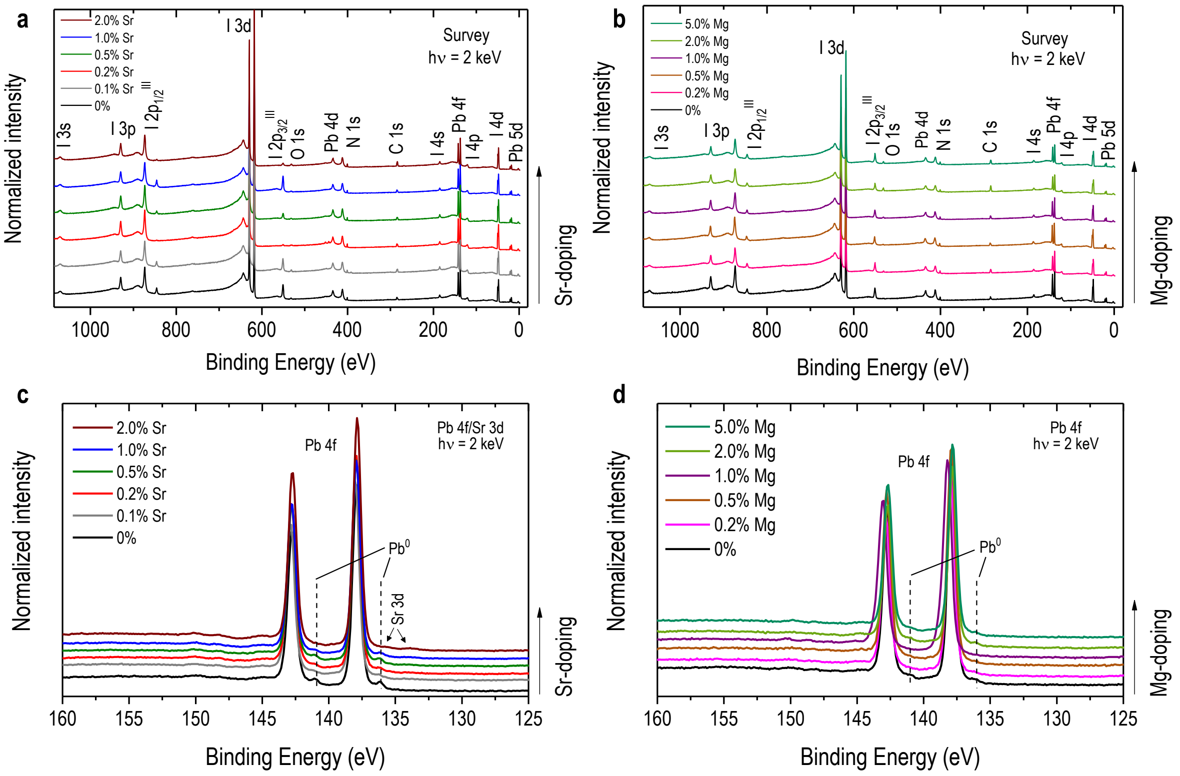

Figure S4.1 Hard X-ray photoelectron spectroscopy (HAXPES) survey spectra of a) Sr doping series and b) Mg doping series. c) Pb 4f/Sr 3d core levels spectra of different Sr doping concentrations and d) Pb 4f of different Mg doping concentrations measured using 2 keV excitation.

The hard X-ray photoelectron spectroscopy (HAXPES) survey spectra of the investigated sample series, shown in **Figure S4.1a, b**, display the photoemission lines of $MAPbI_3$ elements (*i.e.*, C, N, Pb and I) as expected. Signal derived from the In-doped SnO_2 (ITO)-coated substrate (*i.e.*, In- and Sn-related lines) is not detected, indicating an excellent perovskite film coverage. Minute traces of O-related lines are observed ascribed to absorbates, which show the effectiveness to prevent/minimize air exposure of samples prior to HAXPES measurements. (Although O-related intensity could also in principle be derived from the ITO-coated substrate, this origin is ruled out because signal from In- and Sn-related lines was not detected.) Sr- and Mg-related lines are not distinguishable in the survey spectra; however, this is due to the low molar concentrations of the dopants. Note that the core level of Pb 4f are shifted in the same amount to the valence band maximum shift, which will be shown in the **Figure S4.4**.

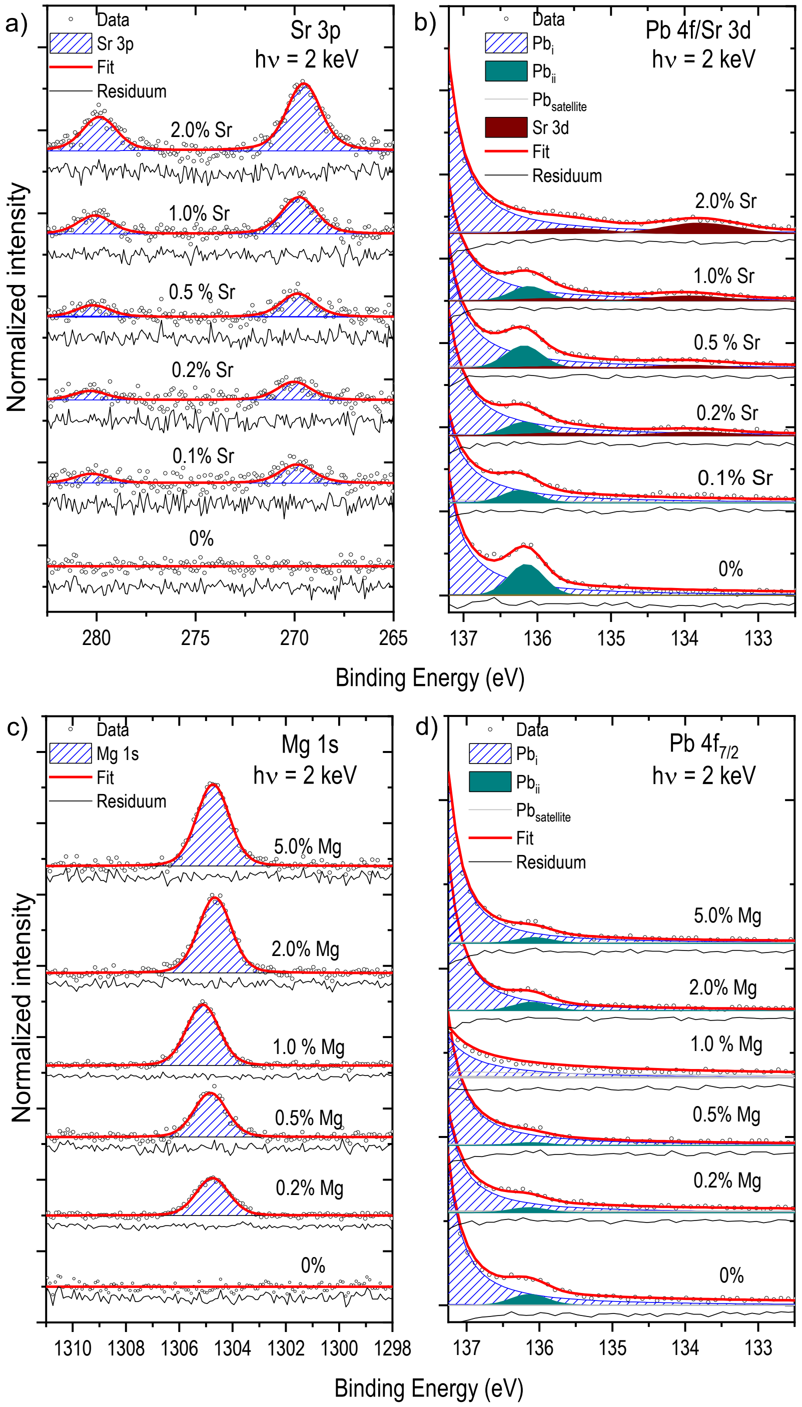

Figure S4.2 Hard X-ray photoelectron spectroscopy (HAXPES) spectra of a) Sr 3p and b) Pb 4f/Sr 3d core levels of $MAPbI_3$ with different Sr doping concentration, and the spectra of the c) Mg 1s and d) Pb 4f core levels of $MAPbI_3$ with different Mg doping concentration. An excitation energy of 2 keV was used for all spectra. b) and d) are shown as magnified views of the energy range of the Pb $4f_{7/2}$ peak focusing on the metallic lead (Pb^0) contribution.

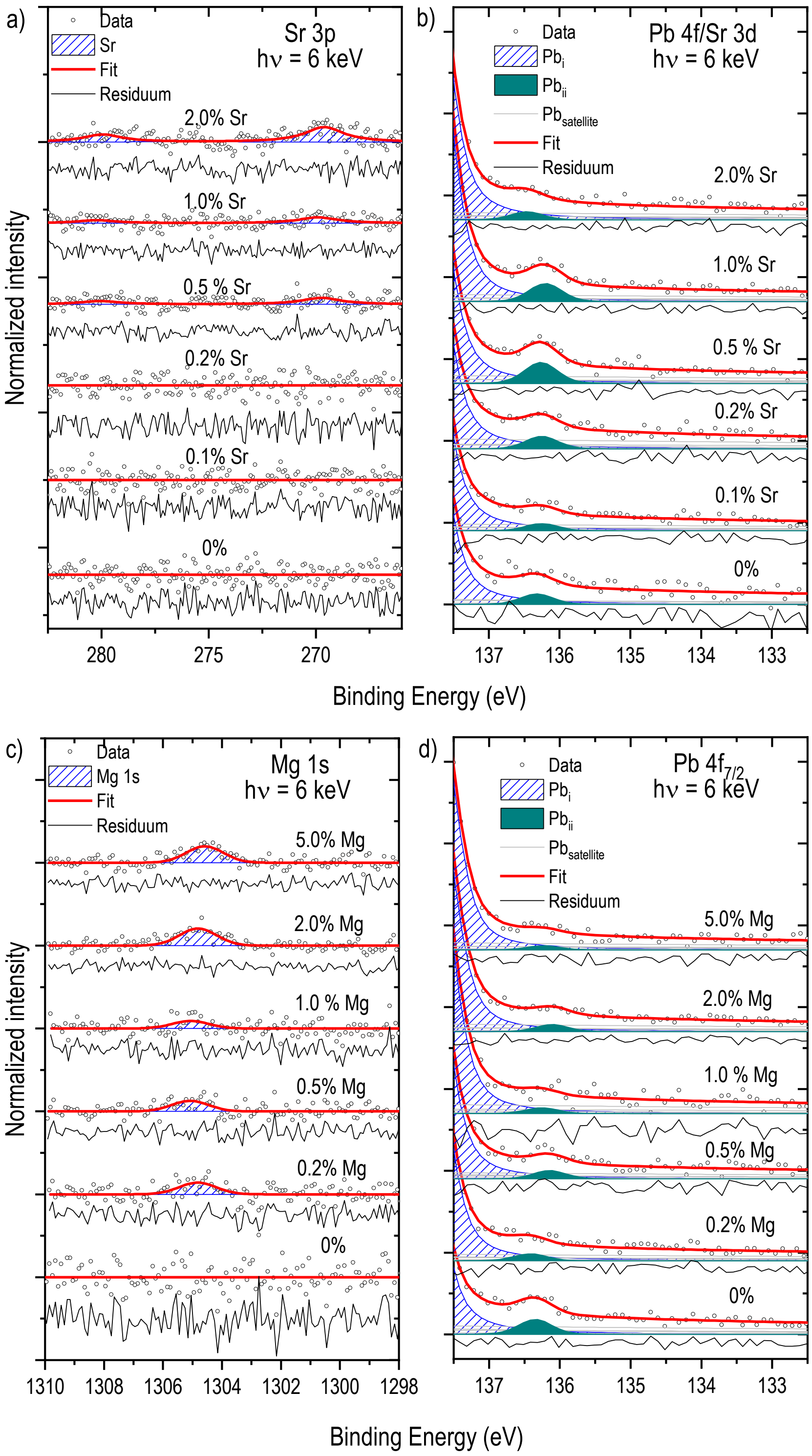

Figure S4.3 Hard X-ray photoelectron spectroscopy (HAXPES) spectra of a) Sr 3p and b) Pb 4f/Sr 3d core levels of $MAPbI_3$ with different Sr doping concentration, and the spectra of the c) Mg 1s and d) Pb 4f core levels of $MAPbI_3$ with different Mg doping concentration. An excitation energy of 6 keV was used for all spectra. b) and d) are shown as magnified views of the energy range of the Pb $4f_{7/2}$ peak focusing on the metallic lead (Pb^0) contribution.

The HAXPES detail spectra in the energy region of the Sr 3p core levels, shown in **Figure S4.2a** and **Figure S3.3a**, display a clear Sr $3p_{3/2}$ signal at a binding energy (BE) of 269.80 ± 0.15 eV for all doped films (even at 0.1% doping level, a concentration in the order of the detection limit of the technique). The BE of the Sr $3p_{3/2}$ line agrees with reports in the literature for Sr in a 2+ oxidation state.[9,20] **Figure S4.2b** and **Figure S4.3b** presents a magnified view of the HAXPES detail spectra in the energy region of the Pb $4f_{7/2}$/Sr 3d core levels. The Sr $3d_{5/2}$ line is found at a BE of 134.00 ± 0.2 eV (*i.e.*, depicted as Pb_i in **Figure S4.2b** and **Figure 4.2d**), in close proximity to the main Pb $4f_{7/2}$ line at a BE of 137.9 ± 0.2 eV shown in **Figure S4.1**, ascribed to Pb in a halide perovskite chemical environment.[20] A secondary Pb $4f_{7/2}$ peak is detected at a BE of 136.1 ± 0.1 eV (*i.e.*, depicted as Pb_{ii} in **Figure S4.2b, d** and **Figure S4b, d**), ascribed to metallic Pb (Pb^0).[63] The HAXPES detail spectra in the energy region of the Mg 1s core level for Mg doped sample series, shown in **Figure S4.2c** and **Figure S4.3c**, display a clear Mg 1s signal at a BE of 1304.8 ± 0.2 eV for all doped films (as low as 0.2% doping level). This BE of the Mg 1s line is in agreement with reports in the literature for Mg in its 2+ oxidation state.[12, 64] We note that the experimental uncertainty in **Figure 4.2a, b** is dominated by the error introduced by the photoionization cross section, inelastic mean free path (IMFP), and electron analyzer transmission correction required to obtain an *absolute* concentration ratio. Thus, the trends observed in different samples measured with the same excitation energy are quite reliable, as are the comparison between trends observed with different excitation energies; the comparison between [Sr]:[Pb] ratios across excitation energies for a specific sample is less reliable due to the large differences in cross section, IMFP, and transmission function.

We acknowledge that exposure of halide perovskites to radiation and/or the experimental conditions required for HAXPES measurements can result in the degradation of the sample which might be indicated by the presence of Pb^0 as can be seen in **Figure S4.2b** and **Figure S4.2d** for 2 keV excitation energy and **Figure S4.3b** and **Figure S4.3d** for 6 keV excitation energy.[65] It is possible that despite careful measurement controls and precautions, these effects may not be completely avoided. Because all the samples of a series are subjected to the same radiation conditions and measurement protocol, if the metallic lead is caused by beam damage, it is expected that the Pb^0 amount should be the same for all the samples. If the observed lower Pb^0 in doped samples compared to undoped samples is due to a greater stability of the doped samples (compared to the undoped material), such an argument would align with the premise that higher stability is most likely due to a less defective material. Hence, whether or not the Pb^0 is formed prior to or during the measurement, it is still a product of defect formation, which would not change our conclusion.

Note that grazing incidence X-ray diffraction (GIXRD) does not detect any traces of Pb^0 in the investigated samples (see discussion in conjunction with **Figure 4.3** in the main manuscript and with **Figure S4.5**, below). Considering that the GIXRD detection limit for the used setup is estimated to be 0.5% of the probed volume, and some of the HAXPES derived Pb^0 contents are above that threshold (see **Figure 3.4**), this might indeed indicate that Pb^0 is a result of the experimental conditions required for the HAXPES measurements. It may also be that Pb^0 is accumulated in the surface region of the sample (see also discussion in conjunction with **Figure S3.6** below), i.e., the volume probed by GIXRD is much larger than the volume probed by HAXPES.

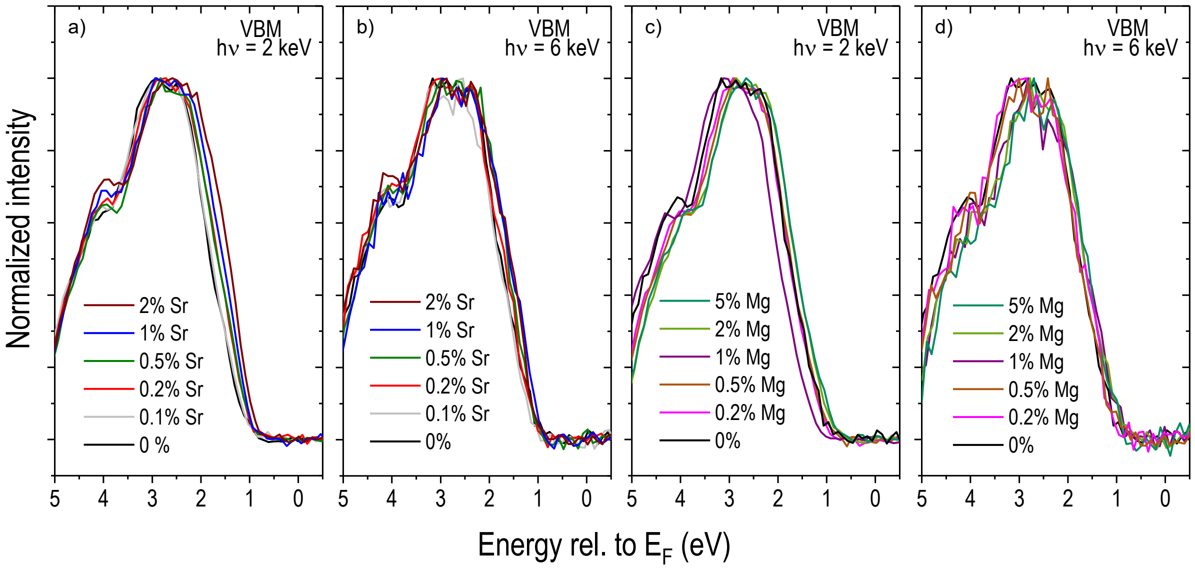

Figure S4.4 Hard X-ray photoelectron spectroscopy (HAXPES) detail spectra of the energy range near the valence band maximum of the a) and b) Sr-doped, c) and d) Mg-doped sample series measured using 2 keV and 6 keV excitation respectively.

To probe the electronic structure of the Sr- and Mg-doped $MAPbI_3$ sample series, HAXPES detail spectra of the energy region near the valence band maximum (VBM) were measured with 2 and 6 keV excitations, shown in **Figure S4.4**. The VBM position with respect to the Fermi level (E_F) was determined by linear approximation of the leading edge of the valence band spectra. Note that we ascribe the derived VBM position to represent the near-surface electronic structure of the doped $MAPbI_3$, since any contribution of Pb^0 (see **Figure 4.4** and discussion above) would induce spectral intensity around the Fermi level, *i.e.*, at 0 eV, which we do not observe in the VB spectra (due to unfavorable photoionization cross sections and insufficient signal-to-noise ratio). The same is true for any metallic (Sr or Mg) surface phase segregated to the sample surface. In the (more likely) case of the formation of iodide or oxide surface segregates, spectral intensity is expected further away from the Fermi level compared to the derived VBM positions as the band gaps of the respective species are above/around 5 eV.[66-68] However, an impact of the presence of Pb^0 and/or surface segregates on the VBM position of the doped $MAPbI_3$ samples due to doping and/or band bending effects cannot be completely excluded.

Nano x-ray fluorescence

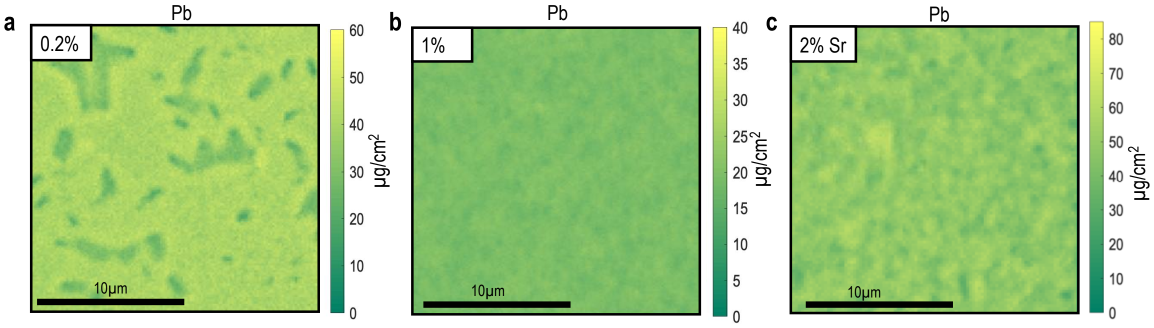

Figure S4.5 Top view of nano X-ray fluorescence (nXRF) Pb concentration maps of a) 0.2% Sr doped, b) 1% Sr doped, and c) 2% Sr doped $MAPbI_3$ thin film. The color scale indicates the amount of Sr present in the investigated area in µg/cm^2.

Compositional inhomogeneity issues of solution processed samples are already documented in literature.[69] However, the observed variation of Pb in the film can also be due to sample degradation during sample transport. The potential formation of PbI_2 would also be in agreement with the possible degradation during HAXPES measurements, most prominently indicated by the amount of detected metallic Pb. Nonetheless, this inhomogeneity does not correlate with the Sr segregation, which is observed in the nXRF Sr maps in **Figure 4.2d**.

Grazing incidence x-ray diffraction (GIXRD)

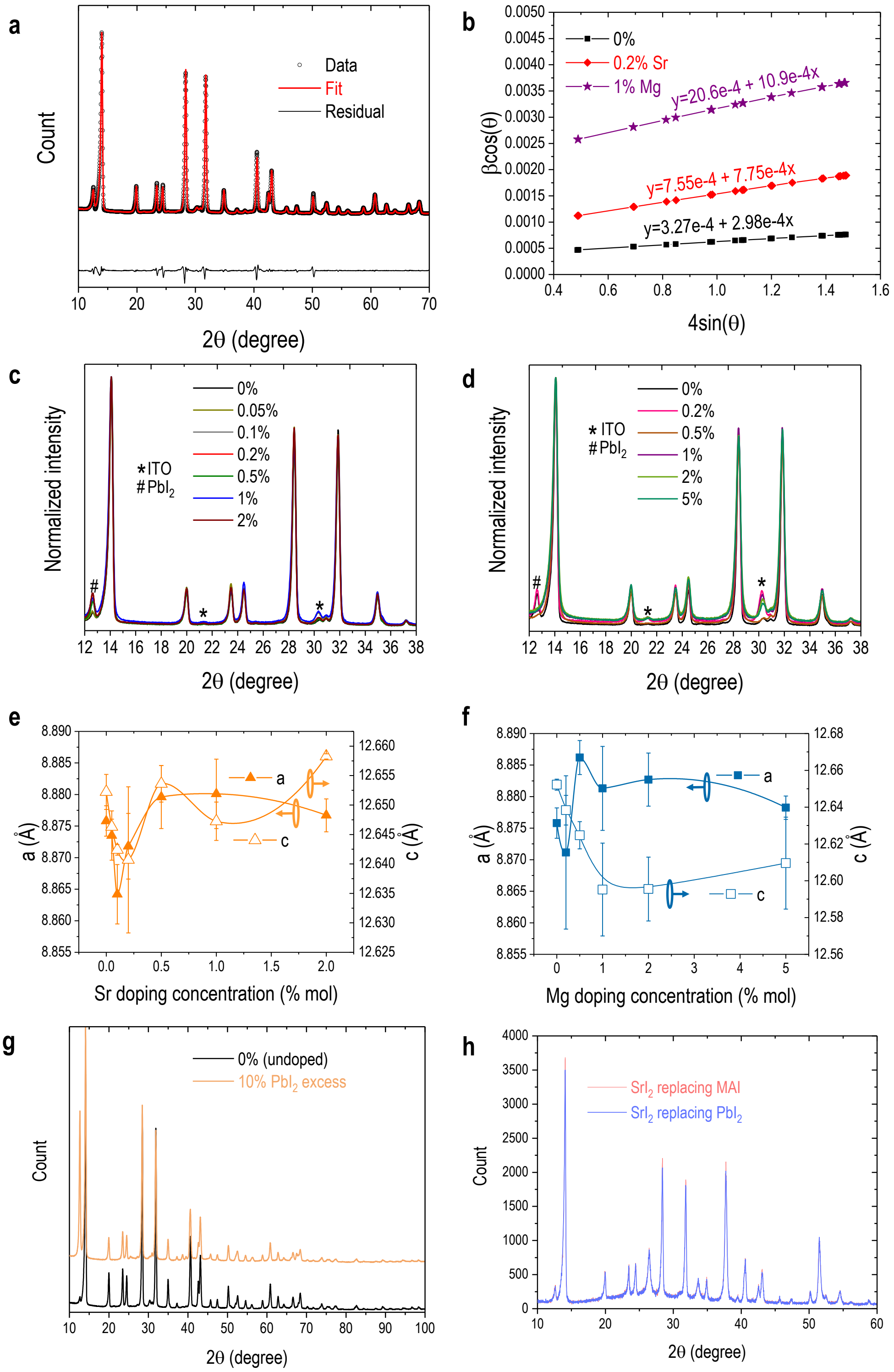

Figure S4.6 a) Example of Le Bail refinement of XRD pattern for thin film analysis. Black circles are measured data whereas red line is the fitting pattern; the black line is the residual between data and fitted value, which is an indication of the goodness of the fit. b) The Williamson-Hall plots of representative samples where the intercept is proportional to the reciprocal of crystallite size, and the slope is the microstrain of the samples. c) and d) show the focused region between 12 degrees and 38 degrees with overlapped patterns of c) the Sr doping series and d) the Mg doping series to show no systematic shifts are detected, however it is clear that peak broadening occurs for the doped samples. The lattice parameters obtained from XRD refinements for e) Sr doping series and f) Mg doping series.

Spline fits of the values are shown as a guide for visual clarification. g) XRD patterns of stoichiometric $MAPbI_3$ and 10% PbI_2 excess $MAPbI_3$. h) Comparison between XRD patterns of samples fabricated by using SrI_2 replacing PbI_2 or MAI in the perovskite precursor solution.

Figure S4.6a shows an example of Le Bail refinement (more fitted patterns are shown in **Figure S4.23**). In our refinement, we included three phases, which are perovskite, lead iodide and ITO. The XRD patterns shows peaks at 24.5 and 30.5 degrees ascribed to the ITO substrate. Although a 0.5 degree incidence angle was used, the GIXRD probing depth is thicker than the perovskite film covering on the ITO substrates. It is noted that the ITO intensity can vary from sample to sample due to variation in the perovskite thickness, which has no effect on the refinement. Moreover, as we observed the presence of PbI_2 peak at 12.7 degrees, which is presumably formed due to the long measurement in air, it is also important to include PbI_2 in the refinement procedure.

The Le Bail method was chosen instead of the Rietveld refinement method due to the ease in the calculation without a requirement of knowing the exact atomic positions and the scattering power of the atoms; hence, it reduces the computation effort.[39] Here, we could use the full line profile analysis because our XRD patterns show all theoretical predicted peaks from the lattice structure of the material. The three phases (ITO, PbI_2, and perovskite) are treated individually in our refinement. Hence, there is no influence of ITO and PbI_2 phase on the derived perovskite microstrain and crystallite size. Using whole pattern refinement avoids wrongly assigned peaks to the perovskite phase when ITO and PbI_2 peaks are in close proximity to perovskite peaks. Therefore, the presented perovskite microstrain is only from the perovskite phase. Although HAXPES spectra show a presence of metallic Pb, XRD measurement shows no presence of Pb^0 as the most pronounced peak at 31.5 is overlapped with perovskite (114) and (213) planes and the peak at 36.5 degrees (**Figure S4.6c, d**) of Pb^0 were not observed. This might be due to the higher concentration of Pb^0 at the surface for which HAXPES is more sensitive than GIXRD. However, it is also possible that Pb^0 forms due to the experimental conditions of the HAXPES measurements (which is discussed in detailed in previous section).

The Le Bail method has been proven to be a powerful tool to give insights into the microstructure properties of the polycrystalline film.[39] The polycrystalline film contains nanoscale domain size in which stacking of layers, and the defects or imperfection lattice structure, *etc.*, yield anisotropic line broadening. We took into account the positions of the XRD peaks as well as the instrument geometry factors to calculate the integral breadths, which relate to the full half width maximum of the peak. This is an important consideration because the highest intensity is commonly found at 14 degree assigned for (110) plane of $MAPbI_3$ thin film, which can be severely affected by the geometry factor of the diffractometer. Different from a single crystal, in the polycrystalline film, the XRD peaks can be described by pseudo Voigt functions. The function is used to consider both Gaussian and Lorentzian contribution to the shape of the peaks in the pattern. Hence, we can assume that the angular dependence microstrain will affect to Gaussian peak broadening contribution (the case of Lorentzian contribution to microstrain is rare so it was excluded from the analysis), whereas the broadening due to crystallite size is from Lorentzian contribution.[59] The refinement is done by calculating the peak position and their corresponded hkl values obtained from material lattice parameters and their space group. Due to the presence of ITO and PbI_2 peaks, these two phases are included in the refinement to identify the correct peak positions. However, due to their low intensity, only peak positions are considered from this phase without refining their lattice parameters. Hence, the calculation of microstrain and crystallite size of these two phases are not performed. The refinement of the perovskite phase after considering the instrument error results in Gaussian and Lorentzian contribution to the integral breadth width. From this contribution, the microstrain is calculated. Note that the calculated microstrain of perovskite phase is not influenced by the presence of ITO and PbI_2 because it was refined as an independent phase.

We note that in the main text, the GIXRD derived microstrain correlated to the inclusion of dopants in the perovskite lattice has a peak at 0.2% Sr doping level (see ***Figure 3.3d***). However, the HAXPES derived VBM trend, which is influenced in this doping regime, has its maximum at 0.1% Sr-doped $MAPbI_3$. (see **Figure 4.4a**). This can be due to the difference in Sr concentrations in the probed volume, suggesting that also the incorporated Sr is more likely to reside near the surface of the film. Nonetheless, the clear trend of microstrain with respect to nominal doping concentration suggests distinctively two different regimes indicating the possibility of Sr^{2+} inclusion in the lattice up until a threshold, and then segregating out of the bulk into a secondary phase (in agreement with the HAXPES derived Sr surface gradient and Sr agglomeration shown in nXRF). Hence, the VBM trend correlating to two distinctive doping regimes is similar with the microstrain evolution (**Figure 4.4d, e**). This similarity seems to be stronger than the VBM - Pb^0 correlation as can be seen in **Figure 4.4c**, **d**, where all doped $MAPbI_3$ samples show a reduction of the Pb^0 content compared to the content in the undoped $MAPbI_3$ samples. In fact, the undoped sample in Sr doping series and Mg doping series have different Pb^0 content (0.012 and 0.007) but similar VBM values (0.94 ± 0.1 eV).

In addition, we used the integral breadths obtained from the Le Bail refinement result to generate Williamson-Hall plot (W-H) (**Figure S4.6b**). By linear fitting of W-H plot, we can obtain the crystallite size D and microstrain ε as follows.

$$\beta\cos(\theta) = (K\lambda/D)+4\varepsilon\sin(\theta)$$

where θ is the Bragg angle, K is a Scherrer constant dependent on the crystallite shape (which can be considered approximately 1)[70] and λ is Cu Kα wavelength

In agreement with Le Bail result and SEM images (as shown in **Figure S4.15** below), the W-H plot shows that the crystallite size decreases upon doping and that microstrain increases for 0.2% Sr and 1% Mg compared to the undoped $MAPbI_3$ sample. Hence, although the microstrain reduces for highly doped $MAPbI_3$ samples, peak broadening is still present because of smaller crystallite sizes. From the refinement result, we present here the lattice parameter of tetragonal $MAPbI_3$ in **Figure S4.6e, *f*** for Sr and Mg doping series as a function of nominal doping concentration.

Figure S3.6g shows the XRD patterns of undoped $MAPbI_3$ and 10% PbI_2 excess sample. It has been shown in the literature that PbI_2 can induce n-doping in $MAPbI_3$ but with more than 20% PbI_2 excess.[32, 71] Here, even with 10% PbI_2 excess sample has higher intensity of PbI_2 peak than the undoped $MAPbI_3$ sample in this study. Therefore, detected PbI_2 in the sample should not affect the n-type doping characteristic shown in HAXPES data.

In the study, the perovskite precursor is prepared by replacing an equal amounts of MAI with SrI_2 or MgI_2 instead of adding it on top of the stoichiometric solution MAI:PbI_2. **Figure S4.6h** shows that the XRD patterns using SrI_2 replacing PbI_2 or MAI are completely overlapped further indicating no significant change resulting from the method of preparation.

Optical characterization

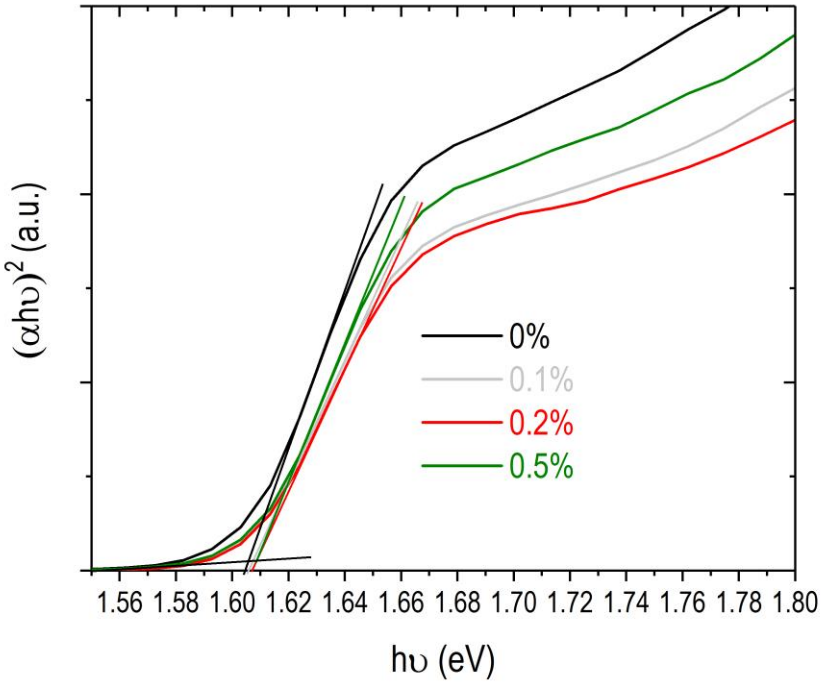

Figure S4.7 Tauc plot of undoped (black line) and different Sr-doping concentrations of $MAPbI_3$ thin films on glass substrates calculated from UV-vis absorption spectra.

DFT calculations

To gain further insight into the doping mechanism by incorporating Sr and Mg into the MAPbI$_3$ lattice, we carried out first-principles calculations on a 2x2x2 MAPbI$_3$ supercell. Previous analyses indicated that the potentially harmful defects are related to under-coordinated iodine centres, either in the form of I$_I^-$ or lead vacancy (V$_{Pb}^{2-}$).[25, 56] Schottky defects, specifically couple vacancies of Pb and I (denoted as V$_{PbI2}$) together with coupled vacancies of MA and I (indicated as V$_{MAI}$), are expected to be the most stable couple defects in the MAPbI$_3$ perovskite. Based on our DFT calculations at the Perdew-Burke-Ernzerhof (PBE) level, defect formation energies of 0.11 and 0.58 eV are calculated for V$_{PbI2}$ and V$_{MAI}$ respectively as can be seen in **Table S4.1**. These results are in qualitative agreement with previous work.

Table S4.1. Defects formation energies of intrinsic and extrinsic defects in MAPbI$_3$ calculated with PBE functional.

Defects	DFE (eV)
Intrinsic defects	
V$_{PbI2}$	0.11
V$_{MAI}$	0.58
V$_I^+$ + I$_i^-$	0.64 (ca. 0.3 for interacting defects)

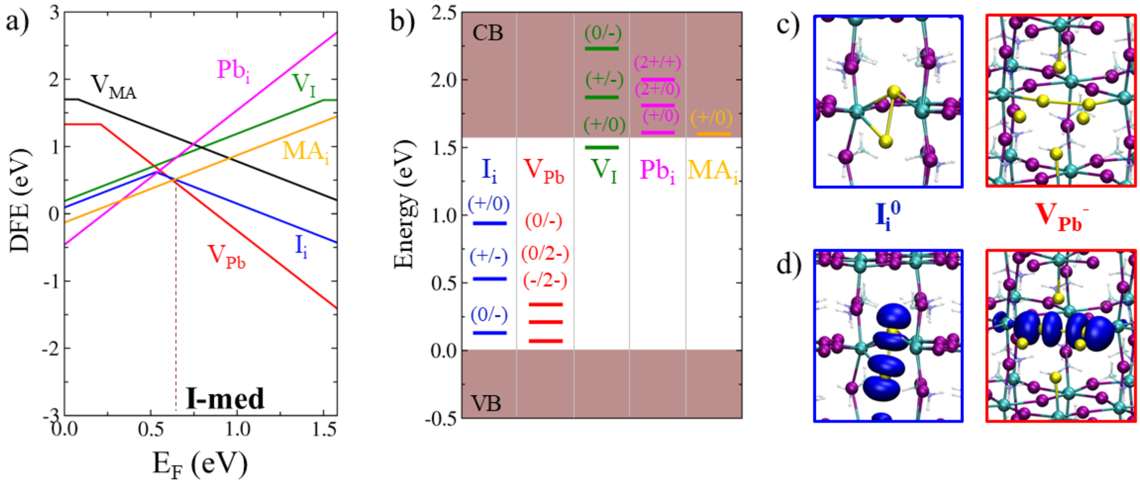

Figure S4.8 a) Defects formation energies diagram of native defects in MAPbI$_3$ calculated at the HSE06-SOC level (α=0.43) in the 2x2x2 supercell, van der Waals included. b) Associated thermodynamic ionisation levels diagram. c) Structures of the I$_i^0$ and V$_{Pb}^-$ defects forming I$_2^-$ dimer in the lattice upon trapping of holes on uncoordinated I ions. d) Plot of the electronic state associated to the trapped holes indicating the localization of holes on defects sites.

Notably, both I_I^- and V_{Pb}^{2-} are among the most stable defects in $MAPbI_3$ and introduce acceptor levels located 0.1-0.2 eV above the valence band shown in **Figure S4.8a, b**. Both I_i^- and V_{Pb}^{2-} can trap holes through the (0/-) and (-/2-) ionization levels with detrimental effects on the photoluminescence properties of $MAPbI_3$.[25] Upon trapping of holes both defects give rise to a metastable state corresponding to coordinated I_2^- species characterized by a I-I bond lengths of 3.2-3.3 Å for interstitials and vacancies, respectively (see **Figure S4.8b, c**). Plots of Kohn-Sham orbitals associated to the trapped holes highlight its localization on defects sites, **Figure S4.8d**.

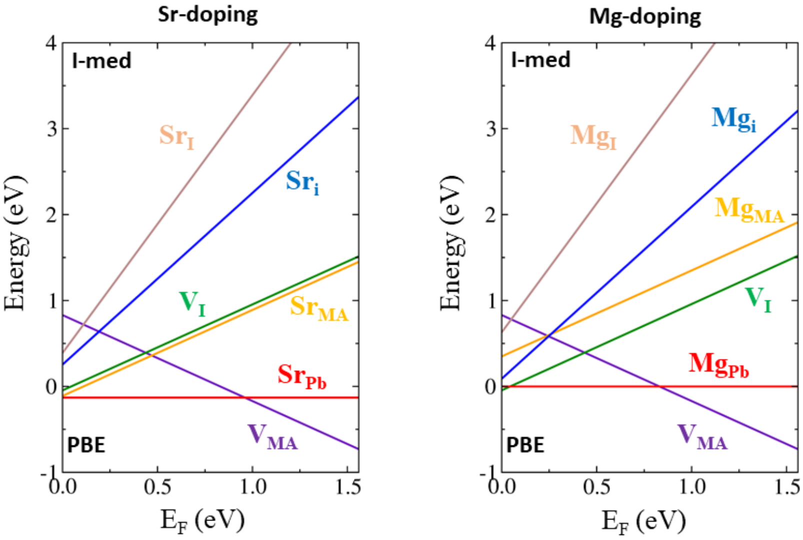

Figure S4.9 Defects formation energies of Sr and Mg doping calculated at the PBE level in I-medium growth conditions.

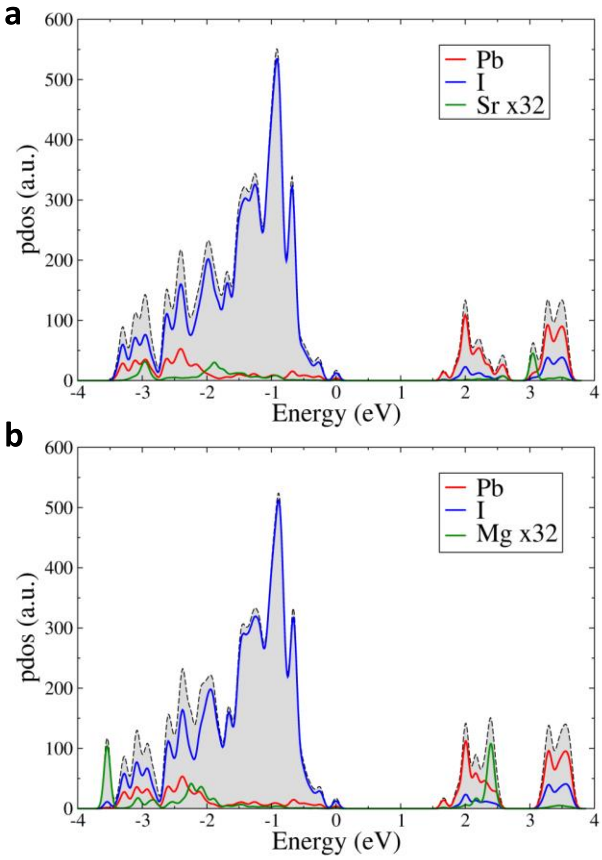

Figure S4.10 Projected density of states (pdos) at the PBE level of the substitutional a) Sr_{Pb} and b) Mg_{Pb} system. The density of states of Sr and Mg has been enhanced (x32) in order to be comparable with Pb density of states.

Table S4.2. Calculated energies of passivation reactions upon doping (PBE).

	Defect Reaction	E (eV)
R1	$V_{PbI2} + SrI_2 = Sr_{Pb} + nil\ (2I_I)$ $V_{PbI2} + MgI_2 = Mg_{Pb} + nil\ (2I_I)$	-0.24 -0.11
R2	$V_{MAI} + SrI_2 = Sr_{MA}^+ + I_i^- + nil\ (I_I)$ $V_{MAI} + MgI_2 = Mg_{MA}^+ + I_i^- + nil\ (I_I)$	0.46 0.92
R3	$2\ V_{MAI} + SrI_2 = V_{MA}^- + Sr_{MA}^+ + nil\ (2I_I)$ $2\ V_{MAI} + MgI_2 = V_{MA}^- + Mg_{MA}^+ + nil\ (2I_I)$	-0.44 0.02
R4	$2\ V_{MAI} + SrI_2 = 2V_{MA}^- + Sr_i^{2+} + nil\ (2I_I)$ $2\ V_{MAI} + MgI_2 = 2V_{MA}^- + Mg_i^{2+} + nil\ (2I_I)$	0.75 0.59
R5	$2\ V_{MAI} + SrI_2 = 2V_{MA}^- + Sr_i^{2+} + nil\ (I_I) + V_I^+ + I_i^-$ $2\ V_{MAI} + MgI_2 = 2V_{MA}^- + Mg_i^{2+} + nil\ (I_I) + V_I^+ + I_i^-$	1.86 1.69
R6	$2\ V_{MAI} + SrI_2 = V_{MA}^- + Sr_{MA}^+ + nil\ (I_I) + V_I^+ + I_i^-$ $2\ V_{MAI} + MgI_2 = V_{MA}^- + Mg_{MA}^+ + nil\ (I_I) + V_I^+ + I_i^-$	0.67 1.12

Figure S4.9 shows the defect formation energies (DFE) of different Sr and Mg incorporation scenarios in iodide medium growth condition. **Table S4.2** shows the corresponding full interaction of Sr^{2+} or Mg^{2+} to the existing intrinsic defects in the system calculated at the PBE level in the diluted limit. Reaction R1 models the saturation of V_{PbI2} in the perovskite in which Sr $^{2+}$or Mg^{2+} fills V_{Pb}^{2-}. Such a process is favored by 0.24 and 0.11 eV for Sr^{2+} and Mg^{2+}, respectively, and it is driven by the high affinity of alkaline metals for iodide within the lattice. The Pb substitution by Sr and Mg does not affect the electronic structure of $MAPbI_3$ at the band edges, as shown by the atoms projected density of states (pdos) reported in **Figure S4.10** in agreement with literature.[72] Based on this result, the inclusion of alkaline earth metal ions can lead to the ordering of both Pb and I sublattices, with beneficial effects in reducing traps states. Sr^{2+} or Mg^{2+} substitution in Pb^{2+} sites is in agreement with experiments reported in **Figure 4.4c, d**, where a lower content of metallic lead Pb^0, *i.e.* the product of V_{Pb}^{2-} formation process, is found in doped $MAPbI_3$ samples. The stabilization of the metal lattice induced by Sr and Mg-doping thus reduces the number of V_{Pb}^{2-} trap states in $MAPbI_3$.

Besides filling V_{Pb}^{2-}, the lattice incorporation mechanism is likely to have more possible routes. This is because the amount of dopants is much higher than V_{Pb}^{2-} even at as low as 0.05% Sr (accounting for $2x10^{18}$ cm^{-3} compared to 10^{10} cm^{-3} V_{Pb}^{2-}).[25] Furthermore, despite having a suitable tolerance factor for Pb^{2+} substitution, a 50% mix of Sr^{2+} does not result in a black film as observed by others and us.[15] This implies that even though tolerance factor is an important consideration, yet it is not the only determining factor. The small ionic radii of Mg^{2+} leads to unfavorable tolerance factor to form a 3D MA-based halide perovskite, yet, in this study, we show that it is possible for Mg^{2+} to incorporate into the perovskite lattice than Sr^{2+}. Thus, it is likely to have more than one incorporation routes. Reactions R2 and R3 (in **Table S4.2**) indicate that Sr^{2+} and Mg^{2+} can also be incorporated in the cation substitution as Sr_{MA}^{+} and Mg_{MA}^{+}. Small incorporation of Sr in $MAPbI_3$ reducing the intrinsic defects concentration of possibly both V_{Pb}^{2-} and V_{MA}^{-} is consistent with the more n-type material seen in low doping concentration. This is because negatively charged V_{Pb}^{2-} and V_{MA}^{-} can result in p-type material.[31] In addition, the increasing microstrain can be an indication of an interstitial doping mechanism. Notably, the formation energy of Mg_i^{2+} is in the same order of magnitude of intrinsic defects formation energy (0.59 eV versus 0.58 eV of formation energy V_{MAI} shown in **Table S4.1**). Thus, there is a high possibility for Mg to stay at the interstitial position in the $MAPbI_3$ structure shown in R4. Therefore, incorporation of Sr and Mg into perovskite lattice can be via substitution of Pb^{2+} and MA^{+} together with interstitial. In all cases, the V_I^{+} can be passivated resulted in nil(I_I), contributing to defect reduction in our doped material.

Figure S4.4 shows an increase in intensity in the spectral feature at 3.9 eV in the measured valence band spectra of the Sr doping sample series compared to undoped sample. In **Figure S4.11**, the projected density of states of $MAPbI_3$ (PBE) is reported without and with one V_{Pb}^{2-}. As can be seen in **Figure S4.11**, electronic states at 3.9 eV are associated to Pb orbitals, whose contribution to the pdos is lower in the case of a vacant system. Thus, the observed increase in intensity in the HAXPES spectral feature might be due to a reduction of density of V_{Pb}^{2-} in the Sr-doped sample. We note that the strong differences between the shape of the HAXPES and the pdos calculations are due to several factors, including the influence of photoionization cross sections, different broadening, and experimental background associated with scattered photoelectrons. However, all of the features in the pdos have analogous features in the measured valence band spectrum.

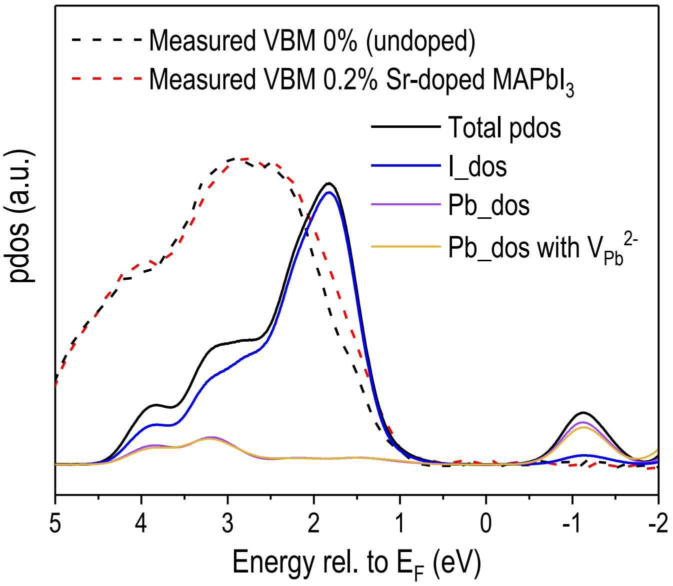

Figure S4.11 Calculated pdos in solid lines and measured VBM in dash line. The system's Pb_dos without V_{Pb}^{2-} is depicted in light purple and with V_{Pb}^{2-} is depicted in orange.

In order to investigate the effects of doping on the thermodynamics of V_{Pb}^{2-}, the DFE of V_{Pb}^{2-} was calculated in the pristine, Sr- and Mg-doped $MAPbI_3$ for different doping contents. Specifically, after including one and two Sr, Mg atoms into the lattice, a V_{Pb}^{2-} has been introduced in the 2x2x2 supercell and the associated DFE recalculated. Results are reported in **Table S4.3**. The doping induces a remarkable stabilization of the metal sub-lattice by increasing the DFE of V_{Pb}^{2-} up to 0.24 and 0.36 eV for Sr and Mg doping, respectively, for 6% doping.

Table S4.3 Defect formation energy variations (ΔDFE) of lead vacancy (V_{Pb}^{2}) defect in different doped systems. In the doped systems Pb has been substituted by one and two Sr, Mg ions, leading to doping of 3 and 6%. The DFE calculated for pristine $MAPbI_3$ has been set to zero.

System	Δ DFE (eV)
V_{Pb}^{2-} , pristine $MAPbI_3$	0.00
V_{Pb}^{2-}, Sr doped $MAPbI_3$ (3%)	0.18
V_{Pb}^{2-}, Sr doped $MAPbI_3$ (6%)	0.24
V_{Pb}^{2-}, Mg doped $MAPbI_3$ (3%)	0.22
V_{Pb}^{2-}, Mg doped $MAPbI_3$ (6%)	0.36

Substitutional Sr and Mg doping thus leads to a sizable decrease of the density of V_{Pb}^{2-} in $MAPbI_3$. The stabilization of Pb in the lattice is corroborated by the reduction in Pb^0 (a product of V_{Pb}^{2-} formation) seen in HAXPES.

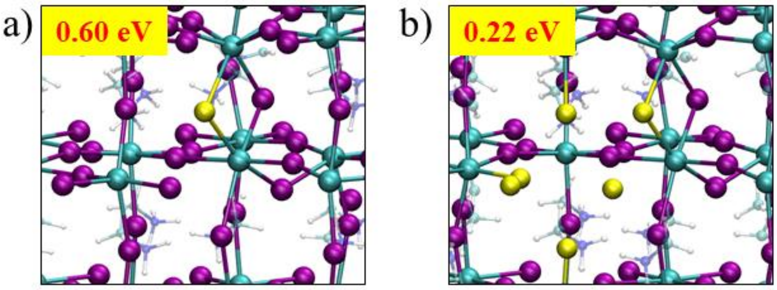

Figure S4.12. Structures and energies of formation of Frenkel couples a) in pristine $MAPbI_3$ and within a V_{Pb}^{2-} center.

In addition, the presence of under-coordinated iodine atoms within the V_{Pb}^{2-} site has a profound effect on the formation of iodine Frenkel defects,[73] *i.e.* the concomitant formation of an iodine vacancy/interstitial pair, whose defect formation energies is reduced from 0.6 to 0.2 eV in the pristine and lead-vacant $MAPbI_3$ bulk (see **Figure S4.12**). The main effect here is likely the weakening of the iodine lattice energy due to the absence of a neighboring Pb, which decreases the formation energy of the iodine vacancy, favoring the formation of the Frenkel pair. Therefore, the initial V_{Pb}^{2-} concentration declines by doping, thus moving the system closer to the pristine case, the Frenkel defects are less likely to form.

Solar cells device parameters

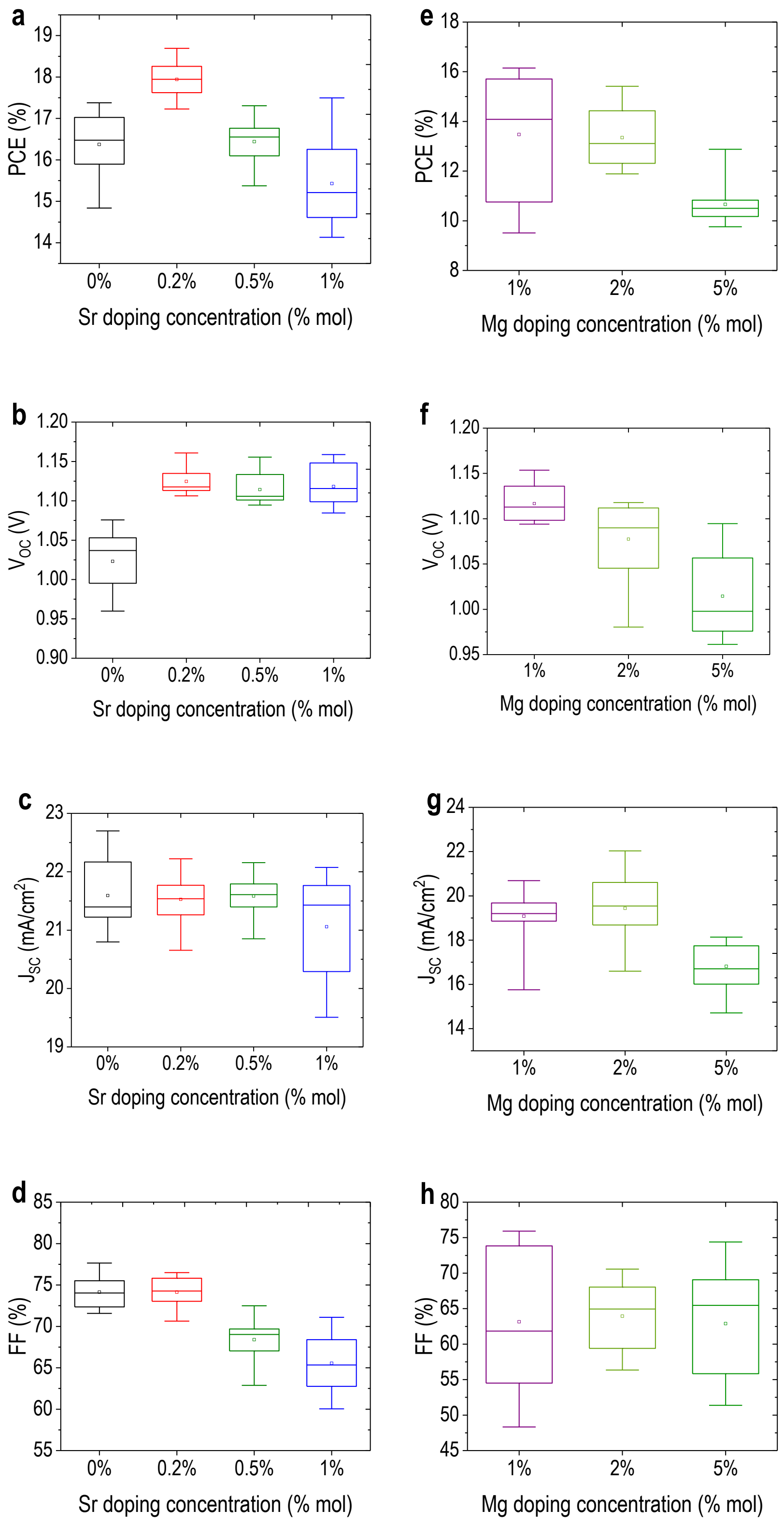

Figure S4.13 Power conversion efficiencies (PCE), open circuit voltage (V_{OC}), short circuit current density (J_{SC}), fill factor (FF) of a, b, c, d) Sr doping series and e, f, g, h) Mg doping series obtained from reverse scans of 15 devices for each condition from various batches. Device's active area is 0.16 cm^2. Scan rate is 100 mV/s.

To elucidate this effect of changing the defect concentration, we measure absolute photoluminescence (PL) in $MAPbI_3$ films with and without the dopants. There is a clear increase of quantum yield in **Figure S4.14a** of doped perovskite compared to undoped material. Taking into account that three following factors:

i) the theoretical calculations suggest that the incorporation of the dopants into the perovskite structure is plausible,

ii) the observed increase of microstrain with the incorporation of the dopants in the low doping concentration regime,

iii) the observed uniform lateral distribution of the Sr signal in the nXRF maps.

We can speculate that the increase of the PL quantum yield (PLQY) upon doping arises from a reduction of detrimental defects in the bulk. Moreover, the lower Pb^0 concentration on the film as shown in **Figure 4.4c** and in **Figure 4.4d** is likely to correlate with less harmful defect formation.[74-75] In particular, it has been shown that the lower Pb^0 presence in the film, the higher quantum yield.[52, 76]

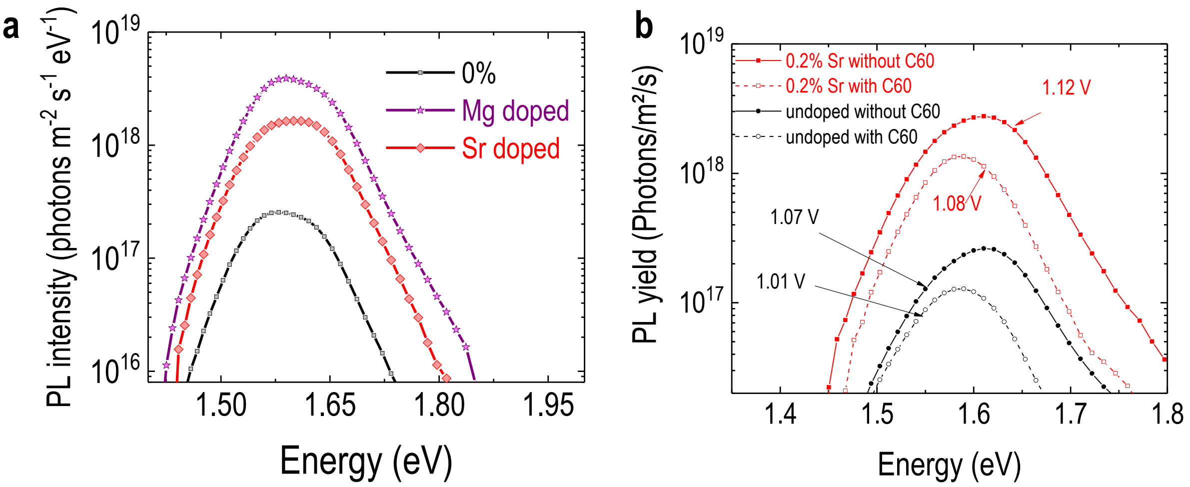

Figure S14 a) Steady-state photoluminescence (PL) spectra for Mg and Sr doped $MAPbI_3$ films on the glass substrates. b) Steady-state photoluminescence of perovskite layer with or without C_{60} on glass/ITO/PTAA/ substrate for quasi-Fermi level splitting calculation

We computed the quasi-Fermi level splitting (QFLS) by the high-energy tail fit method of the absolute PL for these optimal doping concentrations (0.2% Sr and 1% Mg) from the measurements shown in **Figure S4.14b**. This method for quantifying the absorber quality was used for Si solar cells[62, 77] in the past and recently also for halide perovskites.[60, 78] Here, we utilize this method to confirm further that the doping reduces the bulk, rather than interfacial, defects. In HAXPES and nXRF measurement, we find indications for the segregation of Sr^{2+} at *high* Sr doping concentrations, with the Sr-rich phase most likely residing on the very surface of the perovskite. For low doping concentrations, however, we suggest that Sr^{2+} is incorporated into $MAPbI_3$ lattice reducing bulk harmful defects without significant surface segregation. To further underline this, we compare the QFLS difference between a perovskite film with and without a C_{60} overlayer, for doped and undoped $MAPbI_3$ films. C_{60}, being the electron-selective layer, has been identified to dominate non-radiative recombination in efficient p-i-n PSCs, as evidenced by *e.g.* Stolterfoht *et al.*[60] Thus, its interface governs the device's V_{OC}. The difference of QFLS of undoped $MAPbI_3$ in this study with and without C_{60} is around 0.06 eV, which is slightly higher compared to the 0.04 eV observed for the case in 0.2% Sr-doped $MAPbI_3$ (which is calculated from **Figure S4.14b**). This result is reproducible for different batches of samples. Thus, at this (low) doping concentration, trap states reduction in the bulk of the material is the main factor of performance improvement rather than an interfacial passivation. As a result, we believe that the voltage enhancement in the solar cells is due to a higher-quality perovskite upon doping.

We noted that the quasi Fermi level splitting of these cell areas are lower than the measured V_{OC} due to degradation of $MAPbI_3$ in air and under 450 nm light exposure. This gradual degradation after short wavelength exposure has been well documented in the literature,[79] which is also observed by us. This degradation can lead to reduction in QFLS from 15-30 mV over 5 minutes, a period as long as our absolute PL measurement duration. This explains why the reported value here is lower than our average V_{OC} reported in **Figure S4.13**. However, the relative trend might suggest that the bulk quality improves upon doping.

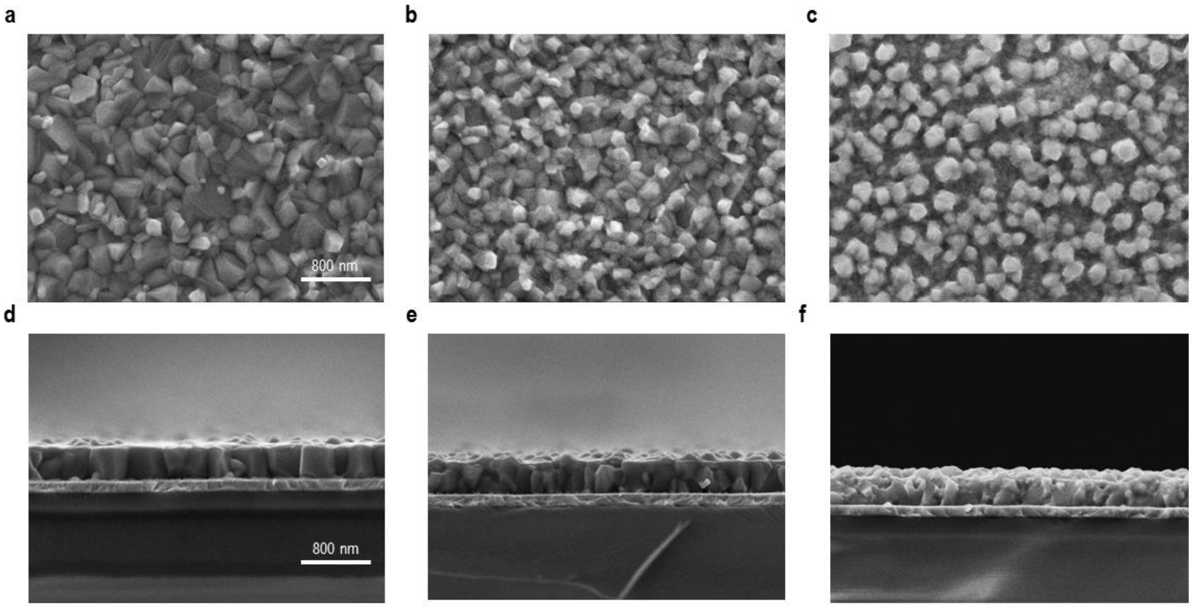

Figure S4.15 Scanning electron microscopy of top view of a) 0%, b) 0.2% Sr, c) 1% Mg doped films and of corresponding cross section of a) 0%, b) 0.2% Sr, c) 1% Mg doped films

Figure S4.13 shows that the undoped devices have an average efficiency at 16.3±0.7%. In comparison, the 0.2% Sr doped perovskite demonstrates superior performance at 17.9±0.4% on average compared to the undoped devices with smaller distribution. The 1% Mg doped devices, despite having excellent V_{OC} (on average 1117±18 mV) comparable to 0.2% Sr devices (on average 1125±16 mV), suffer from low fill factor (FF) and short circuit current (J_{SC}) resulting in an average efficiency of 13.5±2.2%. To understand the underlying cause for this, we studied the morphology of $MAPbI_3$ upon doping. In particular, by incorporating the dopants, the film has smaller grain sizes for both Sr and Mg (**Figure S4.15**), which is in agreement with what observed by Pérez-del-Rey et al.[20] Our previous study on the impact of grain sizes on the device performance showed that the V_{OC} is independent on the grain size of the film when the grain is larger than 100 nm.[80] Yet, other PV parameters are affected by the morphology of the perovskite films. As shown in **Figure S4.15f**, the cross-sectional SEM image of Mg doped $MAPbI_3$ shows that the film consists of several layers of grains, instead of monolithic grains from bottom to top as can be seen for the undoped sample (**Figure S4.15d**). Thus, lower efficiencies in Mg doped devices despite of a better material quality and high V_{OC} are likely due to the presence of grain boundaries that inhibit the charge collection at the contact layers. Further Mg-doping (>1%) worsens the morphology as the crystallite size becomes smaller than 100 nm, eventually reduced V_{OC}. Another explanation is that when segregation dominates the doping process, negative effects on the interface between perovskite and selective layer may arise.

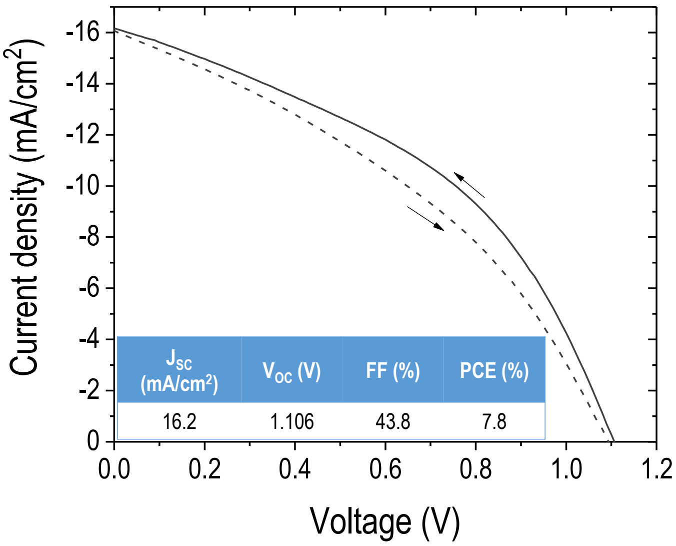

J_{SC} (mA/cm^2)	V_{OC} (V)	FF (%)	PCE (%)
16.2	1.106	43.8	7.8

Figure S4.16 Current density-voltage (J-V) curve of the 2% Sr and 1% Mg co-doped devices. Tabulated values are taken from reverse scan.

Figure S4.16 shows the device performance of a co-doped device (2% Sr and 1% Mg). From the microstrain trends shown in **Figure 4.5a, b**, we are motivated to test the combination between lowest strain condition (at 2% Sr where the segregation dominates the process, hence the lattice relaxes) and the highest strain condition (at 1% Mg). This is to test if the device can benefit from both: surface passivation, which comes from Sr doping, and bulk passivation from Mg doping. However, the device suffers from low J_{SC} and FF similar to what has been observed in Mg doped devices.

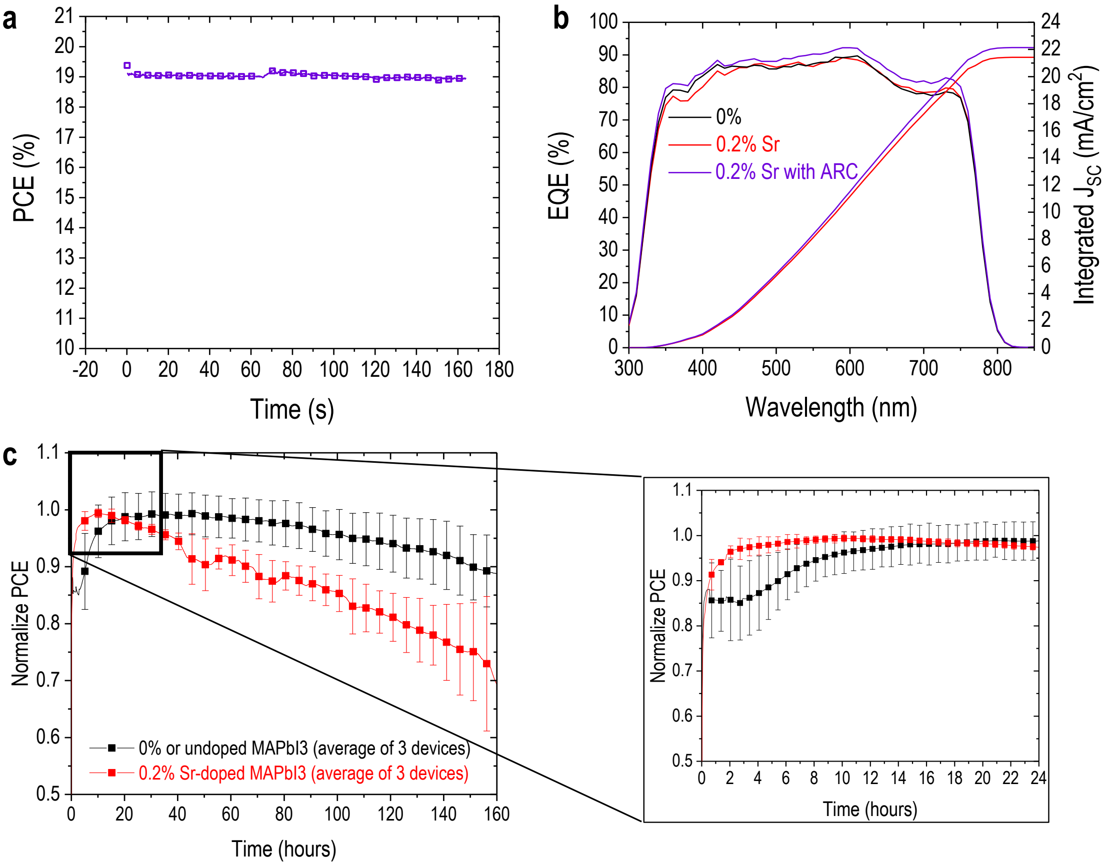

Figure S4.17 a) Continuous maximum point tracking in global AM1.5 equivalent sun simulator for 150 seconds resulting in stabilised efficiency of 19%. b) External quantum efficiency (EQE) of 0% undoped and champion device with 0.2% Sr doping before and after antireflection coating which are in agreement with the J_{SC} from J-V scan. c) Continuous maximum power point tracking in N_2 at 25°C, in simulated global AM1.5 solar spectrum with UV cut-off at 380 nm for 160 hours. A magnified view of the first 24 hour region is also shown. The data is presented as an average of the performance of three devices; the error bar stands for the standard deviation of the performance of the devices.

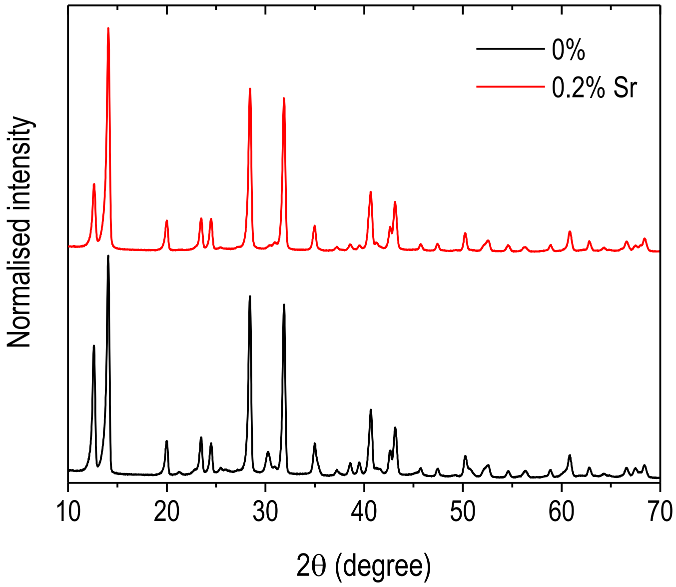

Figure S4.18 Comparison between XRD patterns of 0% and 0.2% Sr doped $MAPbI_3$ without a protective layer after being exposed to ambient atmosphere for 48 hours.

As for the stability of our devices, we tested the continuous maximum power point tracking for 160 hours. We found that Sr doping does not improve the long-term stability (above 100 hours) of the devices. However, Sr doping improves the short-term stability response (below 10 hours). Indeed, a faster transient of Sr-doped device is observed, which might be attributed to faster ion migration or less mobile ionic defects in the first 24 hours. At a longer time scale, the device power output response is the result of a convolution of different degradation mechanisms, which can include the interfaces, the contact materials and the electrodes. We acknowledge that the strained material can promote thin-film degradation, as reported by Zhao *et al.*[81] Hence, we tested the stability of bare perovskite films in ambient conditions. The doped $MAPbI_3$, in fact, shows higher stability compared to undoped $MAPbI_3$. After 48 hours, the detected amount of PbI_2 is lower in doped material as can be seen in **Figure S4.18**. Therefore, the device stack stability poses a complicated picture and thus, the investigation of the long-term degradation mechanisms is out of the scope of the work.

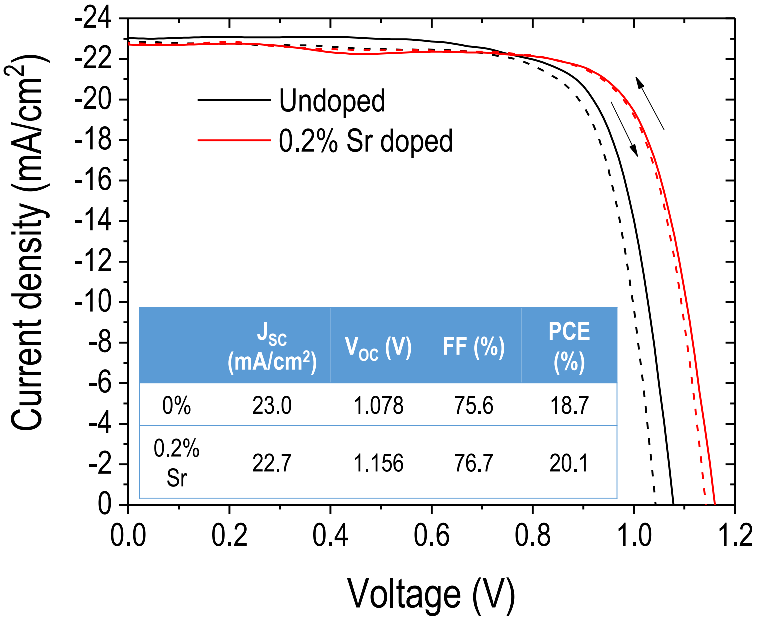

	J_{SC} (mA/cm^2)	V_{OC} (V)	FF (%)	PCE (%)
0%	23.0	1.078	75.6	18.7
0.2% Sr	22.7	1.156	76.7	20.1

Figure S4.19 Current density-voltage (J-V) curve of the 0% (undoped) and 0.2% Sr doped FTO/compact TiO_2/$MAPbI_3$/Spiro-OMETAD/Au devices. Tabulated values are taken from reverse scan.

We note here that even though at the low doping concentration, the $MAPbI_3$ films which become more n-type at our low concentration, nonetheless, achieve high efficiency in both p-i-n and n-i-p structures. Hence, the modification in band alignment with different contact layers might be insufficient to affect device performances, similar to previous reports.[82-83]

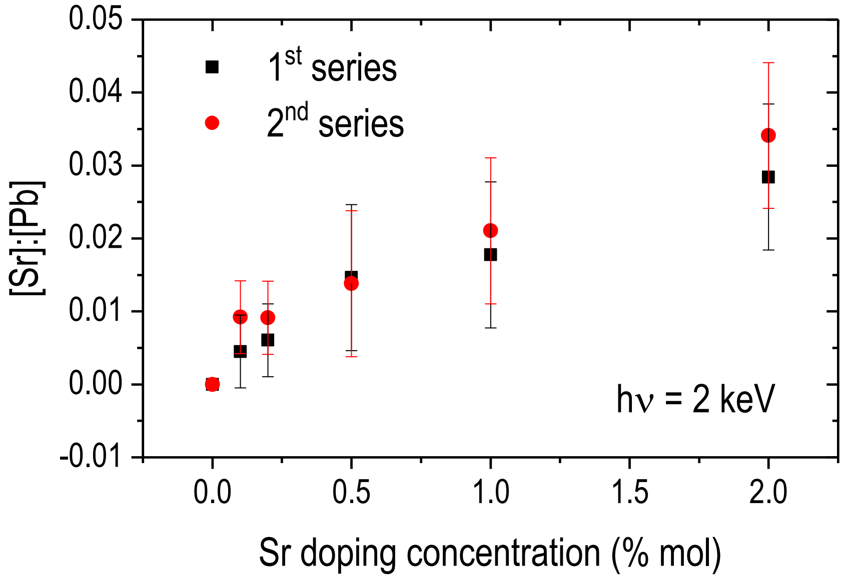

Figure S4.20 [Sr]:[Pb] ratios of 2 different Sr doping sample series determined from the 2 keV HAXPES measurements of the Sr $3p_{3/2}$ and Pb $4f_{7/2}$ core levels.

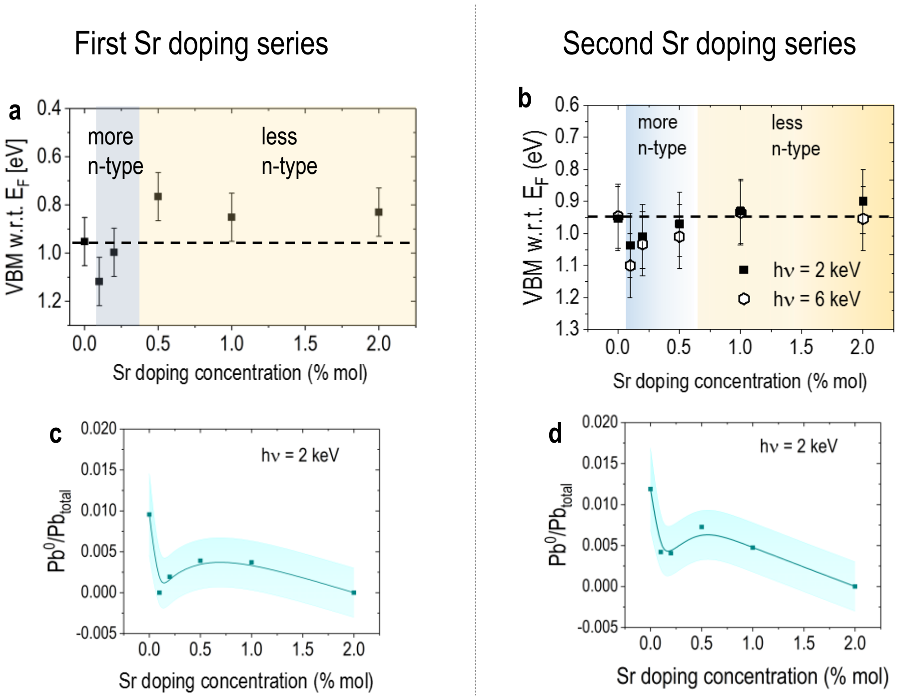

Figure S4.21 a) and b) Position of the valence band maximum (VBM) with respect to the Fermi level (E_F) of two different Sr doping sample series determined from the 2 keV HAXPES measurements. c) and d) The fraction of metallic lead (Pb^0) compared to the total amount of Pb at the surface of two Sr doping sample series, as determined by 2 keV HAXPES measurements.

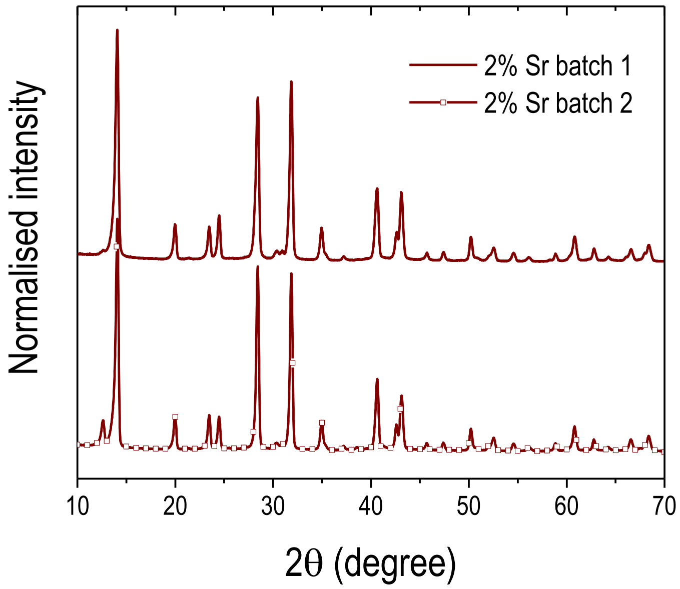

Figure S4.22 The XRD patterns of two different 2% Sr-doped $MAPbI_3$ samples fabricated in different batches and measurement.

We acknowledge the possibility of batch variation mentioned by Fassl *et al.*,[84] hence, we carefully repeated the measurements to increase the certainty of our result. The XRD refinement was done for each condition from 2-4 samples belonging to different batches. **Figure 4.3d-e** show the mean value from those refinements. The HAXPES measurements conducted on two different Sr-doped $MAPbI_3$ sample sets shown in **Figure S4.20** and **Figure S4.21** yield similar conclusion. We also noted that due to batch to batch variation and the XRD measurements in air, the detected PbI_2 might be different samples to samples which is shown in **Figure S4.22**. However, the Le Bail refinement considered PbI_2 phase (if presence), hence this variation has no effect on the obtained microstrain of perovskite phase. In addition, device performance from various batches is reported in **Figure S4.13**.

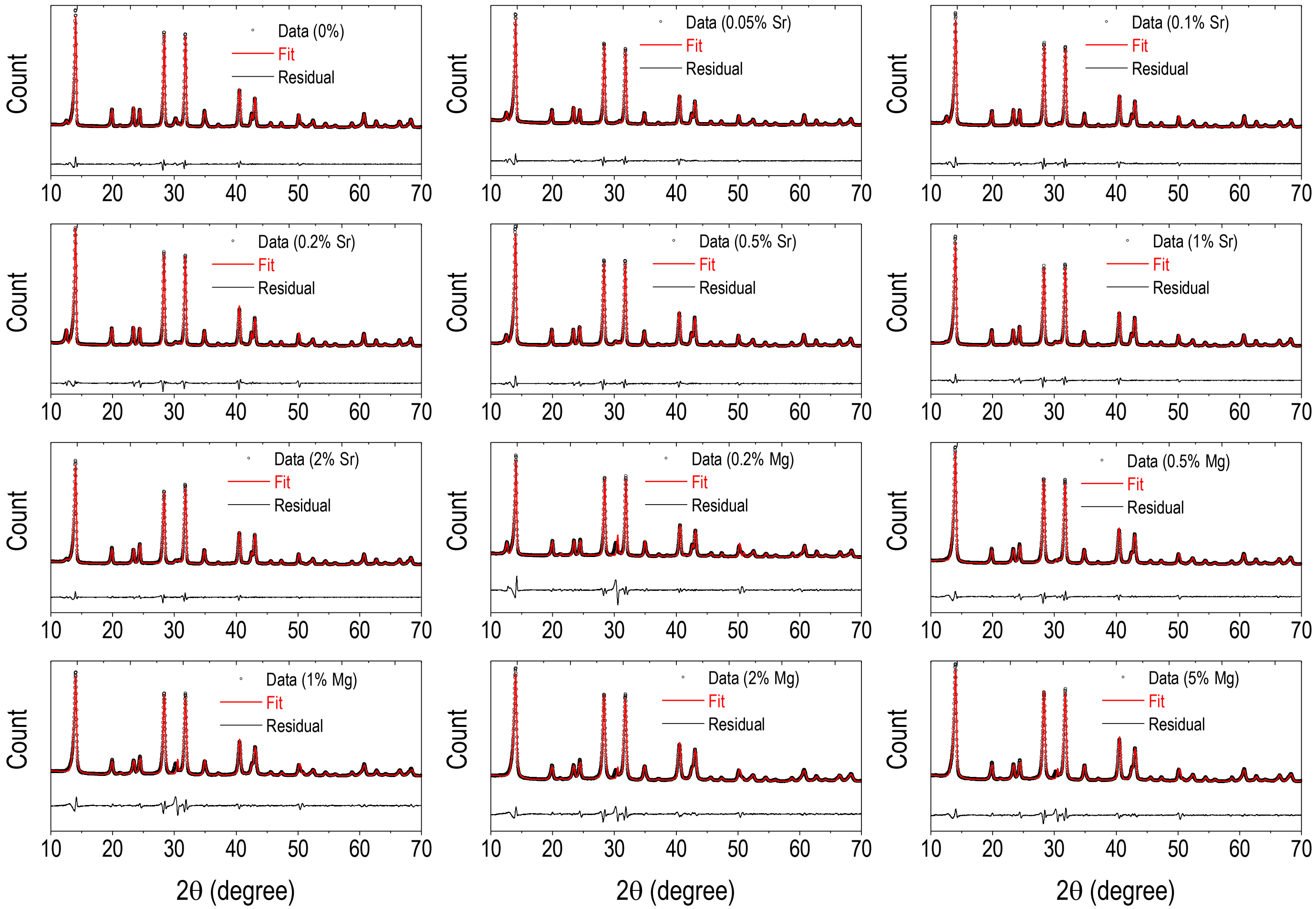

Figure S4.23 Representative measured data set (circle) of $MAPbI_3$ and Sr and Mg-doped material; together with calculated fit (red line) from Le Bail refinement which then be used to calculate the microstrain. The residuum are shown in black line. The conditions of the pattern are shown in legend.

Reference

1. NREL PV Efficiency Chart. https://www.nrel.gov/pv/assets/pdfs/pv-efficiency-chart.20181221.pdf (accessed 02/10/2019).

2. Klug, M. T.; Osherov, A.; Haghighirad, A. A.; Stranks, S. D.; Brown, P. R.; Bai, S.; Wang, J. T.-W.; Dang, X.; Bulović, V.; Snaith, H. J.; Belcher, A. M., Tailoring metal halide perovskites through metal substitution: influence on photovoltaic and material properties. *Energy & Environmental Science* **2017,** *10* (1), 236-246.

3. Saidaminov, M. I.; Kim, J.; Jain, A.; Quintero-Bermudez, R.; Tan, H.; Long, G.; Tan, F.; Johnston, A.; Zhao, Y.; Voznyy, O., Suppression of atomic vacancies via incorporation of isovalent small ions to increase the stability of halide perovskite solar cells in ambient air. *Nature Energy* **2018,** *3* (8), 648.

4. Zheng, X.; Troughton, J.; Gasparini, N.; Lin, Y.; Wei, M.; Hou, Y.; Liu, J.; Song, K.; Chen, Z.; Yang, C.; Turedi, B.; Alsalloum, A. Y.; Pan, J.; Chen, J.; Zhumekenov, A. A.; Anthopoulos, T. D.; Han, Y.; Baran, D.; Mohammed, O. F.; Sargent, E. H.; Bakr, O. M., Quantum Dots Supply Bulk- and Surface-Passivation Agents for Efficient and Stable Perovskite Solar Cells. *Joule* **2019**.

5. Begum, R.; Parida, M. R.; Abdelhady, A. L.; Murali, B.; Alyami, N. M.; Ahmed, G. H.; Hedhili, M. N.; Bakr, O. M.; Mohammed, O. F., Engineering interfacial charge transfer in CsPbBr3 perovskite nanocrystals by heterovalent doping. *Journal of the American Chemical Society* **2016,** *139* (2), 731-737.

6. Saliba, M.; Matsui, T.; Domanski, K.; Seo, J.-Y.; Ummadisingu, A.; Zakeeruddin, S. M.; Correa-Baena, J.-P.; Tress, W. R.; Abate, A.; Hagfeldt, A.; Grätzel, M., Incorporation of rubidium cations into perovskite solar cells improves photovoltaic performance. *Science* **2016,** *354* (6309), 206-209.

7. Kubicki, D. J.; Prochowicz, D.; Hofstetter, A.; Zakeeruddin, S. M.; Grätzel, M.; Emsley, L., Phase Segregation in Cs-, Rb-and K-Doped Mixed-Cation (MA)x(FA)1–xPbI_3 Hybrid Perovskites from Solid-State NMR. *Journal of the American Chemical Society* **2017,** *139* (40), 14173-14180.

8. Zhou, Y.; Chen, J.; Bakr, O. M.; Sun, H.-T., Metal-doped lead halide perovskites: synthesis, properties, and optoelectronic applications. *Chemistry of Materials* **2018,** *30* (19), 6589-6613.

9. Navas, J.; Sánchez-Coronilla, A.; Gallardo, J. J.; Hernández, N. C.; Piñero, J. C.; Alcántara, R.; Fernández-Lorenzo, C.; Desireé, M.; Aguilar, T.; Martín-Calleja, J., New insights into organic–inorganic hybrid perovskite $CH_3NH_3PbI_3$ nanoparticles. An experimental and theoretical study of doping in Pb^{2+} sites with Sn^{2+}, Sr^{2+}, Cd^{2+} and Ca^{2+}. *Nanoscale* **2015,** *7* (14), 6216-6229.

10. Jacobsson, T. J.; Pazoki, M.; Hagfeldt, A.; Edvinsson, T., Goldschmidt's rules and strontium replacement in lead halogen perovskite solar cells: theory and preliminary experiments on $CH_3NH_3SrI_3$. *The Journal of Physical Chemistry C* **2015,** *119* (46), 25673-25683.

11. Pazoki, M.; Jacobsson, T. J.; Hagfeldt, A.; Boschloo, G.; Edvinsson, T., Effect of metal cation replacement on the electronic structure of metalorganic halide perovskites: Replacement of lead with alkaline-earth metals. *Physical Review B* **2016,** *93* (14), 144105.

12. Yang, F.; Kamarudin, M. A.; Kapil, G.; Hirotani, D.; Zhang, P.; Ng, C. H.; Ma, T.; Hayase, S., Magnesium-Doped $MAPbI_3$ Perovskite Layers for Enhanced Photovoltaic Performance in Humid Air Atmosphere. *ACS applied materials & interfaces* **2018,** *10* (29), 24543-24548.

13. Huang, Q.; Zou, Y.; Bourelle, S.; Zhai, T.; Wu, T.; Tan, Y.; Li, Y.; Li, J.; Duhm, S.; Song, T.; Wang, L.; Deschler, F.; Sun, B., Suppressing Defect State in CsPbBr3 Perovskite via Magnesium Substitution for Efficient All-Inorganic Light-Emitting Diodes. *Nanoscale Horizons* **2019,** *4*, 924-932.

14. Wang, K.; Liang, Z.; Wang, X.; Cui, X., Lead replacement in $CH_3NH_3PbI_3$ perovskites. *Advanced Electronic Materials* **2015,** *1* (10), 1500089.

15. Shai, X.; Zuo, L.; Sun, P.; Liao, P.; Huang, W.; Yao, E.-P.; Li, H.; Liu, S.; Shen, Y.; Yang, Y.; Wang, M., Efficient planar perovskite solar cells using halide Sr-substituted Pb perovskite. *Nano Energy* **2017,** *36*, 213-222.

16. Shannon, R. D., Revised effective ionic radii and systematic studies of interatomic distances in halides and chalcogenides. *Acta crystallographica section A: crystal physics, diffraction, theoretical and general crystallography* **1976,** *32* (5), 751-767.

17. Goldschmidt, V. M., Die gesetze der krystallochemie. *Naturwissenschaften* **1926,** *14* (21), 477-485.

18. Li, Z.; Yang, M.; Park, J.-S.; Wei, S.-H.; Berry, J. J.; Zhu, K., Stabilizing perovskite structures by tuning tolerance factor: formation of formamidinium and cesium lead iodide solid-state alloys. *Chemistry of Materials* **2015,** *28* (1), 284-292.

19. Kieslich, G.; Sun, S.; Cheetham, A. K., An extended tolerance factor approach for organic–inorganic perovskites. *Chemical science* **2015,** *6* (6), 3430-3433.

20. Pérez-del-Rey, D.; Forgács, D.; Hutter, E. M.; Savenije, T. J.; Nordlund, D.; Schulz, P.; Berry, J. J.; Sessolo, M.; Bolink, H. J., Strontium Insertion in Methylammonium Lead Iodide: Long Charge Carrier Lifetime and High Fill-Factor Solar Cells. *Advanced Materials* **2016,** *28* (44), 9839-9845.

21. Lau, C. F. J.; Zhang, M.; Deng, X.; Zheng, J.; Bing, J.; Ma, Q.; Kim, J.; Hu, L.; Green, M. A.; Huang, S.; Ho-Baillie, A., Strontium-doped low-temperature-processed $CsPbI_2Br$ perovskite solar cells. *ACS Energy Letters* **2017,** *2* (10), 2319-2325.

22. Caprioglio, P.; Zu, F.; Wolff, C. M. M.; Prieto, J. A. M.; Stolterfoht, M.; Becker, P.; Koch, N.; Unold, T.; Rech, B.; Albrecht, S.; Neher, D., High open circuit voltages in pin-type perovskite solar cells through strontium addition. *Sustainable Energy & Fuels* **2019,** *3*, 550-563.

23. Walsh, A.; Scanlon, D. O.; Chen, S.; Gong, X.; Wei, S. H., Self-regulation mechanism for charged point defects in hybrid halide perovskites. *Angewandte Chemie International Edition* **2015,** *54* (6), 1791-1794.

24. Ming, W.; Chen, S.; Du, M.-H., Chemical instability leads to unusual chemical-potential-independent defect formation and diffusion in perovskite solar cell material $CH_3NH_3PbI_3$. *Journal of Materials Chemistry A* **2016,** *4* (43), 16975-16981.

25. Meggiolaro, D.; Motti, S. G.; Mosconi, E.; Barker, A. J.; Ball, J.; Perini, C. A. R.; Deschler, F.; Petrozza, A.; De Angelis, F., Iodine chemistry determines the defect tolerance of lead-halide perovskites. *Energy & Environmental Science* **2018,** *11* (3), 702-713.

26. Zhang, H.; Li, R.; Zhang, M.; Guo, M., The effect of SrI_2 substitution on perovskite film formation and its photovoltaic properties via two different deposition methods. *Inorganic Chemistry Frontiers* **2018,** *5* (6), 1354-1364.

27. Zhang, H.; Wang, H.; Williams, S. T.; Xiong, D.; Zhang, W.; Chueh, C. C.; Chen, W.; Jen, A. K. Y., $SrCl_2$ Derived Perovskite Facilitating a High Efficiency of 16% in Hole-Conductor-Free Fully Printable Mesoscopic Perovskite Solar Cells. *Advanced Materials* **2017,** *29* (15), 1606608.

28. Wu, M.-C.; Chen, W.-C.; Chan, S.-H.; Su, W.-F., The effect of strontium and barium doping on perovskite-structured energy materials for photovoltaic applications. *Applied Surface Science* **2018,** *429*, 9-15.

29. Würfel, P.; Würfel, U., *Physics of solar cells: from basic principles to advanced concepts*. John Wiley & Sons: 2016.

30. Zhang, S.; Wei, S.-H.; Zunger, A.; Katayama-Yoshida, H., Defect physics of the CuInSe 2 chalcopyrite semiconductor. *Physical Review B* **1998,** *57* (16), 9642.

31. Xiao, Z.; Yuan, Y.; Shao, Y.; Wang, Q.; Dong, Q.; Bi, C.; Sharma, P.; Gruverman, A.; Huang, J., Giant switchable photovoltaic effect in organometal trihalide perovskite devices. *Nature materials* **2015,** *14* (2), 193-198.

32. Wang, Q.; Shao, Y.; Xie, H.; Lyu, L.; Liu, X.; Gao, Y.; Huang, J., Qualifying composition dependent p and n self-doping in CH3NH3PbI3. *Applied Physics Letters* **2014,** *105* (16), 163508.

33. Olthof, S.; Meerholz, K., Substrate-dependent electronic structure and film formation of $MAPbI_3$ perovskites. *Scientific reports* **2017,** *7*, 40267.

34. Tougaard, S., QUASES-IMFP-TPP2M program. *Quases-Tougaard Inc* **2002**.

35. Tanuma, S.; Powell, C. J.; Penn, D. R., Calculations of electron inelastic mean free paths. V. Data for 14 organic compounds over the 50–2000 eV range. *Surface and Interface Analysis* **1994,** *21* (3), 165-176.

36. Mattox, D. M., *Handbook of physical vapor deposition (PVD) processing*. William Andrew: 2010.

37. Attfield, M.; Barnes, P.; Cockcroft, J. K.; Driessen, H. Crystallite Size and Strain. http://pd.chem.ucl.ac.uk/pdnn/peaks/size.htm (accessed 01/03/2018).

38. Yamada, Y.; Yamada, T.; Phuong, L. Q.; Maruyama, N.; Nishimura, H.; Wakamiya, A.; Murata, Y.; Kanemitsu, Y., Dynamic optical properties of CH3NH3PbI3 single crystals as revealed by one-and two-photon excited photoluminescence measurements. *Journal of the American Chemical Society* **2015,** *137* (33), 10456-10459.

39. Le Bail, A.; Jouanneaux, A., A Qualitative Account for Anisotropic Broadening in Whole-Powder-Diffraction-Pattern Fitting by Second-Rank Tensors. *Journal of Applied Crystallography* **1997,** *30* (3), 265-271.

40. Chen, C.; Xu, Y.; Wu, S.; Zhang, S.; Yang, Z.; Zhang, W.; Zhu, H.; Xiong, Z.; Chen, W.; Chen, W., CaI_2: a more effective passivator of perovskite films than PbI_2 for high efficiency and long-term stability of perovskite solar cells. *Journal of Materials Chemistry A* **2018,** *6* (17), 7903-7912.

41. Saliba, M.; Correa-Baena, J.-P.; Wolff, C. M.; Stolterfoht, M.; Phung, N.; Albrecht, S.; Neher, D.; Abate, A., How to make over 20% efficient perovskite solar cells in regular (n–i–p) and inverted (p–i–n) architectures. *Chemistry of Materials* **2018,** *30* (13), 4193-4201.

42. Domanski, K.; Roose, B.; Matsui, T.; Saliba, M.; Turren-Cruz, S.-H.; Correa-Baena, J.-P.; Carmona, C. R.; Richardson, G.; Foster, J. M.; De Angelis, F.; Ball, J. M.; Petrozza, A.; Mine, N.; Nazeeruddin, M. K.; Tress, W.; Grätzel, M.; Steiner, U.; Hagfeldt, A.; Abate, A., Migration of cations induces reversible performance losses over day/night cycling in perovskite solar cells. *Energy & Environmental Science* **2017,** *10* (2), 604-613.

43. Yella, A.; Heiniger, L.-P.; Gao, P.; Nazeeruddin, M. K.; Grätzel, M., Nanocrystalline rutile electron extraction layer enables low-temperature solution processed perovskite photovoltaics with 13.7% efficiency. *Nano letters* **2014,** *14* (5), 2591-2596.

44. Gorgoi, M.; Svensson, S.; Schäfers, F.; Öhrwall, G.; Mertin, M.; Bressler, P.; Karis, O.; Siegbahn, H.; Sandell, A.; Rensmo, H., The high kinetic energy photoelectron spectroscopy facility at BESSY progress and first results. *Nuclear Instruments and Methods in Physics Research Section A: Accelerators, Spectrometers, Detectors and Associated Equipment* **2009,** *601* (1-2), 48-53.

45. Schaefers, F.; Mertin, M.; Gorgoi, M., KMC-1: A high resolution and high flux soft x-ray beamline at BESSY. *Review of Scientific Instruments* **2007,** *78* (12), 123102.

46. Wojdyr, M., Fityk: a general-purpose peak fitting program. *Journal of Applied Crystallography* **2010,** *43* (5-1), 1126-1128.

47. Trzhaskovskaya, M.; Nefedov, V.; Yarzhemsky, V., Photoelectron angular distribution parameters for elements Z= 1 to Z= 54 in the photoelectron energy range 100–5000 eV. *Atomic Data and Nuclear Data Tables* **2001,** *77* (1), 97-159.

48. Trzhaskovskaya, M.; Nefedov, V.; Yarzhemsky, V., Photoelectron angular distribution parameters for elements Z= 55 to Z= 100 in the photoelectron energy range 100–5000 eV. *Atomic Data and Nuclear Data Tables* **2002,** *82* (2), 257-311.

49. Trzhaskovskaya, M.; Nikulin, V.; Nefedov, V.; Yarzhemsky, V., Non-dipole second order parameters of the photoelectron angular distribution for elements Z= 1–100 in the photoelectron energy range 1–10 keV. *Atomic Data and Nuclear Data Tables* **2006,** *92* (2), 245-304.

50. Seah, M.; Smith, G., Quantitative AES and XPS: Determination of the electron spectrometer transmission function and the detector sensitivity energy dependencies for the production of true electron emission spectra in AES and XPS. *Surface and interface analysis* **1990,** *15* (12), 751-766.

51. Scrocco, M., X-ray photoemission spectra of Pb (II) halides: A study of the satellites on the core and valence bands. *Physical Review B* **1982,** *25* (3), 1535.

52. Sadoughi, G.; Starr, D. E.; Handick, E.; Stranks, S. D.; Gorgoi, M.; Wilks, R. G.; Bär, M.; Snaith, H. J., Observation and mediation of the presence of metallic lead in organic–inorganic perovskite films. *ACS applied materials & interfaces* **2015,** *7* (24), 13440-13444.

53. Stoumpos, C. C.; Malliakas, C. D.; Kanatzidis, M. G., Semiconducting tin and lead iodide perovskites with organic cations: phase transitions, high mobilities, and near-infrared photoluminescent properties. *Inorganic chemistry* **2013,** *52* (15), 9019-9038.

54. Perdew, J. P.; Burke, K.; Ernzerhof, M., Generalized Gradient Approximation Made Simple. *Physical Review Letters* **1996,** *77* (18), 3865.

55. Van de Walle, C. G.; Neugebauer, J., First-principles calculations for defects and impurities: Applications to III-nitrides. *Journal of applied physics* **2004,** *95* (8), 3851-3879.

56. Meggiolaro, D.; De Angelis, F., First-Principles Modeling of Defects in Lead Halide Perovskites: Best Practices and Open Issues. *ACS Energy Letters* **2018,** *3* (9), 2206-2222.

57. Heyd, J.; Scuseria, G. E.; Ernzerhof, M., Hybrid functionals based on a screened Coulomb potential. *The Journal of chemical physics* **2003,** *118* (18), 8207-8215.

58. Grimme, S.; Antony, J.; Ehrlich, S.; Krieg, H., A consistent and accurate ab initio parametrization of density functional dispersion correction (DFT-D) for the 94 elements H-Pu. *The Journal of chemical physics* **2010,** *132* (15), 154104.

59. Thompson, P.; Cox, D.; Hastings, J., Rietveld refinement of Debye–Scherrer synchrotron X-ray data from Al2O3. *Journal of Applied Crystallography* **1987,** *20* (2), 79-83.

60. Stolterfoht, M.; Wolff, C. M.; Márquez, J. A.; Zhang, S.; Hages, C. J.; Rothhardt, D.; Albrecht, S.; Burn, P. L.; Meredith, P.; Unold, T.; Neher, D., Visualization and suppression of interfacial recombination for high-efficiency large-area pin perovskite solar cells. *Nature Energy* **2018,** *3* (10), 847.

61. Delamarre, A.; Lombez, L.; Guillemoles, J.-F., Contactless mapping of saturation currents of solar cells by photoluminescence. *Applied Physics Letters* **2012,** *100* (13), 131108.

62. Unold, T.; Gütay, L., Photoluminescence analysis of thin-film solar cells. In *Advanced Characterization Techniques for Thin Film Solar Cells*, Abou-Ras, D.; Kirchartz, T.; Rau, U., Eds. Wiley-VCH Verlag GmbH & Co. KGaA.: 2016; Vol. 1, pp 275-297.

63. Moulder, J. F.; Stickle, W. F.; Sobol, P. E.; Bomben, K. D., *Handbook of X-ray Photoelectron Spectroscopy*. 2nd ed.; Physical Electronics Division, Perkin-Elmer Corporation: 1992.

64. Seyama, H.; Soma, M., X-ray photoelectron spectroscopic study of montmorillonite containing exchangeable divalent cations. *Journal of the Chemical Society, Faraday Transactions 1: Physical Chemistry in Condensed Phases* **1984,** *80* (1), 237-248.

65. Schoonman, J., Organic–inorganic lead halide perovskite solar cell materials: a possible stability problem. *Chemical Physics Letters* **2015,** *619*, 193-195.

66. Pankratov, V.; Popov, A.; Shirmane, L.; Kotlov, A.; Bizarri, G.; Burger, A.; Bhattacharya, P.; Tupitsyn, E.; Rowe, E.; Buliga, V.; Williamse, R., Luminescence and ultraviolet excitation spectroscopy of SrI2 and SrI2: Eu2+. *Radiation Measurements* **2013,** *56*, 13-17.

67. Lu, F.; Wang, W.; Luo, X.; Xie, X.; Cheng, Y.; Dong, H.; Liu, H.; Wang, W.-H., A class of monolayer metal halogenides MX2: Electronic structures and band alignments. *Applied Physics Letters* **2016,** *108* (13), 132104.

68. Heo, S.; Cho, E.; Lee, H.-I.; Park, G. S.; Kang, H. J.; Nagatomi, T.; Choi, P.; Choi, B.-D., Band gap and defect states of MgO thin films investigated using reflection electron energy loss spectroscopy. *AIP Advances* **2015,** *5* (7), 077167.

69. Wieghold, S.; Tresback, J.; Correa-Baena, J.-P.; Hartono, N. T. P.; Sun, S.; Liu, Z.; Layurova, M.; VanOrman, Z. A.; Bieber, A. S.; Thapa, J.; Lai, B.; Cai, Z.; Nienhaus, L.; Buonassisi, T., Halide heterogeneity affects local charge carrier dynamics in mixed-ion lead perovskite thin films. *Chemistry of Materials* **2019,** *31* (10), 3712-3721.

70. Langford, J. I.; Wilson, A., Scherrer after sixty years: a survey and some new results in the determination of crystallite size. *Journal of applied crystallography* **1978,** *11* (2), 102-113.

71. Dänekamp, B.; Müller, C.; Sendner, M.; Boix, P. P.; Sessolo, M.; Lovrincic, R.; Bolink, H. J., Perovskite–perovskite homojunctions via compositional doping. *The journal of physical chemistry letters* **2018,** *9* (11), 2770-2775.

72. Wieghold, S.; Tresback, J.; Correa-Baena, J.-P.; Hartono, N. T. P.; Sun, S.; Liu, Z.; Layurova, M.; VanOrman, Z. A.; Bieber, A. S.; Thapa, J.; Lai, B.; Cai, Z.; Nienhaus, L.; Buonassisi, T., Halide heterogeneity affects local charge carrier dynamics in mixed-ion lead perovskite thin films. *Chemistry of Materials* **2019**.

73. Mosconi, E.; Meggiolaro, D.; Snaith, H. J.; Stranks, S. D.; De Angelis, F., Light-induced annihilation of Frenkel defects in organo-lead halide perovskites. *Energy & Environmental Science* **2016,** *9* (10), 3180-3187.

74. Bi, D.; Yi, C.; Luo, J.; Décoppet, J.-D.; Zhang, F.; Zakeeruddin, S. M.; Li, X.; Hagfeldt, A.; Grätzel, M., Polymer-templated nucleation and crystal growth of perovskite films for solar cells with efficiency greater than 21%. *Nature Energy* **2016,** *1* (10), 16142.

75. Qin, C.; Matsushima, T.; Fujihara, T.; Adachi, C., Multifunctional benzoquinone additive for efficient and stable planar perovskite solar cells. *Advanced Materials* **2017,** *29* (4), 1603808.

76. Cho, H.; Jeong, S.-H.; Park, M.-H.; Kim, Y.-H.; Wolf, C.; Lee, C.-L.; Heo, J. H.; Sadhanala, A.; Myoung, N.; Yoo, S.; Im, S. H.; Friend, R. H.; Lee, T.-W., Overcoming the electroluminescence efficiency limitations of perovskite light-emitting diodes. *Science* **2015,** *350* (6265), 1222-1225.

77. Schick, K.; Daub, E.; Finkbeiner, S.; Würfel, P., Verification of a generalized Planck law for luminescence radiation from silicon solar cells. *Applied Physics A* **1992,** *54* (2), 109-114.

78. Braly, I. L.; deQuilettes, D. W.; Pazos-Outon, L. M.; Burke, S.; Ziffer, M. E.; Ginger, D. S.; Hillhouse, H. W., Hybrid perovskite films approaching the radiative limit with over 90% photoluminescence quantum efficiency. *Nature Photonics* **2018,** *12*, 355-361.

79. Quitsch, W.-A.; deQuilettes, D. W.; Pfingsten, O.; Schmitz, A.; Ognjanovic, S.; Jariwala, S.; Koch, S.; Winterer, M.; Ginger, D. S.; Bacher, G., The role of excitation energy in photobrightening and photodegradation of halide perovskite thin films. *The journal of physical chemistry letters* **2018,** *9* (8), 2062-2069.

80. Correa-Baena, J. P.; Anaya, M.; Lozano, G.; Tress, W.; Domanski, K.; Saliba, M.; Matsui, T.; Jacobsson, T. J.; Calvo, M. E.; Abate, A.; Grätzel, M.; Míguez, H.; Hagfeldt, A., Unbroken Perovskite: Interplay of Morphology, Electro-optical Properties, and Ionic Movement. *Advanced Materials* **2016,** *28* (25), 5031-5037.

81. Zhao, J.; Deng, Y.; Wei, H.; Zheng, X.; Yu, Z.; Shao, Y.; Shield, J. E.; Huang, J., Strained hybrid perovskite thin films and their impact on the intrinsic stability of perovskite solar cells. *Science advances* **2017,** *3* (11), eaao5616.

82. Abate, A.; Planells, M.; Hollman, D. J.; Barthi, V.; Chand, S.; Snaith, H. J.; Robertson, N., Hole-transport materials with greatly-differing redox potentials give efficient TiO 2–[CH 3 NH 3][PbX 3] perovskite solar cells. *Physical Chemistry Chemical Physics* **2015,** *17* (4), 2335-2338.

83. Belisle, R. A.; Jain, P.; Prasanna, R.; Leijtens, T.; McGehee, M. D., Minimal effect of the hole-transport material ionization potential on the open-circuit voltage of perovskite solar cells. *ACS Energy Letters* **2016,** *1* (3), 556-560.

84. Fassl, P.; Lami, V.; Bausch, A.; Wang, Z.; Klug, M. T.; Snaith, H. J.; Vaynzof, Y., Fractional deviations in precursor stoichiometry dictate the properties, performance and stability of perovskite photovoltaic devices. *Energy & environmental science* **2018,** *11* (12), 3380-3391.

Chapter 5 The Role of Grain Boundaries on Ionic Defect Migration

This chapter is based on the peer-reviewed article “**The Role of Grain Boundaries on Ionic Defect Migration in Metal Halide Perovskites**” DOI: 10.1002/aenm.201903735. Reproduced with permission.

Abstract

Halide perovskites are emerging as revolutionary materials for optoelectronics. Their ionic nature and the presence of mobile ionic defects within the crystal structure have a dramatic influence on the operation of thin-film devices such as solar cells, light-emitting diodes, and transistors. Thin films are often polycrystalline and it is still under debate how grain boundaries affect the migration of ions and corresponding ionic defects. Laser excitation during photoluminescence (PL) microscopy experiments leads to formation and subsequent migration of ionic defects, which affects the dynamics of charge carrier recombination. From the microscopic observation of lateral PL distribution, the change in the distribution of ionic defects over time can be inferred. Resolving the PL dynamics in time and space of single crystals and thin films with different grain sizes, thus, provide crucial information about the influence of grain boundaries on the defect movement. In conjunction with experimental observations, atomistic simulations show that defects are trapped at the grain boundaries, thus inhibiting their diffusion. Hence, with this study, we provide a comprehensive picture including experiments highlighting fundamental property of the material while also setting the theoretical framework in which the interaction between grain boundaries and ionic defect migration can be understood.

5.1 Introduction

Halide perovskites have rapidly become an attractive class of materials for optoelectronic applications, including photovoltaics,[1] light-emitting diodes (LEDs),[2] light detection[3] and energy storage.[4] The stoichiometric unit of a halide perovskite with standard formula ABX_3 consists of either one organic or inorganic monovalent ion (A^+) placed in a cage made up of 8 corner-sharing octahedra, each containing one divalent metal ion (B^{2+}) (typically Pb or Sn), and six halides (X^-). All three ionic constituents may give rise to defects that could be vacancies, interstitials or anti-site substitutions.[5] Ionic defects have been shown to be very mobile at room temperature,[6] being able to migrate within the material (lattice) when subjected to temperature or defect concentration gradients, as well as external stimuli such as light or an electric field.[7-8] As this gives rise to substantial transient phenomena in the devices' electrical response, a considerable portion of the literature to date discusses the challenges arising from defects created during device operation and their migration. Not only does ion migration play a crucial role in the device's current-voltage hysteresis,[9-10] but is also attributed the underpinning cause for both reversible and irreversible degradation of the perovskite absorber.[11-12] Since ion migration, and consequent ionic defect movement, are evidently an integral part of the operation and stability of perovskite-based optoelectronic devices, it is imperative to continue gaining an understanding of the migration dynamics.

Ion migration relates closely to the defect chemistry of the material.[13] Theoretical calculations[13-14] and experimental work[15] support the hypothesis that the most abundant defects in methylammonium lead iodide ($MAPbI_3$) perovskites are iodide vacancies ($V_I^\bullet$) and interstitials (I_i') as these have the lowest formation energies and are likely generated as Frenkel pairs. Ionic defect migration has been proposed to occur via efficient vacancy hopping or interstitial kick-off mechanisms.[13] One of the leading questions of the experiments presented here is the effect of grain boundaries (GBs) on ion migration in polycrystalline films, as these cause a discontinuation of the crystal lattice with substantial defect density. This is of particular relevance for solution-processed perovskite thin films, which typically contain a large number of GBs.

The exact interplay of GBs and ionic motion is still under discussion in the literature. Some authors suggest that ionic defect migration could be facilitated by GBs,[16-17] which is based on observations of a more considerable hysteresis at the GBs compared to the grain interior, as concluded by atomic force microscopy experiments.[16] Moreover, the activation energies for ions to migrate from their proper places in the lattice are reportedly higher in single crystals compared to thin films with smaller grains

(~300 nm).[18] This may be due to the increased difficulty for ions to move in the absence of GBs because of the lack of ionic vacancies. On the other hand, others and some of us have observed a reduction in hysteresis for devices containing an absorber layer with larger grain size.[19-20] It was concluded from intensity modulated photocurrent spectroscopy that ionic defect movement is faster when the number of GBs is reduced,[19] which points to GBs inhibiting their migration. Another recent report has shown that even though mobile ions is a prerequisite for hysteresis, the trapping and detrapping of ionic defects plays an important role for slow transients seen in devices.[21]

To extend our understanding about how the microstructure influences ionic defect migration, we recognize the need for direct observations of the migration dynamics and for gaining a spatially resolved microscopic picture. Photoluminescence (PL) microscopy offers the opportunity to study the light absorber material while excluding the influence of other contact layers or metal electrodes that are typically used in optoelectronic devices. Hence, PL microscopy has particularly been used to detect the effect of defect migration in halide perovskites.[8, 22-23] One characteristic signature is the change in relative PL quantum yield, which is directly related to the rate of radiative *versus* non-radiative recombination, which in turn is dictated by the local defect chemistry (and density), which can be altered by light.[24-25] It has been widely reported that light can drive out the iodide content and change the PL yield, or in other words, iodide defects have been shown to alter the PL yield in halide perovskites.[22, 26-27] With PL microscopy we can induce local defect formation and migration while to some extent resolving the microstructure of the material, thus allowing us to correlate the dynamics of defect diffusion to the presence or absence of GBs.

In this study, PL microscopy is used as a means to induce ionic defect migration with the excitation beam, consecutively track the motion (redistribution) of defects in real-time through the resulting fluctuation in PL intensity, and observe the extent to which the material recovers from the limited perturbation state. We opted to use $MAPbI_3$ to limit the possible combinations of constituent ions and their associated defects. Using PL microscopy, we observe changes in the PL signal with sub-second time resolution (50 ms), which allows us to directly resolve defect-induced changes in the optoelectronic properties of the material related to ionic motion. By correlating PL microscopy and energy dispersive X-ray spectroscopy (EDX), we confirm that light promotes ionic diffusion out of the excited spot, creating additional defects in the material. By monitoring the dynamics of the relative PL quantum yield over time and space in films of different grain sizes and crystals of $MAPbI_3$, we can investigate the impact of GBs on the defect migration. With the support of atomistic simulations, we conclude that the GBs inhibit the lateral movement of defects in the material, *i.e.* their spreading across the film, which we also demonstrate with devices comprised of perovskite absorbers of different grain sizes. Here we show that devices are required to have monolithic grains in order to have fast ionic response. The fast transient response in the device can potentially reduce the reversible losses due to slow ion migration seen in devices under operational conditions.[11] Our study gives a broader understanding of how ionic defect migration in halide perovskite relates to the microstructure of the material.

5.1 Results and Discussion

5.1.1 Photo-induced ion migration

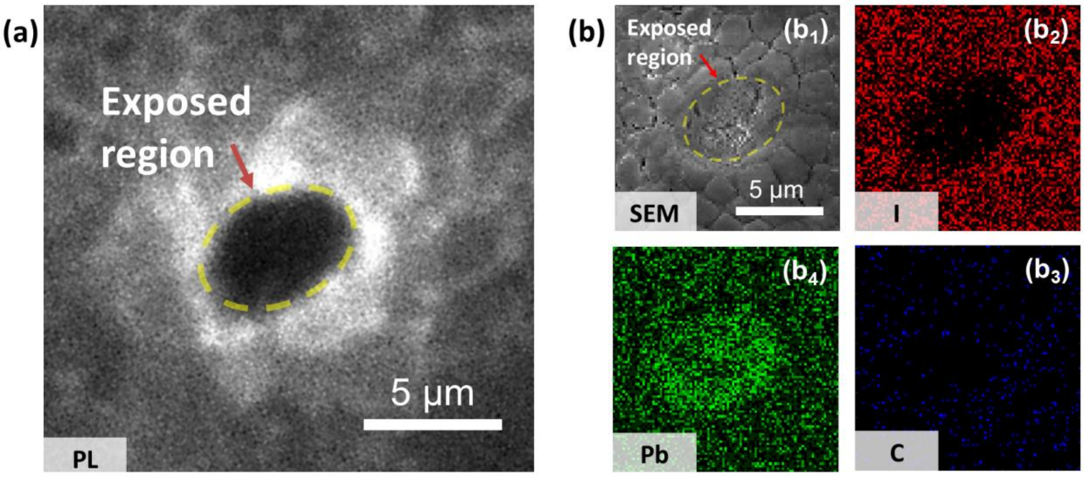

Figure 5.1 (a) Photoluminescence wide-field image directly after 1 minute of focused laser exposure in a $MAPbI_3$ thin film (b) Scanning electron microscopic (SEM) (panel b_1) and energy dispersive x-ray (EDX) images representing elemental distribution of the elements I, C and Pb (panels b_2, b_3, b_4 respectively), recorded from the same film area 45 minutes after laser exposure.

To establish the link between photoluminescence (PL) yield and defect migration, we exposed a $MAPbI_3$ thin film fabricated by a solution-based one-step method[28] (see **Experimental Section** for more details) to 1 minute of continuous wave laser excitation (450 nm). After exposure with focused excitation, we switch to a wide-field excitation scheme in order to obtain a PL map and observe that the region exposed to the focused laser has a significantly reduced PL yield (**Figure 5.1a**). From the scanning electron microscope (SEM) micrograph of the same area **Figure 5.1b$_1$**, it appears as if the region has structurally collapsed to form what resembles a crater. Furthermore, it becomes evident from the EDX images (**Figure 5.1b$_{2\text{-}4}$**) that there is a significant ionic redistribution. Most obvious is the almost complete lack of iodide (**Figure 5.1b$_2$**), which is in agreement with previous reports on halide migration away from the light exposed spot.[22, 26-27] There is also no indication that it has accumulated elsewhere, although it is possible that the EDX image resolution prevents a clear representation of the elemental distribution outside the illuminated region. **Figure 5.1b$_3$** shows a slight reduction of the C signal after laser excitation, which could imply a removal of the methylammonium cation ($CH_3NH_3^+$) due to laser excitation. The signal for Pb, on the other hand, is higher in the exposed region compared to the surrounding regions (**Figure 5.1b$_4$**). At first this may seem counter-intuitive, however consistent with the EDX images of I and C, the increase of the Pb signal just denotes an increase of the concentration of Pb with respect to the other elements, I and C. Whether this is due to the concomitant formation of I_2 and Pb^0 [29] or collapse of the tetragonal structure into PbI_2 due to the removal of MA^+ and I^-,[30] goes beyond the aim of this work. Indeed, the reduced concentration of I and C in the illuminated region can further enhance the Pb signal in EDX imaging because it reduces the re-absorption of Pb-emitted X-rays by MA^+ and I^-.

Most importantly, this correlation between PL and EDX allows us to establish that ion (re)distribution can be driven either directly or indirectly (by thermal effect) by light and it correlates strongly to the changes in PL quantum yield. A reduction of PL yield correlated with a depletion of iodine can be rationalized by migrating ions increasing the defect concentration, which consequently increases the portion of non-radiative recombination. As also reported in several publications,[22, 26-27] we suspect that it is the halide specie having the lowest activation energy, which migrates out from the laser excited spot forming the defects. A recent report by Motti *et al.* shows that a reduction in PL yield after light soaking relates to an increment in the halide interstitial concentration which can trap holes.[31] Moreover, the formation of metallic Pb has been shown to introduce deep traps in the bandgap of $MAPbI_3$ introducing non-radiative recombination centers.[32] It is also worth noting that the reduction of C signal in EDX might be related to formation of MA^+ vacancies which are known to diffuse slowly under light exposure.[33] Identifying the type of point defects generated and set in motion by intense light exposure requires additional measurements stretching out of the scope of this work and is therefore the focus of a follow up study.

5.1.2 Tracking ion migration via spatially resolved photoluminescence

To further understand the effect of microstructure on the ion migration, we compare $MAPbI_3$ samples in form of polycrystalline thin films of different grain sizes and a crystal grown by inverted crystallization[34] (fabrication details is in **Experimental Section**). Having established that we can induce ionic drift with a focused laser beam, we subject the samples to a measurement protocol in which the excitation beam is either focused into a spot (FWHM of 2.5 µm) in the center of the field of view, or spread across the entire field of view spanning an area up to 40 µm diameter (defocused). A detailed description of the experimental setup and measurement protocol can be found in S.I. Note 1.

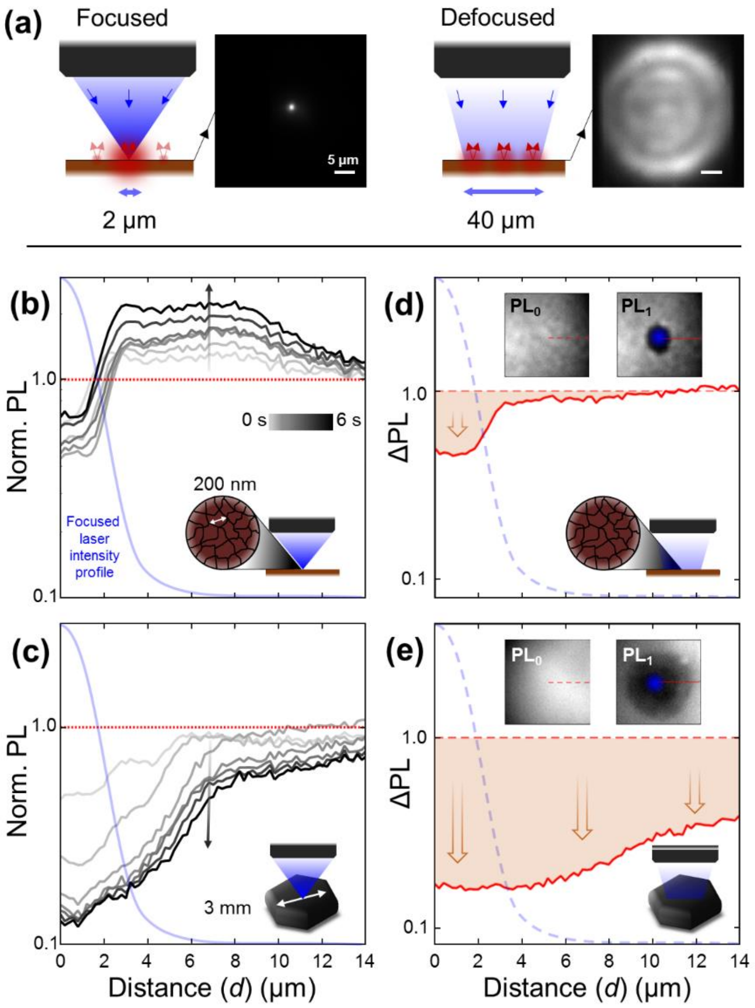

Figure 5.2 (a) The excitation modes used in this study: a focused mode where the excitation area has a diameter of 2.5 µm and a defocused mode where the excitation area has a diameter of 40 µm. PL images of fluorescent highlighter ink on a glass substrate demonstrating the excitation area for each mode (scale bar represents 5 µm in both images). Irrespective of the excitation mode used, photoluminescence (PL) signals from samples are collected from the entire field of view. The evolution of normalized PL during the first six seconds of exposure to the focused excitation of the (b) thin film and (c) crystal as a function of radial distance, *d*, from the center of focused laser excitation spot. The

gray-scale bar in panel (b) indicates the elapsed time after which the traces in (b-c) are extracted. The light-blue curve shows the normalized laser intensity profile when the light is focused, also indicated in the insets as blue spots. Spatially resolved changes in PL intensity (ΔPL) are shown in (d) for a thin film and in (e) for a crystal comparing the distribution of PL before and after the focused excitation. The red shaded area represents the amount PL has dropped. The top two insets in panel (d) and (e) show the PL images with defocused excitation before and after a 20 s period of focused excitation. The schematic insets in panels d-e indicate the sample and excitation mode used.

Figure 5.2a schematically illustrates the two modes also showing the corresponding excitation spot sizes. In both excitation modes, the excitation power is kept constant, which means the excitation density in the focused mode increases by over two orders of magnitude compared to the defocused mode. Irrespective of whether the excitation is focused or defocused, the PL emission from the sample is collected from the entire field of view (40 µm diameter) of the sample at a frame rate of 20 Hz. This provides a unique opportunity to not only detect the spatially evolving PL signal from the area of the sample which is not directly excited in the focused mode, but also detect any changes in the PL as a result of focusing the laser (comparing defocused PL images before (PL_0) and after focusing the laser (PL_1) – see inset of **Figure 5.2d-e**).

Figure 5.2b-c show a spatially resolved time evolution of PL from the thin film and a freshly cleaved surface of the crystal in the focused mode excitation interval (a few selected frames over 6 seconds, see S.I. for complete videos: SV1 for the thin film and SV2 for the crystal). Since the redistribution of PL is radially symmetric with respect to the point of excitation, we plot the normalized PL intensity as a function of the distance d from the centre of the laser spot (d = 0 µm). The radial distribution of PL intensity extracted at each time instant (PL(d,t)) is normalized to the initial PL distribution (PL(d,t=0)) measured just as the focused excitation is turned on. For both samples, a reduction of the normalized PL (values below the red dotted line) is observed for $d < {\sim}2$ µm. We note that this correlates well with the region where the focused excitation laser directly strikes the sample (blue line). Overall, the PL signal of the film and crystal shows relevant qualitative differences both in the shape and variation with time. In the crystal, the PL diminishes over a broad range (broader than the excitation spot) upon excitation with the focused beam. On the contrary, PL in the film decreases only in the laser spot; outside this region PL increases. Moreover, while for the crystal PL(d,t) keeps decreasing with time during the first 6 s of the measurement, in the film PL(d,t) continuously increases.

An interesting feature for both samples is that PL is detected at distances far from the excitation point. Charge carrier diffusion lengths in metal halide perovskites have been reported to be on the order of a few µm,[35-36] which may certainly explain our observations. Another contributing factor may also be photon recycling.[37] We are reluctant to attribute this to PL caused by direct absorption of photons from the tail of the focused excitation source primarily for the reason that the PL profiles for neither sample (grey traces) resemble that of the focused excitation profile. Regardless of how the PL far from the focused excitation spot is generated, it is more importantly established that there are changes in the spatially distributed PL yield evolving over seconds (slow time scale), which we attribute to ionic defect redistribution. This is in agreement with a study by Li *et al.*,[23] in which PL changes are also observed in space in a $MAPbI_3$ thin film due to an applied electric field-induced ions redistribution.

Although we have strong evidence for light inducing ionic redistribution, we refrain from proposing by which mechanism this occurs at this stage. In a recent report, light-driven ion migration has been attributed to photochemical processes involving various rates of trapping and detrapping of charge carriers interacting with halide defects.[38] Alternatively, it has been also proposed that light can induce local electric fields that causing ionic defect migration, although different explanations of how that field arises have been proposed including photo-induced Stark effect,[39] as well as an interaction between charge carriers and surface adhered superoxide species.[40]

The comparison between the PL images before (PL_0) and after (PL_1) focusing the excitation can provide information on lasting changes (in minutes or hours) in the spatially distributed PL intensity caused by the focused excitation. For a simplified comparison between samples, we extract the relative change in PL intensity $\Delta PL(d) = \frac{PL_1(d)}{PL_0(d)}$, again as a function of radial distance (*d*). In **Figure 5.2d**, we demonstrate that ΔPL shows a significant reduction in the range between d = 1-4 μm (red shaded area) for the thin film. Comparing this to the FWHM of the focused laser distribution profile (blue curve), this reduction of PL coincides with the region receiving the direct excitation from the focused laser. The insets show the PL images before and after the focused excitation where the PL reduction is observed. A value of $\Delta PL<1$ indicates an increase of defect-mediated non-radiative recombination, which is associated with a redistribution of ions and subsequent defect formation as discussed above. Subjecting the freshly cleaved crystal to the same measurement procedure results in a noticeably larger reduction of ΔPL observed at a greater radial distance compared to the thin film (**Figure 5.2e**), which is also evident in the PL images (see insets in **Figure 5.2e**). At a radial distance of d = 12 μm, ΔPL = 1 for the thin film (no lasting effect from focused excitation), as opposed to the crystal case, where $\Delta PL \approx 0.3$. We, therefore, conclude that there is stronger resistance to the spatial redistribution of ionic defects in the thin film compared to the crystal.

5.1.3 Grain boundaries as an energy barrier for ion migration

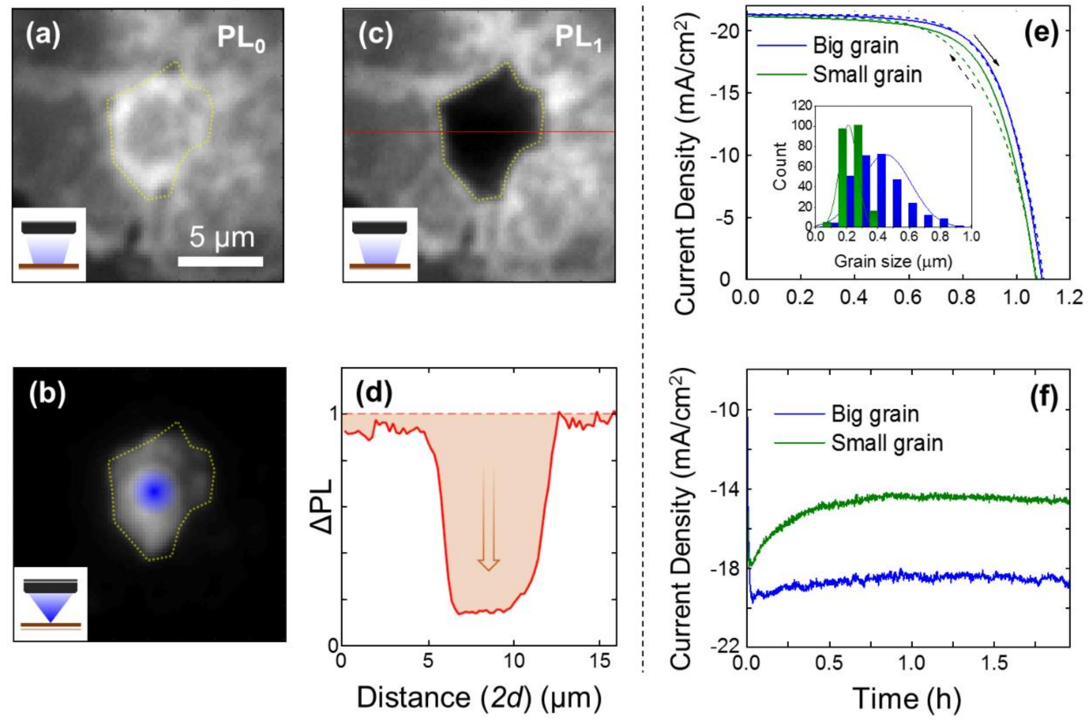

Figure 5.3 The evolution of the PL signal during focused mode excitation on a big grain film. (a) Initial defocused mode PL_0, (b) focused mode snapshots over time in which the laser excitation spot is indicated by a blue circle. (c) PL at defocused excitation mode (PL_1). (d) Relative change ΔPL as a function of distance along the red line in (c). The device behaviour employing different grain sizes: (e) current density-voltage curves of the devices measured under AM 1.5 solar simulator with scan rate of 100 mV/s, arrows indicate scan direction (inset is the grain size distributions of identical perovskite films), (f) current response at 0.1 V bias for 2 hours of corresponding devices under one sun illumination.

As shown in Figure S5.2a, the average grain size of the thin film shown in **Figure 5.2** is ~200 nm, which is approximately one order of magnitude smaller than the diameter of the focused excitation spot (~2.5 µm). Therefore, the laser spot directly impinges on an area containing several grains, which is not the case for the crystal (see Figure S5.2b, S.I.). Hence, we prepare a thin film containing large grains, which also serves as an intermediate scenario between the small grain thin film and the crystal. SEM micrographs demonstrate that this "big-grain film" has grains with sizes equivalent to, or even larger than, the focused laser excitation spot (see Figure S5.2c, S.I.). As such, we can focus the excitation into a single grain while observing the effect on the neighbouring grains that are not directly excited. Here, we depend on SEM micrographs to define the size of the grains. We acknowledge that these can vary from what is determined by SEM,[41] and that a group of grains can be mistaken for a single one using this technique.[42] However, this study emphasizes the difference in the GB density in the three samples with notably different microstructure (further optical and morphological characterization the samples can be found in SI note 2 and 3). Hence, we are confident that adequate information can still be drawn from relative differences between SEM analyses.

In **Figure 5.3**, we isolated a relatively large grain (~5 μm diameter) and subjected it to the same measurement procedure as for the thin film and crystal. We did not correlate SEM micrographs with PL measurements but could identify the grain boundaries in the PL microscope as regions of particularly increasing PL intensity for the first 30 seconds of exposure to light. This photobrightening at GBs can be explained by an intense light-induced healing of defects,[43] that, in comparison to the bulk of the grain where the defect density is lower, occurs at a faster rate. In **Figure 5.3a**, the PL map is shown in defocused mode (PL_0) prior to focusing the excitation, where the large grain is highlighted with a dashed yellow line. When the excitation is focused into the grain (blue spot), we observe from the normalized PL images that emission is coming strictly from the grain that is directly excited (**Figure 5.3b**) and not from outside its GB. This points to GBs either efficiently mediating non-radiative recombination or that charge carriers are simply deflected, which has been previously proposed.[5, 44] As the focused excitation remains, we observe similar spatial redistribution of PL to what occurs in the single crystal (see video SV3 in S.I.), establishing the light-induced ionic defect migration. As the excitation is switched back to defocused mode (PL_1), we can confirm that PL remains significantly reduced exclusively for the grain that was excited (**Figure 5.3c**). This becomes more obvious in **Figure 5.3d** when plotting ΔPL from a cross-section of the field of view (indicated by the red line in **Figure 5.3c**), where not only a strong reduction of PL is observed for the excited grain, but also that PL remains largely unaffected outside the boundaries of the large grain. Thus, this intermediate case strengthens the hypothesis that GBs introduce barriers for ion migration.

We further fabricated devices in n-i-p architecture using thin films of different grain sizes to examine the effect of ionic defect dynamics in real working solar cells. **Figure 5.3e** shows the current density-voltage curves of devices employing two distinct grain size distributions, in which the 'big grain' device has average absorber grain size of 400 nm compared to an average grain size of 200 nm for the 'small grain' device. The devices have fairly similar performance where the small-grain and big-grain devices show short circuit current density of 21.1 and 21.3 mA/cm^2, open circuit voltage of 1074 and 1095 mV, and fill factor of 66.4 and 68.0% respectively (forward scan), resulting in 15.0 and 15.8% power conversion efficiencies. The small-grain device exhibits a slight hysteresis compared to the big-grain device which might indicate a difference in the ionic response time. Furthermore, the devices were subjected to 0.1 V bias to track the current transient behaviour under illumination (**Figure 5.3f**). As expected, the big grain device has a faster current response with less variance under a steady bias. Thus, in agreement with a previous report by Correa-Baena *et al.*,[19] the microstructure of the film can be linked to the device's behaviour, in which the electronic transient on long time scales has been attributed to the ionic double layers introduced by ionic defect migration.[11, 45]

5.1.4 Dark recovery

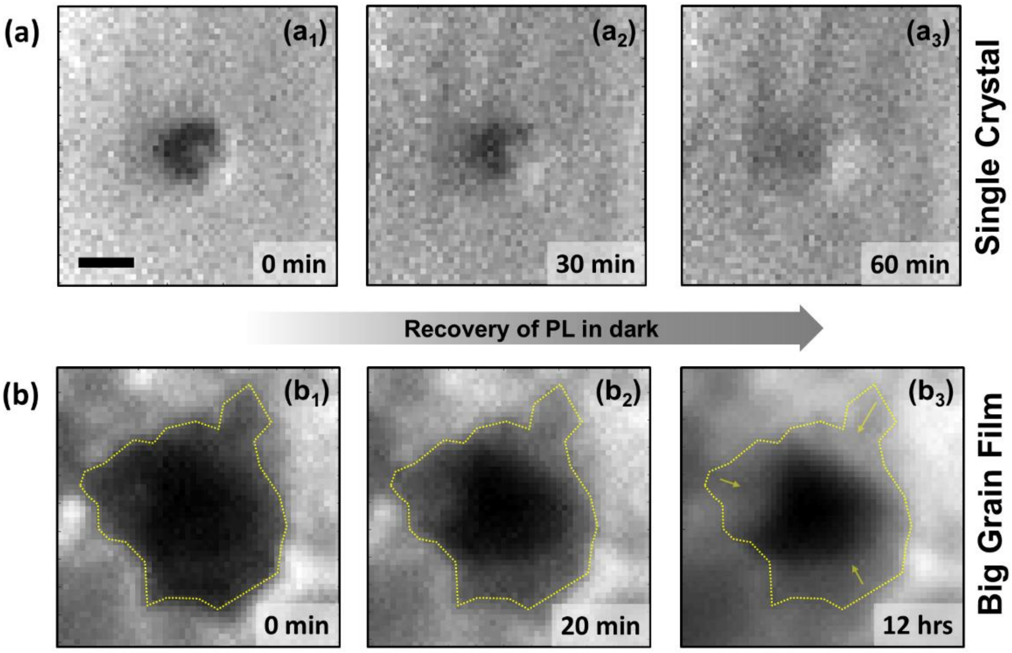

Figure 5.4 The PL images demonstrating the recovery of PL in dark over time for (a) single crystal, and (b) big-grain film (yellow dotted line indicates the boundary of one single grain). Light is only switched on for the time required to acquire the image (< 1 second). The time-stamp in the bottom right corner indicates the time after which focused light-soaking finished and recovery began. For the single crystal there is nearly a complete recovery of PL within 60 minutes of recovery in dark, whereas for the big-grain film the recovery is only partial after 12 hours. Scale bar represents 2 μm in all images.

Having established that the light-induced ion migration is inhibited by GBs, we study the effect of allowing the sample to rest in the dark after light soaking, which has for PSC devices been reported to restore performance.[11] For both the crystal and the big-grain film, where a noticeable ion migration is detected over large areas, we observe the self-healing (recovery of PL) occurring at different time scales (**Figure 5.4a**) which is also observed by several reports,[27, 46-47] and the phenomenon is attributed to ionic defect migration.[48] The main difference in the recovery between the two samples here are the time scales and the extent to which recovery occurs (**Figure 5.4b**). Complete recovery occurs for the crystal within 1 hour, while the recovery for the big-grain film is still incomplete after 12 hours. We note that for the big-grain film, recovery starts from the GB perimeter and progresses to the center of the grain, where the PL yield remains low even after 12 hours. The longer recovery time seen along the perimeter of the grain might be due to either a higher intrinsic defect concentration and/or an intra-grain microstructure evolution constraint, which prevents the restoration of the initial state. We propose that the ions that have been driven towards, and possibly accumulated or "kinetically trapped" at the GBs, can return and "heal" only the damaged part in its proximity.

It is important to note here that we observe a morphology change in the big grain film (Figure S5.3) and similarly in the small grain film (**Figure 5.1**) after the light exposure. More importantly, the fact that the PL yield can recover implies that constituent ions did not leave the samples after excitation, but rather redistribute in the sample. We attribute the recovery to ionic defect annihilation, which leads to a reduction of non-radiative recombination, and thus, recovery of PL yield.

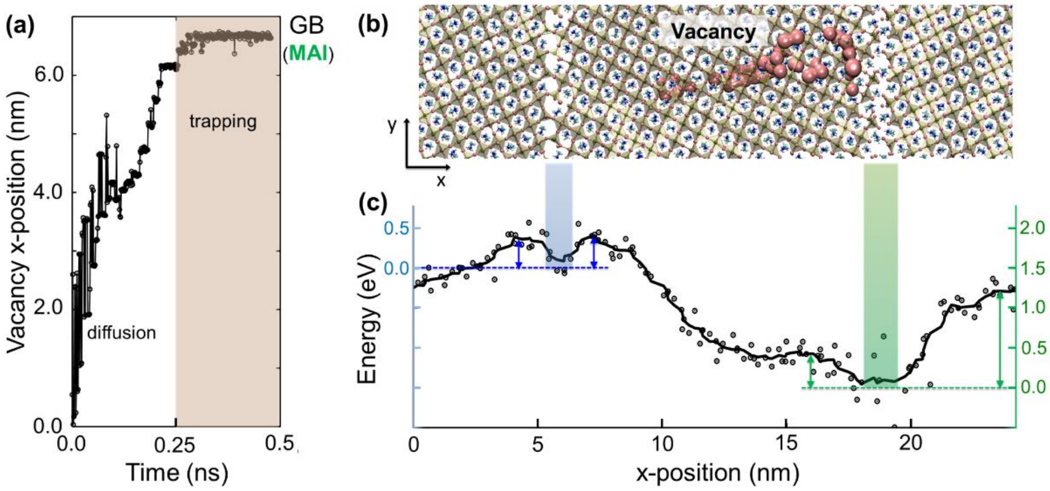

Figure 5.5 (a) The dynamics (*i.e.* x position versus time) of a vacancy in the crystal grain is simulated by molecular dynamics (MD) and it shows that the grain boundaries are able to trap the defects: during the first 0.25 ns of annealing the vacancy diffuses within the grain until it approaches one of the grain boundaries where it remains trapped until the end of the simulation. (b) The atomistic structure of the polycrystalline $MAPbI_3$ model consists of a crystal grain with planar $\Sigma 5/(102)$ boundaries, *i.e.* PbI-terminated (left) and MAI-terminated (right); (c) Potential energy versus position, obtained by placing the iodine vacancy at different atomic sites (along the dashed line); two local energy minima are found at the boundaries (shadowed regions) with the lowest one at the MAI-terminated boundary; the energy barriers for the release of defects are also indicated by arrows.

Atomistic simulations support the hypothesized scenario. Classical molecular dynamics (MD) makes it possible to simulate large-scale models of $MAPbI_3$ including point-defects and GBs. Interatomic forces of $MAPbI_3$ can be modelled by the MYP force field developed by Mattoni *et al.*[49-50] and have been successfully applied to study vibrations and thermodynamic properties of $MAPbI_3$, degradation in water[51-52] as well as diffusion of point-defects.[6] Here, we apply MD to simulate the diffusion of one iodine vacancy (*i.e.* the most mobile point defect in $MAPbI_3$[6]) in presence of the $\Sigma 5/(102)$ grain boundary, *i.e.* a prototypical boundary in $MAPbI_3$ forming along the (102) crystallographic plane with 53.1° tilt angle.[53] The calculated dynamics shows that the mobility of the iodine vacancy is strongly reduced by the presence of boundaries. **Figure 5.5a** shows the position-time plot of the distance between vacancy and GB. The trajectory within the atomistic model is also represented in **Figure 5.5b**. The vacancy is initially placed at the centre of a crystal grain annealed at 400 K for 0.5 ns. We chose this temperature due to higher diffusivity of ions at higher temperature. Note that the diffusion mechanism is unchanged between 400 K and 300 K, whereas higher temperature shortens the simulation time. When the defect is far from the boundary, it diffuses randomly through stochastic jumps induced by temperature. Accordingly, the mean square displacement increases with time and the defect is able to reach the GB after 0.25 ns. Hereafter, the distance of the defect from the boundary remains (essentially) constant until the end of the simulation, indicating a trapping of the defect at the GB. These findings provide a theoretical evidence that GBs can trap defects, thus reducing the overall diffusivity of iodide defects in polycrystalline films.

The physical origin of the trapping can be explained in energetic terms. Grain boundaries are regions of extended defects, typically presenting a local disorder (*e.g.* coordination defects, strain, *etc.*) with a corresponding excess of local energy. Accordingly, the energy of a defect at a GB is lower than in the bulk of the crystalline grain. This is confirmed by the potential energy of the vacancy as a function of the position along the polycrystalline system reported in **Figure 5.5c**, bottom panel. In practice, we compute the potential energy of the system in which we placed an iodine vacancy at different positions along the x direction of the polycrystalline sample after a local relaxation (dashed line in **Figure 5.5b**). The energy profile shows local minima at both GBs (PbI-terminated and MAI-terminated), indicating these positions are energetically favoured with respect to bulk crystalline regions. In order for the defect to escape from the boundaries it is necessary to overcome an energy barrier $\Delta E^{\dagger} \approx 0.5$ eV (1 eV) for the PbI-terminated (MAI-terminated) boundaries. This result is in agreement with the finite temperature dynamics discussed above during which the vacancy is easily captured at the MAI-terminated boundary and hardly released due to the disordered nature of this boundary, constituting a higher energy barrier.

Present experimental and MD results bring us to the following conceptual scheme. i) When the film is excited by the laser, the defect concentration ($V_I^{\bullet}$ I_i’ and possibly the corresponding MA defects) increases (**Figure 5.1**). ii) Defects can migrate towards and get trapped by the absolute energy minimum (MAI-terminated GB), or toward the local minimum (PbI-terminated GB) because of Brownian-like random dynamics, in which defects jump from site to site due to thermal fluctuations (**Figure 5.5a-b**). A net force associated with the energy profile shown in **Figure 5.5c** makes the random jumps asymmetric, which result in a net attraction toward the grain boundaries, where they get trapped. iii) When the perturbation, here the focused laser, ceases its action, the system tends to restore the equilibrium defect concentration by annihilating the excess defects (see **Figure 5.4**). iv) This requires that complementary defects get de-trapped from the grain boundaries, meet and annihilate. In other words, the recovery time is determined by the de-trapping time, which, following the transition state theory,[10, 13, 54] depends exponentially on the barrier $\tau = \hbar/k_B T \, exp\left[\Delta E^{\dagger}/k_B T\right]$, with $\hbar$ Planck constant, k_B Boltzmann constant and T temperature. Thus, a recovery time of minutes/hours, as experimentally observed in **Figure 5.4**, corresponds to a barrier of ~ 0.9/1.1 eV, which is similar to the predictions drawn from the herein shown MD simulations.

5.2 Conclusion

In this study, we related signatures of ion migration to the microstructure of $MAPbI_3$ and studied the effects as well as kinetics of ionic defect migration by photoluminescence (PL) microscopy. By analysing the lateral evolution of PL intensity in a thin film and crystal induced by a focused excitation beam, we concluded that grain boundaries inhibit ion movement. The change in PL yield stems from migrating iodide ions that are likely to saturate corresponding vacancies. At the same time, the PL yield reduction comes from the removal of ions from their crystalline sites, which introduces non-radiative recombination centres. This reduction can last for minutes and hours; however, this process can be partially or fully reversible depending on the microstructure. The recovery of PL confirms the possibility of defects being trapped at GBs proximity, which can migrate back to defective crystalline sites to "heal" the lattice upon cessation of the excitation. The experimental findings are supported by molecular dynamics simulations, confirming the trapping of the iodine vacancy at the grain boundaries. The trapping is explained by the presence of potential energy minima for defects at the grain boundaries. The slow recovery process in the dark can be explained by the presence of energy barriers that defects have to overcome in order to detrap from GBs, after which they can migrate in the crystalline bulk of the grain to encounter the complementary defect and annihilate. We expect that our findings will also help explain the issues faced with long term stability of perovskite solar cells since mobile ionic defects have been shown to play a vital role in degradation mechanisms.[31]

Methods

Samples fabrication:

The glass substrates are cleaned with Mucasol (2%), Acetone and Iso-propanol in ultrasonicator for 15 minutes respectively. Then the substrates are dried with N_2 gun and cleaned in an UV-O_3 cleaner for another 15 minutes. The cleaned substrates are immediately transferred to a glovebox (N_2 atmosphere) to fabricate the perovskite thin films. The perovskite solutions are made of stoichiometric PbI_2 (Tokyo Chemical Industry, 98% purity) and CH_3NH_3I (Dyenamo, 99% purity) in a mixed solvent ratio 6:1 of N,N-Dimethylformamide (Sigma Aldrich, anhydrous, 99.8%) and Dimethyl Sulfoxide (Sigma Aldrich, anhydrous, 99.8%). To make the big-grain films, 2% of PbI_2 is replaced by $Pb(SCN)_2$. The solution is shaken at 60°C for 5 minutes to dissolve all components. 100 µL of perovskite solution is dropped on cleaned substrates, then the following spin coating program is used: 20 seconds at 4000 rpm with ramping steps for 2 seconds to 1000 rpm then 3 seconds to 4000 rpm. 5 seconds before the end of the program, 500 µL Ethyl acetate (Sigma Aldrich, anhydrous, 99.8%) is dropped on the substrates to form a compact film. Immediately after the spin coating, wet perovskite films are annealed at 100 °C for 1 hour. To make the crystal, stoichiometry PbI_2 (Tokyo Chemical Industry, 98% purity) and CH_3NH_3I (Dyenamo, 99% purity) are dissolved in γ-Butyrolactone (*ReagentPlus®*, ≥99%). Subsequently, the solution is heated to 150 °C for 3-8 hours to form crystals. The inverted crystallization method to grow crystal is adopted from Saidaminov *et al.*[34] All the chemicals are used as received.

Solar cells fabrication

The ITO (In-doped SnO_2) substrates are cleaned with the same procedure as above. The cleaned ITO substrates are then coated with $SnCl_2$ (2mg/mL in ethanol) by using 4000 rpm for 30 seconds spin coating program. The wet layers are annealed at 180°C for 1 hour. Then the substrates are transferred to N_2 filled glovebox to deposit perovskite layer as mentioned above. Notably, to make small grain devices, the perovskite layer is annealed at 60°C for 10 minutes then 50 minutes at 100°C whereas big grain devices are annealed at 140°C in first step. Following the perovskite layer, Spiro-OMETAD is used as hole selective layer in which 36.15 mg of Spiro-OMETAD is dissolved in 1 mL of chlorobenzene, doped with 14.40 µL 4-*tert*-Butylpyridine (Sigma Aldrich, 98%), 8.75 µL of Li-TFSI (bis(trifluoromethane)sulfonimide lithium salt, 99.95% trace metals basis, Sigma Aldrich) (300 mg per mL of acetonitrile), and 14.50 µL FK209 (Co(II) salt, Sigma Aldrich)

(500 mg/mL of acetonitrile). Finally, 80 nm of Au (Alfa Aesar, 99.99% purity) is evaporated on top at less than 1 angstrom per second rate to finish the device.

Photoluminescence spectroscopy:

A schematic of the photoluminescence spectroscopy setup is shown in Figure S5.1 (S.I.). The measurement was performed in a homebuilt inverted microscope based on the Olympus IX-71 body. For excitation, we employ the 458 nm line of a CW Argon laser. The only exception is for **Figure 5.1** in which we used a 450 nm diode laser (Thorlabs CPS450). The excitation is either focused or collimated at the back aperture of the objective (Olympus LUCPlanFL 40, NA 0.6) with the use of a collimating lens where the former yields a wide-field excitation spot ("defocused mode") and the latter yields a focused spot ("focused mode"). All the data shown in the study was obtained from measurements which were carried out in ambient conditions. In the supporting information we demonstrate similar phenomenon of redistribution of PL in space for a single crystal (see videos SV2 for measurement in air and SV4 for measurement in N_2, S.I.).

Time-resolved photoluminescence (trPL) measurements were carried out in a home-built setup with an excitation wavelength of 660 nm from a pulsed supercontinuum laser light source (SuperK Extreme) operating at 304 kHz repetition rate. The spot size was 25-35 μm in diameter and the pulse fluence of 10-30 nJ/cm^2 was chosen in order to generate an equivalent number of charge carriers as would be expected under 1 sun conditions (1.5E+21 photons $\cdot m^{-2} \cdot s^{-1}$). PL was collected panchromatically and the decay was recorded using time-correlated single photon counting with a PicoHarp TCSPC Module by PicoQuant.

Scanning electron microscopic and Energy-dispersive X-ray spectroscopy:

The SEM/EDX images are acquired with Hitachi S4100 at 30k magnification. The voltages used for SEM and EDX are 5 keV and 12.5 keV respectively.

Classical Molecular Dynamics (MD):

The model of a polycrystal with Σ5/102 twin boundaries was obtained by: (i) cutting an orthorhombic crystal of $MAPbI_3$ with (102) surfaces; (ii) generating a replica by a mirror-symmetry about one of the surfaces; (iii) merging the two crystals after a relative shift aimed at optimal match of atoms at the boundary; (iv) applying periodic boundary conditions. The 4032-atoms model obtained by this procedure was first optimized by conjugate gradient forces minimization, then heated to 300 K or 400 K and annealed for 0.3 ns. Vacancy was generated by removal of one iodine atom and its position identified by calculating atomic coordination. The vacancy trajectory and diffusion was studied during 0.5 ns constant number of particles, pressure and temperature (NPT) dynamics at 400 K and 1 bar.

The energy profile was obtained by: (i) choosing an atomic configuration equilibrated at 300 K; (ii) selecting the iodine atoms along a linear region orthogonal to the boundaries (see Figure 5); (iii) placing one vacancy at each of the selected positions; (iv) optimizing positions and energy by forces minimization; (iv) collecting all data as a function of position. The profile is obtained by a local running average. All simulations were performed by using the LAMMPS code.[55]

5.3 Supporting Information

SI videos

aenm201903735-sup-0002-VideoS1.mp4	Supplemental Video 1 (SV1)
aenm201903735-sup-0003-VideoS2.mp4	Supplemental Video 2 (SV2)
aenm201903735-sup-0004-VideoS3.mp4	Supplemental Video 3 (SV3)
aenm201903735-sup-0005-VideoS4.mp4	Supplemental Video 4 (SV4)

5.3.1 Micro-Photoluminescence

For excitation, we employ the 458 nm line of a CW Argon laser. The only exception is for **Figure 5.1** in which we used a 450 nm diode laser (Thorlabs CPS450). The excitation is either focused or collimated at the back aperture of the objective (Olympus LUCPlanFL 40, NA 0.6) with the use of a collimating lens where the former yields a wide-field excitation spot ("defocused mode") and the latter yields a focused spot ("focused mode") shown in **Figure S5.1A**. The two images in the schematic show PL images generated from a reference film demonstrating the excitation spot size for the two modes. In both modes, light is collected from the entire field of view spanning up to 40 μm in diameter. The undesired back reflection from the excitation is filtered out at the dichroic mirror after which the desired PL is passed through a tube lens forming an image at the same position we place a variable slit. With the use of a relay lens, the image is passed to the CCD camera (Princeton Instruments Pro-EM).

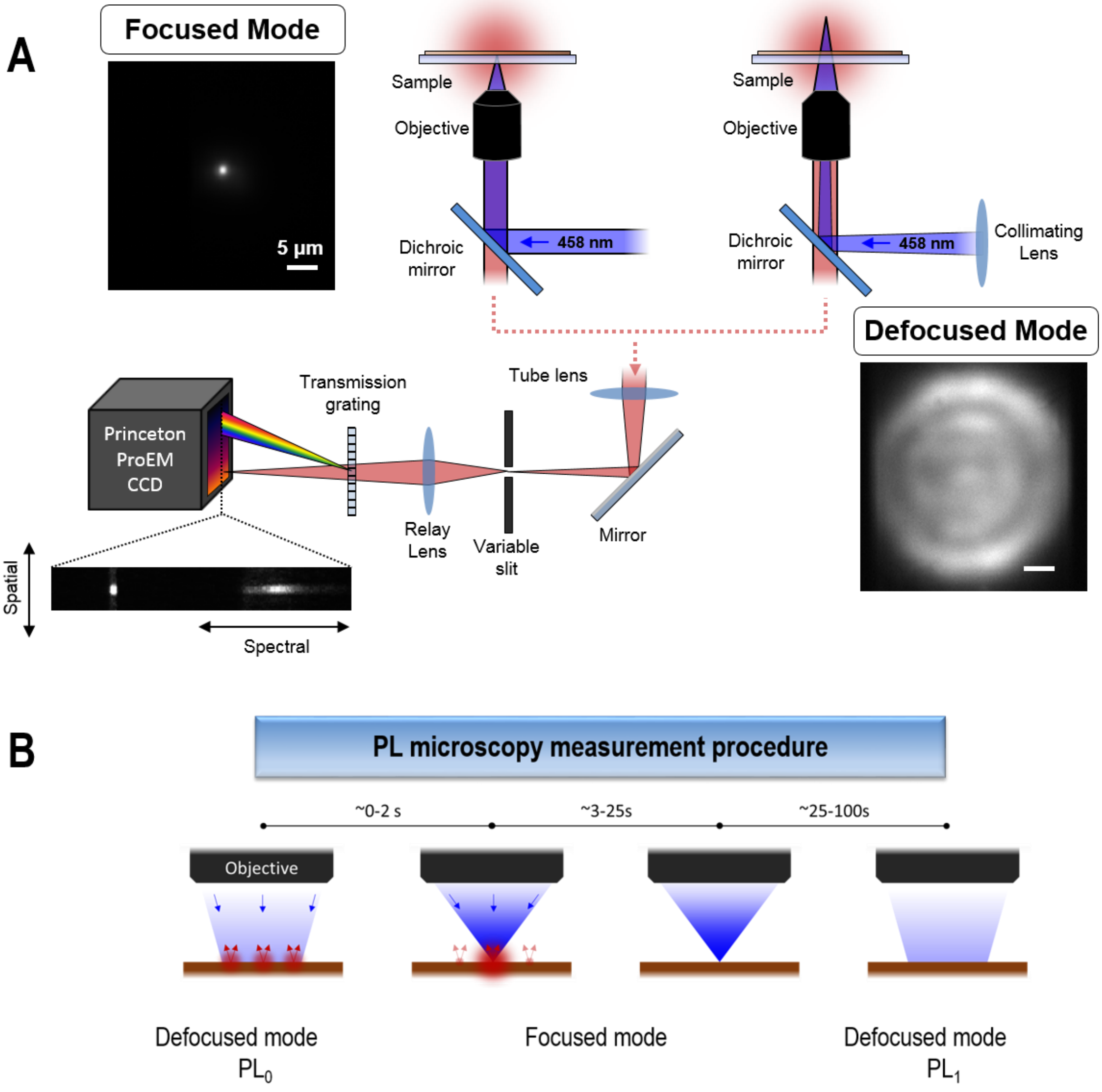

Figure S5.1. A) Schematic of the experimental setup. The images are acquired in the two excitation modes (focused – left, defocused – right) by collecting PL from a substrate covered with high-lighter ink. Switching between the two modes is done via the 'collimating lens'. The scale bar in both images represents 5 µm. B) Schematic of the measurement procedure from left to right where the sample is initially exposed to a defocused/wide-field excitation. The PL image acquired in this mode is referred to as PL_0. After a few seconds, the excitation is focused for a few seconds, after which the defocused excitation mode is returned to record the image PL_1. The blue arrows represent the direction of the excitation and the red arrows the PL. The transparency of the blue shaded region represents the excitation density.

Alternating between the two modes can be done within a few 100 ms by flipping a lens in and out of the excitation path. In comparison to the rate at which PL changes were observed (several 100 ms to seconds), the transition is negligible. Each measured region had no prior exposure to light before recording any PL. The measurements started with the excitation in the defocused mode, after which the excitation was changed the focused mode for 20 seconds. Finally, the excitation was returned to the defocused mode in order to compare the spatial distribution of PL prior to the defocused mode. **Figure S5.1B** schematically shows the measurement procedure from left to right for a typical experiment, with the time for each excitation mode indicated in seconds. The excitation density for focused mode is 2540 W/cm^2. In the measurements where we compare a PL image prior to (PL_0) and after (PL_1) focused excitation, we extract the relative PL changes in the measure $\Delta PL = PL_0/PL_1$, as described in the main text.

5.3.2 Microstructure of the sample

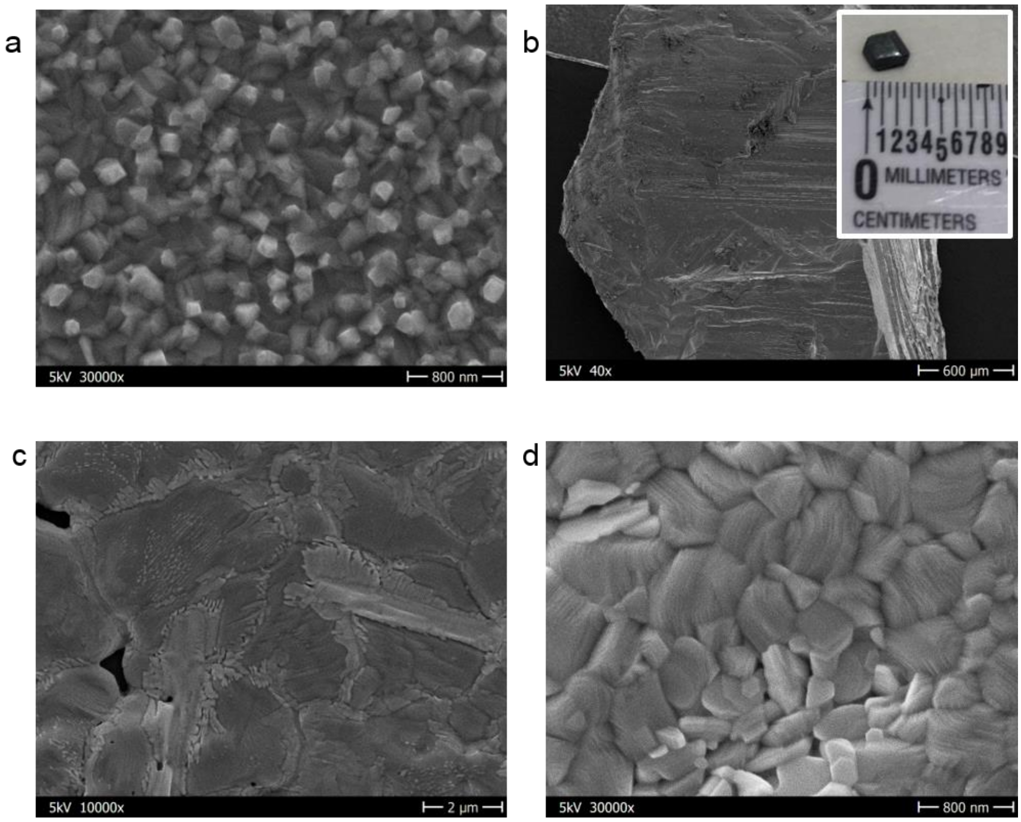

Figure S5.2 The different samples used in this study: a) the top view SEM micrograph of thin film, b) the cross-sectional SEM micrograph of crystal and the photograph of one representative crystal, and c) the top view SEM micrograph of big-grain film used for PL measurement, d) the top view SEM micrograph of big grain film used for device fabrication

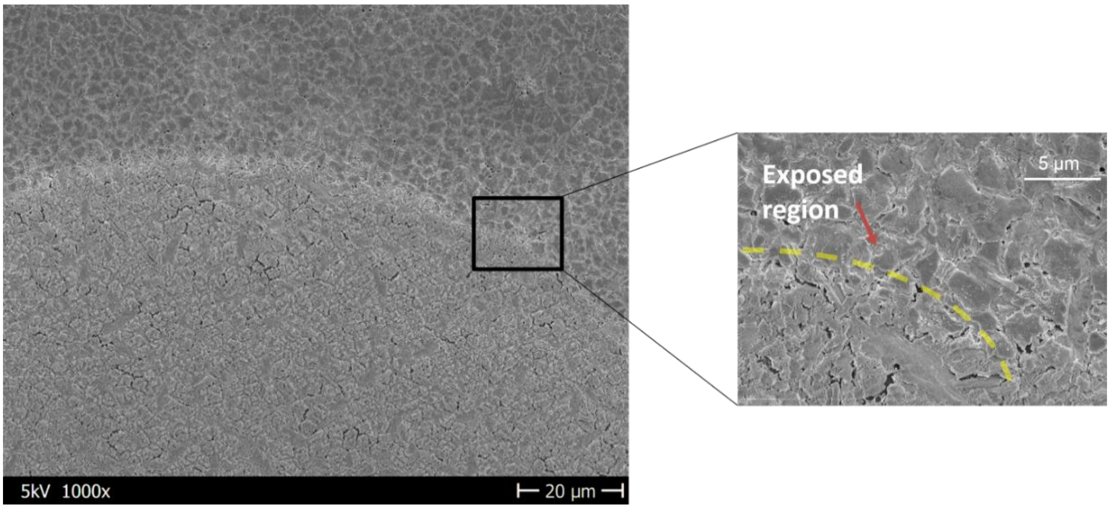

Figure S5.3 Light-induced morphology change in big grain film. The light exposure part exhibits thinning similar to small grain with more cracks and holes compare to the outside area.

5.3.3 Optical characterization

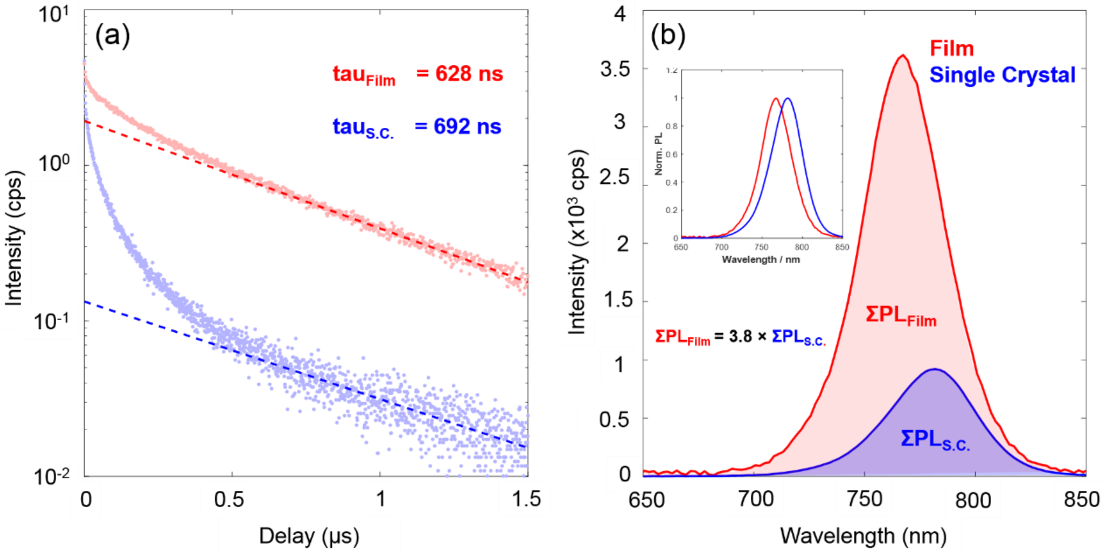

Figure S5.4 (a) TRPL decays measured for thin-film (small grain) (red) and crystal (black) with 660 nm excitation wavelength. Pulse fluence was 25 nJ·cm^{-2} and 30 nJ·cm^{-2} for the thin film and single crystal respectively. The monomolecular lifetime is obtained by fitting the tail with a single exponential and is indicated with the dashed colored lines. Lifetimes extracted for the two samples are comparable (628 ns and 692 ns respectively). (b) PL spectra measured of the thin film (red) and single (crystal) plotted without normalization. The integrated intensities according to the shaded region demonstrate a yield 3.8 times higher for the thin film. Normalized PL spectra in the inset show a red-shifted peak for the single crystal which may be caused by re-absorption of the PL generated within the thick crystal.

Figure S5.4a shows time-resolved PL (TRPL) measurements which indicate a similar decay time between the crystal and film besides at early times. Applying an exponential tail fit to both decays (dashed lines) both the thin film and single crystal exhibit long lifetimes of ~628 ns and 692 ns respectively, assuring a high-quality material with similar *surface* defect densities. Since PL is here limited by the non-passivated air interface, it does not allow for conclusions about the bulk crystal defect densities. However, it is important to note that the surface-dominated TRPL decay time of the single crystal is similar to that of the film. It has been shown by Zhong *et al.*[48] that the surface defect density can affect how the material behaves under light soaking. Hence, in this study, we chose samples with similar surface defect densities, underlining that the massive difference in the density of grain boundaries dictates the halide migration dynamics.

In **Figure S5.4b** we also show the PL spectra of the film and crystal acquired with the same measurement conditions (excitation density, exposure time and camera gain). From the spectrally integrated PL, it can be seen that the relative PL yield of the film is 3.8 times higher than the single crystal. Nonetheless, this can be attributed to the photobrightening effect well documented in the literature.[43] This, in conjunction with potential errors due to scattering or reflections caused by differences in the sample morphology, certainly introduce relevant fluctuations where this value should be taken lightly. Since the difference in the relative PL yield is not orders of magnitude, we assume that the PLQYs of the two samples are comparable, which is also corroborated by the monomolecular lifetime being similar (**Figure S5.4a**).

Another notable feature is that the PL peak of the single crystal is slightly red-shifted compared to the film. The difference in PL peak positions is likely due to the thickness difference between crystal and film which causes the reabsorption of emitted PL in crystal.[56] We fit the two spectra with an asymmetric Voigt line shape,[57] and find the asymmetry coefficient (α) which can detect whether the peak is asymmetric toward shorter ($-2 > \alpha > 0$) or longer ($0 > \alpha > 2$) wavelengths. We find that the emission peak from the film is essentially symmetric ($\alpha = -0.008$) while the peak from the single crystal exhibits relevant asymmetry toward higher energies ($\alpha = -0.09$). This is a typical signature of reabsorption of photons overlapping with the absorption spectrum of the material and is therefore a plausible explanation for why the peaks differ. Moreover, since the time-resolved PL was measured panchromatically, this reabsorption feature is not observed.

References

1. Saliba, M.; Matsui, T.; Seo, J.-Y.; Domanski, K.; Correa-Baena, J.-P.; Nazeeruddin, M. K.; Zakeeruddin, S. M.; Tress, W.; Abate, A.; Hagfeldt, A.; Grätzel, M., Cesium-containing triple cation perovskite solar cells: improved stability, reproducibility and high efficiency. *Energy & environmental science* **2016,** *9* (6), 1989-1997.
2. Lin, K.; Xing, J.; Quan, L. N.; de Arquer, F. P. G.; Gong, X.; Lu, J.; Xie, L.; Zhao, W.; Zhang, D.; Yan, C.; Li, W.; Liu, X.; Lu, Y.; Kirman, J.; Sargent, E. H.; Xiong, Q.; Wei, Z., Perovskite light-emitting diodes with external quantum efficiency exceeding 20 per cent. *Nature* **2018,** *562* (7726), 245.
3. Dou, L.; Yang, Y. M.; You, J.; Hong, Z.; Chang, W.-H.; Li, G.; Yang, Y., Solution-processed hybrid perovskite photodetectors with high detectivity. *Nature communications* **2014,** *5*, 5404.
4. Ahmad, S.; George, C.; Beesley, D. J.; Baumberg, J. J.; De Volder, M., Photo-Rechargeable Organo-Halide Perovskite Batteries. *Nano letters* **2018,** *18* (3), 1856-1862.
5. Meggiolaro, D.; De Angelis, F., First-Principles Modeling of Defects in Lead Halide Perovskites: Best Practices and Open Issues. *ACS Energy Letters* **2018,** *3* (9), 2206-2222.
6. Delugas, P.; Caddeo, C.; Filippetti, A.; Mattoni, A., Thermally activated point defect diffusion in methylammonium lead trihalide: anisotropic and ultrahigh mobility of iodine. *The journal of physical chemistry letters* **2016,** *7* (13), 2356-2361.
7. Eames, C.; Frost, J. M.; Barnes, P. R.; O'regan, B. C.; Walsh, A.; Islam, M. S., Ionic transport in hybrid lead iodide perovskite solar cells. *Nature communications* **2015,** *6*, 7497.
8. Zhao, C.; Chen, B.; Qiao, X.; Luan, L.; Lu, K.; Hu, B., Revealing underlying processes involved in light soaking effects and hysteresis phenomena in perovskite solar cells. *Advanced Energy Materials* **2015,** *5* (14), 1500279.
9. Snaith, H. J.; Abate, A.; Ball, J. M.; Eperon, G. E.; Leijtens, T.; Noel, N. K.; Stranks, S. D.; Wang, J. T.-W.; Wojciechowski, K.; Zhang, W., Anomalous hysteresis in perovskite solar cells. *The journal of physical chemistry letters* **2014,** *5* (9), 1511-1515.
10. Meloni, S.; Moehl, T.; Tress, W.; Franckevičius, M.; Saliba, M.; Lee, Y. H.; Gao, P.; Nazeeruddin, M. K.; Zakeeruddin, S. M.; Rothlisberger, U.; Graetzel, M., Ionic polarization-induced current–voltage hysteresis in $CH_3NH_3PbX_3$ perovskite solar cells. *Nature communications* **2016,** *7*, 10334.
11. Domanski, K.; Roose, B.; Matsui, T.; Saliba, M.; Turren-Cruz, S.-H.; Correa-Baena, J.-P.; Carmona, C. R.; Richardson, G.; Foster, J. M.; De Angelis, F.; Ball, J. M.; Petrozza, A.; Mine, N.; Nazeeruddin, M. K.; Tress, W.; Grätzel, M.; Steiner, U.; Hagfeldt, A.; Abate, A., Migration of cations induces reversible performance losses over day/night cycling in perovskite solar cells. *Energy & Environmental Science* **2017,** *10* (2), 604-613.
12. Khenkin, M. V.; Anoop, K.; Visoly-Fisher, I.; Galagan, Y.; Di Giacomo, F.; Patil, B. R.; Sherafatipour, G.; Turkovic, V.; Rubahn, H.-G.; Madsen, M.; Merckx, T.; Uytterhoeven, G.; Bastos, J. P. A.; Aernouts, T.; Brunetti, F.; Lira-Cantu, M.; Katz, E. A., Reconsidering figures of merit for performance and stability of perovskite photovoltaics. *Energy & Environmental Science* **2018,** *11* (4), 739-743.
13. Azpiroz, J. M.; Mosconi, E.; Bisquert, J.; De Angelis, F., Defect migration in methylammonium lead iodide and its role in perovskite solar cell operation. *Energy & Environmental Science* **2015,** *8* (7), 2118-2127.
14. Walsh, A.; Scanlon, D. O.; Chen, S.; Gong, X.; Wei, S. H., Self-regulation mechanism for charged point defects in hybrid halide perovskites. *Angewandte Chemie International Edition* **2015,** *54* (6), 1791-1794.
15. Yuan, Y.; Chae, J.; Shao, Y.; Wang, Q.; Xiao, Z.; Centrone, A.; Huang, J., Photovoltaic switching mechanism in lateral structure hybrid perovskite solar cells. *Advanced Energy Materials* **2015,** *5* (15), 1500615.
16. Shao, Y.; Fang, Y.; Li, T.; Wang, Q.; Dong, Q.; Deng, Y.; Yuan, Y.; Wei, H.; Wang, M.; Gruverman, A.; Shield, J.; Huang, J., Grain boundary dominated ion migration in polycrystalline organic–inorganic halide perovskite films. *Energy & Environmental Science* **2016,** *9* (5), 1752-1759.
17. Yun, J. S.; Seidel, J.; Kim, J.; Soufiani, A. M.; Huang, S.; Lau, J.; Jeon, N. J.; Seok, S. I.; Green, M. A.; Ho-Baillie, A., Critical role of grain boundaries for ion migration in formamidinium and methylammonium lead halide perovskite solar cells. *Advanced Energy Materials* **2016,** *6* (13), 1600330.

18. Xing, J.; Wang, Q.; Dong, Q.; Yuan, Y.; Fang, Y.; Huang, J., Ultrafast ion migration in hybrid perovskite polycrystalline thin films under light and suppression in single crystals. *Physical Chemistry Chemical Physics* **2016,** *18* (44), 30484-30490.

19. Correa-Baena, J. P.; Anaya, M.; Lozano, G.; Tress, W.; Domanski, K.; Saliba, M.; Matsui, T.; Jacobsson, T. J.; Calvo, M. E.; Abate, A.; Grätzel, M.; Míguez, H.; Hagfeldt, A., Unbroken Perovskite: Interplay of Morphology, Electro-optical Properties, and Ionic Movement. *Advanced Materials* **2016,** *28* (25), 5031-5037.

20. Leijtens, T.; Hoke, E. T.; Grancini, G.; Slotcavage, D. J.; Eperon, G. E.; Ball, J. M.; De Bastiani, M.; Bowring, A. R.; Martino, N.; Wojciechowski, K.; McGehee, M. D.; Snaith, H. J.; Petrozza, A., Mapping Electric Field-Induced Switchable Poling and Structural Degradation in Hybrid Lead Halide Perovskite Thin Films. *Advanced Energy Materials* **2015,** *5* (20), 1500962.

21. Caddeo, C.; Filippettia, A.; Mattoni, A., The Dominant Role of Surfaces in the Hysteretic Behavior of Hybrid Perovskites. *Nano Energy* **2019**, 104162.

22. deQuilettes, D. W.; Zhang, W.; Burlakov, V. M.; Graham, D. J.; Leijtens, T.; Osherov, A.; Bulović, V.; Snaith, H. J.; Ginger, D. S.; Stranks, S. D., Photo-induced halide redistribution in organic–inorganic perovskite films. *Nature communications* **2016,** *7*, 11683.

23. Li, C.; Guerrero, A.; Zhong, Y.; Gräser, A.; Luna, C. A. M.; Köhler, J.; Bisquert, J.; Hildner, R.; Huettner, S., Real-Time Observation of Iodide Ion Migration in Methylammonium Lead Halide Perovskites. *Small* **2017,** *13* (42), 1701711.

24. Chen, S.; Wen, X.; Huang, S.; Huang, F.; Cheng, Y. B.; Green, M.; Ho-Baillie, A., Light illumination induced photoluminescence enhancement and quenching in lead halide perovskite. *Solar Rrl* **2017,** *1* (1), 1600001.

25. Merdasa, A.; Kiligaridis, A.; Rehermann, C.; Abdi-Jalebi, M.; Stöber, J.; Louis, B.; Gerhard, M.; Stranks, S. D.; Unger, E. L.; Scheblykin, I. G., Impact of Excess Lead Iodide on the Recombination Kinetics in Metal Halide Perovskites. *ACS Energy Letters* **2019,** *4*, 1370-1378.

26. Galisteo-López, J. F.; Li, Y.; Míguez, H. n., Three-dimensional optical tomography and correlated elemental analysis of hybrid perovskite microstructures: an insight into defect-related lattice distortion and photoinduced ion migration. *The journal of physical chemistry letters* **2016,** *7* (24), 5227-5234.

27. Galisteo-López, J. F.; Calvo, M. E.; Míguez, H., Spatially Resolved Analysis of Defect Annihilation and Recovery Dynamics in Metal Halide Perovskite Single Crystals. *ACS Applied Energy Materials* **2019,** *2* (10), 6967-6972.

28. Jeon, N. J.; Noh, J. H.; Kim, Y. C.; Yang, W. S.; Ryu, S.; Seok, S. I., Solvent engineering for high-performance inorganic–organic hybrid perovskite solar cells. *Nature materials* **2014,** *13* (9), 897.

29. Cappel, U. B.; Svanström, S.; Lanzilotto, V.; Johansson, F. O.; Aitola, K.; Philippe, B.; Giangrisostomi, E.; Ovsyannikov, R.; Leitner, T.; Föhlisch, A.; Svensson, S.; Mårtensson, N.; Boschloo, G.; Lindblad, A.; Rensmo, H., Partially reversible photoinduced chemical changes in a mixed-ion perovskite material for solar cells. *ACS applied materials & interfaces* **2017,** *9* (40), 34970-34978.

30. Merdasa, A.; Bag, M.; Tian, Y.; Källman, E.; Dobrovolsky, A.; Scheblykin, I. G., Super-resolution luminescence microspectroscopy reveals the mechanism of photoinduced degradation in CH3NH3PbI3 perovskite nanocrystals. *The Journal of Physical Chemistry C* **2016,** *120* (19), 10711-10719.

31. Motti, S. G.; Meggiolaro, D.; Martani, S.; Sorrentino, R.; Barker, A. J.; De Angelis, F.; Petrozza, A., Defect Activity in Metal–Halide Perovskites. *Advanced Materials* **2019**, 1901183.

32. Sadoughi, G.; Starr, D. E.; Handick, E.; Stranks, S. D.; Gorgoi, M.; Wilks, R. G.; Bär, M.; Snaith, H. J., Observation and mediation of the presence of metallic lead in organic–inorganic perovskite films. *ACS applied materials & interfaces* **2015,** *7* (24), 13440-13444.

33. Senocrate, A.; Moudrakovski, I.; Acartürk, T.; Merkle, R.; Kim, G. Y.; Starke, U.; Grätzel, M.; Maier, J., Slow CH3NH3+ diffusion in CH3NH3PbI3 under light measured by solid-state NMR and tracer diffusion. *The Journal of Physical Chemistry C* **2018,** *122* (38), 21803-21806.

34. Saidaminov, M. I.; Abdelhady, A. L.; Murali, B.; Alarousu, E.; Burlakov, V. M.; Peng, W.; Dursun, I.; Wang, L.; He, Y.; Maculan, G.; Goriely, A.; Wu, T.; Mohammed, O. F.; Bakr, O. M., High-quality bulk hybrid perovskite single crystals within minutes by inverse temperature crystallization. *Nature communications* **2015,** *6*, 7586.

35. Stranks, S. D.; Eperon, G. E.; Grancini, G.; Menelaou, C.; Alcocer, M. J.; Leijtens, T.; Herz, L. M.; Petrozza, A.; Snaith, H. J., Electron-hole diffusion lengths exceeding 1 micrometer in an organometal trihalide perovskite absorber. *Science* **2013,** *342* (6156), 341-344.

36. Merdasa, A.; Tian, Y.; Camacho, R.; Dobrovolsky, A.; Debroye, E.; Unger, E. L.; Hofkens, J.; Sundström, V.; Scheblykin, I. G., "Supertrap" at Work: Extremely Efficient Nonradiative Recombination Channels in MAPbI3 Perovskites Revealed by Luminescence Super-Resolution Imaging and Spectroscopy. *ACS nano* **2017,** *11* (6), 5391-5404.

37. Pazos-Outón, L. M.; Szumilo, M.; Lamboll, R.; Richter, J. M.; Crespo-Quesada, M.; Abdi-Jalebi, M.; Beeson, H. J.; Vrućinić, M.; Alsari, M.; Snaith, H. J.; Ehrler, B.; Friend, R. H.; Deschler, F., Photon recycling in lead iodide perovskite solar cells. *Science* **2016,** *351* (6280), 1430-1433.

38. Motti, S. G.; Meggiolaro, D.; Barker, A. J.; Mosconi, E.; Perini, C. A. R.; Ball, J. M.; Gandini, M.; Kim, M.; De Angelis, F.; Petrozza, A., Controlling competing photochemical reactions stabilizes perovskite solar cells. *Nature Photonics* **2019,** *13*, 532–539.

39. Pazoki, M.; Jacobsson, T. J.; Kullgren, J.; Johansson, E. M.; Hagfeldt, A.; Boschloo, G.; Edvinsson, T., Photoinduced stark effects and mechanism of ion displacement in perovskite solar cell materials. *ACS nano* **2017,** *11* (3), 2823-2834.

40. Anaya, M.; Galisteo-López, J. F.; Calvo, M. E.; Espinós, J. P.; Míguez, H., Origin of light-Induced photophysical effects in organic metal halide perovskites in the presence of oxygen. *The journal of physical chemistry letters* **2018,** *9* (14), 3891-3896.

41. Adhyaksa, G. W.; Brittman, S.; Āboliņš, H.; Lof, A.; Li, X.; Keelor, J. D.; Luo, Y.; Duevski, T.; Heeren, R. M.; Ellis, S. R.; Fenning, D. P.; Garnett, E. C., Understanding detrimental and beneficial grain boundary effects in halide perovskites. *Advanced Materials* **2018,** *30* (52), 1804792.

42. Kutes, Y.; Zhou, Y.; Bosse, J. L.; Steffes, J.; Padture, N. P.; Huey, B. D., Mapping the photoresponse of CH3NH3PbI3 hybrid perovskite thin films at the nanoscale. *Nano letters* **2016,** *16* (6), 3434-3441.

43. Tian, Y.; Peter, M.; Unger, E.; Abdellah, M.; Zheng, K.; Pullerits, T.; Yartsev, A.; Sundström, V.; Scheblykin, I. G., Mechanistic insights into perovskite photoluminescence enhancement: light curing with oxygen can boost yield thousandfold. *Physical Chemistry Chemical Physics* **2015,** *17* (38), 24978-24987.

44. Yang, M.; Zeng, Y.; Li, Z.; Kim, D. H.; Jiang, C.-S.; van de Lagemaat, J.; Zhu, K., Do grain boundaries dominate non-radiative recombination in $CH_3NH_3PbI_3$ perovskite thin films? *Physical Chemistry Chemical Physics* **2017,** *19* (7), 5043-5050.

45. Courtier, N. E.; Cave, J. M.; Foster, J. M.; Walker, A. B.; Richardson, G., How transport layer properties affect perovskite solar cell performance: insights from a coupled charge transport/ion migration model. *Energy & Environmental Science* **2019,** *12* (1), 396-409.

46. Ceratti, D. R.; Rakita, Y.; Cremonesi, L.; Tenne, R.; Kalchenko, V.; Elbaum, M.; Oron, D.; Potenza, M. A. C.; Hodes, G.; Cahen, D., Self-Healing Inside APbBr3 Halide Perovskite Crystals. *Advanced Materials* **2018,** *30* (10), 1706273.

47. Merdasa, A.; Tsarev, S.; Akbulatov, A. F.; Troshin, P.; Unger, E. L., Microscopic insight into the reversibility of photodegradation in MAPbI3 thin films. *J. Lumin.* **2019**, 116916.

48. Zhong, Y.; Luna, C. A. M.; Hildner, R.; Li, C.; Huettner, S., In situ investigation of light soaking in organolead halide perovskite films. *APL Materials* **2019,** *7* (4), 041114.

49. Mattoni, A.; Filippetti, A.; Saba, M.; Delugas, P., Methylammonium rotational dynamics in lead halide perovskite by classical molecular dynamics: the role of temperature. *The Journal of Physical Chemistry C* **2015,** *119* (30), 17421-17428.

50. Mattoni, A.; Filippetti, A.; Caddeo, C., Modeling hybrid perovskites by molecular dynamics. *J. Phys.: Condens. Matter* **2016,** *29* (4), 043001.

51. Caddeo, C.; Melis, C.; Saba, M. I.; Filippetti, A.; Colombo, L.; Mattoni, A., Tuning the thermal conductivity of methylammonium lead halide by the molecular substructure. *Physical Chemistry Chemical Physics* **2016,** *18* (35), 24318-24324.

52. Caddeo, C.; Saba, M. I.; Meloni, S.; Filippetti, A.; Mattoni, A., Collective Molecular Mechanisms in the CH3NH3PbI3 Dissolution by Liquid Water. *ACS nano* **2017,** *11* (9), 9183-9190.

53. Long, R.; Liu, J.; Prezhdo, O. V., Unravelling the effects of grain boundary and chemical doping on electron–hole recombination in CH3NH3PbI3 perovskite by time-domain atomistic simulation. *Journal of the American Chemical Society* **2016,** *138* (11), 3884-3890.

54. Truhlar, D. G.; Garrett, B. C.; Klippenstein, S. J., Current status of transition-state theory. *The Journal of physical chemistry* **1996,** *100* (31), 12771-12800.

55. Plimpton, S., Fast parallel algorithms for short-range molecular dynamics. *Journal of computational physics* **1995,** *117* (1), 1-19.

56. Hong, D.; Li, J.; Wan, S.; Scheblykin, I. G.; Tian, Y., Red-shifted Photoluminescence from Crystal Edges Due to Carrier Redistribution and Re-absorption in Lead Triiodide Perovskite. *The Journal of Physical Chemistry C* **2019**.

57. Kojima, I.; Kurahashi, M., Application of asymmetrical Gaussian/Lorentzian mixed function for X-ray photoelectron curve synthesis. *J. Electron. Spectrosc. Relat. Phenom.* **1987,** *42* (2), 177-181.

Chapter 6 Ionic Defect Migration-Induced Amorphization and Phase Segregation

This chapter is based on the peer-reviewed article "**Ion Migration-Induced Amorphization and Phase Segregation as a Degradation Mechanism in Planar Perovskite Solar Cells**". The manuscript is under review by the time of writing this dissertation. Reproduced with permission.

Abstract

The operation of halide perovskite optoelectronic devices, including solar cells and LEDs, is strongly influenced by mobile ions in halide perovskites. This is particularly true when considering the long-term stability of these devices. A detailed understanding of the ion migration driven degradation pathways is critical in order to design effective stabilization strategies. Nonetheless, despite substantial research in this first decade of perovskite photovoltaics, the long-term effects of ion migration remain elusive due to the complex chemistry of lead halide perovskites. Here, by linking materials chemistry to device optoelectronics, this study highlights that, along with phase segregation, electrical bias induced perovskite amorphization is a crucial degradation mechanism causing losses in power conversion efficiency in planar perovskite solar cells. In particular, depending on the biasing potential and the injected charge, halide segregation occurs, forming crystalline iodide-rich domains which govern light emission and participate in light absorption and photocurrent generation. However, the loss of crystallinity strongly limits charge collection efficiency.

6.1 Introduction

Metal halide perovskites have achieved extraordinary results as a photovoltaic (PV) material, recently surpassed 25% in certified power conversion efficiency (PCE).[1,2] This outstanding achievement is made possible by perovskites' advantageous optoelectronic properties, including long charge carrier diffusion length[3] and steep light absorption onset.[4] The stoichiometry for the perovskite structure is ABX_3, where A is a monovalent cation (*e.g.* methylammonium (MA^+), formamidinium (FA^+) or caesium (Cs^+)), B is a divalent cation (commonly Pb^{2+} or Sn^{2+}), and X is a halide. Tuning the composition of this class of materials varies their bandgaps.[5,6] Hence, halide perovskites can be a suitable absorber material for both single junction and multi-junction solar cells.[7] Notably, the facile deposition of hybrid perovskites offers an opportunity for incorporation with commercial PV technologies, such as silicon, in a tandem architecture.[8] Further, compositional engineering has been a pivotal step to improve the efficiency and stability of perovskite solar cells. This has enabled the adoption of FA-based perovskites, which have better thermal stability than methylammonium lead iodide ($MAPbI_3$).[9–11] Saliba *et al.* introduced the "triple cation" perovskite with a $Cs_{0.05}(FA_{0.83}MA_{0.17})_{0.95}Pb(I_{0.83}Br_{0.17})_3$ stoichiometry, henceforth labelled CsFAMA, which is now a standard in the perovskite community.[12]

Lead halide perovskites are mixed ionic-electronic conductors, and this has a profound impact on solar cell behaviour. Hysteresis in current density-voltage (J-V) scans has been attributed at least partially to ion migration,[13,14] which is broadly identified as one of the leading causes of perovskite solar cells' instability,[15] compromising the structural integrity of the perovskite film and of the whole device.[16–19] Together with ion migration, chemical and electrochemical[20] interactions of perovskite constituent ions with the selective contacts[21–23] and electrodes[24–26] can degrade the devices. However, the detailed mechanisms behind ion migration-driven hysteresis and degradation remain elusive, due to the chemical complexity of perovskite systems and the coupling between electronic and ionic current, which renders experimental design challenging.

Applying an electrical bias to a solar cell is the most direct way to investigate ion-driven instabilities in a full device. For instance, in our previous work, we investigated hysteresis in the dark, which is linked to interface instability due to the interaction of perovskite with selective contacts.[21] The importance of selective contacts on the electrical bias stability was further highlighted by an *in-situ* transmission electron microscopy (TEM) investigation by Jung *et al.*, who observed the migration of oxygen from TiO_2 to

$MAPbI_3$ in forward bias.[27] In a similar experiment, morphological and chemical degradation was observed at the spiro-OMeTAD / $MAPbI_3$ interface due to the interaction between iodide and spiro-OMeTAD.[28] Different studies reported the formation of PbI_2 as a degradation product due to biasing of $MAPbI_3$ films.[29–32] However, most of these studies employed ad-hoc devices (*e.g.* lateral devices), which are not entirely representative of standard solar cell architectures. Similarly, investigations on 'half-cell' configurations are also unrepresentative, where both electrostrictive behaviour of perovskite films[33] and the formation of periodically striped ferroelastic domains have been observed with scanning probe microscopy.[34] Similarly, Luchkin *et al.* showed changes in surface topography upon biasing the perovskite film.[35] It remains to be seen whether the same phenomenon occurs in a full device, where both perovskite surfaces are covered with a selective contact and an electrode. Furthermore, upon biasing, the devices are subjected to charge injection, which might induce unpredictable processes if only the ions' drift-diffusion behavior is accounted for. For instance, there is clear evidence that a high concentration of charge carriers and interface electrochemistry drive halide segregation.[36–38]

In this work, we investigated the effects of ion migration and charge injection by forward biasing planar p-i-n perovskite solar cells (PSCs) on a time scale of hours, simulating to a certain extent the electrical load experienced during 1 day of PV operation. We aim to advance the understanding of PSCs instabilities due to ionic conductivity by bridging the gap between the materials chemistry and the device performances and optoelectronics. Except for TEM, all characterizations were performed *in-situ*, with the bias applied directly on the sample during the measurement to minimize (or avoid) the effects of relaxation and fully observe the consequences of electrical bias on the device.

We found perovskite amorphization as the primary mechanism behind the loss in PV performances. In addition, the device optoelectronics behaviour is also affected by halide segregation. The iodide-rich crystalline domains govern the light emission and participate (inefficiently) in the generation of photocurrent. The charge collection is severely hindered by the amorphous phase, pointing to degradation at the interfaces between perovskite and charge selective layers.

6.2 Result and discussion

6.2.1 Device performance upon biasing

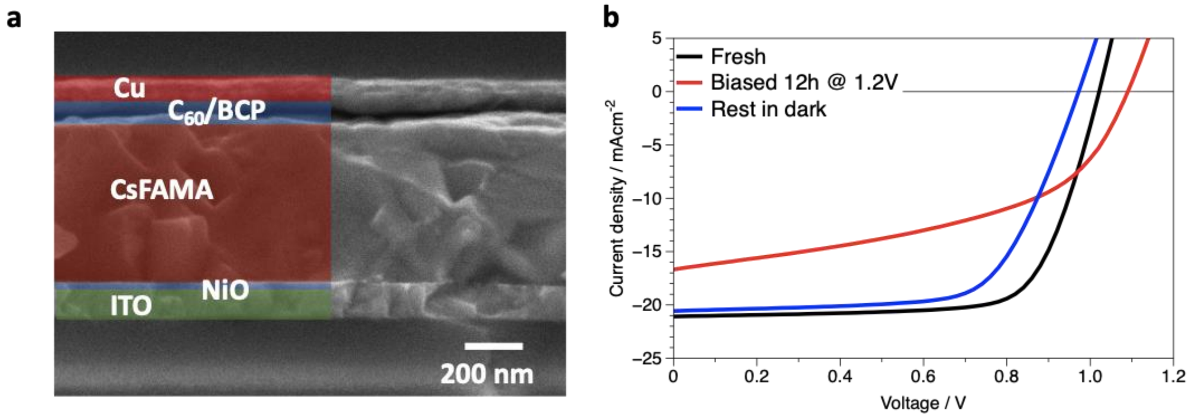

Figure 6.1 **a** SEM cross-section and architecture of the PSCs employed in this work. CsFAMA stands for the $Cs_{0.05}((FAPbI_3)_{0.83}(MAPbBr_3)_{0.17})_{0.95}$ perovskite composition. **b** J-V curves of a fresh cell (black), after bias at 1.2 V in the dark for 12 hours (red), and after rest in the dark for 6 hours (blue).

In this study, we employed a planar p-i-n configuration consisting of glass/ITO/NiO/CsFAMA/C_{60}/BCP/Cu (**Figure 6.1a**). This is one of the most promising systems in term of stability.[39, 40] Moreover, the lack of hysteresis in p-i-n devices simplifies the analysis of the device behaviour. With our fabrication procedure, detailed in the experimental section, we obtain devices with negligible hysteresis and PCEs approaching 18%, in line with NiO-based PSCs in literature.[41–44] Statistics and reproducibility of PV parameters are reported in the Supporting Information (SI), Figure S6.1.

In **Figure 6.1b**, we report the effect on J-V curves of 12 hours of polarization at 1.2 V in the dark. In this condition, we are simulating/accelerating the effect of operating voltage on ion migration and at a current density similar to under PV operation (further discussion on this point is in note SI6.1 and Figure S6.2, SI). This stress test considerably decreases the short circuit current (J_{SC}, from 21.1 $mAcm^{-2}$ to 16.5 $mAcm^{-2}$) and fill factor (FF, from 73% to 48%) of the device while increasing the open circuit voltage (V_{OC}) by 70 mV. Overall, the device efficiency is reduced by about 50% (relative), from 16% to 8% (absolute). Note that a similar effect on the J-V curve is obtained when biasing the device at 1 V, slightly below the V_{OC} (Figure S6.3). This *biased-state* is not stable, and after resting in the dark and in inert (N_2) atmosphere for 6 hours, the FF and J_{SC} partially recover their initial values and the V_{OC} stabilises below its initial value. This slow recovery from the *biased-state* might stem from the gradual relaxation of ionic distribution induced by the bias, similarly to the case of reversible PCE losses over a day (stress) / night (recovery) cycling.[15]

To gain insight into the crystal quality of the perovskite layer during the stress test, we performed *in-situ* X-ray diffraction (XRD) while biasing at 1.2 V in the dark. It must be noted that the diameter of the incident X-ray beam is about 1 cm at the sample surface, while the width of one cell is 0.6 cm. Therefore, XRD patterns were collected partially from the adjacent unbiased area, thus quantitative analysis underestimates the observed phenomena. A duplicate XRD measurement without biasing was done to exclude the possibility of X-ray beam-induced perovskite damage influencing our results. In this control experiment, we observed no changes in the diffraction patterns after 8 hourly scans (Figure S6.4).

6.2.2 Material characterisation: amorphization at the interfaces

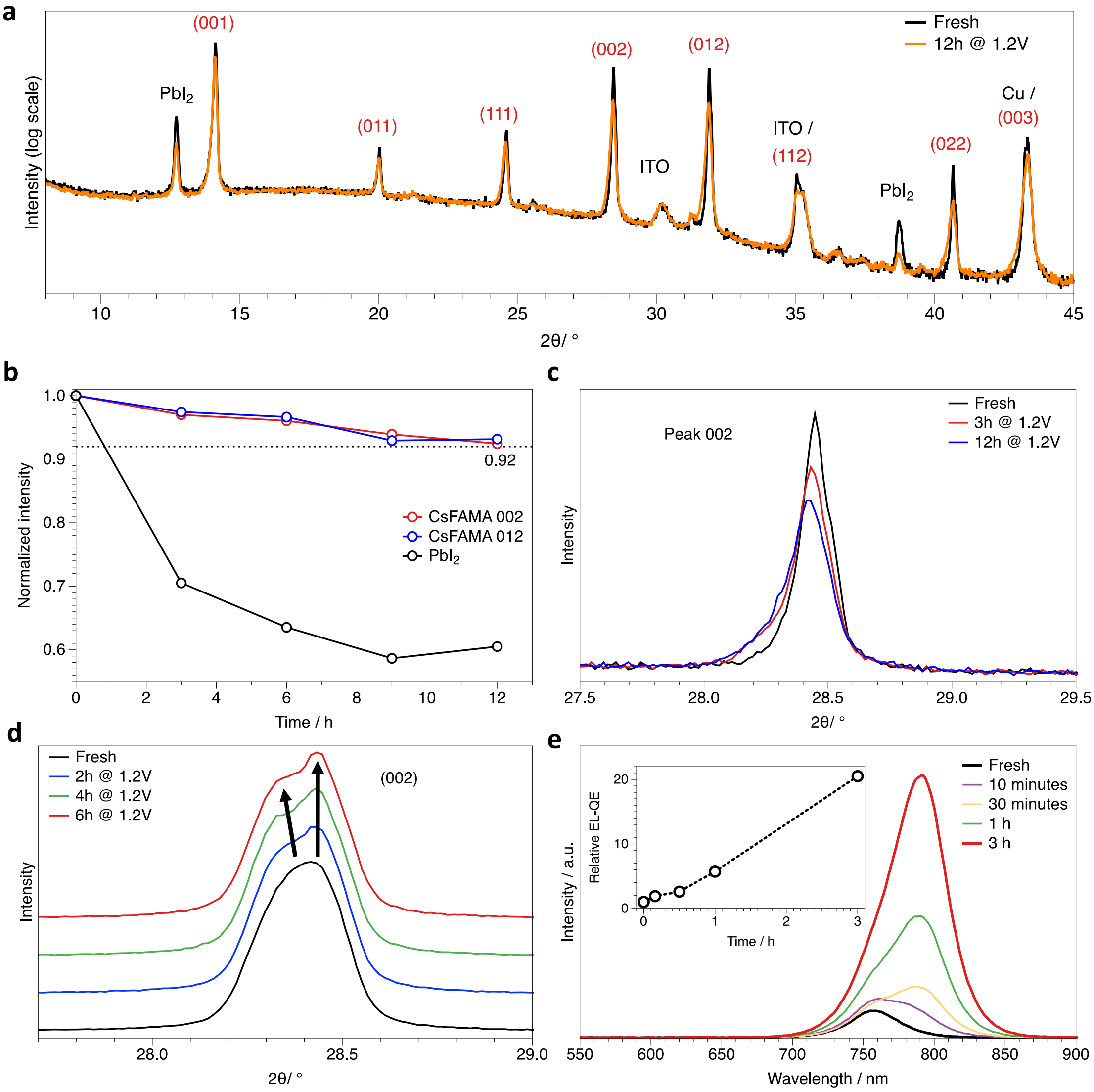

Figure 6.2 **a** Comparison between the XRD patterns of the fresh sample (black) and collected after 12h of continuous forward bias at 1.2 V (orange). The intensity is plotted on a logarithmic scale to highlight low-intensity peaks and to confirm that no crystalline phases are present other than Cu, ITO, PbI_2 and perovskite. Indexing of XRD peaks from perovskite is depicted in red, taken from ref[45]. There is overlapping of perovskite peaks with ITO (~35°) and Cu (~43°), as explained in Figure S6.5. **b** Variation of the integrated intensity of selected peaks during biasing. **c** Detail from (a) highlighting the peak associated with the (002) plane of the perovskite phase at ~28.4°. **d** Evolution of the perovskite peak at 28.4°, obtained from in-situ GIWAXS measurements, showing peak splitting upon biasing at 1.2 V in the dark. **e** Evolution of EL spectrum upon biasing the cell at 1.2 V in the dark. In the inset, the EL quantum efficiency (EL-QE) is plotted relative to the fresh sample (EL-QE = 1), which increases by a factor of 20 after 3 hours of biasing. A gradual transition of peak emission wavelength from 760 nm for the fresh sample to 790 nm after 3h bias is observed.

In **Figure 6.2a**, we show the comparison of the full XRD pattern of the fresh sample and after 12 hours of biasing at 1.2 V in the dark. In **Figure 6.2b**, we show the decline of the integrated intensity of representative peaks (*i.e.* 12.7° for PbI_2 and 14.2° and 28.4° for perovskite) over stress time, which is proportional to the variation of the coherently diffracting domain of the pertaining crystalline phase.[46,47] Interestingly, the PbI_2 XRD peak decreases by 40% (see also Figure SI5), suggesting that crystalline PbI_2 is not the degradation product of CsFAMA perovskite under the effect of bias, as in the case of $MAPbI_3$.[48] Along with the reduction of crystalline PbI_2, the loss of perovskite crystallinity is observed, with the reduction of scattering intensity around 10% indicating a reduction in the long range ordering of the structure and pointing towards amorphization. It is widely accepted that biasing a PSC leads to the formation of ionic space charge at the interfaces of perovskite with selective contacts, which affects the doping profile and charge dynamics at the interfaces; this is considered the main reason for J-V hysteresis.[13,49] Our results show that in addition to above effects, ion migration on a time scale comparable to daily PV operations induces the partial collapse of the perovskite structure. The asymmetric broadening of perovskite XRD peaks (representative 002 peak is magnified in **Figure 6.2c**) can be explained by either the introduction of inhomogeneous tensile strain[50] or the appearance of new species with the same perovskite crystalline structure and a slightly larger unit cell. A synchrotron-based *in-situ* grazing incidence wide angle X-ray scattering (GI-WAXS) experiment clarified that the evolution of the peak shape arises from peak splitting, as shown in **Figure 6.2d**. This result is similar to the finding by Andaji-Garmaroudi *et al.*[51] and is a strong indicator of halide segregation,[52] with the additional crystalline species reasonably being ascribed to an iodide-rich perovskite (see Figure S6.7).

To confirm the presence of iodide phase, the devices were subjected to electroluminescence (EL) measurement to examine this hypothesis. As can be seen in **Figure 6.2e**, the appearance of iodide rich domains is evident from the evolution of the EL spectrum upon biasing, in agreement with the results from Ruf *et al.* employing the same CsFAMA stoichiometry as in this work.[53] A low-bandgap emitting species is detected already after a few minutes, and it governs light emission after 3h of biasing at 1.2 V. The EL peak of the 3h *biased-state* stabilizes at 790 nm (1.57 eV), a 30 nm red-shift from the pristine state's 760 nm peak (1.63 eV). The iodide-rich phase after 3h biasing is not a pure iodide triple-cation perovskite ($Cs_{0.05}(FA_{0.83}MA_{0.17})_{0.95}PbI_3$), whose emission peak is located at 805 nm (1.54 eV, see Figure S6.8). A putative halide ratio of this low-bandgap emitting species can be obtained by estimating a linear relation between the bandgap and halide composition,[7] which yields an iodide percentage of 94%. In this calculation, we assume that the A-site cation composition does not change in the low-bandgap perovskite. The stable EL peak position upon biasing of the $Cs_{0.05}(FA_{0.83}MA_{0.17})_{0.95}PbI_3$ perovskite (see Figure S6.8) supports this assumption. Thus, the observed EL peak shift is likely due to halide segregation rather than cation segregation[54]. Nevertheless, further investigations are needed to definitively establish the cation composition in this lower bandgap region. The increase of EL quantum efficiency (EL-QE) is always observed in cases of halide segregation.[37, 52] However, this is also seen with $Cs_{0.05}(FA_{0.83}MA_{0.17})_{0.95}PbI_3$ or $MAPbI_3$ (Figure S6.8), despite constant EL peak position. This suggests a possible convolution of different processes rather than only halide segregation causing the increase in EL-QE. The evolution of optoelectronic properties of halide perovskite in time scales of seconds to minutes can be rationalized through ion migration-induced defect formation or annihilation,[55–57] and similar argument can be used to explain the increment of EL-QE.

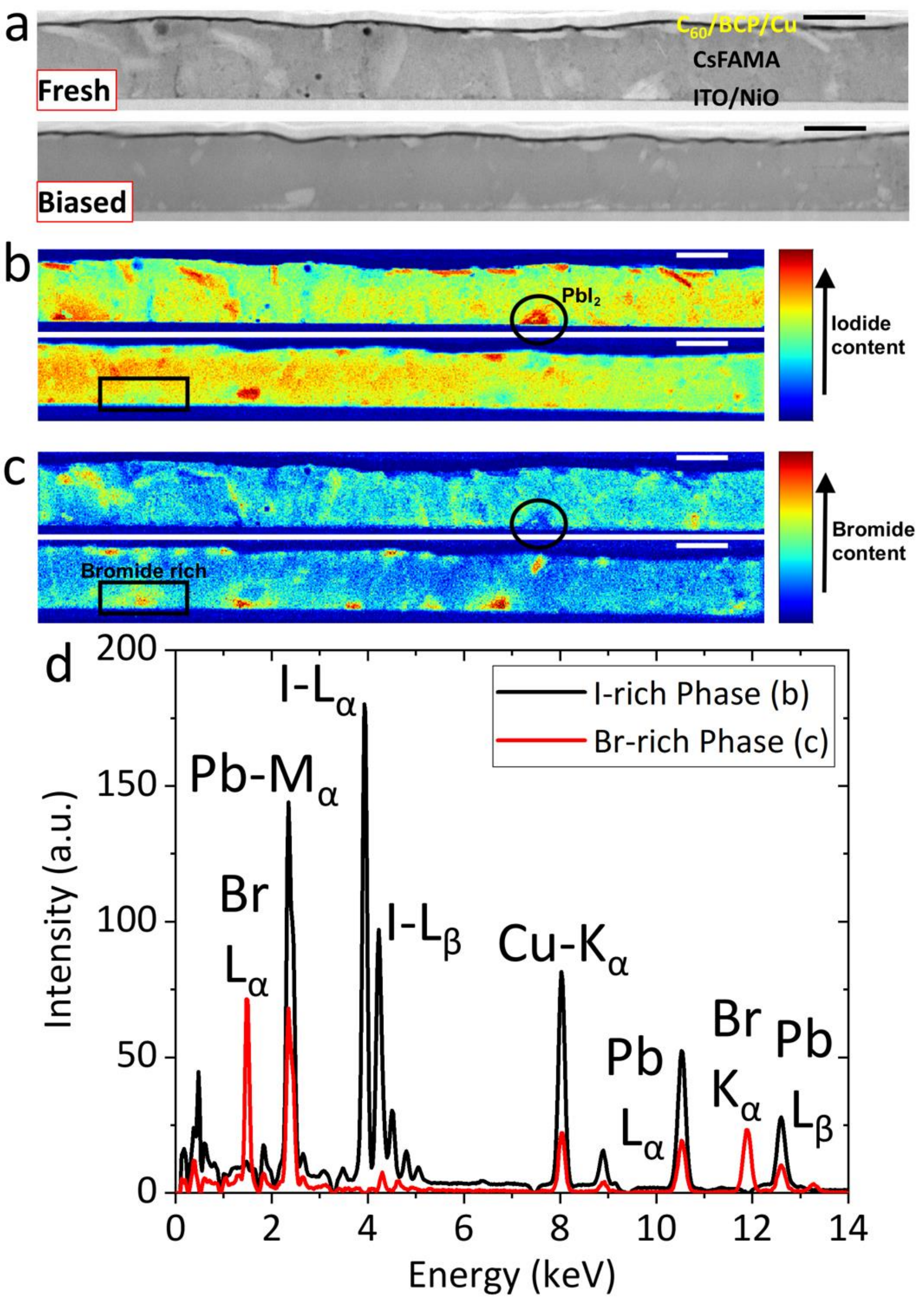

Figure 6.3 **a** Cross-sectional scanning transmission electron microscopy-high-angle annular dark-field (STEM-HAADF) micrographs for the fresh PSC (top) and after 12h at 1.2 V bias in the dark (bottom). The dark circular spot in the STEM-HAADF micrograph for the fresh device arises from localized beam damage. **b-c** Non-negative matrix factorization (NMF) loadings (maps) of selected components, with the fresh sample at the top and biased sample at the bottom of each pair (b) iodide-rich perovskite phase and PbI_2 (see the main text for a detailed discussion) and (c) bromide-rich perovskite phase. **d** NMF factors (spectra) of the loadings displayed in (b) and (c). All scale bars are 0.5 µm. Numbers on the colour scale in (b, c) are in a.u. Copper peaks in (d) are from the TEM sample grid.

Together with crystallinity, the morphology and chemical composition of the perovskite film are essential figures of merit in halide perovskite PV. To gain insights into the effect of biasing on perovskite film morphology and composition inside the device, a scanning transmission electron microscopy (STEM) characterization on cross-sections of full devices was performed. **Figure 6.3a** shows the cross-sectional high-angle annular dark-field (HAADF) images of the fresh and biased samples. The comparison of the HAADF micrographs with and without biasing shows that the structural integrity of the device is preserved. We did not detect any copper penetration from the electrode into the active layers underneath (Figure S6.9). This indicates a negligible influence of the metal electrode on changes in the device J-V curves and optoelectronic properties.[17] Further, **Figure 6.3a** shows changes in the spatial distribution of the relatively bright spots in the perovskite layer. These are distributed throughout the whole film in the fresh device but accumulated at both perovskite-selective contact interfaces after biasing. We treated the energy-dispersive X-ray (STEM-EDX) spectroscopic data with non-negative matrix factorization (NMF) for extraction of physically interpretable components to gain insight on the perovskite chemical composition (see the methods or ref 58 for more details on this). Selected NMF components are displayed in **Figure 6.3b, c** and Figure S6.9. The colour of each pixel in a component's loading (map) indicates the relative contribution of that component's factor (spectrum) in that pixel's original EDX spectrum. Hence, **Figure 6.3b** shows the spatial distribution of iodine and lead while **Figure 6.3c** does the same for bromine and lead. The fresh perovskite device exhibits both iodide and bromide component as expected. However, we can see that after biasing, the iodide-rich phase becomes more dominant in the bulk of the perovskite layer (**Figure 6.3b**) while small bromide-rich areas form at both perovskite-selective contact interfaces (**Figure 6.3c**). The composition contrast of these iodide/bromide rich phases is more evident in **Figure 6.3d** where the iodide rich cluster has different elemental intensity compared to the bromide one.

Another exciting feature is the appearance of the red features (grains) in **Figure 6.3b**. These grains (representative grain is circled) are unique because they show substantial contribution (red) from the iodide-rich component but very close to zero contribution (dark blue) from the bromine-rich component. Since crystalline PbI_2 is revealed by XRD analysis, we suggest that these grains are PbI_2. Biasing reduced both the number and size of these grains (**Figure 6.3c**), in good agreement with our XRD data and suggests that there is a PbI_2 loss (*e.g.* a dissolution of these crystallites within the film). With similar reasoning, we can infer that the bromide-rich areas formed after biasing in **Figure 6.3c** are not representative of $PbBr_2$ because the NMF components are showing moderate iodide content in **Figure 6.3b** (area denoted by the rectangle). We note that an amorphous window has been reported in the compositional space of $FAPb(I_xBr_{1-x})_3$, when $0.3 < x < 0.5$.[59] This can explain the lack of an evident shoulder at high angles for bromide rich phase in XRD (**Figure 6.3c** and Figure S6.5) and GI-WAXS (**Figure 6.3d** and Figure

S6.6) perovskite peaks, despite the presence of those bromide rich grains at the interfaces with selective contacts.

6.2.3 Effect of amorphization on the devices

The anti-correlation found between V_{OC} and crystallinity after biasing is intriguing and unexpected. In fact, the rise in V_{OC} (and FF) of NiO-based p-i-n mixed-cation, mixed-halide PSCs after illumination has been correlated with a light-induced lattice strain relaxation by Tsai *et al.*[60] Similarly, lattice strain in perovskite films has been shown to correlate with the magnitude of non-radiative recombination.[61] This relation between perovskite crystallinity and carrier dynamics has been further supported by other reports.[62, 63] Moreover, an amorphous or nearly-amorphous matrix is expected to have a large defect concentration, which should promote nonradiative recombination, detrimentally affecting the V_{OC}. Nonetheless, an enhancement of photoluminescence quantum yield in the vicinity of amorphous grain boundaries compared to grain interior has been observed in a ~30 µm-grain size $MAPbBr_3$ film.[64] Similarly, Xiong *et al.* have demonstrated efficient luminescence from amorphous perovskite nanoparticles.[65] Notably, by simultaneously monitoring PV parameters and perovskite film formation, Alsari *et al.* observed a peak in the V_{OC} when a large amount of amorphous material was not yet crystallized, pointing to a self-passivation effect by the amorphous starting material.[66] Therefore, a definitive rationalization of the enhanced V_{OC} cannot be provided based solely on this study since very little is known about amorphous hybrid perovskite states in literature.

Nonetheless, a passivation mechanism activated during the stress test has to be considered, and we speculate that it is due to three effects. Firstly, defects healing due to the excess iodide from the crystallised PbI_2 reduction can be a reasonable mechanism as halide vacancies are the dominant defects in halide perovskite.[67] Secondly, the bromide rich phase, which is expected to have wider band-gap than the original CsFAMA perovskite, can act as an interfacial passivation layer. Thirdly, the improved compositional uniformity of the perovskite bulk highlighted by the TEM analysis is likely to contribute to the increase in V_{OC}[68]. By investigating the dynamics of EL in $MAPbI_3$-based LED, Rand *et al.* proposed that short-range ion migration can have a defect-curing effect (increase of EL-QE), while long-range ion migration should be detrimental, leading to structural collapse (decrease of EL-QE).[69] In our case, ion migration can improve the bulk quality of perovskite by homogenization, as long as there is no ion accumulation. On the other hand, if the migrating ions accumulate at the interfaces, the excessive defect concentration could drive the collapse of the perovskite lattice.

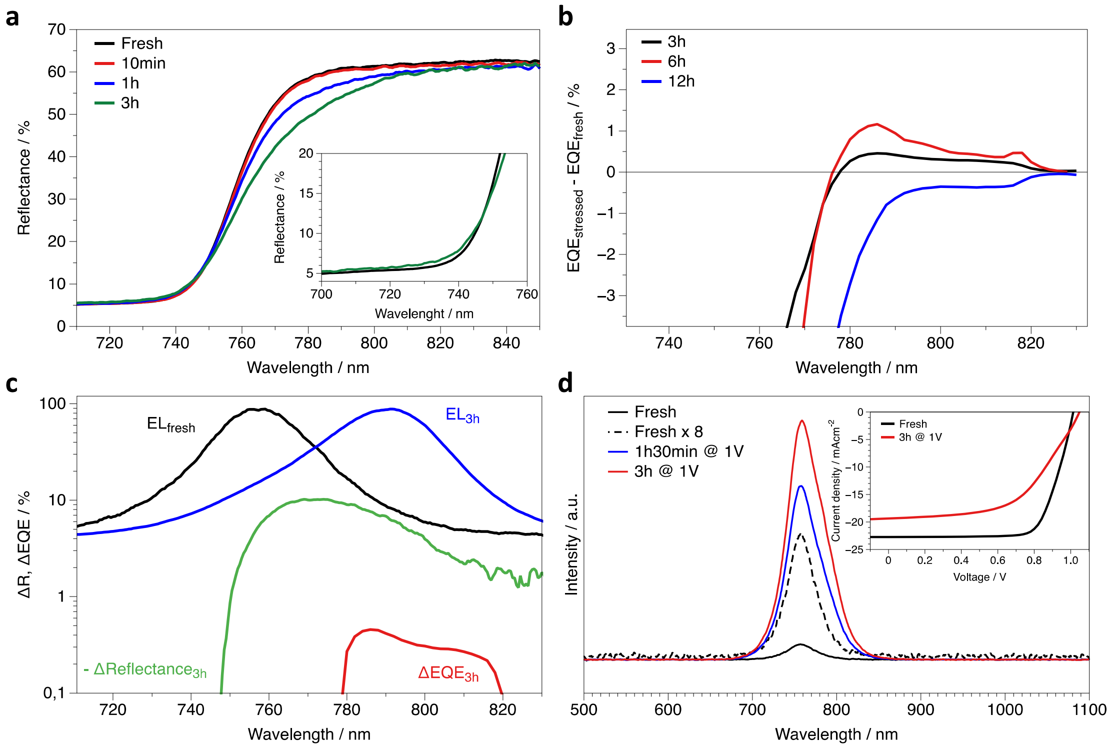

Figure 6.4 a In-situ reflectance experiment of full device biased at 1.2 V in the dark. In the inset is highlighted the increase in reflectance attributable to the diminution of the original perovskite composition. **b** Differential external quantum efficiency ($\Delta EQE = EQE_{biased} - EQE_{fresh}$) around the bandgap of the perovskite. The EQE is measured with a 2 nm step size. **c** Comparison of variation in EQE (**Figure 6.4b**), reflectance (**Figure 6.4a** with the sign changed from negative to positive), and EL peak position (**Figure 6.2e**) after 3h of biasing. The increase in the EQE at longer wavelengths is in close correlation with the light emission from the low bandgap perovskite and the decrease of the reflectance. EL curves are plotted with respect to the x-axis (peak emission wavelength) only, for comparison with $-\Delta Reflectance_{3h}$ and ΔEQE_{3h}. **d** Evolution of EL peak upon biasing at 1.0 V (injected current density around 1 mAcm^{-2}). In the inset, the effect of this stress test on J-V curves.

Two hypotheses can explain the worsening of charge extraction, which is the reason for PCE loss. The first hypothesis is that the iodide-rich domains trap the charges, thus reducing J_{SC} and FF. The second hypothesis is that the amorphous perovskite at the interfaces hinders charge transport and collection, due to poor conductivity of this amorphous material.[64,70] We investigated the role of the iodide-rich phase by looking at the modification in light absorption and photo-current generation at wavelengths longer than 760 nm (bandgap of the CsFAMA perovskite). **Figure 6.4a** shows the results of an *in-situ* reflectance experiment on the biased devices near the bandgap region (Figure S6.10 shows the complete spectra in agreement with our previous work[71]). Here we observe a significant and gradual decrease of reflectance for wavelengths above 750 nm, accompanied by a small increase in the 720-745 nm range (inset, in agreement with the loss of the original perovskite composition due to amorphization). The decrease in reflectance above the bandgap can stem from light absorption from the iodide rich phase as well as from an increase of energetic disorder of the perovskite, leading to a broader absorption onset (the two mechanisms can co-exist).

In **Figure 6.4b**, we show the differential external quantum efficiency (EQE) around the bandgap of the perovskite, obtained by subtracting the EQE of the fresh device from the EQE after biasing (EQE_{biased} - EQE_{fresh}, see experimental section for more details on this analysis). Although the differential EQE is negative at wavelengths shorter than 750 nm (greater than 1.65 eV), remarkably, below the band gap (>770 nm) EQE increased by 1-2% (absolute). This enhancement increases further with longer biasing (3h to 6h), but then disappears at 12h. In **Figure 6.4c** we compare the differential reflectance and EQE after 3 hours of bias with the EL peak positions from the original CsFAMA and from the low band gap specimen. An excellent agreement is found between the small positive contribution to the EQE upon biasing (ΔEQE_{3h}) and the EL peak governed by the iodide-rich phase, proving that the iodide-rich perovskite (inefficiently) contributes to the photocurrent. For the sake of clarity, we stress that the positive signal in the differential EQE above 770 nm is decidedly weak. Nonetheless, the conclusion that iodide-rich phase can contribute to the photo-current is supported by the analysis of PTAA-based devices (see Figure S6.11), for which the EQE below the band-gap is markedly higher, implying that the efficiency of photocurrent generation from the low band gap domains depends also on the selective contacts. Notably, the selective contacts also influence the device degradation pathways (discussion in conjunction with Figure S6.11).

To understand if charge trapping and inefficient photocurrent generation from iodide-rich domains are the primary sources of FF and J_{SC} losses, we performed a stress test at 1 V in the dark. In this case, the injected charge is markedly lower than at 1.2 V and appears not enough to induce halide segregation[37] as proven by the stable EL peak position (**Figure 6.4d**). Nonetheless, the effect on the J-V curve is very close to what is obtained at 1.2 V, with a decrease in FF and J_{SC} and an increase of V_{OC} (see also Figure S6.3). This finding supports the second hypothesis: the primary mechanism behind PCE loss is the worsened charge extraction caused by amorphization of perovskite.

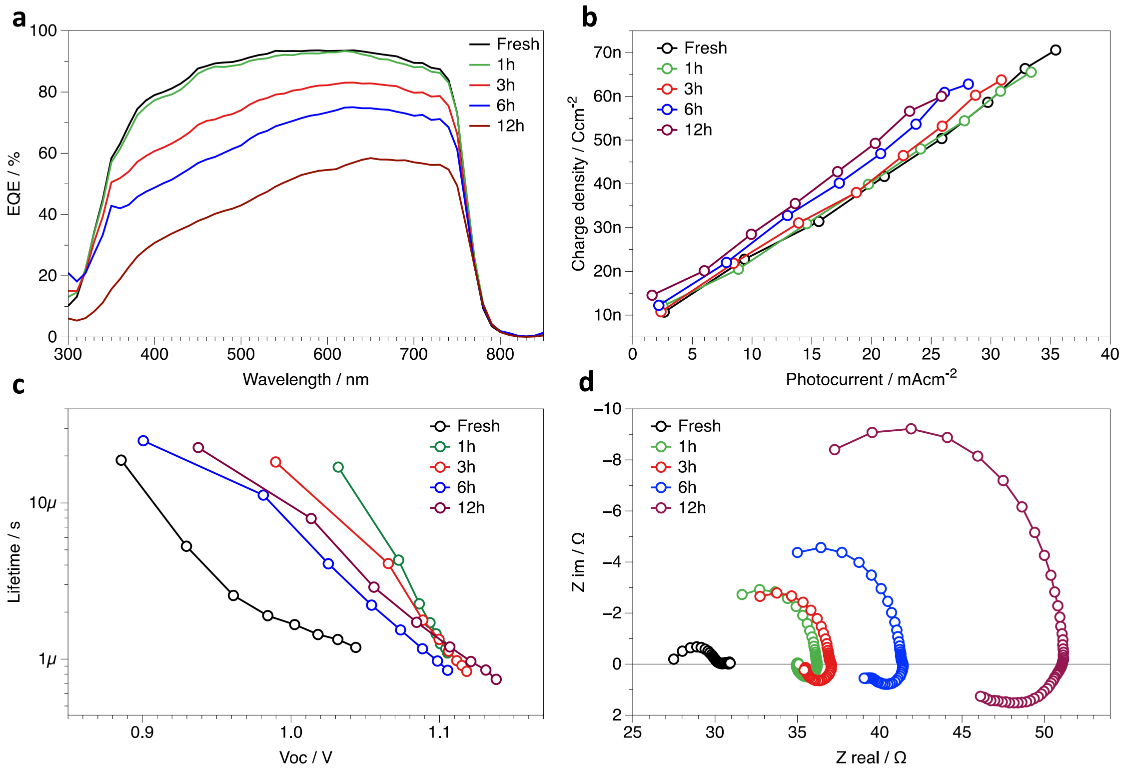

Figure 6.5 a Variation in external quantum efficiency (EQE) upon biasing at 1.2 V in the dark showing asymmetry in the EQE reduction. **b** Evolution of charge accumulation with respect to the J_{SC} over biasing time as obtained from the charge extraction experiment whilst biasing the device at 1.2 V in the dark. **c** Evolution of carrier lifetimes with respect to the V_{OC} over biasing time as obtained from transient photovoltage experiment upon biasing the device at 1.2 V in the dark. **d** Nyquist plot showing evolution of spectroscopic impedance at 1.2 V in the dark upon biasing the device in the same conditions.

The evolution of the EQE upon biasing, as shown in **Figure 6.5a**, exhibits a substantial drop of EQE, especially at short wavelengths range (350-450 nm). The extinction coefficient of perovskite at short wavelengths is very high (*ca.* 10^5cm^{-1}),[72] implying a steep hole-electron pair generation profile. Therefore, the EQE in this part of the spectrum is more sensitive to the quality of the interface closer to the direction of the incoming light (NiO/perovskite in this case). The high photocurrent loss in this wavelength range supports the hypothesis that perovskite amorphization is mainly localized at the interfaces. Charge extraction (CE) experiments confirm a lower J_{SC} for biased devices (**Figure 6.5b** and Figure S6.12). The J_{SC} loss increases with the duration of the stress test and is more significant at high illumination levels. Interestingly, from the analysis of the charge density accumulated in the device and extracted only after the light pulse is switched off, it appears that more recombination is introduced into the device upon biasing. In fact, at high illumination levels, we observe a decrease in both the photocurrent and the charge density extracted in dark, which implies that a more substantial part of the photo-generated charges recombines without being collected. This contradicts the higher V_{OC} and carrier lifetimes obtained from transient photovoltage (TPV) analysis after biasing (**Figure 6.5c** and Figure S6.13). A reasonable explanation is that the amorphous material is introducing parasitic absorption, reducing the number of photons reaching the crystalline and photoactive perovskite, without introducing strong recombination paths (as discussed before). The reduction in interface quality is further confirmed by *in-situ* electrochemical impedance spectroscopy (EIS) measurements, where EIS is performed during biasing (**Figure 6.5d**). The spectrum for the fresh device is composed of two semicircles, as commonly observed for PSCs. Upon biasing we observe a resistance increase in the high-frequency semicircle, which points to a rise in recombination resistance and charge transport/transfer resistance.[73, 74] At the same time, the negative induction at low frequencies arise. This negative induction has been linked to the modulation of the energetic barrier for charge injection (from the selective contact into perovskite) due to ion migration,[75] and it is generally observed for poor performing interfaces,[76] further confirming the interfacial nature of the degradation.

6.3 Conclusion

The reasons underlying power conversion efficiency losses of perovskite solar cells due to ion migration are investigated. We found that prolonged, bias-induced ion migration in planar perovskite solar cells induces the amorphization of perovskite and halide segregation when enough charge is injected into the device. Interestingly, the V_{OC} increases likely due to a combination of self-passivation from the amorphous perovskite and homogenization of the perovskite bulk. However, the loss in perovskite crystallinity hinders charge collection, significantly reducing J_{SC} and FF and ultimately results in a lower PCE. The ion migration driven amorphization of perovskite might be a fundamental degradation mechanism for optoelectronic devices. As a solution strategy, we believe that fine compositional engineering[77] or the introduction of additives into the perovskite[40, 78] might be suitable. Nonetheless, the overlapping effects of bias-induced perovskite amorphization, thermal decomposition and light-induced degradation are critical topics for further investigation, in order to disentangle each specific mechanism. As a final consideration, the ion migration-induced loss of perovskite crystallinity might have consequences for characterization techniques based on prolonged DC polarization, employed for example to investigate ion migration in lead halide perovskites, and therefore should be taken in consideration.

Methods

NiO deposition

Patterned indium tin oxide (ITO) glass substrates (25x25 mm, 15 Ω sq^{-1}, patterned by Automatic Research GmbH), cleaned for 20 min with Mucasol 2% solution in deionized water, Acetone, and Isopropanol in an ultrasonic bath, were treated in an UV-ozone cleaner for 15 min.

Nickel oxide is deposited from a 0.15M $NiCl_2 \cdot 6H_2O$ (Alfa Aesar) solution in anhydrous 2-methoxyethanol (99.8%, Sigma Aldrich) with the addition of 20μL/mL of HNO_3 65% (Sigma Aldrich). After shaking the solution overnight at 60°C the spin-coating deposition of NiOx occurs via the following program: 500rpm (1s acceleration) for 1s and 4000rpm (2s acceleration) for 30s. After the spin-coating the substrate is dried sequentially at 75°C for 10 minutes, at 120°C for 15 minutes and is then annealed at 300°C for 1 hour.

PTAA deposition

PTAA (Sigma Aldrich) was dissolved at a concentration of 2mg/mL in anhydrous toluene (Sigma Aldrich). The deposition was perfomed by spin-coating at 5000 rpm for 30 seconds and annealing at 100°C for 10 minutes in glove box.

Perovskite deposition

For $Cs_{0.05}((FAPbI_3)_{0.83}(MAPbBr_3)_{0.17})_{0.95}$ perovskite, $PbBr_2$ (1.5M) and PbI_2 (1.5M) were dissolved in a mixture of anhydrous DMF:DMSO (4:1 volume ratio) (Sigma Aldrich) and added to FAI (1.09:1 molar ratio) and MABr (1.09:1 molar ratio) powders respectively, to obtain MAPbBr3 and FAPbI3 solutions with a final concentration of 1.24 M. These two solutions were then mixed in a 17:83 volume ratio. Finally, the Caesium cation was added from a 1.5 M CsI solution in DMSO in a 5:95 volume ratio. The Perovskite solution was spin-coated on top of the HTM layer using the following program: 4000 rpm (5 s acceleration) for 35 s (total time – 40 s). After 25 s, 600 µl of Ethyl Acetate was dropped on the spinning substrate. After the spin-coating program, the perovskite-coated sample is annealed at 100°C for 60 min on a hotplate. For the $Cs_{0.05}((FAPbI_3)_{0.83}(MAPbI_3)_{0.17})_{0.95}$ perovskite the same procedure as for the $Cs_{0.05}((FAPbI_3)_{0.83}(MAPbBr_3)_{0.17})_{0.95}$ composition has been followed, just modifying the solution composition to obtain the desired stoichiometry. The $MAPbI_3$ perovskite precursor is 1.2 M of PbI_2 (Tokyo Chemical

Industry), and CH_3NH_3I (Dyenamo) in mixed solvent DMF:DMSO 6:1 by volume ratio. The solution is put in thermal shaker at 60°C for 5 minutes. The spin coating program for $MAPbI_3$ is with 4000 rpm for 30 s, ramping for 5 s. 500 µL of ethyl acetate is used to as antisolvent quenching step after 20 s of spin coating.

Electron selective contact and metal electrode

On top of the perovskite, 23 nm of C_{60} and 8 nm of BCP were deposited by thermal evaporation (Mbraun ProVap 3G) with evaporation rates below 0.2 A°/s at a pressure of under 1E-6 mbar. Finally, 100 nm of Cu was evaporated at a rate of 0.08-1.0 A°/s. The active area is defined by the overlap of patterned ITO and the metal electrode, which is 0.16 cm2.

Photovoltaic Performances Characterization

Current-voltage (J-V) characteristics under 1 sun equivalent illumination were recorded using a Wavelabs Sinus-70 LED class AAA calibrated with a Silicon reference solar cell from Fraunhofer ISE. J-V scans were performed with a Keithley 2400 SMU, controlled by a measurement control program written in LabView. The voltage values are swept in 20 mV steps with variable integration time and settling time after voltage application to control the scan rate.

Optoelectronics Characterization

Transient PhotoVoltage (TPV), Charge Extraction (CE), IPCE and electroluminescence (EL) were performed with a commercial modular instrument for advanced photo-electrical characterization (Arkeo from Cicci Research s.r.l.). In the case of TPV and CE the setup is based on a high speed Waveform Generator that drives a high speed LED (5000 Kelvin). The device is connected to a transimpedance amplifier and a differential voltage amplifier to monitor short circuit current or open circuit voltage. The light intensity can be varied between 0.1 and 2 equivalent suns. EQE analysis was performed with a commercial apparatus (Arkeo – Cicci Research s.r.l.) based on a 300 W Xenon lamp monochromatic light (300 to 1100 nm @ 2nm of resolution) with thermal controlled stage. A source meter with 1pA of resolution is directly connected to the device and NIST calibrated Silicon detector. For the differential EQE shown in figure 5b and 5c we recorded the EQE between

700 nm and 830 nm with 2nm of resolution. Electroluminescence spectra were recorded with a commercial apparatus (Arkeo – Cicci Research s.r.l.) composed by a CCD spectrometer. The devices were biased employing the same setup. The EL spectra were acquired at a driving voltage of 2.25V and with a fast acquisition time (the measurement takes less than 5 seconds). The fast acquisition time assures that the halide segregation is not induced by the high current density (above 100mAcm^{-2}) during the acquisition time, as shown in figure 5d. The optical coupling system is composed by a lens condenser attached to a multimode optical fiber bundle. The Arkeo (Cicci Research s.r.l) apparatus allows to overlap a constant biasing to TPV, CE, EQE, EL and other techniques. The bias was applied continuously and switched off only during the measurements described. Impedance spectroscopy were perfomed with an FRA-equipped Solarlab XM Potentiostat.

In-situ X-ray Diffraction

The biasing was performed with a high-precision source-meter directly connected within the XRD chamber. We needed to ship the samples to perform this experiment, and this is probably the reason behind the relatively higher content of PbI_2 found in the diffractograms, with respect to what we find when characterizing the cells where fabricated (see for instance ref [71]). XRD was performed using a Panalytical X'Pert Pro MPD diffractometer (Cu Kα radiation), with patterns collected continuously (the time required to collect a single diffractogram is 1 hour). More details on the experiment are provided in supporting information, Figure SI5.

In-situ reflectance

In-situ reflectance spectra were acquired with a UV-Vis 2550 spectrophotometer from Shimadzu, calibrated with $BaSO_4$. The biasing was performed during the measurement with a Keithley 2400 SMU with analogue control.

Scanning transmission electron microscopy (STEM) characterization

Cross-sectional lamellae of fresh and biased (12 hours at 1.2V in dark) devices were prepared and thinned to electron transparency by focused ion beam milling (FEI Helios Nanolab Dualbeam FIB/SEM) using a standard protocol[79] with minimal (~2 minutes) exposure to air between lamella preparation and STEM characterisation. For the biased device, lamella milling was performed immediately after the biasing regime was finished. Cross-sectional HAADF imaging and EDX spectroscopy were carried out in a FEI Tecnai Osiris operated at 200 kV and equipped with a Bruker Super-X EDX silicon drift detector with a total collection solid angle of ~0.9 sr. To minimize beam damage, EDX spectrum images were acquired with a defocused beam ($\Delta f = -0.5$ µm), probe current of ~250 pA, spatial sampling of 10 nm/pixel, and dwell time of 50 ms/pixel. Data were acquired with Tecnai Imaging and Analysis (TIA) and analysed with HyperSpy[80]. The data was treated with non-negative matrix factorization (NMF) for decomposition into easily identifiable components.

In-situ grazing incidence synchrotron wide angle X-ray scattering

Grazing incidence synchrotron wide angle X-ray scattering data was acquired at the KMC2 beamline at BESSY II synchrotron (Helmholtz Zentrum Berlin). Samples were biased *in-situ* in air and in the dark and scattered X-rays were acquired at a range of scattering angles every 15 minutes, at grazing incidence angles of 2° and 4°, through the Cu top contact. The photon energy of the beam was set to 8048 eV, matching Cu Kα radiation.

6.4 Supporting Information

SI Note 1

The choice of biasing potential deserves some discussion. Except for reverse biasing due to partial shadowing of modules, during its lifespan, a solar cell will stay most of the time at maximum point voltage (V_{MP}) in operation, or open circuit voltage (V_{OC}), if illuminated but not connected to an external load. Biasing around V_{OC}, therefore, appears to be a reasonable choice. The NiO-based devices herein investigated generally yield a V_{OC} in the range of 1.00 - 1.08 V (Figure SI1d), and the adoption of PTAA as the hole selective layer yields 1.08 - 1.15 V (Figure SI1d). With the same CsFAMA composition, V_{OC} values above 1.2 V have been demonstrated when employing SnO_2 as the electron selective layer.[81] Further, by taking into account the band gap of the CsFAMA perovskite of 1.6 eV, the theoretical V_{OC} would be 1.3 V and the theoretical V_{MP} would be 1.2 V.[82] Therefore, a reasonable biasing potential should fall between 1.0 V and 1.3 V. Except when stated otherwise, we selected 1.2 V to conduct the experiments because it has already been attained as a V_{OC} value and thus represents a practical limit in this sense. Moreover, the current density at 1.2 V in the dark in our devices is of a similar magnitude to the short circuit current or current at maximum power point during photovoltaic operation. We remark that the dark current (whose injection is impossible to avoid in this context) flows in the opposite direction to the photo-current, which might bring different charge accumulation behaviour or different electrochemistry with respect to the operating mechanism. However, the deconvolution of the degradation pathways induced by bias and light (along with the understanding of their combination) would be a fundamental insight to understand how perovskite solar cells degrade. Finally, we remark that biasing at even higher potentials might be relevant for other applications, such as light-emitting diodes, and might deserve future investigation.

Figure S6.1

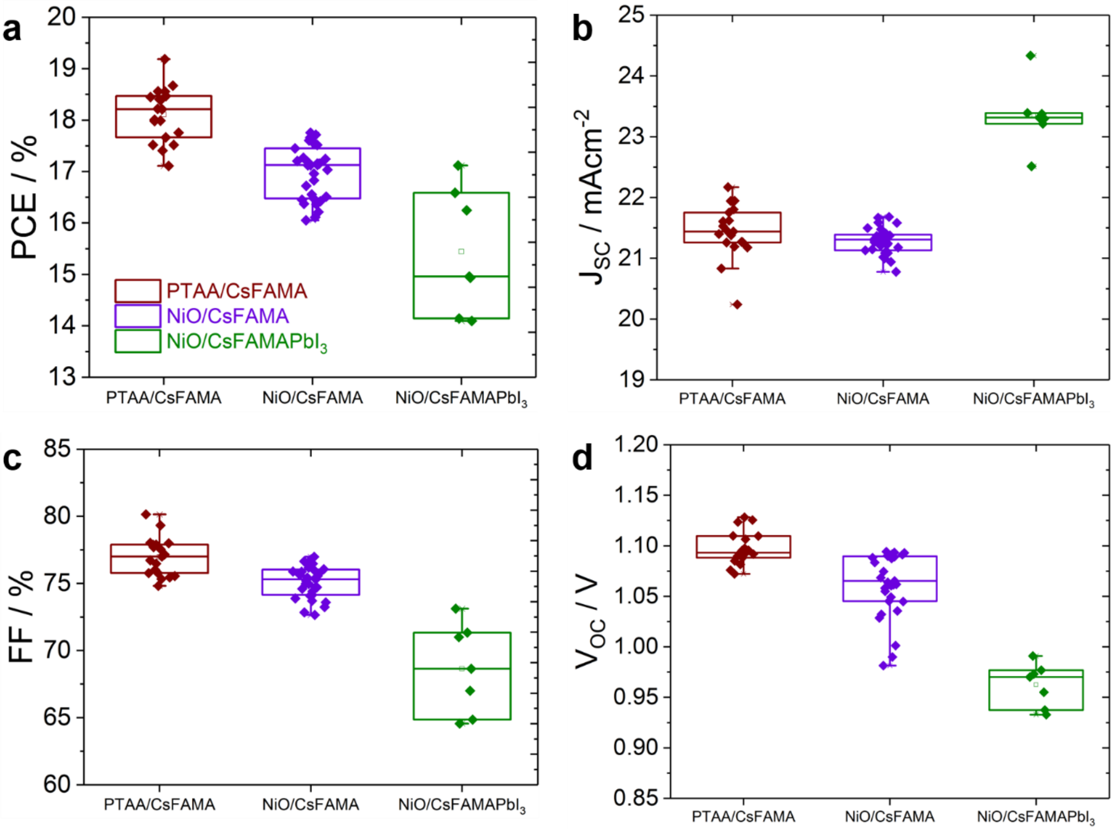

Photovoltaic performance statistics of devices employed in this study, obtained from reverse J-V scans at 100 mV/s with simulated AM1.5g spectrum: **a**. power conversion efficiency (PCE), **b**. short circuit current (J_{SC}), **c**. fill factor (FF), **d**. open circuit voltage (V_{OC}).

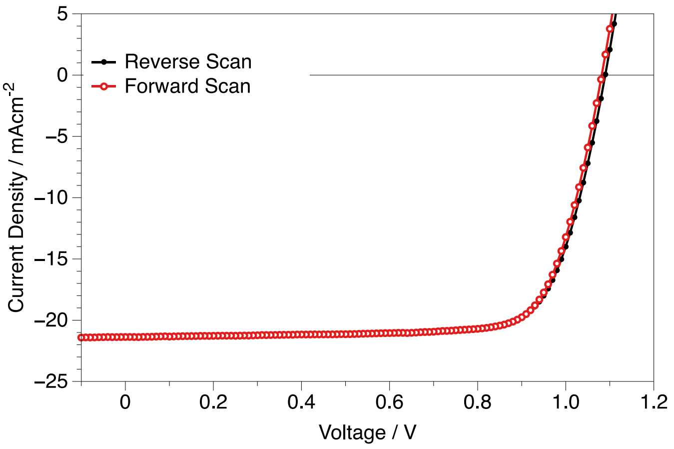

J-V scan of a typical NiO-based p-i-n PSC with negligible hysteresis.

Figure SI2

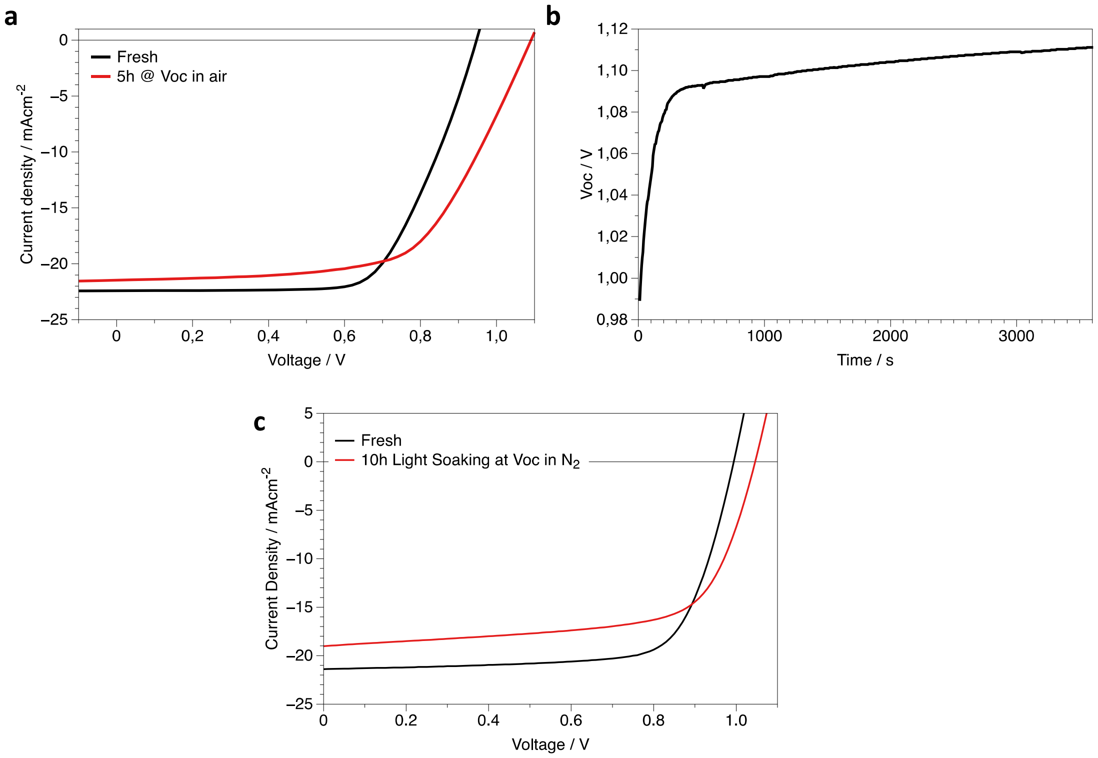

a J-V curve before (black) and after (red) a light soaking stress test in air. **b** 1h of V_{OC} rise in time. The V_{OC} remains stable after the plateau is attained. **c** J-V curve before (black) and after (red) a light soaking stress test in nitrogen.

In **Figure S6.1** we report the results of a light soaking stress test performed in air (**Figure S6.2a**) or in nitrogen (**Figure S6.2c**) for an un-encapsulated device. This preliminary test was performed to have a first insight into the practical implication of the mechanism we investigated in real photovoltaic conditions. Notably, the behaviour of PV parameters is similar to what we observed with the stress discussed in this work: V_{OC} strongly increases, while J_{SC} and FF decrease. This result suggests that the ion migration driven mechanism we investigated might also be relevant in photovoltaic operation. Here, the V_{OC} was around 1.1 V for most of the time (see Figure S6.2b, measured in air). Nonetheless, we want to stress that future investigations are required in order to understand in detail the overlapping effects of ion migration driven mechanisms with those caused by light and thermal induced degradation.

Figure S6.3

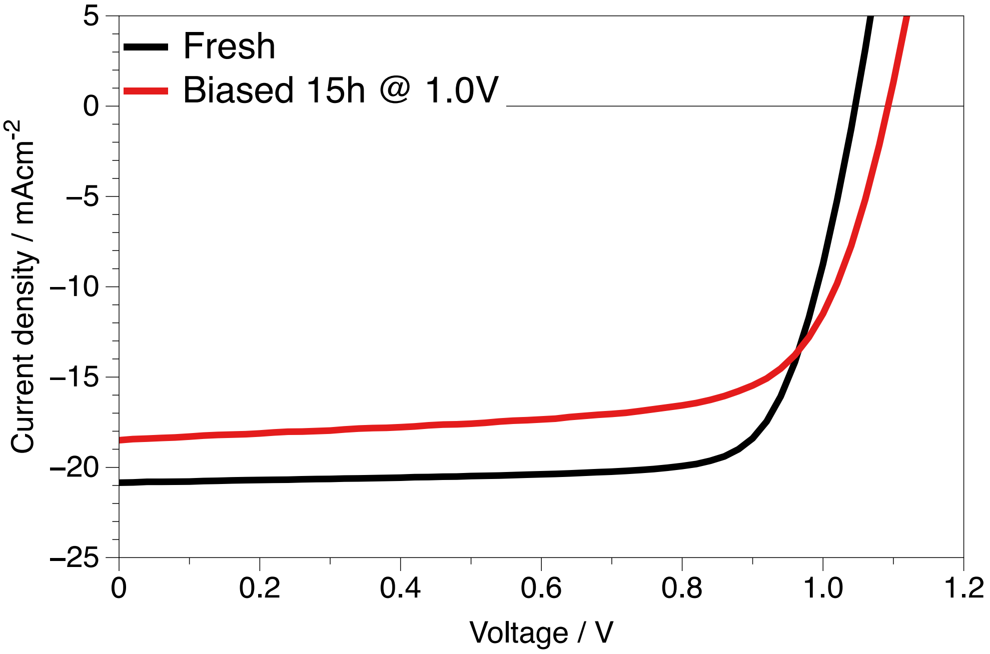

The effect on the J-V curve of a prolonged (15h) bias at 1 V in dark.

At the injected current due to 1 V, there is no halide segregation in CsFAMA mix halides device as can be seen from the electroluminescence measurement shown in **Figure 6.4d**.

Figure S6.4

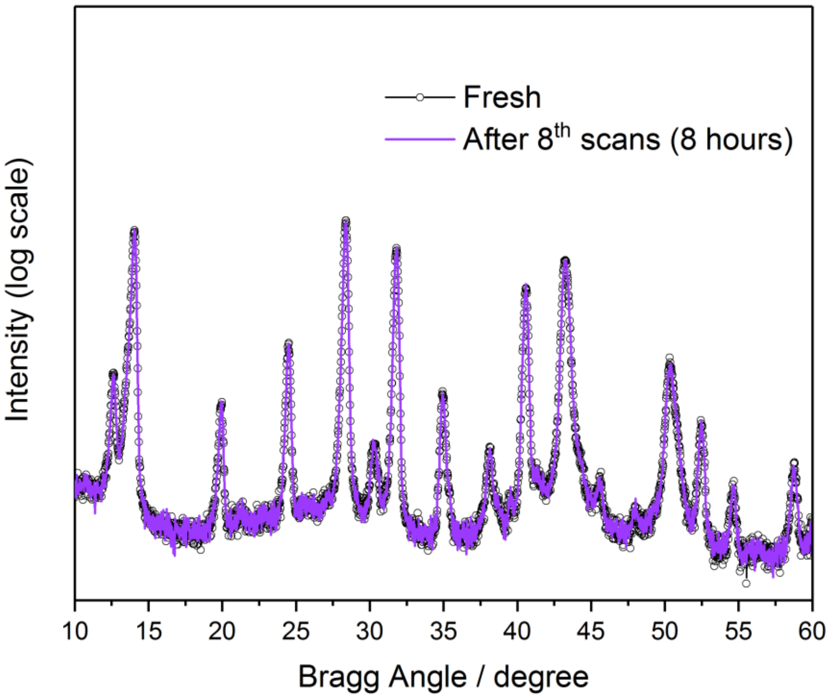

XRD patterns of a fresh sample and after 8 XRD scans (one scan per hour, without bias and otherwise similar conditions to the *in-situ* bias XRD measurement).

Figure S6.5

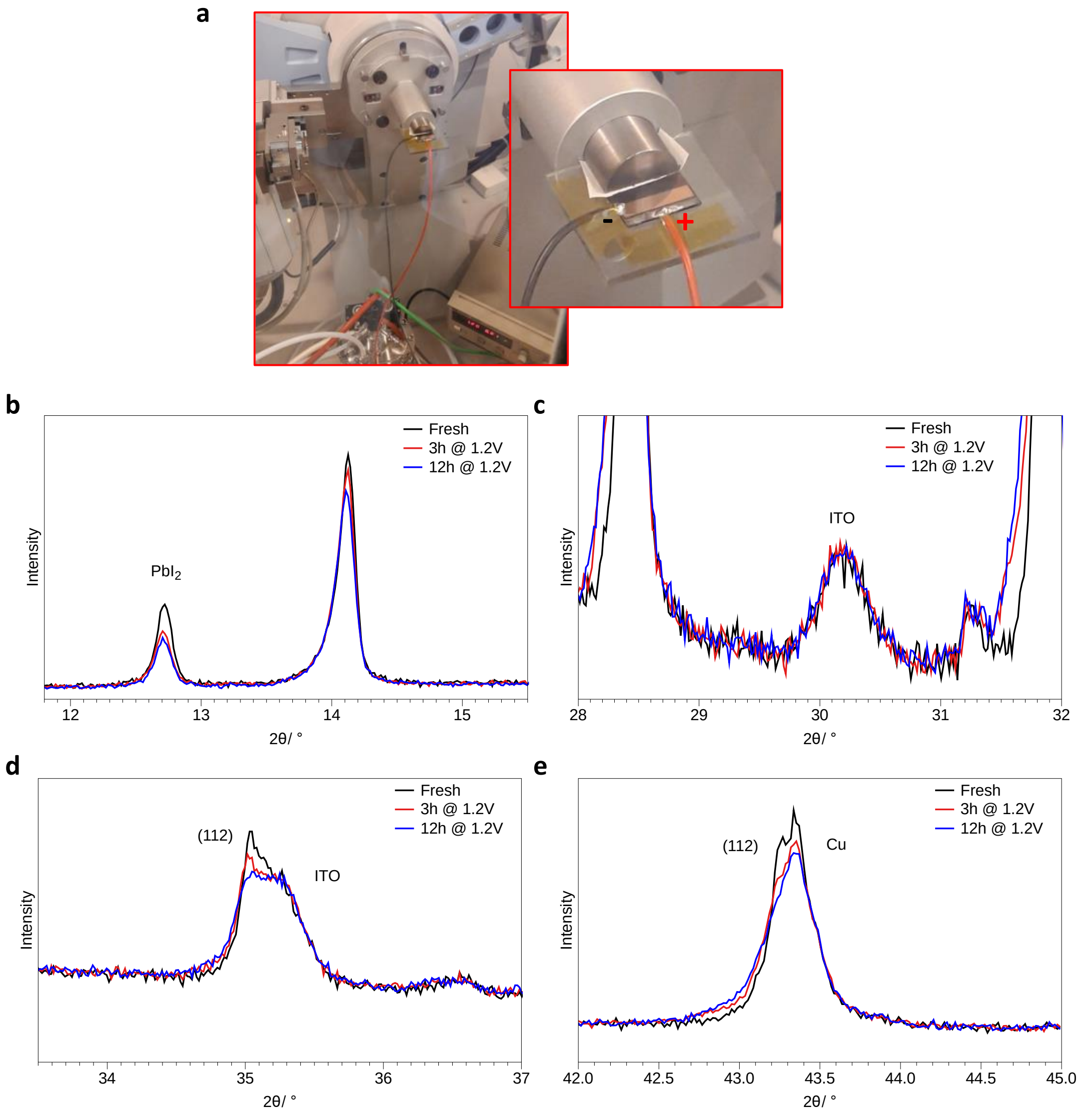

a Picture of the setup employed for the *in situ* XRD. The device (coincident with the copper stripe) is mounted on a glass holder by means of an adhesive tape. The contacts have been ultrasonically soldered to ensure higher mechanical stability and Kapton tape has been employed to fix the wires to the support to avoid any movement of the device over the whole experiment. The polarity of the contacts is specified in the magnification of the sample holder. The device is polarized at 1.2 V and about 10 mA are recorded by the source-meter, as it can be appreciated in the image. **b** Highlighting the PbI_2 XRD main peak at 12.7° and of the main perovskite peak at 14.1°. **c** Magnification on the ITO peak around 30°, which shows no variation of intensity and peak shape over the whole experiment. **d** Magnification of the feature around 35° which is composed of an overlapping peak from perovskite (at lower angles) and a peak from ITO (at higher angles), with the decrease in intensity completely attributable to the perovskite peak. **e** Magnification of the feature around 43° which is composed of overlapping peaks from perovskite (at lower angles) and Cu (at higher angles), and again the decrease in intensity is attributable to the perovskite peak.

Figure S6.6

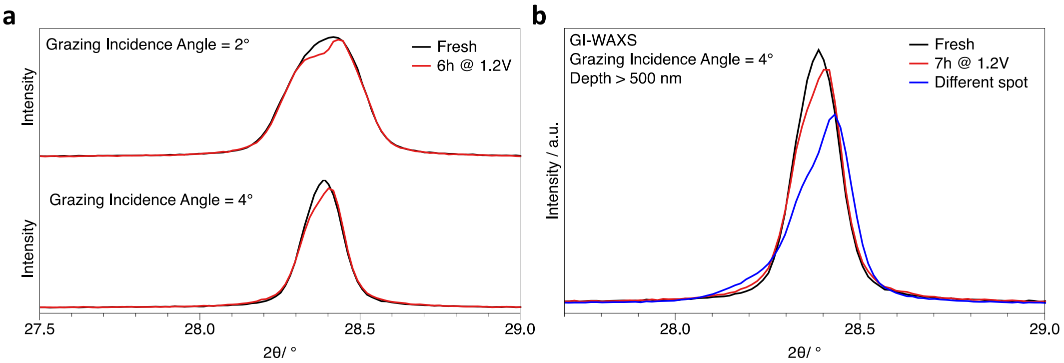

GIWAXS measurement pattern with focused at 28.4° peak for fresh samples and biased sample

From the analysis on integrated intensity of *in situ* GIWAXS signal at 28.4° it is possible to estimate a higher degree of amorphization from the dataset collected with a grazing incidence angle of 2°, which is expected to be more surface sensitive. For instance after about 5 hours of biasing the integrated intensity drop is of about 1.2% when the grazing incidence angle is 4° and of about 4% when the grazing incidence angle is 2°. This fact supports the interface degradation mechanism we propose, however, we refrain from using the quantitative analysis on this dataset because it appears that the scattered signal intensity depends on the spot position across the pixel area (see figure b). This fact could arise from slight misalignments due to sample holder movement (changing the effective volume from which X-rays are scattered) or from non-uniformity in the degradation behavior over the device area.[83, 84]

The measurement at different spot next to the area, in which the beam hit during the in-situ measurement, confirms that the beam damage can be neglected.

Figure S6.7

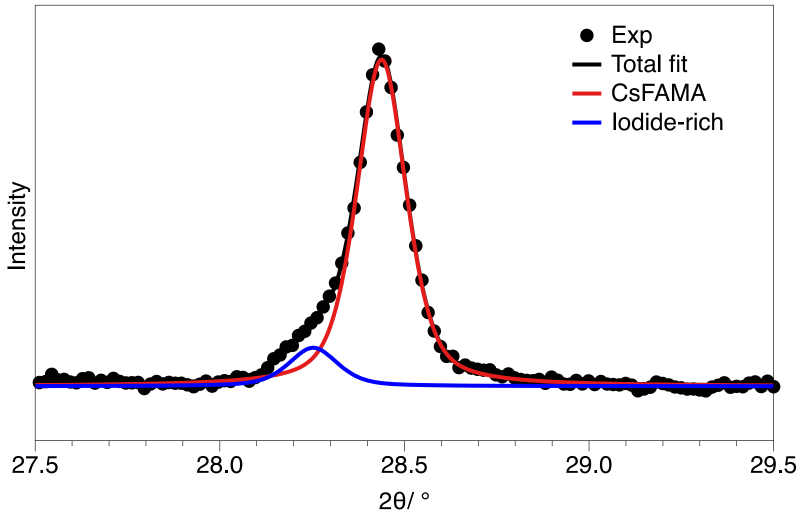

Fit employing two components for the XRD peak at 28.44° (a = 6.271 Å) after 3h of biasing. The blue-component is at 28.25° (a = 6.313 Å) (estimated from Bragg's law assuming cubic crystal structure), and the positions of the two peaks are constant over the whole experiment. From the relative intensities of the fitted XRD peaks of the original CsFAMA and of the iodide-rich composition after 3h of biasing, we can estimate that about 10 vol% of the latter is enough to dominate light emission, with an intense peak at 790 nm detectable (Figure 2e), likely due to fast funnelling to the low bandgap system.[85]

Figure S6.8

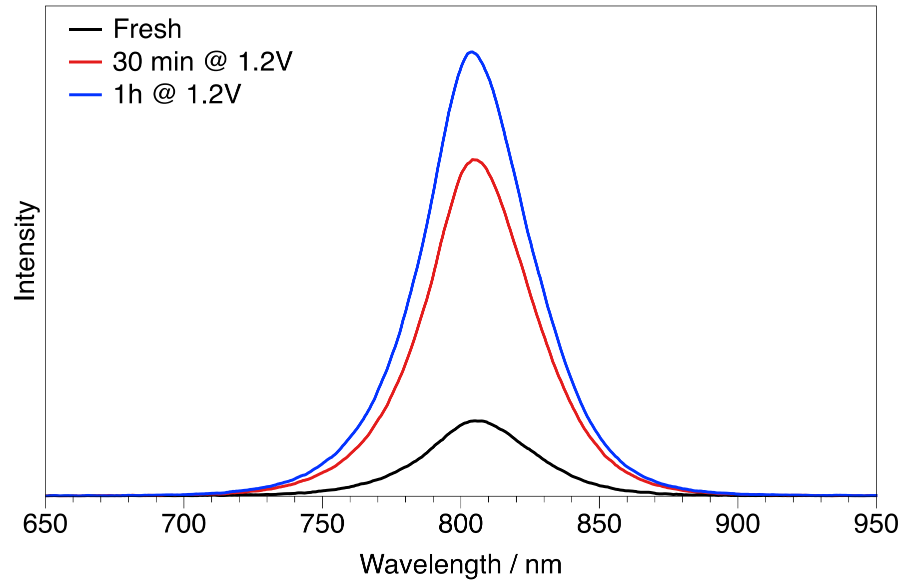

Electroluminescence (EL) spectrum evolution of $Cs_{0.05}(FA_{0.83}MA_{0.17})_{0.95}PbI_3$ perovskite upon biasing at 1.2 V in dark.

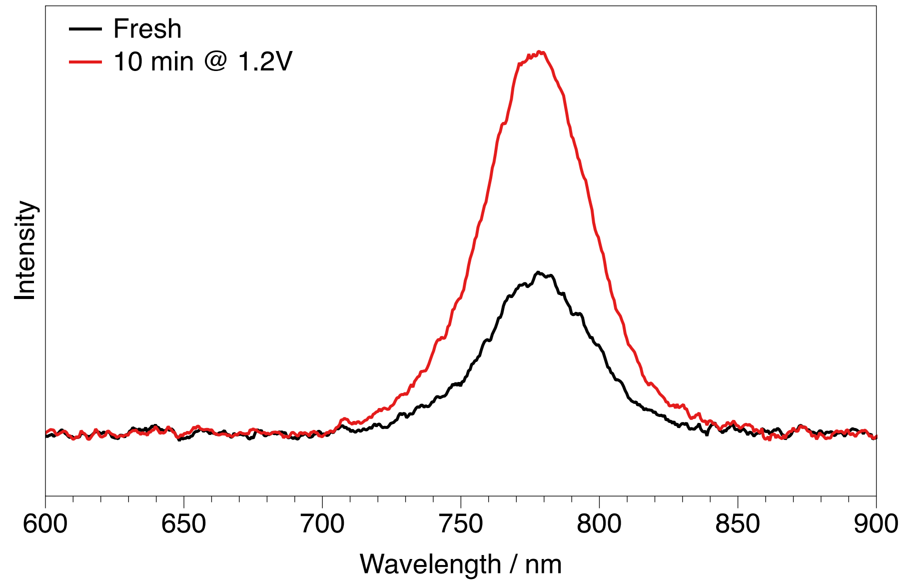

EL spectrum evolution of $MAPbI_3$ perovskite upon biasing at 1.2 V in dark.

As can be seen in the figures, no shift of the peak is detectable while biasing pure iodide perovskite cells, pointing to stable cation mixing throughout the measurement. Meanwhile, the EL quantum efficiency (PL-QE) increases similar to the mixed halide CsFAMA perovskite.

Figure S6.9 NMF Analysis of STEM-EDX Data

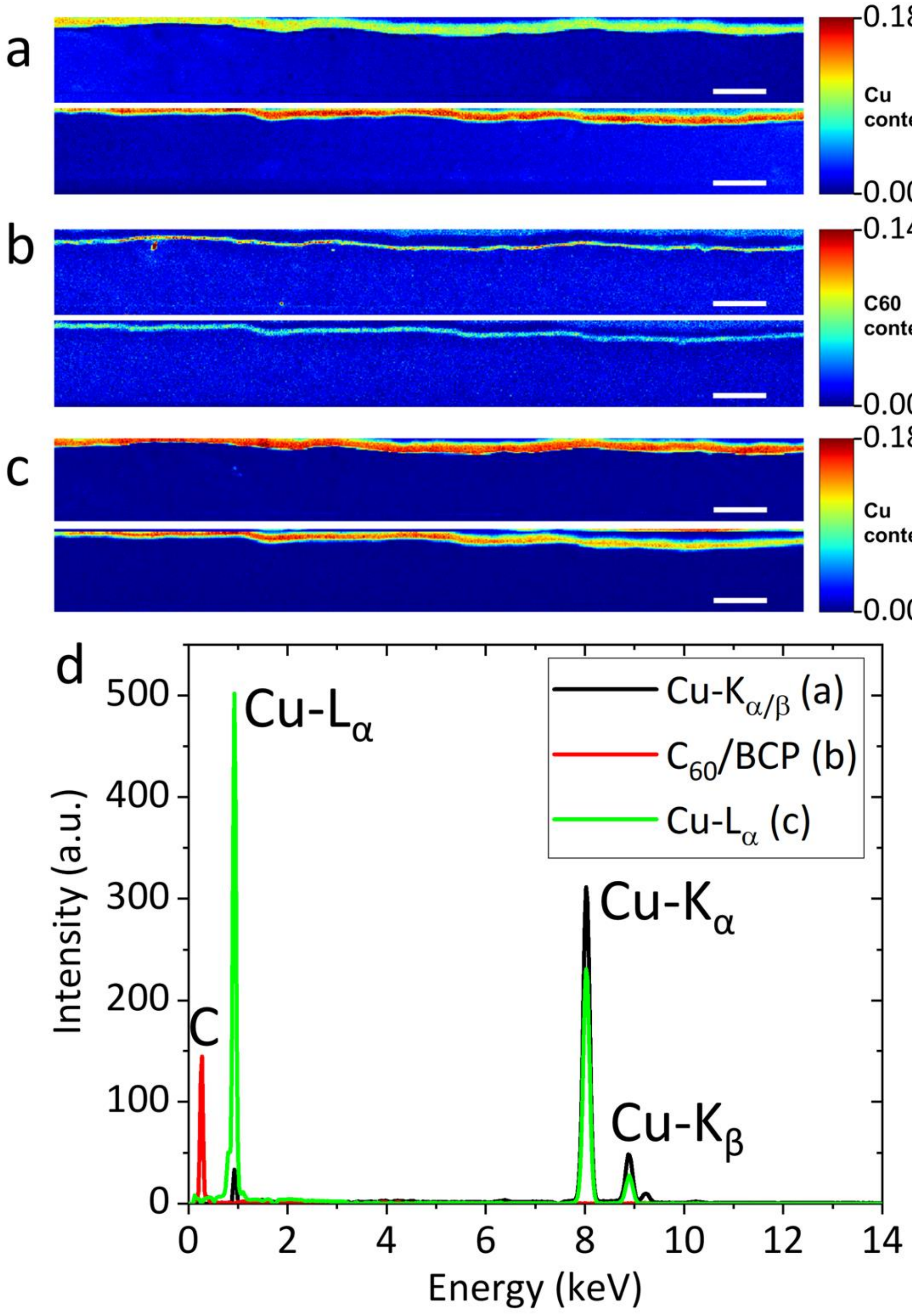

a-c NMF loadings (maps) of three selected components, with the fresh sample at the top and biased sample at the bottom of each pair: **a** copper electrode (Cu-$K_{\alpha/\beta}$ line), **b** C_{60}/BCP electron transport layer, and **c** copper electrode (Cu-L_α line). **d** NMF factors (spectra) of the loadings shown in (a-c). All scale bars are 0.5 µm. Numbers on the colour scale in (a-c) are in a.u.

Figure S6.10

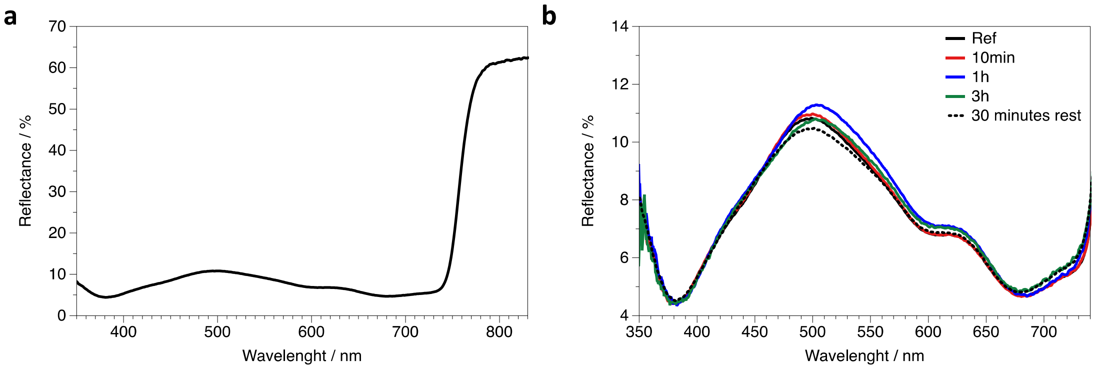

a Reflectance of the full device stack, measured from the glass side. **b** Variation of the reflectance in the 350-750 nm range in the *in-situ* experiment discussed in the main text.

Upon biasing, some slight variation in the complete visible range is observed, as shown above. The decrease of PbI_2 content might be one of the reasons behind changes at short wavelengths, and the selective contacts as well might have an effect.

Figure S6.11 PTAA as HSL

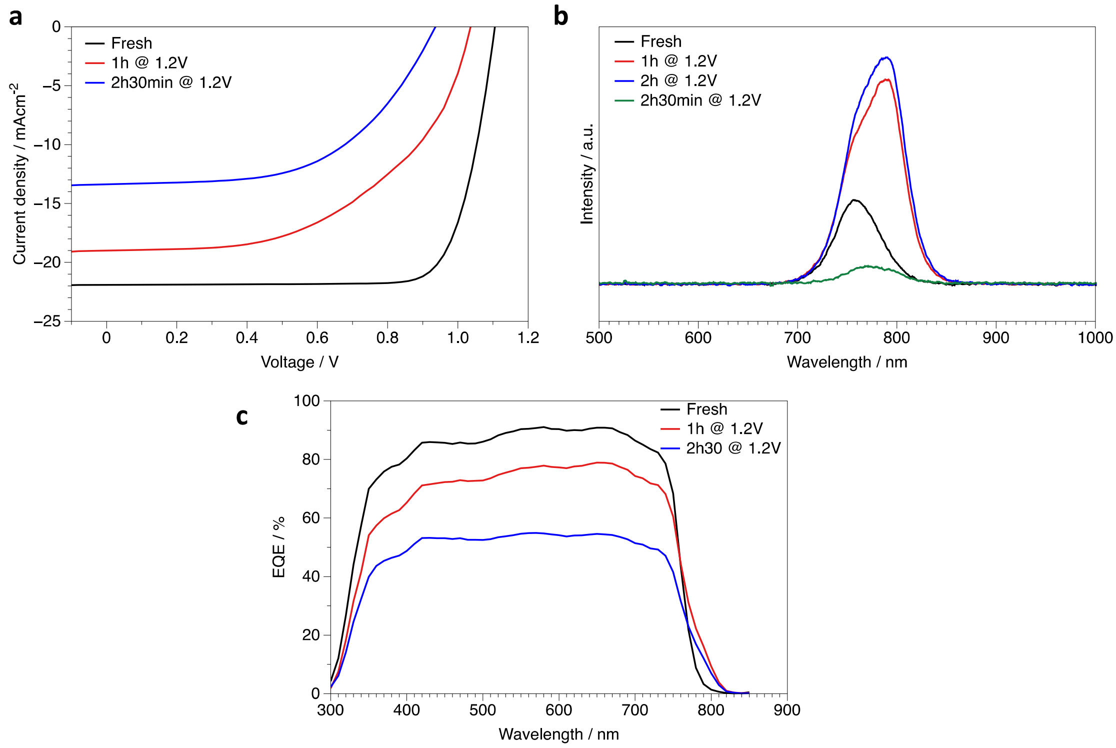

a Effect on JV curves under AM1.5g illumination of the electrical bias (1.2V in dark) on pin PSCs employing PTAA as hole selective layer. **b** Effect of electrical bias on the EL. **c** Effect of the electrical bias on the EQE.

By means of photoelectrical characterizations, we investigated different architectures and configurations of PSCs. We found, as expected, that the degradation path is different depending on the selective contacts. The case of PTAA-based devices is particularly interesting, which is otherwise identical to the NiO-based devices discussed in this work. The PTAA-based devices have efficiency values higher than 19%, which is at the state-of-the-art for p-i-n PSCs (**Figure S6.1**). Nonetheless, the devices appeared overall less stable to electrical bias, hence, the *biased state* after 12h is not presented here (degraded devices yield a straight line in the fourth J-V quadrant). Further, the degradation dynamics was different. Within the first hour (**Figure S6.10b, c**), we found similar changes in EL (increase of efficiency and halide segregation, with the same low band gap species arising) and a similar asymmetric drop in the EQE (larger drop at short wavelengths). Interestingly, the impact on the EQE of the iodide-rich species appears decidedly larger (around 800nm) than in case of NiO-based devices (also in this case a contribution from an enhanced energetic disorder is possible). However, soon after this, a different mechanism emerged for all cells investigated. The strong decrease in EQE becomes uniform across the measured wavelength range, *i.e.* not more pronounced at short wavelengths. We can imagine two different scenarios (not in contradiction to one another) explaining the different degradation routes depending on the hole selective contact. First, PTAA itself might degrade due to ion migration across this very thin layer which has been proven to be a poor ionic barrier.[16] Second, the electric field distribution inside the device, an aspect that has been proven to depend simultaneously on both selective contacts,[86] can change differently as degradation progresses.

Figure SI12

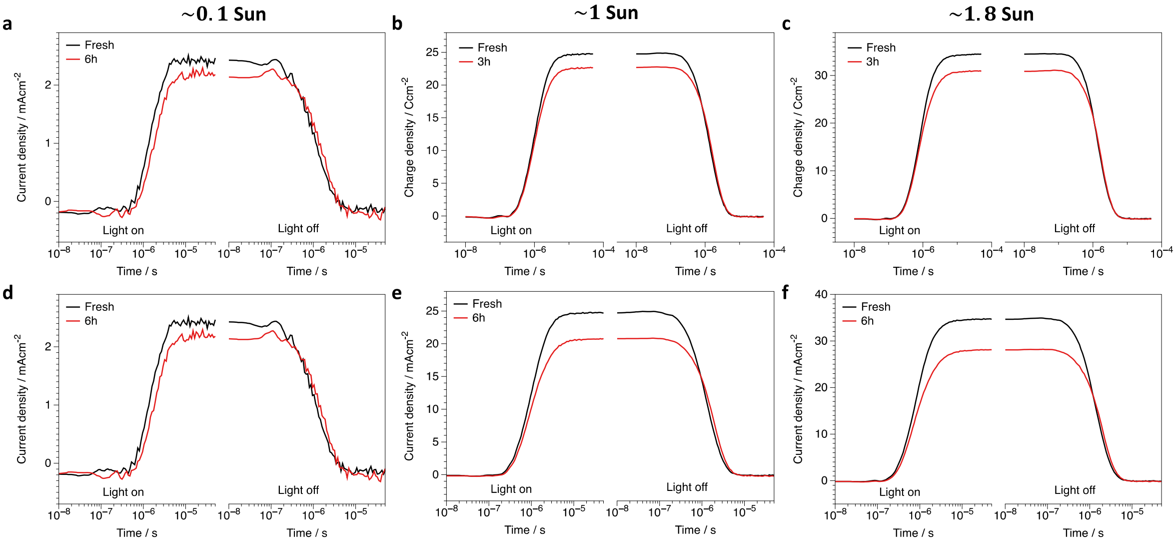

a, b, c) Photocurrent rise and decay obtained in the charge extraction experiments for the fresh device and the same biased for 3h at 1.2 V in dark at different light intensities. **d, e, f)** Photocurrent rise and decay obtained in the charge extraction experiments for the fresh device and the same device biased for 6h at 1.2 V in the dark at different light intensities. In all cases, a decrease of the photocurrent at the plateau of the rise step is obtained upon biasing and a slower extraction of the residual charge is observed when the light is switched off.

Figure SI13

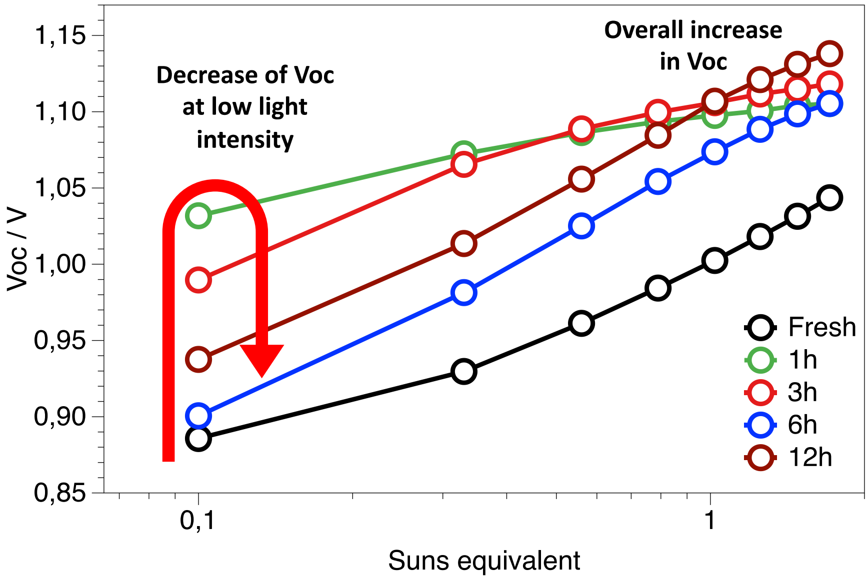

It is interesting to show that the increase in V_{OC} as obtained from the TPV experiment is non-monotonic over the duration of the stress test. At high illumination (around or above 1 Sun equivalent) the increase in V_{OC} is weakly dependent on the stress duration. This is in line with the plateau in the V_{OC} vs time plot attained after around 1h and shown in **Figure S6.2**. At lower illumination levels the situation is different, with the devices biased for more than 1h showing a subsequent V_{OC} decrease, suggesting that the bias induced passivation mechanism is light-intensity dependent. For instance, the charge dynamics at the PbI_2 / perovskite interface has been shown to be fluence dependent.[87] Here, similar concepts could apply to the Br-rich perovskite / CsFAMA interface. Further, we discussed the literature on the possible role of amorphous materials as passivating agent in the main text. However, we have to state that not enough is known about the amorphous / crystalline interface to propose a convincing mechanism on this point, which deserves future investigation.

References

1. NREL Best Research-Cell Efficiencies. Available at: https://www.nrel.gov/pv/assets/pdfs/pv-efficiencies. (Accessed: January 21st 2020)
2. Kojima, A., Teshima, K., Shirai, Y. & Miyasaka, T. Organometal Halide Perovskites as Visible-Light Sensitizers for Photovoltaic Cells. *J. Am. Chem. Soc.* **131**, 6050–6051 (2009).
3. Stranks, S. D. *et al.* Electron-Hole Diffusion Lengths Exceeding 1 Micrometer in an Organometal Trihalide Perovskite Absorber. *Science (80-.).* **342**, 341–344 (2013).
4. Wolf, S. de *et al.* Organometallic Halide Perovskites: Sharp Optical Absorption Edge and. *J. Phys. Chem. C* **5**, 1035–139 (2014).
5. Eperon, G. E. *et al.* Formamidinium lead trihalide: A broadly tunable perovskite for efficient planar heterojunction solar cells. *Energy Environ. Sci.* **7**, 982–988 (2014).
6. Sutton, R. J. *et al.* Bandgap-Tunable Cesium Lead Halide Perovskites with High Thermal Stability for Efficient Solar Cells. *Adv. Energy Mater.* **6**, 1–6 (2016).
7. Unger, E. L. *et al.* Roadmap and roadblocks for the band gap tunability of metal halide perovskites. *J. Mater. Chem. A* **5**, 11401–11409 (2017).
8. Bush, K. A. *et al.* 23.6%-efficient monolithic perovskite/silicon tandem solar cells with improved stability. *Nat. Energy* **2**, 17009 (2017).
9. Yi, C. *et al.* Entropic stabilization of mixed A-cation ABX3metal halide perovskites for high performance perovskite solar cells. *Energy Environ. Sci.* **9**, 656–662 (2016).
10. Mcmeekin, D. P. *et al.* A mixed-cation lead mixed-halide perovskite absorber for tandem solar cells. *Science (80-.).* **351**, 151–155 (2016).
11. Binek, A., Hanusch, F. C., Docampo, P. & Bein, T. Stabilization of the Trigonal High-Temperature Phase of Formamidinium Lead Iodide. *J. Phys. Chem. Lett.* **6**, 1249–1253 (2015).
12. Saliba, M. *et al.* Cesium-containing triple cation perovskite solar cells: Improved stability, reproducibility and high efficiency. *Energy Environ. Sci.* **9**, 1989–1997 (2016).
13. Richardson, G. *et al.* Can slow-moving ions explain hysteresis in the current–voltage curves of perovskite solar cells? *Energy Environ. Sci.* **9**, 1476–1485 (2016).
14. Snaith, H. J. *et al.* Anomalous Hysteresis in Perovskite Solar Cells. *J. Phys. Chem. Lett.* **5**, 1511–1515 (2014).
15. Domanski, K. *et al.* Migration of cations induces reversible performance losses over day/night cycling in perovskite solar cells. *Energy Environ. Sci.* **10**, 604–613 (2017).
16. Kakavelakis, G. *et al.* Extending the Continuous Operating Lifetime of Perovskite Solar Cells with a Molybdenum Disulfide Hole Extraction Interlayer. **1702287**, 1–15 (2018).
17. Guerrero, A. *et al.* Interfacial Degradation of Planar Lead Halide Perovskite Solar Cells. *ACS Nano* **10**, 218–224 (2016).
18. Domanski, K. *et al.* Not All That Glitters Is Gold: Metal-Migration-Induced Degradation in Perovskite Solar Cells. *ACS Nano* **10**, 6306–6314 (2016).
19. Cacovich, S. *et al.* Gold and iodine diffusion in large area perovskite solar cells under illumination. *Nanoscale* **9**, 4700–4706 (2017).
20. Frolova, L. A., Dremova, N. N. & Troshin, P. A. The chemical origin of the p-type and n-type doping effects in the hybrid methylammonium–lead iodide (MAPbI 3) perovskite solar cells. *Chem. Commun.* **51**, 14917–14920 (2015).
21. Di Girolamo, D. *et al.* Stability and Dark Hysteresis Correlate in NiO-Based Perovskite Solar Cells. *Adv. Energy Mater.* **9**, 1901642 (2019).
22. Carrillo, J. *et al.* Ionic Reactivity at Contacts and Aging of Methylammonium Lead Triiodide Perovskite Solar Cells. *Adv. Energy Mater.* **6**, 1–22 (2016).
23. Sekimoto, T. *et al.* Influence of a Hole-Transport Layer on Light-Induced Degradation of Mixed Organic–Inorganic Halide Perovskite Solar Cells. *ACS Appl. Energy Mater.* **2**, 5039–5049 (2019).
24. Kerner, R. A. & Rand, B. P. Electrochemical and Thermal Etching of Indium Tin Oxide by Solid-State Hybrid Organic–Inorganic Perovskites. *ACS Appl. Energy Mater.* **2**, 6097–6101 (2019).
25. Pospisil, J. *et al.* Reversible Formation of Gold Halides in Single-Crystal Hybrid-Perovskite/Au Interface upon Biasing and Effect on Electronic Carrier Injection. *Adv. Funct. Mater.* **29**, 1900881 (2019).
26. Wu, S. *et al.* A chemically inert bismuth interlayer enhances long-term stability of inverted perovskite solar cells. *Nat. Commun.* **10**, 1161 (2019).
27. Jung, H. J. *et al.* Stability of Halide Perovskite Solar Cell Devices: In Situ Observation of Oxygen Diffusion under Biasing. *Adv. Mater.* **30**, 1802769 (2018).

28. Jeangros, Q. *et al.* In Situ TEM Analysis of Organic-Inorganic Metal-Halide Perovskite Solar Cells under Electrical Bias. *Nano Lett.* **16**, 7013–7018 (2016).

29. Li, C. *et al.* Real-Time Observation of Iodide Ion Migration in Methylammonium Lead Halide Perovskites. *Small* **13**, 1–10 (2017).

30. Leijtens, T. *et al.* Mapping Electric Field-Induced Switchable Poling and Structural Degradation in Hybrid Lead Halide Perovskite Thin Films. *Adv. Energy Mater.* **5**, 1500962 (2015).

31. Deng, X. *et al.* Electric field induced reversible and irreversible photoluminescence responses in methylammonium lead iodide perovskite. *J. Mater. Chem. C* **4**, 9060–9068 (2016).

32. Rizzo, A. *et al.* Understanding lead iodide perovskite hysteresis and degradation causes by extensive electrical characterization. *Sol. Energy Mater. Sol. Cells* **189**, 43–52 (2019).

33. Bo, C. *et al.* Large Electrostrictive Response in Lead Halide Perovskites. *Nat. Mater.* **17**, 11020–1026 (2018).

34. Kim, D. *et al.* Light- and bias-induced structural variations in metal halide perovskites. *Nat. Commun.* **10**, 444 (2019).

35. Luchkin, S. Y. *et al.* Reversible and irreversible electric field induced morphological and interfacial transformations of hybrid lead iodide perovskites. *ACS Appl. Mater. Interfaces* **9**, 33478–33483 (2017).

36. Bischak, C. G. *et al.* Origin of Reversible Photoinduced Phase Separation in Hybrid Perovskites. *Nano Lett.* **17**, 1028–1033 (2017).

37. Braly, I. L. *et al.* Current-Induced Phase Segregation in Mixed Halide Hybrid Perovskites and its Impact on Two-Terminal Tandem Solar Cell Design. *ACS Energy Lett.* **2**, 1841–1847 (2017).

38. Samu, G. F. *et al.* Electrochemical Hole Injection Selectively Expels Iodide from Mixed Halide Perovskite Films. *J. Am. Chem. Soc.* **141**, 10812–10820 (2019).

39. Najafi, M. *et al.* Highly Efficient and Stable Flexible Perovskite Solar Cells with Metal Oxides Nanoparticle Charge Extraction Layers. *Small* **14**, 1–10 (2018).

40. Bai, S. *et al.* Planar perovskite solar cells with long-term stability using ionic liquid additives. *Nature* **571**, 245–250 (2019).

41. Chen, W. *et al.* Molecule-Doped Nickel Oxide: Verified Charge Transfer and Planar Inverted Mixed Cation Perovskite Solar Cell. *Adv. Mater.* **30**, 1800515 (2018).

42. Abzieher, T. *et al.* Electron-Beam-Evaporated Nickel Oxide Hole Transport Layers for Perovskite-Based Photovoltaics. *Adv. Energy Mater.* **9**, 1802995 (2019).

43. Park, I. J. *et al.* Highly Efficient and Uniform 1 cm 2 Perovskite Solar Cells with an Electrochemically Deposited NiO x Hole-Extraction Layer. *ChemSusChem* **10**, 2660–2667 (2017).

44. Hu, C. *et al.* Tuning the A-site cation composition of FA perovskites for efficient and stable NiO-based p-i-n perovskite solar cells. *J. Mater. Chem. A* **5**, 21858–21865 (2017).

45. Xie, L.-Q. *et al.* Understanding the Cubic Phase Stabilization and Crystallization Kinetics in Mixed Cations and Halides Perovskite Single Crystals. *J. Am. Chem. Soc.* **139**, 3320–3323 (2017).

46. Giacovazzo, C. *et al.* *Fundamentals of Crystallography.* (Oxford University Press, 2011). doi:10.1093/acprof:oso/9780199573653.001.0001

47. Di Girolamo, D. *et al.* Dual effect of humidity on cesium lead bromide: enhancement and degradation of perovskite films. *J. Mater. Chem. A* **7**, 12292–12302 (2019).

48. Yuan, Y. *et al.* Electric-Field-Driven Reversible Conversion Between Methylammonium Lead Triiodide Perovskites and Lead Iodide at Elevated Temperatures. *Adv. Energy Mater.* **6**, 1501803 (2016).

49. Lopez-Varo, P. *et al.* Effects of Ion Distributions on Charge Collection in Perovskite Solar Cells. *ACS Energy Lett.* **2**, 1450–1453 (2017).

50. *X-Ray and Neutron Diffraction in Nonideal Crystals.*

51. Andaji-Garmaroudi, Z. *et al.* A Highly Emissive Surface Layer in Mixed-Halide Multication Perovskites. *Adv. Mater.* **31**, (2019).

52. Hoke, E. T. *et al.* Reversible photo-induced trap formation in mixed-halide hybrid perovskites for photovoltaics. *Chem. Sci.* **6**, 613–617 (2015).

53. Ruf, F. *et al.* The Bandgap as a Moving Target: Reversible Bandgap Instabilities in Multiple-Cation Mixed-Halide Perovskite Solar Cells. *ACS Energy Lett.* **3**, 2995–3001 (2018).

54. Schelhas, L. T. *et al.* Insights into operational stability and processing of halide perovskite active layers. *Energy Environ. Sci.* **12**, 1341–1348 (2019).

55. Motti, S. G. *et al.* Controlling competing photochemical reactions stabilizes perovskite solar cells. *Nat. Photonics* **13**, 532–539 (2019).

56. DeQuilettes, D. W. *et al.* Photo-induced halide redistribution in organic-inorganic perovskite films. *Nat. Commun.* **7**, (2016).

57. Merdasa, A. *et al.* Super-resolution luminescence microspectroscopy reveals the mechanism of photoinduced degradation in CH3NH3PbI3perovskite nanocrystals. *J. Phys. Chem. C* **120**, 10711–10719 (2016).
58. Cacovich, S. *et al.* Unveiling the Chemical Composition of Halide Perovskite Films Using Multivariate Statistical Analyses. *ACS Appl. Energy Mater.* **1**, 7174–7181 (2018).
59. Rehman, W. *et al.* Charge-Carrier Dynamics and Mobilities in Formamidinium Lead Mixed-Halide Perovskites. *Adv. Mater.* **27**, 7938–7944 (2015).
60. Tsai, H. *et al.* Light-induced lattice expansion leads to high-efficiency perovskite solar cells. *Science (80-.).* **360**, 67–70 (2018).
61. Jones, T. W. *et al.* Lattice strain causes non-radiative losses in halide perovskites. *Energy Environ. Sci.* **12**, 596–606 (2019).
62. Zhu, C. *et al.* Strain engineering in perovskite solar cells and its impacts on carrier dynamics. *Nat. Commun.* **10**, 815 (2019).
63. Zhang, L. *et al.* Strain induced electronic structure variation in methyl-ammonium lead iodide perovskite. 1–9 (2018). doi:10.1038/s41598-018-25772-3
64. Adhyaksa, G. W. P. *et al.* Understanding Detrimental and Beneficial Grain Boundary Effects in Halide Perovskites. *Adv. Mater.* **30**, 1804792 (2018).
65. Xing, J. *et al.* High-Efficiency Light-Emitting Diodes of Organometal Halide Perovskite Amorphous Nanoparticles. *ACS Nano* **10**, 6623–6630 (2016).
66. Alsari, M. *et al.* In situ simultaneous photovoltaic and structural evolution of perovskite solar cells during film formation. *Energy Environ. Sci.* **11**, 383–393 (2018).
67. Abdi-Jalebi, M. *et al.* Maximizing and stabilizing luminescence from halide perovskites with potassium passivation. *Nature* **555**, 497–501 (2018).
68. Zhao, L. *et al.* Electrical Stress Influences the Efficiency of CH 3 NH 3 PbI 3 Perovskite Light Emitting Devices. *Adv. Mater.* **29**, 1605317 (2017).
69. Wang, Y. *et al.* Pressure-Induced Phase Transformation, Reversible Amorphization, and Anomalous Visible Light Response in Organolead Bromide Perovskite. *J. Am. Chem. Soc.* **137**, 11144–11149 (2015).
70. Di Girolamo, D. *et al.* From Bulk to Surface: Sodium Treatment Reduces Recombination at the Nickel Oxide/Perovskite Interface. *Adv. Mater. Interfaces* **6**, 1900789 (2019).
71. Mahesh, S. *et al.* Revealing the origin of voltage loss in mixed-halide perovskite solar cells. *Energy Environ. Sci.* **50**, 675 (2020).
72. De Wolf, S. *et al.* Organometallic halide perovskites: Sharp optical absorption edge and its relation to photovoltaic performance. *J. Phys. Chem. Lett.* **5**, 1035–1039 (2014).
73. Guerrero, A. *et al.* Properties of Contact and Bulk Impedances in Hybrid Lead Halide Perovskite Solar Cells Including Inductive Loop Elements. *J. Phys. Chem. C* **120**, 8023–8032 (2016).
74. Pockett, A. *et al.* Microseconds , milliseconds and seconds : perovskite solar cells †. *Phys. Chem. Chem. Phys.* **19**, 5959–5970 (2017).
75. Moia, D. *et al.* Ionic-to-electronic current amplification in hybrid perovskite solar cells: ionically gated transistor-interface circuit model explains hysteresis and impedance of mixed conducting devices. *Energy Environ. Sci.* **12**, 1296–1308 (2019).
76. Ebadi, F., Taghavinia, N., Mohammadpour, R., Hagfeldt, A. & Tress, W. Origin of apparent light-enhanced and negative capacitance in perovskite solar cells. *Nat. Commun.* **10**, 1–9 (2019).
77. Matsui, T. *et al.* Compositional Engineering for Thermally Stable, Highly Efficient Perovskite Solar Cells Exceeding 20% Power Conversion Efficiency with 85 °C/85% 1000 h Stability. *Adv. Mater.* **31**, 1806823 (2019).
78. Li, N. *et al.* Cation and anion immobilization through chemical bonding enhancement with fluorides for stable halide perovskite solar cells. *Nat. Energy* **4**, 408–415 (2019).
79. Kosasih, F. U. & Ducati, C. Characterising degradation of perovskite solar cells through in-situ and operando electron microscopy. *Nano Energy* **47**, 243–256 (2018).
80. De La Pena, F. *et al.* Electron Microscopy (Big and Small) Data Analysis With the Open Source Software Package HyperSpy. *Microsc. Microanal.* **23**, 214–215 (2016).

Chapter 7 Conclusion and Outlook

7.1 Discussion of the work

The works in this dissertation aim to provide a fundamental understanding of **ionic defect formation** upon intentional doping, as well as the **ionic defect migration** concerning the microstructure of the sample, and its effect on the device stability in hours timescale similar to real working condition. This section aims to present the background research of the works included in the cumulative thesis as well as the discussion how the main finding links to the fundamental understanding of the defect chemistry in halide perovskite.

7.1.1 The doping mechanism of perovskite: insights into the defect formation upon impurity inclusion

a. Background and the relation with the current literature

Chapter 4 focuses on the effect of intentional introduction impurity into the material. This doping procedure has been used extensively in halide perovskite to improve its efficiency and stability.[1-2] Incorporating a small amount of foreign metal cations (less than 10%) such as Rb in the perovskite absorber has been an efficient way to improve device performance and stability.[2] Although Rb and K can be too small to form perovskite,[2-3] its positive effect to improve perovskite solar cells (PSCs) is widely acknowledged especially to suppress the hysteresis seen in devices. Saliba *et al.* demonstrated more than 21% stabilised efficiency for 5% Rb incorporated into triple cation CsFAMA perovskite ($Cs_{0.05}((FAPbI_3)_{0.83}(MAPbI_3)_{0.17})_{0.95}$ where formamidinium is FA, and methylammonium is MA) thanks to the better crystallisation of the perovskite film.[2] Later, solid-state nuclear magnetic resonance showed that unlike Cs which could replace FA in the A site, Rb segregated outside perovskite phase,[3] as $RbPbI_3$ photoactive perovskite phase is not realised even at high temperature.[2]

For divalent ions such as alkaline earth metal cations: Sr and Ca, or transition metal Cd, and Co, they have been speculated that they can replace lead in the perovskite structure ABX_3 from early theoretical calculations.[4-7] Because of the similarity of ionic radii and electronic charge to Pb^{2+}, Sr^{2+} becomes a strong candidate for lead substitution. The methylammonium strontium iodide ($MASrI_3$) based perovskite is predicted to have a large bandgap of 3.6-3.7eV[6, 8] which is not suitable for single-junction PSCs. However, several studies show that using Sr to replace Pb results in lower optical bandgap Sr-incorporated-$MAPbI_3$ compared to intrinsic $MAPbI_3$ confirming by UV-vis absorption.[4, 9] Furthermore, by the time of writing, a synthesised $MASrI_3$ isolated perovskite phase has not been realised in practice[5-6] which poses a question whether the Sr can substitute Pb in the metal halide perovskite structure. On the contrary, Sr segregated phases are also reported to passivate the perovskite film or modify the interfacial energy level between perovskite and contact layer.[10-12] Lau *et al.* used Sr in the mixed halide inorganic perovskite $CsPbI_2Br$. Through X-ray photoelectron spectroscopy, they identified enriched Sr surface of the perovskite.[11] This Sr-rich coating acted as a passivation layer and significantly reduced the temperature processing of the inorganic perovskite.[11] Similarly, 2% Sr-doped $MAPbI_3$ showed superior charge carrier lifetime and resulted in a high fill factor (as high as 85%) device due to passivation effect from $Sr(C_2H_3O_2)_2$ segregation phase.[10] On the other hand, recently, Saidaminov *et al.* proposed that divalent metal ion such as Cd^{2+} can reduce the lattice strain in $FAPbI_3$ which enhances the stability of the perovskite.[13] They reasoned that the inclusion of Cd^{2+} in the lattice to replace Pb^{2+} (which has a smaller ionic radius compared to Pb^{2+}) suppressed the formation of iodide vacancy by increasing its formation energy. Furthermore, filling vacancy reduced the lattice strain which could enhance the black phase stability.[14]

The uncertainty in the literature on the role of dopants in the perovskite film electronic and structural properties motivates us to extend the investigated doping regime of methylammonium lead iodide. **Chapter 4** uses Sr and Mg as two representatives for divalent doping mechanism investigation. Although the mixed cation mixed halide perovskite has been widely used for the highly efficient, stable PSCs, this study opts to use methylammonium lead iodide to have a simple system. In addition, to exclude the effect of different anions, which might change the crystallisation process of the perovskite inducing more complication in the analysis, the study uses SrI_2 and MgI_2 in the perovskite precursor to create a similar crystallisation growth environment for the thin film as well as provide iodide ions to passivate defects. The study result argues that there are different mechanisms of doping depending on the concentration of the dopants in the films, which led to different conclusions in the literature. **Chapter 4** proposes two doping regimes that result in different electronic and chemical environment of the films. At high concentration, the dopant is more likely to segregate to the surface of the film whereas the low concentration dopant is more likely to reside within the lattice of the perovskite. The low doping level enables dopants to be included in the lattice and thus, affects the defect formation energy of the material. In particular, the dopants can reduce the formation energy of harmful defects, and in turn, lead to higher quality material.

b. Discussion

The incorporation of Sr and Mg in $MAPbI_3$ may occur through various processes: i) substitution of Pb (Sr_{Pb} or Mg_{Pb}); ii) Sr or Mg sitting on an interstitial position (Sr_i^{2+} or Mg_i^{2+}); iii) substitution of the cation (Sr_{MA}^+ or Mg_{MA}^+). A theoretical calculation shows that one of the most common defects in $MAPbI_3$ is the Pb vacancy (V_{Pb}^{2-}) which can trap holes through (-/2-) ionization levels with detrimental effects on the photoluminescence (PL) properties of $MAPbI_3$.[15] This harmful defect locates at ~0.1 eV above the valance band creating a deep trap, which can potentially reduce the efficiency of PSCs.[16] As lattice inclusion via Pb substitution by Sr^{2+} is feasible shown by calculation,[6] filling V_{Pb}^{2-} by the divalent doping atoms (resulted in Sr_{Pb} or Mg_{Pb}) can enhance PSCs performance considering no new detrimental defects formed. Theoretical calculations have also predicted that the presence of a monovalent cation in the interstitial position of the lattice increases the formation energy of iodine Frenkel defects, which are formed by iodine leaving its proper site to generate an interstitial iodide (I_i^-) coupled with an iodide vacancy (V_I^+).[17] Hence, the possibility of Sr^{2+} and Mg^{2+} at the interstitial site (Sr_i^{2+} or Mg_i^{2+}) may also have a positive impact on device performance by stabilising I related defects. Also, as the MA vacancies (V_{MA}^-) are also well documented by experiments to be present in perovskite,[18] it is worth considering the substitution of MA cation (Sr_{MA}^+ or Mg_{MA}^+). Although V_{MA}^- only introduces shallow trap states, which has a relatively low impact on device performances,[19] they can trigger the degradation of halide perovskites.[20] Hence, passivating this defect is expected to be essential for the long term stability of PSCs.

Using hard X-ray photoemission spectroscopy (HAXPES) and X-ray fluorescence, two doping regimes are clearly observed. At low doping concentration (less than 0.5% in Sr and less than 1% in Mg doping case), the dopants can be distributed quite uniformly in the film. On the contrary, the surface segregation at high doping concentration is confirmed by HAXPES where the detected Sr (and somewhat Mg) amount on the surface is much greater than the nominal doping concentration. As a bulk technique, XRF provides an elemental distribution analysis of the samples to compliment the HAXPES data. It is shown that at high doping concentration, segregated phase appears whereas a uniform distribution of dopant can be seen at a lower concentration. This might explain the discrepancy results seen in literature where the lattice incorporation can depend on the perovskite lattice, initial growth condition, and its intrinsic defect concentration.

To examine the lattice inclusion and phase segregation threshold, microstrain analysis from X-ray diffraction (XRD) patterns offers an insight. The microstrain analysis shows a clear trend where the microstrain increases with the doping concentration until a maximum and then decreases at high doping concentration. This is strong evidence of lattice inclusion at the low doping concentration where the dopant can induce lattice distortion. The lattice inclusion evidence is also corroborated with the theoretical calculation. By introducing the dopant into the system, the dopants can passivate vacancies of Pb, MA and be at the interstitial position. The Sr^{2+} and Mg^{2+} doping results in a less amount of detected metallic lead. Metallic lead is a by-product of lead-related defect formation, thus, its reduction links to a defect concentration reduction in perovskite. Moreover, the perovskite exhibits a more n-type material at low doping concentration, which is, furtherly, correlated to the reduction of vacancies concentration. In Mg^{2+} case, the high microstrain of the doped sample indicates that the element can be at the interstitial position due to its small ionic radius. This is in agreement with the PL measurement showing a better quality material and the resulted open circuit voltage enhancement in devices. Hence, the lattice inclusion regime can be beneficial for defect reduction in perovskite.

The result of this work indicates that doping can change the defect formation energy of perovskite, especially at the lattice inclusion regime. The work also shows the possibility to use alkaline earth metal ions in perovskite to improve the material quality.

7.1.2 The role of microstructure in ionic defect migration

a. Background and the relation with current literature

Chapter 5 revolves around the dynamic of ionic defect migration. Since ionic defect migration is an integral part of perovskite solar cells (PSCs) performance, understanding ionic defect migration is imperative for devices optimisation and material design. The ionic migration (where ions leave its proper site) can create defects that change the defect concentration and distribution in the material, and ions are suspected to move via defect hoping mechanism.[21] Thus, ionic defect migration is related to the existing defects in the material. Hence, the defect concentrated grain boundaries (GBs) in polycrystalline material can play a significant role in the movement of ions through the material. Notably, one of the most commonly used fabrication methods for PSCs is solution processing which forms a polycrystalline film, it is vital to consider the effect of GBs on ionic defect migration.

It has been an ongoing debate in the literature on how the defective area GBs affect ion migrations. Some reports have shown that GBs facilitate the route for ion migration[22-23] where it is observed a larger hysteresis at the GBs compared the grain interior.[22] Moreover, the activation energies for ion migrations are higher in single crystal or in larger grain film compared to small grain film[24] which might indicate the difficulties for ions to move with the absence of GBs or large defect concentration. On the other hand, it has been observed a hysteresis reduction in devices with large grain size compared to small ones.[25-26] Thus, in large grain devices, the ionic movement is faster.[25]

To extend the understanding of this relation, in the study in **Chapter 5**, micro-photoluminescence (PL) is used as a method to track ion movement. PL has been widely used to detect the effect of ionic defect migration of perovskite.[27] This powerful contactless technique offers the opportunity to exclude the influence of other layers or contacts on the signals. It has been shown that the reduction in PL yield relates to ions movement[28] which can create trap states to quench PL, especially at a high light intensity.[29]

In **Chapter 5**, we observe the change in PL signal in hundreds of millisecond timescale which correspond to ionic induces a change in the methylammonium lead iodide ($MAPbI_3$). By resolving the dynamic of PL yield over time and space of different grain sizes film and single crystal of $MAPbI_3$, it is able to investigate the impact of GBs on the ion migration in perovskite. **Chapter 5** concludes that the GBs inhibit the movement of ions in the lateral direction.

b. Discussion

In the study of **Chapter 5**, to probe the change of the material due to light, the material is excited with a blue laser and then subjected to EDX measurement. The obtained elemental distribution of the sample after laser exposure shows that light can remove ions out of the material, in particular, iodide signal and somewhat in carbon signal (relating to the cation MA+) reduce after the laser exposure. This is clearly an indication of light-induced defect formation. This reduction in the iodide signal within the laser-excited spot correlates to the PL yield decrease. Hence, the couple between PL yield and ionic defect formation and migration is clear. **Chapter 5** uses PL microscopy to track the changes in material caused by ionic defect migration over time and space.

To probe the migration of these defects, the sample PL yield is tracked in different configurations (focused and defocused mode by light) while collecting PL yield from a large area of the sample. It is shown that the PL yield in the focus mode starts to increase around the laser focus point resembling a ring. The ring slowly moves outside the laser exposed spot. It is worth noticing that the PL time resolution, in this case, is in hundreds of ms scale, which is much slower than the charge dynamic. Hence, this can be attributed to ionic defect migration. Nonetheless, the real evidence for the PL signal to link to ionic defect migration is the difference between focused and defocused mode. During the focused mode, the presence of the charge carriers (as seen in PL signal) is seen much further away from the excited point which is similar for both thin film and single crystal. However, the long-lasting PL yield reduction is different for thin-film and single crystal. In particular, the PL yield reduction is localised at the laser exposed area in the thin film (with high GBs density) whereas the reduction in yield is in a much larger area of the single crystal (with low GBs density). This movement is starkly different can be attributed directly to the difference in GBs density of the two samples. In another word, lower GBs density allows a longer diffusion length of the ionic defect.

It is undeniable that aside from the microstructure, the thin-film and single crystal might have different photo-physic properties, hence, an intermediate case of big grain thin-film is used to confirm the hypothesis of GBs blocking ionic migration. It is shown that the PL yield reduction is restricted at the laser-excited grain. Furthermore, the dark recovery of the yield of the sample also corroborates the previous observation. The PL yield recovers from the GB of the grain. This means that highly defective area at GBs block ionic defect migration, and the kinetic trapped ionic defect can migrate back and recover (partially) the degraded area of the sample. This is corroborated by the theoretical simulation where the low potential energy at the GBs is the driving force for the ionic defect to diffuse towards the GBs, however, the ionic defects are trapped at the GBs. To release the ionic defect, an energy barrier needs to be overcome. Since this is a thermal process, it will require a long time for ions to be released at room temperature. This is well-aligned with experimentally observed recovery time.

The study combines both experiment measurement and theoretical simulation provides strong evidence that GBs block ionic defect migration. This is in an agreement with the observation in devices where a faster ionic response is detected in a big grain device compared to a small grain device. The study shows that the GBs might block ions to move from the material to the interfaces of the device where the ions can have (photo)chemical reaction with contact layer material or the electrodes. Thus, the inhibition of ions from perovskite to other layers can have a positive effect in that case. However, the accumulation of ionic defects within the grain is expected to promote the intrinsic degradation pathway from defects as mentioned in **section 1.2.2** Hence, it is still preferable to prevent light-induced ionic defect migration in solar cells. In the case where the ionic defect migration cannot be avoided, the monolithic grain of the perovskite layer in a solar cell is still beneficial to avoid ionic defect accumulation inside the perovskite. To prevent the (photo)chemical reaction to contact layers and metal electrodes, it is essential to choose a robust and inert material as contact layers in perovskite-based devices. In addition, as the ionic defect can migrate back and “heal” the sample, this underlines the importance of day/night cycling for long-term stability testing of PSCs.

7.1.3 Amorphization of perovskite due to bias-induced ionic defect migration

a. Background and the relation with the current literature

In **Chapter 6**, the study focuses on the device's performance under the forward bias to assess the influence of electric field especially on the mix halide compositions which is present in the working conditions. The operational electric field can have a strong impact on ionic defect migration. The ionic bonds in the halide perovskite give rise to ionic defect migration under bias, which is the main cause behind hysteresis seen in current density-voltage (J-V) scans.[30-31] It also affects the long-term stability of the material where the cation at the A site is suspected to migrate at a long timescale such as hours or days.[18] Therefore, it is crucial to investigate how the device behaves in hours duration in bias conditions.

Moreover, despite the advantage of a tunable bandgap to achieve high efficiency, the mixed halide perovskite can suffer from halide segregation due to light and bias.[32-33] It has been seen for methylammonium based perovskite ($MAPbI_xBr_{3-x}$). Upon illumination, the iodide and bromide component which initially mixed became two separate phases which result in two corresponded photoluminescence (PL) peaks.[32] Interestingly, depending on the A site, the threshold in which this phenomenon happens is different. For example, less than 20% Br in the mix for MA-based perovskite provide photostability[32] and the stable composition can stretch further with the inclusion of nonpolar A site such as Cs.[34] Hence, it is required to investigate further the widely used triple cation CsFAMA ($Cs_{0.05}((FAPbI_3)_{0.83}(MAPbI_3)_{0.17})_{0.95}$ where formamidinium is FA, and methylammonium is MA) composition in the device under bias.

Halide segregation is often linked to the photo-stability of mixed halide perovskite. However, it has been shown that the presence of charge carriers is important for this to happens. Using a computation method, Bischak *et al.* developed a model of interaction between the photogenerated charge carriers and the polarons. This effect induces the lattice strain within the halide perovskite structure.[35] The strain due to distortion increases the enthalpy of the system. Demixing into two different halide domains consequently becomes more thermodynamically favourable. Emphasising the presence of charge carriers instead of light, Braly *et al.* also reported halide segregation due to current injection in electroluminescence (EL) measurement.[36] Moreover, it has been proposed that the electronic traps at the grain boundaries and surface promote halide migration.[37] Upon light exposure, photogenerated charge carriers fill the trap states such as halide vacancies, and form an electric field which causes halide migration. Hence, using forward bias, the study of **Chapter 6** shows that the injected current together with the electric field can cause halide segregation in devices, which is in agreement with literature. However, it is found that perovskite amorphization is also a direct result of bias stress due to prolonged ionic defect migration, which strongly limits the charge collection efficiency, thus reducing fill factor (FF) and short circuit current (J_{SC}).

b. Discussion

By applying a forward bias to the PSCs, it is expected that the ionic nature of perovskite will be strongly affected by the electric field introduced by bias stress. Thus, it is possible to investigate the effect of long term ionic defect migration on the device performance. The long timescale of 6-12 hours is similar to the operational time for solar cells in working condition. Upon biasing at 1.2 V, the device's open circuit voltage (V_{OC}) increases whereas both J_{SC} and FF decrease. This overall degrades the device's performance. The device can recover partially while resting in dark without bias. To understand the bias effects on the material, the study uses extensively in situ X-ray diffraction (XRD) and grazing incidence wide-angle X-ray scattering (GIWAXS) to detect the changes in material composition during biasing. The formation of crystalline iodide rich phase is seen in XRD peak splitting. This is confirmed by EL measurement where a low bandgap peak emerged quickly upon bias. Using multivariate data analysis (Non-negative matrix factorisation) to extract data from scanning transmission electron microscopic (STEM) image, it is found that the bromide rich phase accumulates at the interface especially between perovskite and NiO as the hole selective layer.

However, the halide segregation is not the only factor affecting device performance. The XRD and GIWAXS result shows surprisingly the amorphization of the perovskite upon biasing. The perovskite intensity reduction is a strong indication of amorphous phase formation. This amorphous phase is attributed to the bromide rich phase at the interface shown in STEM. This is because of the absence of XRD peak belonging to bromide rich crystalline phase in the patterns collected from the biased device. Furthermore, in situ GIWAXS shows a stronger amorphization at the surface of the device compared to the bulk. Hence, it is likely that the amorphous phase is mainly at the interfaces. One can expect a more disordered system (the growth of amorphous phase) to result in a lower V_{OC} device,[38] however, the biased device shows a higher V_{OC} compared to fresh device. This can be due to the improvement of bulk quality. It is possible that the ionic defect migration from the bulk can relax the lattice strain and increase the V_{OC} in agreement with a recent report.[39] This can corroborate with a more homogenous bulk shown in the TEM image. However, as little is known about the amorphous phase of perovskite, it is difficult to assign this as the only factor to increase V_{OC}. In fact, several reports have shown that the amorphous area of perovskite sample can show a high luminescence yield,[40-41] though the atomic insight behind this is not well understood.

Another possibility is the amorphous bromide phase act as a wide bandgap passivation layer. The wide bandgap material can act as a barrier for one type of charge carrier similar to the positive effect of PbI_2 excess seen in devices,[42] which reduces the loss of V_{OC} due to interfacial recombination.[43] However, without an exact composition of the bromide phase, it is challenging to construct the band alignment in the biased device. To confirm the role of halide segregation in the V_{OC} enhancement, the PSCs are biased at 1 V which has lower injected current density eventually leading to a stable EL peak. Despite the absence of halide segregation, the device exhibits similar behaviour as the V_{OC} increases significantly. Hence, it is unlikely that halide segregation alone results in a V_{OC} enhancement, and further study is required to give an exact explanation.

On the contrary to the increased V_{OC}, the J_{SC} and FF of the biased cells reduce substantially compared to the fresh cell. The measured external quantum efficiency (EQE) reduces overtime upon biasing especially at shorter wavelengths. The short wavelength photons have shorter penetration depth compared to long wavelength photons, which implies a poor charge extraction at the interface between perovskite and NiO (the direction where the light comes in). Moreover, the charge extraction measurement also shows that a considerable amount of photogenerated charge carriers recombines without being collected, even though the charge carrier recombination lifetime obtained from transient photovoltage increases upon bias corresponding to higher V_{OC}. Hence, the poor charge extraction at the interface of perovskite and contact layer is the main reason for the reduction in J_{SC} and FF. Thus, the negative effect of amorphous bromide rich phase is evidenced, and the perovskite amorphization is a degradation pathway for PSCs in a bias condition.

To conclude, this study result emphasises the long-term stability of PSCs in the presence of an electric field. Due to the ionic defect migration, the composition of perovskite can change in the operational condition. It is an important point to consider for PSCs stability testing. As mentioned in **section 7.1.2** the recovery of perovskite as ionic defect migrating back to their lattice sites implies that dark/night cycling testing is more accurate to predict the lifetime of perovskite-based solar cells in real working conditions.

7.2 Outlook

These studies mentioned above can lead to future works. Although **Chapter 4** provides strong evidence of lattice inclusion for divalent metal ions, it lacks of experimental determined exact positions of the dopants in the lattice. Moreover, theoretical calculation shows that the dopants orbitals have no contribution to the band edge when they substitute lead in halide perovskite, it might be different when the dopants are at interstitial or cation substitution. The microstrain caused by lattice inclusion can further alter the band structure due to the modification of Pb-I bond angle. Hence, this opens new questions to understand the introduction of impurities inside halide perovskite.

Chapter 5 focuses on the light-induced ionic defect migration with respect to the microstructure of the samples, i.e. the grain boundary density. Ongoing follow-up work will focus on the mechanism behind the phenomena. This study will try to provide a thermodynamic explanation of how the light drives ionic defect to migrate from their lattice sites. It is anticipated that the conclusion from the simple system of methylammonium lead iodide can be applied to a more complex system (mix halide mix cation perovskite) which can be in interest of a future work. The fundamental aspect of this phenomenon can have an influence on the material design for device optimisation.

The study in **Chapter 6** has tried to provide a comprehensive picture of ionic defect migration in the device, however, the study was done with devices in the dark. Building up from these findings, further work on the material changes during operational (combination between light and bias) will be beneficial to understand the degradation mechanism. In addition, an innovative method is still missing to mitigate the challenges raised due to ionic defect migration.

Reference

1. Saliba, M.; Matsui, T.; Seo, J.-Y.; Domanski, K.; Correa-Baena, J.-P.; Nazeeruddin, M. K.; Zakeeruddin, S. M.; Tress, W.; Abate, A.; Hagfeldt, A., Cesium-containing triple cation perovskite solar cells: improved stability, reproducibility and high efficiency. *Energy & environmental science* **2016,** *9* (6), 1989-1997.
2. Saliba, M.; Matsui, T.; Domanski, K.; Seo, J.-Y.; Ummadisingu, A.; Zakeeruddin, S. M.; Correa-Baena, J.-P.; Tress, W. R.; Abate, A.; Hagfeldt, A.; Grätzel, M., Incorporation of rubidium cations into perovskite solar cells improves photovoltaic performance. *Science* **2016,** *354* (6309), 206-209.
3. Kubicki, D. J.; Prochowicz, D.; Hofstetter, A.; Zakeeruddin, S. M.; Grätzel, M.; Emsley, L., Phase Segregation in Cs-, Rb-and K-Doped Mixed-Cation (MA)x(FA)1–xPbI_3 Hybrid Perovskites from Solid-State NMR. *Journal of the American Chemical Society* **2017,** *139* (40), 14173-14180.
4. Navas, J.; Sánchez-Coronilla, A.; Gallardo, J. J.; Hernández, N. C.; Piñero, J. C.; Alcántara, R.; Fernández-Lorenzo, C.; Desireé, M.; Aguilar, T.; Martín-Calleja, J., New insights into organic–inorganic hybrid perovskite $CH_3NH_3PbI_3$ nanoparticles. An experimental and theoretical study of doping in Pb^{2+} sites with Sn^{2+}, Sr^{2+}, Cd^{2+} and Ca^{2+}. *Nanoscale* **2015,** *7* (14), 6216-6229.
5. Jacobsson, T. J.; Pazoki, M.; Hagfeldt, A.; Edvinsson, T., Goldschmidt's rules and strontium replacement in lead halogen perovskite solar cells: theory and preliminary experiments on $CH_3NH_3SrI_3$. *The Journal of Physical Chemistry C* **2015,** *119* (46), 25673-25683.
6. Pazoki, M.; Jacobsson, T. J.; Hagfeldt, A.; Boschloo, G.; Edvinsson, T., Effect of metal cation replacement on the electronic structure of metalorganic halide perovskites: Replacement of lead with alkaline-earth metals. *Physical Review B* **2016,** *93* (14), 144105.
7. Klug, M. T.; Osherov, A.; Haghighirad, A. A.; Stranks, S. D.; Brown, P. R.; Bai, S.; Wang, J. T.-W.; Dang, X.; Bulović, V.; Snaith, H. J.; Belcher, A. M., Tailoring metal halide perovskites through metal substitution: influence on photovoltaic and material properties. *Energy & Environmental Science* **2017,** *10* (1), 236-246.
8. Wang, K.; Liang, Z.; Wang, X.; Cui, X., Lead replacement in $CH_3NH_3PbI_3$ perovskites. *Advanced Electronic Materials* **2015,** *1* (10), 1500089.
9. Shai, X.; Zuo, L.; Sun, P.; Liao, P.; Huang, W.; Yao, E.-P.; Li, H.; Liu, S.; Shen, Y.; Yang, Y.; Wang, M., Efficient planar perovskite solar cells using halide Sr-substituted Pb perovskite. *Nano Energy* **2017,** *36*, 213-222.
10. Pérez-del-Rey, D.; Forgács, D.; Hutter, E. M.; Savenije, T. J.; Nordlund, D.; Schulz, P.; Berry, J. J.; Sessolo, M.; Bolink, H. J., Strontium Insertion in Methylammonium Lead Iodide: Long Charge Carrier Lifetime and High Fill-Factor Solar Cells. *Advanced Materials* **2016,** *28* (44), 9839-9845.
11. Lau, C. F. J.; Zhang, M.; Deng, X.; Zheng, J.; Bing, J.; Ma, Q.; Kim, J.; Hu, L.; Green, M. A.; Huang, S.; Ho-Baillie, A., Strontium-doped low-temperature-processed $CsPbI_2Br$ perovskite solar cells. *ACS Energy Letters* **2017,** *2* (10), 2319-2325.
12. Caprioglio, P.; Zu, F.; Wolff, C. M.; Prieto, J. A. M.; Stolterfoht, M.; Koch, N.; Unold, T.; Rech, B.; Albrecht, S.; Neher, D., High Open Circuit Voltages in pin-Type Perovskite Solar Cells through Strontium Addition. *arXiv preprint arXiv:1810.12262* **2018**.
13. Saidaminov, M. I.; Kim, J.; Jain, A.; Quintero-Bermudez, R.; Tan, H.; Long, G.; Tan, F.; Johnston, A.; Zhao, Y.; Voznyy, O.; Sargent, E. H., Suppression of atomic vacancies via incorporation of isovalent small ions to increase the stability of halide perovskite solar cells in ambient air. *Nature Energy* **2018,** *3* (8), 648-654.
14. Zheng, X.; Wu, C.; Jha, S. K.; Li, Z.; Zhu, K.; Priya, S., Improved phase stability of formamidinium lead triiodide perovskite by strain relaxation. *ACS Energy Letters* **2016,** *1* (5), 1014-1020.

15. Meggiolaro, D.; Motti, S. G.; Mosconi, E.; Barker, A. J.; Ball, J.; Perini, C. A. R.; Deschler, F.; Petrozza, A.; De Angelis, F., Iodine chemistry determines the defect tolerance of lead-halide perovskites. *Energy & Environmental Science* **2018,** *11* (3), 702-713.

16. Landi, G.; Neitzert, H. C.; Barone, C.; Mauro, C.; Lang, F.; Albrecht, S.; Rech, B.; Pagano, S., Correlation between electronic defect states distribution and device performance of perovskite solar cells. *Advanced Science* **2017,** *4* (10), 1700183.

17. Son, D.-Y.; Kim, S.-G.; Seo, J.-Y.; Lee, S.-H.; Shin, H.; Lee, D.; Park, N.-G., Universal approach toward hysteresis-free perovskite solar cell via defect engineering. *Journal of the American Chemical Society* **2018,** *140* (4), 1358-1364.

18. Domanski, K.; Roose, B.; Matsui, T.; Saliba, M.; Turren-Cruz, S.-H.; Correa-Baena, J.-P.; Carmona, C. R.; Richardson, G.; Foster, J. M.; De Angelis, F.; Ball, J. M.; Petrozza, A.; Mine, N.; Nazeeruddin, M. K.; Tress, W.; Grätzel, M.; Steiner, U.; Hagfeldt, A.; Abate, A., Migration of cations induces reversible performance losses over day/night cycling in perovskite solar cells. *Energy & Environmental Science* **2017,** *10* (2), 604-613.

19. Yin, W.-J.; Shi, T.; Yan, Y., Unusual defect physics in CH3NH3PbI3 perovskite solar cell absorber. *Applied Physics Letters* **2014,** *104* (6), 063903.

20. Leijtens, T.; Hoke, E. T.; Grancini, G.; Slotcavage, D. J.; Eperon, G. E.; Ball, J. M.; De Bastiani, M.; Bowring, A. R.; Martino, N.; Wojciechowski, K.; McGehee, M. D.; Snaith, H. J.; Petrozza, A., Mapping Electric Field-Induced Switchable Poling and Structural Degradation in Hybrid Lead Halide Perovskite Thin Films. *Advanced Energy Materials* **2015,** *5* (20), 1500962.

21. Azpiroz, J. M.; Mosconi, E.; Bisquert, J.; De Angelis, F., Defect migration in methylammonium lead iodide and its role in perovskite solar cell operation. *Energy & Environmental Science* **2015,** *8* (7), 2118-2127.

22. Shao, Y.; Fang, Y.; Li, T.; Wang, Q.; Dong, Q.; Deng, Y.; Yuan, Y.; Wei, H.; Wang, M.; Gruverman, A.; Shield, J.; Huang, J., Grain boundary dominated ion migration in polycrystalline organic–inorganic halide perovskite films. *Energy & Environmental Science* **2016,** *9* (5), 1752-1759.

23. Yun, J. S.; Seidel, J.; Kim, J.; Soufiani, A. M.; Huang, S.; Lau, J.; Jeon, N. J.; Seok, S. I.; Green, M. A.; Ho-Baillie, A., Critical role of grain boundaries for ion migration in formamidinium and methylammonium lead halide perovskite solar cells. *Advanced Energy Materials* **2016,** *6* (13), 1600330.

24. Xing, J.; Wang, Q.; Dong, Q.; Yuan, Y.; Fang, Y.; Huang, J., Ultrafast ion migration in hybrid perovskite polycrystalline thin films under light and suppression in single crystals. *Physical Chemistry Chemical Physics* **2016,** *18* (44), 30484-30490.

25. Correa-Baena, J. P.; Anaya, M.; Lozano, G.; Tress, W.; Domanski, K.; Saliba, M.; Matsui, T.; Jacobsson, T. J.; Calvo, M. E.; Abate, A.; Grätzel, M.; Míguez, H.; Hagfeldt, A., Unbroken Perovskite: Interplay of Morphology, Electro-optical Properties, and Ionic Movement. *Advanced Materials* **2016,** *28* (25), 5031-5037.

26. Nie, W.; Tsai, H.; Asadpour, R.; Blancon, J.-C.; Neukirch, A. J.; Gupta, G.; Crochet, J. J.; Chhowalla, M.; Tretiak, S.; Alam, M. A.; Wang, H.-L.; Mohite, A. D., High-efficiency solution-processed perovskite solar cells with millimeter-scale grains. *Science* **2015,** *347* (6221), 522-525.

27. deQuilettes, D. W.; Zhang, W.; Burlakov, V. M.; Graham, D. J.; Leijtens, T.; Osherov, A.; Bulović, V.; Snaith, H. J.; Ginger, D. S.; Stranks, S. D., Photo-induced halide redistribution in organic–inorganic perovskite films. *Nature communications* **2016,** *7,* 11683.

28. Fassl, P.; Ternes, S.; Lami, V.; Zakharko, Y.; Heimfarth, D.; Hopkinson, P. E.; Paulus, F.; Taylor, A. D.; Zaumseil, J.; Vaynzof, Y., Effect of Crystal Grain Orientation on the Rate of Ionic Transport in Perovskite Polycrystalline Thin Films. *ACS applied materials & interfaces* **2018,** *11* (2), 2490-2499.

29. Chen, S.; Wen, X.; Huang, S.; Huang, F.; Cheng, Y. B.; Green, M.; Ho-Baillie, A., Light illumination induced photoluminescence enhancement and quenching in lead halide perovskite. *Solar Rrl* **2017,** *1* (1), 1600001.

30. Snaith, H. J.; Abate, A.; Ball, J. M.; Eperon, G. E.; Leijtens, T.; Noel, N. K.; Stranks, S. D.; Wang, J. T.-W.; Wojciechowski, K.; Zhang, W., Anomalous hysteresis in perovskite solar cells. *J. Phys. Chem. Lett* **2014,** *5* (9), 1511-1515.

31. Unger, E. L.; Hoke, E. T.; Bailie, C. D.; Nguyen, W. H.; Bowring, A. R.; Heumüller, T.; Christoforo, M. G.; McGehee, M. D., Hysteresis and transient behavior in current–voltage measurements of hybrid-perovskite absorber solar cells. *Energy & Environmental Science* **2014,** *7* (11), 3690-3698.

32. Hoke, E. T.; Slotcavage, D. J.; Dohner, E. R.; Bowring, A. R.; Karunadasa, H. I.; McGehee, M. D., Reversible photo-induced trap formation in mixed-halide hybrid perovskites for photovoltaics. *Chemical Science* **2015,** *6* (1), 613-617.

33. Ruf, F.; Rietz, P.; Aygüler, M. F.; Kelz, I.; Docampo, P.; Kalt, H.; Hetterich, M., The Bandgap as a Moving Target: Reversible Bandgap Instabilities in Multiple-Cation Mixed-Halide Perovskite Solar Cells. *ACS Energy Letters* **2018,** *3* (12), 2995-3001.

34. Bischak, C. G.; Wong, A. B.; Lin, E.; Limmer, D. T.; Yang, P.; Ginsberg, N. S., Tunable polaron distortions control the extent of halide demixing in lead halide perovskites. *The journal of physical chemistry letters* **2018,** *9* (14), 3998-4005.

35. Bischak, C. G.; Hetherington, C. L.; Wu, H.; Aloni, S.; Ogletree, D. F.; Limmer, D. T.; Ginsberg, N. S., Origin of reversible photoinduced phase separation in hybrid perovskites. *Nano letters* **2017,** *17* (2), 1028-1033.

36. Braly, I. L.; Stoddard, R. J.; Rajagopal, A.; Uhl, A. R.; Katahara, J. K.; Jen, A. K.-Y.; Hillhouse, H. W., Current-Induced Phase Segregation in Mixed Halide Hybrid Perovskites and its Impact on Two-Terminal Tandem Solar Cell Design. *ACS Energy Letters* **2017,** *2* (8), 1841-1847.

37. Dequilettes, D. W.; Zhang, W.; Burlakov, V. M.; Graham, D. J.; Leijtens, T.; Osherov, A.; Bulovic, V.; Snaith, H. J.; Ginger, D. S.; Stranks, S. D., Photo-induced halide redistribution in organic-inorganic perovskite films. *Nature Communications* **2016,** *7*, 11683.

38. Tress, W., Perovskite solar cells on the way to their radiative efficiency limit–insights into a success story of high open-circuit voltage and low recombination. *Advanced Energy Materials* **2017,** *7* (14), 1602358.

39. Tsai, H.; Asadpour, R.; Blancon, J.-C.; Stoumpos, C. C.; Durand, O.; Strzalka, J. W.; Chen, B.; Verduzco, R.; Ajayan, P. M.; Tretiak, S.; Even, J.; Alam, M. A.; Kanatzidis, M. G.; Nie, W.; Mohite, A. D., Light-induced lattice expansion leads to high-efficiency perovskite solar cells. *Science* **2018,** *360* (6384), 67-70.

40. Adhyaksa, G. W.; Brittman, S.; Āboliņš, H.; Lof, A.; Li, X.; Keelor, J. D.; Luo, Y.; Duevski, T.; Heeren, R. M.; Ellis, S. R.; Fenning, D. P.; Garnett, E. C., Understanding detrimental and beneficial grain boundary effects in halide perovskites. *Advanced Materials* **2018,** *30* (52), 1804792.

41. Xing, J.; Yan, F.; Zhao, Y.; Chen, S.; Yu, H.; Zhang, Q.; Zeng, R.; Demir, H. V.; Sun, X.; Huan, A.; Xiong, Q., High-efficiency light-emitting diodes of organometal halide perovskite amorphous nanoparticles. *ACS nano* **2016,** *10* (7), 6623-6630.

42. Jacobsson, T. J.; Correa-Baena, J.-P.; Halvani Anaraki, E.; Philippe, B.; Stranks, S. D.; Bouduban, M. E.; Tress, W.; Schenk, K.; Teuscher, J. l.; Moser, J.-E.; Rensmo, H.; Hagfeldt, A., Unreacted PbI2 as a double-edged sword for enhancing the performance of perovskite solar cells. *Journal of the American Chemical Society* **2016,** *138* (32), 10331-10343.

43. Stolterfoht, M.; Wolff, C. M.; Márquez, J. A.; Zhang, S.; Hages, C. J.; Rothhardt, D.; Albrecht, S.; Burn, P. L.; Meredith, P.; Unold, T.; Neher, D., Visualization and suppression of interfacial recombination for high-efficiency large-area pin perovskite solar cells. *Nature Energy* **2018,** *3* (10), 847.

Appendix A[2]

1. The effect of annealing time

The solvents used in the perovskite precursor solution deposited on the substrate are removed by thermal annealing at 100oC after the spin-coating process.[341] This process of annealing, and solvent evaporation from the perovskite film, usually takes up to 60 minutes.[141]

However, it was recently reported that some residual DMSO in MAPI layers might be beneficial for high homogeneity and to passivate recombination defects.[342] Also, longer exposure time to thermal annealing could induce thermal degradation in already formed MAPI films.[343] Additionally, the solvent concentration increases in the glovebox during spin coating due to the use of antisolvent treatment. This solvent-rich atmosphere can also influence film formation. For that reason, it could be argued that prolonged exposure to a solvent-saturated glovebox atmosphere might also be detrimental for the film formation during annealing, particularly regarding the devices prepared as the last ones in a batch. From those arguments, different annealing times were attempted within a batch: 60 min for the first half of the devices prepared and 20 min for the second half of the devices prepared.

As seen in **Table A**, the performance parameters' range of samples annealed for 60 min and 20 min were somewhat similar, excluding FF. The FF median value decreased by nearly 4 percentage points. That could be attributed to an incomplete crystallization process or presence of excessive residual solvent when annealing for only 20 min. As a result, a decrease in PCE was also seen showing that the annealing time of 60 min for the first half of the batch is the adequate protocol.

---

[2] This Appendix is a part of a Master thesis written by Gabrielle Sousa e Silva. She conducted this work in Helmholtz-Zentrum Berlin within my project to obtain the degree of Master of Science at the Technische Universität Berlin. Adapted with permission.

Table A. Performance parameters for 60 min and 20 min annealing times.

	Condition	**Jsc (mA/cm2)**	**Voc (V)**	**FF (%)**	**PCE (%)**
Median	60 min	21.1	1.040	73.1	16.1
	20 min	21.2	1.044	69.1	15.3
Minimum	60 min	20.5	0.974	62.4	13.5
	20 min	20.7	0.968	58.9	12.0
Maximum	60 min	21.5	1.094	76.3	17.1
	20 min	21.5	1.076	75.7	17.3

*These data refers to one batch of devices.

However, annealing time does not seem to be a determinant parameter. It remained unclear if the reduction in performance was only due to the shorter annealing time or whether it is a combination of the shorter annealing time employed and the higher solvent- saturated glovebox atmosphere in the second half of the batch. As a result, since the increase in solvent concentration inside the glovebox cannot be solved, and because annealing for 60 min did not seem to degrade the films thermally, it appears prudent establishing 60 min as the annealing time for an adequate crystallization process for the whole batch.

2. The effect of perovskite precursor solvents ratio

For solution-based technologies such as PSCs, the ‘solvent engineering technique’ can be seen as a fundamental approach to control the nucleation and crystal growth of the perovskites in order to achieve smooth and compact films with uniform surface morphology, which ultimately influences photovoltaic performance. Solvent engineering process was an important method to overcome the primary obstacles to improve further halide perovskite since its first appearance as a photovoltaic material. As an outcome, DMF-intermediate phase was found to be essential in perovskite precursor solutions, and DMSO became the most widely used solvent in combination with DMF for PSCs.[341]

As suggested by Zai *et al.*, the ideal mixture of solvent can vary with the perovskite composition employed.[344] That is because, DMF does not dissolve the inorganic perovskite precursor well while DMSO exhibits stronger polarity and coordination ability, which delays the fast interaction between the organic halide (MAI) and lead halide (PbI_2).[341] For that reason, aiming the best $MAPbI_3$ performance, the volume ratio of DMF and DMSO were optimised. Starting with a higher concentration of DMSO as DMF:DMSO 4:1, as it is employed for triple cation double halide perovskite,[141] following 6:1, 9:1, 12:1 and finally to no DMSO in the mixture (DMF:DMSO 1:0).

In **Figure A.1**, the box charts of the performance parameters show a clear trend of optimal characteristics for the mix DMF:DMSO 6:1, including better reproducibility. This result is in alignment to some extent with the literature on MAPI, which shows a ratio of DMF:DMSO as 85:15 as the optimum mixture of the solvents.[345] Additionally, the morphological analysis of the perovskite films using different solvent ratio corroborates with the findings regarding photovoltaic performance. In **Figure A.2**, it is seen the detrimental effect of reducing the DMSO content from the optimal ratio of 6:1, which presents a compact film morphology as well as big grain sizes, while upon decreasing DMSO the film does not present a definite crystalline structure but rather becoming an amorphous layer. Thus, the apparent bigger grain size for 9:1 ratio does not correlate with higher V_{OC} or J_{SC}. For these films made with more DMF, pinholes are seen in SEM images. The films cross-sectional SEM image shows voids as the perovskite layer detaches from the substrate. These are probably due to a rapid crystallisation process, trapping solvents in the interface with the substrate. Despite the discontinuity of the perovskite layer attaching to the PTAA layer, a considerable current density is achieved with these devices. However, the perovskite layer using only DMF in the precursor presents predominantly large disconnected regions which correlate with the plumping in Jsc and Voc values seen in the devices.

To conclude, those results agree with the literature that a minimum amount of DMSO, in this case 16.67% of the solvent mix volume, is necessary to allow the dissolution of the inorganic cation, which in this case is lead (Pb+2).

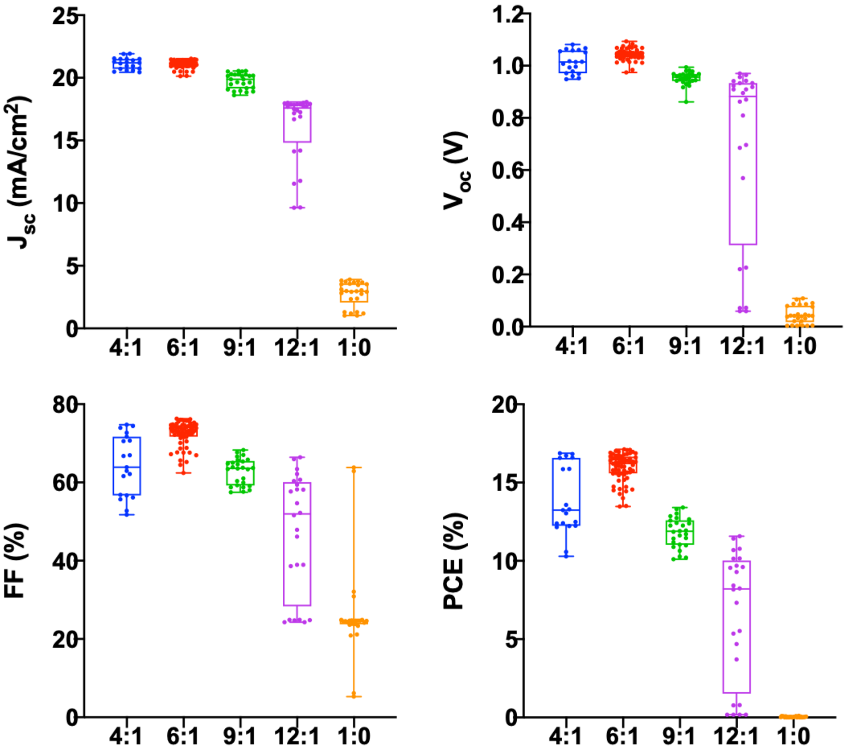

Figure A.1 Box charts of photovoltaic parameters upon solvent engineering. These data refers to two batches of devices.

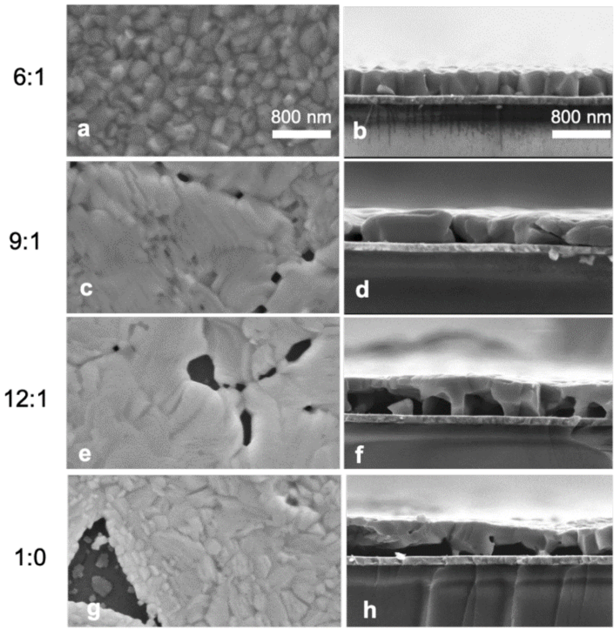

Figure A.2 SEM of films prepared with different solvent ratios (DMF:DMSO).

3. The role of antisolvent volume

The process of obtaining smooth and compact films in PSC is also related to the addition of an anti-solvent treatment, which can extract the precursor solvent.[200] Not several solvents can be employed as an antisolvent treatment in the p-i-n architecture since the layer below the absorber layer is the organic polymer PTAA, which should not be dissolved by the antisolvent employed, *e.g.* widely used chlorobenzene and toluene. The use of the solvent ethyl acetate (EA) was an outcome of the fabrication processes' development, as it substituted the former diethyl ether as the antisolvent for PSCs in inverted architecture.[87] The use of EA resulted in improved V_{OC} and PCE in comparison with diethyl ether. However, since the volume of antisolvent could also play a role in the film formation, different volumes of EA were tried to observe their effects on device performance. The volumes employed were: 400 µL, 500 µL, 600 µL and 700 µL.

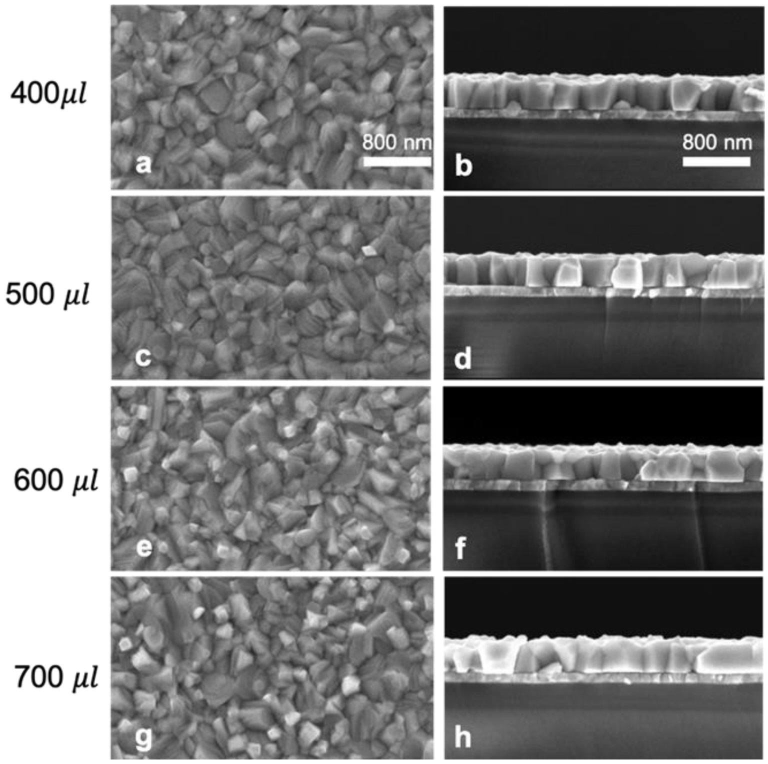

Figure A.3 SEM images of films prepared with different EA volumes. Respectively top view and cross-section of films prepared with increasing EA volume of (a)(b) 400 µL, (c)(d) 500 µL, (e)(f) 600 µL and (g)(h) 700 µL.

As it is shown in **Figure A.3**, the variation in antisolvent volume has a negligible effect on the film's morphology. Nevertheless, a higher number of small grains on the top of the layers with 600 µL and 700 µL of EA can be observed. The presence of those grains can be detrimental, since they act as superficial crystals, not monolithically grown from bottom to the top. Hence, the films are used in solar cells to check the performance.

As in **Figure A.4**, the performance parameters did not vary substantially, in alignment with the similar morphology obtained. The usage of 500 µL delivered the best median PCE. While the usage of 600 µL presented the highest current density, higher in 0.23mA/cm2 in comparison with 500 µL for the median values, its fill factor reduces. Hence, 500 µL EA is adopted to prepare $MAPbI_3$ layer in this project.

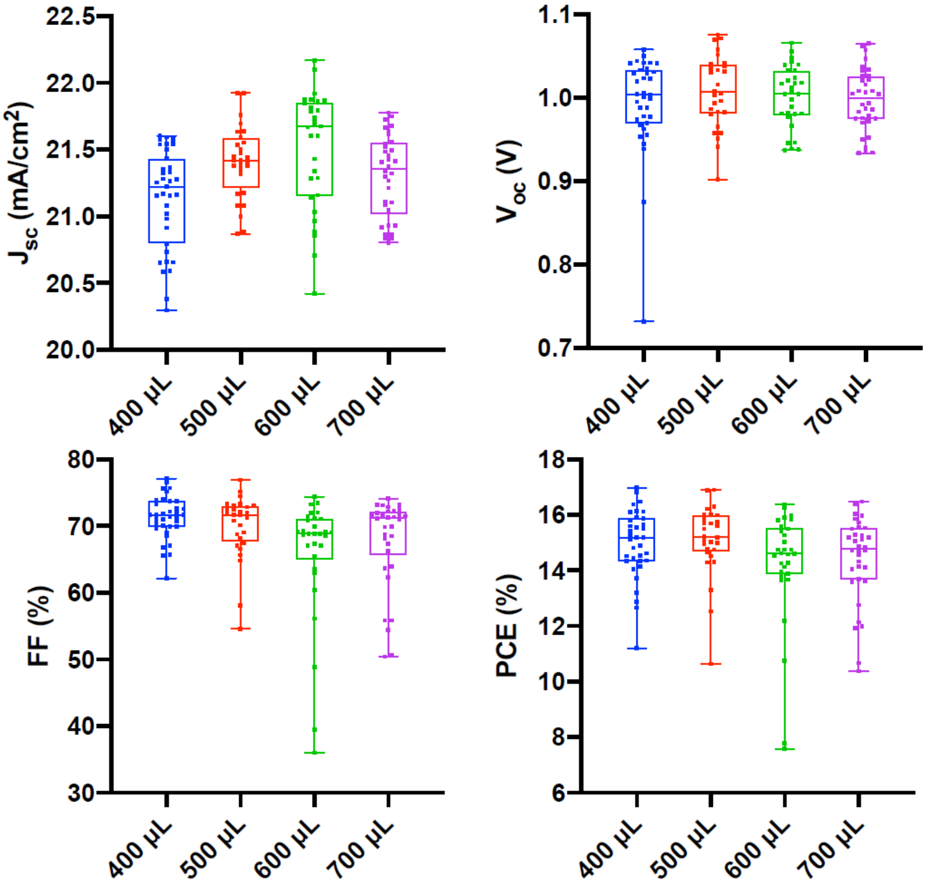

Figure A.4 Box charts of photovoltaic performance with increasing EA volume. These data refers to one batch of devices.

Reference

1. Jung, M.; Ji, S.-G.; Kim, G.; Seok, S. I., Perovskite precursor solution chemistry: from fundamentals to photovoltaic applications. *Chemical Society Reviews* **2019,** *48* (7), 2011-2038.
2. Saliba, M.; Matsui, T.; Seo, J.-Y.; Domanski, K.; Correa-Baena, J.-P.; Nazeeruddin, M. K.; Zakeeruddin, S. M.; Tress, W.; Abate, A.; Hagfeldt, A., Cesium-containing triple cation perovskite solar cells: improved stability, reproducibility and high efficiency. *Energy & environmental science* **2016,** *9* (6), 1989-1997.
3. Tan, Q.; Hinrichs, K.; Mao-Dong, H.; Fengler, S.; Rappich, J.; Prajongtat, P.; Nickel, N. H.; Dittrich, T., Temperature Dependent Diffusion of DMSO in CH3NH3PbI3 Precursor Films During Layer Formation and Impact on Solar Cells. *ACS Applied Energy Materials* **2019,** *2* (7), 5116-5123.
4. Juarez-Perez, E. J.; Hawash, Z.; Raga, S. R.; Ono, L. K.; Qi, Y., Thermal degradation of $CH_3NH_3PbI_3$ perovskite into NH_3 and CH_3I gases observed by coupled thermogravimetry–mass spectrometry analysis. *Energy & Environmental Science* **2016,** *9* (11), 3406-3410.
5. Zai, H.; Zhang, D.; Li, L.; Zhu, C.; Ma, S.; Zhao, Y.; Zhao, Z.; Chen, C.; Zhou, H.; Li, Y.; Chen, Q., Low-temperature-processed inorganic perovskite solar cells via solvent engineering with enhanced mass transport. *Journal of Materials Chemistry A* **2018,** *6* (46), 23602-23609.
6. Ren, Y.-K.; Liu, S.-D.; Duan, B.; Xu, Y.-F.; Li, Z.-Q.; Huang, Y.; Hu, L.-H.; Zhu, J.; Dai, S.-Y., Controllable intermediates by molecular self-assembly for optimizing the fabrication of large-grain perovskite films via one-step spin-coating. *Journal of Alloys and Compounds* **2017,** *705*, 205-210.
7. Dunlap-Shohl, W. A.; Zhou, Y.; Padture, N. P.; Mitzi, D. B., Synthetic approaches for halide perovskite thin films. *Chemical reviews* **2018,** *119* (5), 3193-3295.
8. Stolterfoht, M.; Wolff, C. M.; Márquez, J. A.; Zhang, S.; Hages, C. J.; Rothhardt, D.; Albrecht, S.; Burn, P. L.; Meredith, P.; Unold, T.; Neher, D., Visualization and suppression of interfacial recombination for high-efficiency large-area pin perovskite solar cells. *Nature Energy* **2018,** *3* (10), 847.

Appendix B

This appendix complies tables which are included in **Chapter 2** for general reference.

Table B.1 Optoelectronic properties of $MAPbI_3$ compared with established technologies, *i.e.* c-Si and GaAs. The values are taken from references number embedded in the table.

Parameters	$MAPbI_3$ polycrystalline film	c-Si (p-type)	GaAs
Charge carrier lifetime (ns)	628*	1000[11] (doping density $10^{14}cm^{-3}$)	19[12] (hole's in n-type with doping density $<10^{18}cm^{-3}$)
Diffusion length (μm)	1-2[13]	≈300[14-15]	6.6[16] (p-type)
Mobility ($cm^2V^{-1}s^{-1}$)	35[13]**	≈1300[17] (doping density $10^{15}cm^{-3}$)	≈7000 (doping density $10^{15}cm^{-3}$)
Urbach energy (meV)	15[10]	11[10, 18]	7.5[19]
Absorption coeffient at 550 nm (cm^{-1})	1e5[10]	6.39e03[20]	5e4[10]

*Measured value in this work (fitting from time resolved photoluminescence assuming intrinsic material)

**Summation of both holes and electrons

Table B.2 Ionic radii of A, B, X which can be used to calculate the possibility to form 3D halide perovskite.

	Ionic radii (pm)	Ref
$CH_3NH_3^+$	217	24
$HC(NH_2)_2^+$	253	
Cs^+	177	
Pb^{2+}	119	28
I^-	220	
Br	196	
Cl	181	

*Note: B and X ionic radii are in the octahedral coordination

Table B.3 Representative halide perovskite compounds and their crystal structure, space group, and lattice parameters.

Perovskite	Crystal structure	Space group	Lattice parameters	Ref
$CH_3NH_3PbI_3$ ($MAPbI_3$)	Orthorhombic (<165 K)	Pnma	a = 8.87 b = 12.63 c = 8.58	29
	Tetragonal (165-327 K)	I4/mcm	a = 8.81 b = 8.81 c = 12.71	
	Cubic (>327 K)	$Pm\bar{3}m$	a = 6.32 b = 6.32 c = 6.32	
$CH_3NH_3PbBr_3$ ($MAPbBr_3$)	Orthorhombic (<144.5 K)	$Pna2_1$	a = 7.97 b = 8.58 c = 11.85	30
	Tetragonal (149.5-155.1 K)	P4/mmm	a = 5.89 b = 5.89 c = 5.86	
	Tetragonal (155.1-236.9 K)	I4/mcm	a = 8.32 b = 8.32 c = 11.83	
	Cubic (>155 K)	$Pm\bar{3}m$	a = 5.90 b = 5. 90 c = 5. 90	
$CH_3NH_3PbCl_3$ ($MAPbCl_3$)	Orthorhombic (<172.9 K)	$P222_1$	a = 5.67 b = 5.63 c = 11.18	30
	Tetragonal (172.9-178.8 K)	P4/mmm	a = 5.66 b = 5.66 c = 5.63	
	Cubic (>178.8 K)	$Pm\bar{3}m$	a = 5.67 b = 5.67 c = 5.67	
$HC(NH_2)_2PbI_3$ ($FAPbI_3$)	Trigonal (<150 K)	P3	a = 17.79 b = 17.79 c = 10.90	31-32
	Hexagonal (293 K)	$P6_3mc$	a = 8.66 b = 8.66 c = 7.90	
	Trigonal (>393 K)	$P\bar{3}m1$	a = 8.98 b = 8.98 c = 11.00	
	Cubic (>393 K)	$Pm\bar{3}m$	a = 6.36 b = 6.36 c = 6.36	
$HC(NH_2)_2PbBr_3$ ($FAPbBr_3$)	Orthorhombic (<150 K)	Pnma	a = 8.37 b = 11.86 c = 8.38	33
	Tetragonal (150-275 K)	P4/mbm	a = 8.42 b = 8.42 c = 5.95	
	Cubic (>275 K)	$Pm\bar{3}m$	a = 5.99 b = 5.99 c = 5.99	
$HC(NH_2)_2PbCl_3$ ($FAPbCl_3$)	Cubic	$Pm\bar{3}m$	a = 5.67 b = 5.67 c = 5.67	34
$CsPbI_3$	Orthorhombic (<587 K)	Pbma	a = 6.10 b = 6.26 c = 6.25	35
	Orthorhombic (<450 K)	Pnma	a = 6.34 b = 5.61 c = 6.11	
	Tetragonal (450-550 K)	P4/mbm	a = 6.24 b = 6.24 c = 6.30	
	Cubic (>550 K)	$Pm\bar{3}m$	a = 6.30 b = 6.30 c = 6.30	
$CsPbBr_3$	Orthorhombic (<361 K)	Pnma	a = 8.24 b = 11.74 c = 8.20	36-38
	Tetragonal (361-403 K)	P4/mbm	a = 8.45 b = 8.45 c = 8.46	
	Cubic (>403 K)	$Pm\bar{3}m$	a = 6.02 b = 6.02 c = 6.02	
$CsPbCl_3$	Orthorhombic (<315 K)	Pnma	a = 5.75 b = 11.44 c = 8.09	39-41
	Tetragonal (315-320 K)	P4/mbm	-	
	Cubic (>320 K)	$Pm\bar{3}m$	a = 5.74 b = 5.74 c = 5.74	

Table B.4 Defect concentration and their depth inside the bandgap determined by experimental methods. Trap depth is with respect to conduction band minimum. Adpated with more data points from ref [68] under a a Creative Commons Attribution (CC BY) license.

Method	Defect concentration (cm^{-3})	Trap depth (eV)	Ref
Thermally stimulated current	$> 10^{15}$	0.5*	[69]
	9.14×10^{16}	0.18*	[70]
		0.49*	
	1.60×10^{16}	0.186*	[71]
Deep level transient spectroscopy	1.30×10^{15}	0.62	[64]
	3.90×10^{14}	0.75	
	9.50×10^{14}	0.76	
	8.81×10^{13}	0.78*	[72]
	5.24×10^{14}	0.78*	
	5.60×10^{12}	0.23	[73]
	6.90×10^{12}	0.5	
	1.20×10^{13}	0.59	
	1.30×10^{13}	0.6	
	1.80×10^{16}	0.49	[74]
	1.20×10^{14}	0.64	[75]
	3.70×10^{14}	0.75	
	2.80×10^{14}	0.81	
Thermal admittance spectroscopy	$\approx 10^{16}$	1.44	[76]
	$\approx 7.2 \times 10^{15}$	≈0.41	[77]

*The trap depth with respect to the band edge, however, not specified whether if it's CBM or VBM

Table B.5 Representative calculated values for the most stable intrinsic defects of MAPbI$_3$;[52, 54, 85] and extrinsic impurities (additives) in MAPbI$_3$ unless stated otherwiseBi,[86-87]Ni,[88]Al,[89] Ce,[90] Sb,[91] Mn,[92] Sr, Mg,[93] Ca, Co,[94] Cd,[95] Zn,[96] Fe,[97] Li,[98-100] Na,[101] Cu, Ag,[102] Au,[103] K,[104] Rb,[56] Cs.[105]

	Defect	Concentration (cm^3)	Defect formation energy (eV)	Energetic level	Proposed impacts on the material native defects
Point defects	$V_I^{\bullet}$	5×10^{20}	0.08	(0/+) Shallow near CBM	-
	V_{Pb}''		0.08	(-/2-) Shallow near VBM (0/2-); (0/-) Deep trap states	-
	V_{MA}'		0.16	(0/-); (0/2-) Shallow near VBM	-
	I_i'		0.32	(0/-) (-/+); (0/+) Deep trap states	-
	$Pb_i^{\bullet\bullet}$		1.03	(All oxidation states) Inside conduction band	-
	$MA_i^{\bullet}$		0.75		-
Pair defects	nil $\rightarrow V_{MA}' + V_{Pb}'' + 3V_I^{\bullet} + MAPbI_3$	2×10^{19}	0.14	-	-
	nil $\rightarrow V_{MA}' + V_I^{\bullet} + MAI$	2×10^{20}	0.08	-	-
	nil $\rightarrow V_{Pb}'' + 2V_I^{\bullet} + PbI_2$	8×10^{17}	0.22	-	-
Trivalent metals	$Bi_{Pb}^{\bullet}$ (in MAPbBr$_3$)	Up to 10%		(+/0) Shallow near CBM delocalised causing bandgap narrowing	
	$Bi_{Pb}^{\bullet}$ (in CsFAPbI$_3$)	Less than 1%		(+/0) Shallow near CBM delocalised (+/0) Deep trap states localised	
	Al^{3+}	0.15%			Assisting the growth resulted in more oriented film
	$Ce_{Pb}^{\bullet}$ (in CsPbBr$_3$)		<2 for all growth conditions	Shallow near CBM	
	$Sb_{Pb}^{\bullet}$	Up to 25% investigated		Deep trap states n-type doping	

Divalent	Ni^{2+}	Less than 10%			Absorbed into PbI_3' at grain boundary reducing deep trap
	Mg_{Pb}	Less than 5% to be included in the lattice	-0.11		No contribution to band edge n-doping at low doping regime due to reduction in V_{Pb}'' and V_{MA}' concentration
Divalent metals	Ca_{Pb}				Increase grain size, reducing the defect concentrations increasing V_{OC}
	Sr_{Pb}	Less than 1% to be included in the lattice	-0.24		No contribution to band edge n-doping at low doping regime due to reduction in V_{Pb}'' and V_{MA}' concentration
	Mn_{Pb}	Up to 3% can be included to the lattice			Slightly lower non-radiative recombination
	Co_{Pb}	Up to 3% to have positive impact		Modifying band edges. Introducing lattice defects at high concentrations	
	Cd_{Pb} (in $CsFAMAPb(I_xBr_{1-x})_3$	Around 2%			Increasing the harmful intrinsic defects formation energy (vacancies) by reducing lattice strain
	Zn_{Pb}	2.5%			Acting as reducing agents to prevent iodide defects formation
	$Fe_i^{\bullet\bullet}$	Up to 0.03% in perovskite without effects on device performance		Deep trap states	
Monovalent metal	$Li_i^{\bullet}$	Up to 10%	0.02-0.1		Occupying interstitial site: - Increasing background charge carrier (n-type doping), subsequently filling traps - Increasing the activation energy for ionic defect migration - Increasing the I Frenkel pair defect formation energy

	Na'_{Pb}			p-type doping (hole concentration increases significantly)	
	Cu'_{Pb} Ag'_{Pb}	0.1%		No state within the bandgap, however lattice distortion causes VBM and CBM positions change leading to Fermi level change (more intrinsic material)	Halide vacancies charge compensation
Monovalent metal	Au'_{Pb}		-0.31	Deep trap states	
	K^+	Up to 10% to have positive impact			Passivating halide vacancy Depleting bromide from the bulk
	Rb^+	5% as optimal			Promoting crystallisation Defect passivation
	Cs^+ (in $(MAPbBr_3)_{0.15}(FAPbI_3)_{0.85}$)	5% as optimal			Stabilising perovskite phase Promoting crystallisation

List of publications

First authorship peer-review publications

The Doping Mechanism of Halide Perovskite Unveiled by Alkaline Earth Metals

Nga Phung,[$] Roberto Félix,[$] Daniele Meggiolaro, Amran Al-Ashouri, Gabrielle Sousa e Silva, Claudia Hartmann, Juanita Hidalgo, Hans Köbler, Edoardo Mosconi, Barry Lai, Rene Gunder, Meng Li, Kai-Li Wang, Zhao-Kui Wang, Kaiqi Nie, Evelyn Handick, Regan G. Wilks, Jose A. Marquez, Bernd Rech, Thomas Unold, Juan-Pablo Correa-Baena, Steve Albrecht, Filippo De Angelis, Marcus Bär, Antonio Abate*

[§]These authors contribute equally

Status: Published (DOI: 10.1021/jacs.9b11637)

The Role of Grain Boundaries on Ionic Defect Migration in Metal Halide Perovskites

Nga Phung, Amran Al-Ashouri, Simone Meloni, Alessandro Mattoni, Steve Albrecht, Eva L. Unger, Aboma Merdasa,* Antonio Abate*

Status: Accepted (DOI: 10.1002/aenm.201903735)

Ion Migration-Induced Amorphization and Phase Segregation as a Degradation Mechanism in Planar Perovskite Solar Cells

Diego Di Girolamo,[§] Nga Phung,[§] Felix Utama Kosasih, Francesco Di Giacomo, Fabio Matteocci, Joel A. Smith, Marion A. Flatken, Silver H. Turren Cruz, Lucio Cinà, Alessandro Latini, Giorgio Divitini, Caterina Ducati, Aldo Di Carlo,* Danilo Dini,* and Antonio Abate*

§These authors contribute equally

Status: Under review

First authorship review and book chapter

The Impact of Nano- and Microstructure on the Stability of Perovskite Solar Cells

Nga Phung, Antonio Abate

Status: Published (DOI: 10.1002/smll.201802573)

Stability of materials and complete devices

*Chapter 9 from Characterization Techniques for Perovskite Solar Cell Materials

Nga Phung, Antonio Abate

Status: Published (DOI: 10.1016/B978-0-12-814727-6.00009-8)

Co-authored publications

Suppression of electron trapping in $MAPbI_3$ perovskite by Sr^{2+} doping

Rokas Jasiūnas, Rokas Gegevičius, Marius Franckevičius,* Nga Phung, Antonio Abate, Vidmantas Gulbinas

Status: Under review

From Bulk to Surface: Sodium Treatment Reduces Recombination at the Nickel Oxide/Perovskite Interface

Diego Di Girolamo, Nga Phung, Marko Jošt, Amran Al-Ashouri, Ganna Chistiakova, Junming Li, José A Márquez, Thomas Unold, Lars Korte, Steve Albrecht, Aldo Di Carlo, Danilo Dini, Antonio Abate

Status: Published (DOI: 10.1002/admi.201900789)

Unravelling fullerene–perovskite interactions introduces advanced blend films for performance-improved solar cells

Jorge Pascual, Silvia Collavini, Sebastian F Völker, Nga Phung, Elisa Palacios-Lidon, Lourdes Irusta, Hans-Jürgen Grande, Antonio Abate, Ramón Tena-Zaera, Juan Luis Delgado

Status: Published (DOI: 10.1039/C9SE00438F)

Enhancement in lifespan of halide perovskite solar cells

Qiong Wang, Nga Phung, Diego Di Girolamo, Paola Vivo, Antonio Abate

Status: Published (DOI: 10.1039/C8EE02852D)

Efficient and stable inorganic perovskite solar cells manufactured by pulsed flash infrared annealing

Sandy Sanchez, Neururer Christoph, Bernard Grobety, Nga Phung, Ullrich Steiner, Michael Saliba, Antonio Abate

Status: Published (DOI: 10.1002/aenm.201802060)

How to Make over 20% Efficient Perovskite Solar Cells in Regular (n–i–p) and Inverted (p–i–n) Architectures

Michael Saliba, Juan-Pablo Correa-Baena, Christian M Wolff, Martin Stolterfoht, Nga Phung, Steve Albrecht, Dieter Neher, Antonio Abate

Status: Published (DOI: 10.1021/acs.chemmater.8b00136)

Flash Infrared Annealing for Antisolvent-Free Highly Efficient Perovskite Solar Cells

Sandy Sanchez, Xiao Hua, Nga Phung, Ullrich Steiner, Antonio Abate

Status: Published (DOI: 10.1002/aenm.201702915)

International conference contributions

Oral contributions

nanoGe Fall Meeting 2019

Asia-Pacific International Conference on Perovskite, Organic Photo-voltaics and Optoelectronics (IPEROP 2019)

4th International Conference on Perovskite Solar Cells and Optoelectronics (PSCO18)

2018 (European Materials Research Society) E-MRS Fall Meeting

Poster contribution

11th International Conference on Hybrid and Organic Photovoltaics 2019 (HOPV 2019)

Title: Visualisation of ion movement in halide perovskite by photoluminescence

Acknowledgement

First and foremost, I would like to express my gratitude toward my PhD supervisor Dr. Antonio Abate for his tremendous support. Thank you for providing me guidance when I needed and for always being generous and considerate so that I could balance my personal life and my work. I am also grateful for the support of Prof. Dieter Neher so that I can reach my finish line.

On my journey, I cannot thank enough Dr. Aboma Merdasa for the scientific adventures (thank you for our long discussions/emails/midnight thoughts/random walk in literature review...), and above all for his constant encouragement. I also want to thank Gabrielle Sousa e Silva, Dr. Diego Di Girolamo, Amran Al-Ashouri, Ece Aktas, Maryam Sajedi for the great collaborations and for the friendships. Special thanks to Dr. Simone Meloni for clearing up my confusion about the defect fundamental physics.

To make my PhD even more enjoyable, I am surrounded by awesome people who I could spend my best times and endure my worst times with. For that, I am grateful to be in the same team with Joel A. Smith, Laura Canil, Marion A. Flatken, Dr. Jorge Pascual Mielgo, Dr. Silver Hamill Turren Cruz, Hans Köbler, Juanita Hidalgo, Dr. Thi Tuyen Ngo and other (visiting) members of EE-NMIP and HySPRINT laboratory who I cannot name all.

I have been very fortunate to be involved in a lot of collaborative projects and so could meet many people whom I am excited to work with. In addition, I would like to thank all the technicians of HySPRINT, X-ray Core Labs and the beamline scientists for their enormous assistance.

Last but not least, I am extremely thankful for my family. Without you, I will not be here.